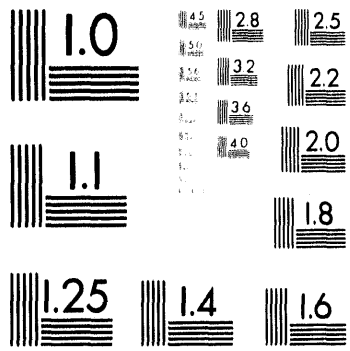
1.0
1.1
1.25
1.4
1.6
1.8
2.0
2.2
2.5
2.8
3.2
3.6
4.0
4.5
5.0

1 of 4

ornl

ORNL/TM-12389

OAK RIDGE
NATIONAL
LABORATORY

MARTIN MARIETTA

CCM
CONTINUITY CONSTRAINT METHOD:

A Finite-Element Computational Fluid Dynamics Algorithm
for Incompressible Navier-Stokes Fluid Flows

P. T. Williams

MANAGED BY
MARTIN MARIETTA ENERGY SYSTEMS, INC.
FOR THE UNITED STATES
DEPARTMENT OF ENERGY

ORNL/TM-12389

Computing Applications Division

CCM
CONTINUITY CONSTRAINT METHOD:

A Finite-Element Computational Fluid Dynamics Algorithm
for Incompressible Navier-Stokes Fluid Flows

P. T. Williams

This work was prepared as partial fulfillment of the
requirements for the degree of
Doctor of Philosophy in Engineering Science,
University of Tennessee, Knoxville,
May 1993.

September 1993

Prepared by the
OAK RIDGE NATIONAL LABORATORY
Oak Ridge, Tennessee 37831
managed by
MARTIN MARIETTA ENERGY SYSTEMS, INC.
for the
U.S. DEPARTMENT OF ENERGY
under contract DE-AC04-84OR21400

CONTENTS

CONTENTS (continued)

LIST OF FIGURES

FIGURE **PAGE**

LIST OF FIGURES (continued)

Figure **Page**

LIST OF FIGURES (continued)

Figure **Page**

LIST OF FIGURES (continued)

Figure **Page**

LIST OF TABLES

TABLE **PAGE**

NOMENCLATURE

a	acoustic celerity (sound speed)
a_c , a_{nb}	finite volume coefficients in SIMPLE method
a_{ij}	element located in row-i and column-j of matrix A
A	nxn matrix
A_e	face areas of finite volumes in SIMPLE method
A_j	kinematic flux vector jacobian
Ar	Archimedes number
b	right-hand-side "load" vector of linear algebra problem $Ax = b$
b_i	body force vector
$b(v_i , q)$	bilinear form
B	iteration matrix for Jacobi iteration
BW	matrix band width
c	artificial sound speed in pseudocompressibility method
c_p	mass-specific heat capacity
C_μ	constant in Prandtl-Kolmogorov relation
C_1 , C_2	constants in k-ε turbulence model
d_e	parameter in SIMPLE method
D	discrete divergence error, material derivative operator, diffusion matrix, diagonal matrix
D^s	generalized derivatives up to and including order s
DET_e	element-centered det J
e	internal energy
Ec	Eckert number

E_{ij}	element-centered metric data
f	kinematic flux vector
f^v	viscous flux vector
f_μ, f_1, f_2	wall proximity functions in turbulence model
F	barotropic equation of state
F_n	normal surface traction vector
F_t	tangential surface traction vector
$\|F(Q)\|$	Newton residual vector
$\mathcal{F}$	differential operator
g	acceleration of gravity
g	gravity vector
g_n	gravity unit vector
G	iteration matrix
Gr	Grashof number
$H^1(\Omega)$	Sobolev functional space
I	identity matrix
J	transformation jacobian
k	thermal conductivity, turbulent kinetic energy, iteration index
K^p	Krylov subspace of order p
l	Prandtl's mixing length
l_r	reference length scale
$L^2(\Omega)$	linear space of square-integrable functions
L	lower triangular matrix
M	partial differential equation operator, Gauss-Seidel iteration matrix

$\mathcal{L}_\omega$	SOR iteration matrix
m_p	number of fixed pressure degrees-of-freedom
m_u	number of fixed velocity degrees-of-freedom
M	mass matrix, preconditioning matrix
n	normal coordinate, total number of equations
n_i	boundary surface normal unit vector
n_p	number of pressure (continuity) equations
n_u	number of velocity equations
$\{N\}$	vector of element basis functions
p	pressure, iteration index
p_m	modified pressure
P	kinematic pressure, permutation matrix
Pe	Peclet number
Pr	Prandtl number
Pr^t	turbulent Prandtl number
PR	matrix profile
$\wp$	orthogonal projection operator
q	continuum state-variable
q_i	conduction heat transfer vector
q_{wall}	wall heat flux
Q	orthogonal projection operator, permutation matrix, splitting matrix, discrete state-variable
Q_i	approximation expansion coefficients
$\{Q\}$	discrete approximation of state-variables

Q_0	applied boundary heat flux
$\| q \|_k$	Sobolev norm
$\| q \|_0$	L^2 norm
r	number of degrees-of-freedom
r^p	pth residual vector
Ra	Rayleigh number
Re	Reynolds number
Re^t	turbulent Reynolds number
Re^+	turbulent wall coordinate
$\{R\}$	residual vector
s	source term
S	congruence transformation matrix
t	time
T	temperature
T_r	reference temperature
T_{wall}	wall boundary temperature
T_∞	ambient boundary temperature
u_i	velocity vector
u_n	outward normal velocity component at boundary
u_τ	tangential velocity component at boundary
u_r	reference velocity scale
u_Γ	normal boundary velocity on a staggered mesh
U	upper triangular matrix
$\{U\Gamma\}_e$	element velocity components

v_Γ	tangential boundary velocity on a staggered mesh
w_i	Dirichlet velocity data
WF	matrix wave front
x	vector of unknowns in linear algebra problem $Ax = b$
x_i	spatial coordinate
$\{XJ\}_e$	vector of nodal coordinate data
Z	subspace of solenoidal functions
Z^h	subspace of discrete solenoidal functions

Greek symbols

α	thermal diffusivity, artificial dissipation parameter, underrelaxation parameter in SIMPLE
α_k , β_k	conjugate gradient iteration parameters
α_p	underrelaxation parameter for pressure correction equation in SIMPLE
β	coefficient of volume expansion, splitting parameter, artificial dissipation parameter
γ	parameter in hybrid pseudocompressibility method
Γ	boundary
Γ_D	boundary where Dirichlet velocity data is specified
Γ_N	boundary where Neumann velocity data is specified
$\Gamma_{D\Theta}$	boundary where Dirichlet temperature data is specified
$\Gamma_{N\Theta}$	boundary where Neumann temperature data is specified
δ_{ij}	Kronecker delta
Δt	time step
ε	isotropic dissipation function, convergence tolerance

ε_{ij}	strain-rate tensor
ε'_{ij}	deviatoric strain-rate tensor
ε_{ijk}	permutation tensor
η_i	transform coordinates
θ	implicitness parameter
Θ	dimensionless potential temperature
Θ_0	Dirichlet potential temperature data
κ	bulk viscosity
λ	second coefficient of viscosity, penalty parameter
λ_i	eigenvalues of matrix A
μ	dynamic viscosity, first coefficient of viscosity
ν	kinematic viscosity
ν^t	turbulent eddy viscosity
ρ	density
ρ_p	Chebyshev acceleration parameters
ρ_r	reference density
ρ_0	constant reference density
σ_k , σ_ε	constants in k-ε turbulence model
σ_{ij}	Cauchy stress tensor
σ'_{ij}	deviatoric stress tensor
τ_i	boundary surface tangential unit vector
Φ	potential function, dissipation function
Φ_i	test function space
ψ	streamfunction, test function

Ψ_i	vector potential, approximation trial space
ω	vorticity, radian frequency, SOR iteration parameter
ω_i	vorticity vector
Ω	domain

ABSTRACT

As the field of computational fluid dynamics (CFD) continues to mature, algorithms are required to exploit the most recent advances in approximation theory, numerical mathematics, computing architectures, and hardware. Meeting this requirement is particularly challenging in incompressible fluid mechanics, where primitive-variable CFD formulations that are robust, while also accurate and efficient in three dimensions, remain an elusive goal. This dissertation asserts that one key to accomplishing this goal is recognition of the dual role assumed by the pressure, i.e., a mechanism for instantaneously enforcing conservation of mass and a force in the mechanical balance law for conservation of momentum. Proving this assertion has motivated the development of a new, primitive-variable, incompressible, CFD algorithm called the Continuity Constraint Method (CCM). The theoretical basis for the CCM consists of a finite-element spatial semi-discretization of a Galerkin weak statement, equal-order interpolation for all state-variables, a θ-implicit time-integration scheme, and a quasi-Newton iterative procedure extended by a Taylor Weak Statement (TWS) formulation for dispersion error control. Original contributions to algorithmic theory include: (a) formulation of the unsteady evolution of the divergence error, (b) investigation of the role of non-smoothness in the discretized continuity-constraint function, (c) development of a uniformly H^1 Galerkin weak statement for the Reynolds-averaged Navier-Stokes pressure Poisson equation, (d) derivation of physically and numerically well-posed boundary conditions, and (e) investigation of sparse data structures and iterative methods for solving the matrix algebra statements generated by the algorithm. In contrast to the general family of "pressure-relaxation" incompressible CFD algorithms, the CCM does not use the pressure as merely a mathematical device to constrain the velocity distribution to conserve mass. Rather, the mathematically smooth and physically-motivated genuine pressure is an underlying replacement for the non-smooth continuity-constraint function to control inherent dispersive-error mechanisms. Dominated by this dispersive-error mode, the non-smoothness of the discrete continuity-constraint function is proven to play a critical role in its ability to remove the divergence error in the discrete velocity distribution. The genuine pressure is calculated by the diagnostic pressure Poisson equation, evaluated using the verified solenoidal velocity field. This new separation of tasks also produces a genuinely clear view of the totally distinct boundary conditions required for the continuity-constraint function and genuine pressure. A broad range of 3-dimensional verification, benchmark, and validation test problems, as computed by the code CFDL.PHI3D, completes this dissertation.

1. INTRODUCTION

1.1 PURPOSE

As the field of computational fluid dynamics (CFD) continues to mature, new algorithms are required that are capable of exploiting the most recent advances in numerical mathematics, computing architectures, and hardware. This requirement is particularly true in the area of incompressible fluid mechanics, where there has been a continual interest in primitive-variable CFD formulations that are accurate, efficient, and robust in three dimensions. Since most incompressible fluid flows of practical engineering interest are turbulent and possibly unsteady, the issues of turbulence closure and time-accuracy must also be addressed. For turbulent flows, the promises of direct numerical simulation (DNS), where all of the relevant length scales are resolved with highly refined meshes, and large eddy simulation (LES), where the smallest length scales are modeled, have yet to be realized (Moin, 1992); therefore, some form of turbulence modeling based upon the Reynolds-averaged form of the Navier-Stokes (RANS) equations is necessary to approximate the effects of turbulence upon the mean flow. For a time-accurate solution in three dimensions, an implicit time-integration technique with its potential for high-order accuracy and larger usable time-steps is becoming the method of choice for current CFD algorithms.

1.2 APPLICATIONS

In the preface to his classic text on fluid dynamics, Batchelor (1967) explains why he chose to focus on incompressible fluids: "I regard flow of an incompressible viscous fluid as being at the centre of fluid dynamics by virtue of its fundamental nature and its practical importance." Whereas compressible fluids and irrotational flows tend to be the primary concern of aerodynamicists, applications for incompressible fluids and isochoric flows cut across the boundaries of almost every engineering discipline. The fields of industrial and environmental fluid mechanics are dominated by fluids for which the incompressibility condition is a valid assumption (Hunt, 1991).

Industrial fluid mechanics (IFM) covers those aspects of the design, manufacture, and operation of industrial products that are related to fluid-flow problems. Examples of IFM applications involving incompressible fluids include flows of liquids in chemical processing plants, recirculating cooling water in power plants, water flows in open channels, and air flows in the heating and ventilation of rooms and cooling of electrical equipment. Environmental fluid mechanics (EFM) refers to fluid motions in the lower atmosphere, in the ground, and in rivers, lakes, and seas that relate in some way to problems connected to the environment.

In a recent review paper, Hunt (1991) presents several examples of current industrial and environmental fluid-flow problems. Incompressible CFD plays an integral role in the solution process for many of these problems. For example, safety and accident analyses now rely on a combination of scale model experiments and computational experiments as a part of the "fluid-dynamicist's tool kit". Turbulence, heat transfer, forced convection, buoyancy-driven source terms, and mass transport of toxic and/or reacting (e.g., combustion reactions) materials are physical phenomena typically included in computational models.

The investigation of the disastrous fire at the King's Cross underground station is an important case-study of how fluid-flow problems associated with accidents and safety-related issues are now being studied and how the results of such EFM studies influence subsequent government decisions. On November 18, 1987, near the end of the evening rush-hour, a fire began beneath and near the entrance of a wooden upward-moving escalator located in a tunnel sloping up from the train platforms to the large ticket hall of King's Cross station, one of London's busiest underground and railway terminals. The fire burned slowly for about 15 minutes and then spread rapidly upward and ignited the escalator in the upper part of the tunnel. Intense fumes and smoke developed on the escalator and in the ticket hall. The fire killed 31 people and seriously injured over 80. The follow-up investigation focused on a number of key technical questions involving the growth and movement of the fire up through the tunnel. Included in these studies were experimental scale models and a computational model. The CFD analyses used the 3-dimensional incompressible finite volume code FLOW3D to simulate the motion of the turbulent flame front that flowed up the tunnel. It was postulated that the flame front was driven by the steady release of buoyant air at the original point of ignition of the fire and by air movement induced by arriving trains. The CFD model produced quantitative and qualitative data on the structure and speed of the resulting buoyant plume. These data assisted in the design and interpretation of subsequent scale-model experiments. "This investigation is just one example where fluid-dynamics computer codes have greatly helped in solving environmental and safety problems where there are many processes and the geometry of the flow is quite complex" (Hunt, 1991).

1.3 ORIGINAL CONTRIBUTIONS

Recognition of the dual role of the pressure in the incompressible Navier-Stokes conservation law system has motivated this investigation of a new time-accurate primitive variable CFD algorithm. Upon imposition of the incompressibility condition, the pressure assumes the dual roles of both a Lagrangian multiplier instantaneously enforcing an isochoric constraint on the flow field (conservation of mass) and of a dynamical state-variable acting as a part of the mechanical force balance law for the flow (conservation of linear momentum) (cf. Gresho and Sani, 1987, and Pelletier et al., 1989). The proposed algorithm accommodates both of these requirements by (1) applying a continuity-constraint potential function to enforce a robust conservation of mass and (2) using the derived Reynolds-averaged pressure Poisson equation with mathematically well-posed and physically-motivated Neumann boundary conditions to obtain an accurate and discretely continuous pressure solution.

A critical requirement for demonstrating the feasibility of this algorithm, as an accurate and cost-effective CFD finite-element technique, is its successful extension to 3-dimensional flows. As original contributions to the study of incompressible CFD, this dissertation presents:

(a) a derivation of an accurate expression for the unsteady evolution of the divergence error, thus providing a firm and exact theoretical foundation for the continuity-constraint algorithm,

(b) an investigation of the separate roles of the non-smooth continuity-constraint function, ϕ^h, and the smooth physically-motivated genuine pressure P^h,

(c) an investigation of the Galerkin weak statement for the Reynolds-averaged pressure Poisson equation, thus determining the required order of the Sobolev functional space for the turbulent diffusion (eddy viscosity) source term,

(d) an investigation and resolution of physically and numerically well-posed boundary conditions for the selected state-variable serving as the mass-conserving constraint function,

(e) an implementation of the CCM using a finite element semi-discretization of a Galerkin weak statement with an optional Taylor Weak Statement extension for Ω in $\mathbb{R}^3$,

(f) an efficient solution strategy for work-station-based computing,

(g) an investigation of sparse iterative solvers and sparse data structures for solving the terminal linear algebra problems required by the algorithm, and

(h) a verification and benchmarking for isothermal and nonisothermal test cases in $\mathbb{R}^3$.

1.4 SCOPE

A discussion of the mathematical formulations that constitute the conservation law system for incompressible fluids is presented in Chapter 2. In Chapter 3, a review of the history of computational methods for incompressible fluids and a summary of the current state-of-the-art for incompressible CFD algorithms are presented. The present method, the Continuity Constraint Method (CCM), is described in Chapter 4. Numerical linear algebra issues for the CCM are addressed in Chapter 5, and the resulting implementation on a UNIX workstation is discussed in Chapter 6. In Chapter 7, relevant 3-dimensional benchmarking studies used to validate the theory and implementation of the CCM are given, and, finally, conclusions and recommendations resulting from this research are presented in Chapter 8.

2. CONSERVATION LAW SYSTEM

In the continuum description of fluids, the governing physical equations can be grouped into four classes: (1) kinematic relations concerned only with the geometry of motion, (2) kinetics and mechanical balance laws relating forces (stresses) to motion (strain-rates), (3) thermodynamic principles producing equilibrium relations between heat, work, and system properties, and (4) constitutive laws which relate kinematic variables to kinetic variables for specific material groups (Reddy, 1986). The conservation law system for incompressible viscous fluids consists of a coupled set of partial differential equations that draw from all four categories. These physical laws are the conservation of mass, conservation of linear momentum, and conservation of energy. Even though the theoretical treatments by Navier (1822) and Stokes (1845) were concerned only with the mechanical balance laws (Lamb, 1932), the complete set of equations is now commonly referred to as the Navier-Stokes equations for Newtonian fluids. The details of the derivation of these equations can be found in any basic text on fluid or continuum mechanics, for example the books by Aris (1962), Batchelor (1967), Spencer (1980), Shames (1962), or White (1974). This chapter will present the equations in their general continuum forms and demonstrate how the incompressibility condition produces the specific equation set addressed by incompressible CFD algorithms.

2.1 INCOMPRESSIBILITY CONDITION

All fluids are compressible to a greater or lesser degree. By assuming the density is constant, the incompressibility condition represents an idealization of the physical behavior of liquids and gases for certain flow conditions and thermodynamic states. This idealization assumes that any density perturbations due to either pressure or temperature variations are sufficiently small to be negligible (Tritton, 1988). Small variations in density (due to temperature and/or species-concentration gradients) inducing buoyancy body forces can be accommodated under the incompressibility condition by adding buoyancy source terms to the momentum equations. The incompressibility condition requires that the kinetic equation of state for the fluid have a special barotropic form, specifically,

$$F(p, \rho) = F(\rho) = \rho - \rho_0 = 0 \tag{1}$$

where p is the thermodynamic (or thermostatic) pressure, and ρ_0 is the assumed constant density.

Rosenhead (1963) presents an extensive discussion of the conditions under which fluids may be considered incompressible. For steady and unsteady liquid flows, the absence of cavitation and liquid-vapor phase changes are the primary requirements for neglecting temperature and pressure effects. In order to exclude the effects of high frequency acoustic waves, the term $\omega L_r/a$ must be small, where ω is the radian frequency of small pressure waves, L_r is an appropriate length scale, and a is the acoustic celerity (speed). In gas flows, the frequency ω also refers to oscillations of any nearby solid boundaries. Again $\omega L_r/a$ must be small, implying a slowly varying flow. Three additional conditions must be met for gas flows: (1) a low Mach number, $U_r/a \leq 0.2$, (2) small relative temperature differences, $(T_{wall}-T_\infty)/T_\infty$, near boundaries , and (3) a small reference length scale, gL_r/a^2, relative to atmospheric length scales (for terrestrial gravitational effects) where $g = |g_i|$ is the magnitude of the gravitational acceleration vector.

2.2 CONSERVATION OF MASS

The principle of conservation of mass (or the continuity principle) states that, for a material body in motion, the total mass of the body remains unchanged during the motion. d'Alembert first developed the continuity equation in 1752 for the steady rotationally symmetric motion of a perfect gas, and its generalized form was derived by Euler in 1757 (Malvern, 1969).

The general form of the continuity equation is

$$\mathcal{L}(\rho) = \frac{1}{\rho}\frac{D\rho}{Dt} + \frac{\partial u_j}{\partial x_j} = 0 \tag{2}$$

where t is time, x_j is the spatial coordinate, ρ is the density, $u_i(x_j, t)$ is the velocity vector field, and $D(\cdot)/Dt$ is the material derivative operator defined as

$$\frac{D(\bullet)}{Dt} \equiv \frac{\partial(\bullet)}{\partial t} + u_j \frac{\partial(\bullet)}{\partial x_j} \tag{3}$$

In Eqs. (2)-(3) and throughout this dissertation, the Einstein index summation convention will be followed; that is, repeated latin indices imply summation over the dimension of the domain. From Eq. (2), the assumption of constant density results in

$$\mathcal{L}(\rho_0) = -\frac{1}{\rho_0}\frac{D\rho_0}{Dt} = \frac{\partial u_j}{\partial x_j} = 0 \tag{4}$$

where the divergence of the velocity field, $\partial u_j/\partial x_j$, is called the dilatation (expansion) rate. Therefore, for an incompressible fluid to conserve mass, its velocity vector field must necessarily be solenoidal, and its motion must be isochoric or volume preserving. One often sees references in the literature to *incompressible flows*. Strictly speaking, this is incorrect. A fluid may be considered incompressible, but the resulting flow is isochoric. Isochoric flows may also be produced by compressible fluids.

2.3 CONSERVATION OF MOMENTUM

Newton's second law of motion for a single mass particle can be extended to a system of mass particles, assuming that Newton's third law holds for the action and reaction of internal forces, to produce the momentum principle. In its continuum form, this principle is a basic postulate of continuum mechanics (Malvern, 1969). The conservation of linear momentum can be stated in terms of Cauchy's first law of motion,

$$\mathcal{L}(u_i) = \rho\frac{Du_i}{Dt} - \frac{\partial \sigma_{ij}}{\partial x_j} - \rho b_i = 0 \tag{5}$$

where ρb_i is a body-force vector field and σ_{ij} is the Cauchy stress tensor. Equation (5) is a mechanical balance law in that the inertial force of a material body, associated with the product of its mass and acceleration, is balanced by all external surface and body forces. If one assumes that the conservation of the moment of momentum (for the nonpolar case) also holds, then the symmetry of σ_{ij} can be deduced. When distributed moments exist in the fluid, Eq. (5) is still valid; however, the stress tensor is in general no longer symmetric.

A fundamental assumption in the formulation of Eq. (5) is that the continuum is viewed from an inertial (or Galilean) frame of reference. An inertial reference frame is one which is not accelerating. A rotating coordinate system is a special case of a non-inertial reference frame for which corrections to the accelerations terms in Eq. (5) are available. These corrections take the form of Coriolis ($2\omega\times\boldsymbol{u}$) and centrifugal ($\omega\times(\omega\times\boldsymbol{r})$) accelerations that are added to the inertial terms in Eq. (5), where ω is the angular velocity of the reference frame, and $\boldsymbol{r}$ is a position vector for the material particle under study. When Coriolis inertial forces represent dominant terms in the conservation of momentum, then the resulting condition produces *geostrophic* flows (Tritton, 1988).

2.4 CONSERVATION OF ENERGY

The energy equation arises from the energy-balance postulate of the first law of thermodynamics, wherein the time-rate of change of the total energy (kinetic plus internal energy) is equal to the sum of the work done on the system by all external forces and the heat transfer rate into the system from both external and distributed internal heat sources. First derived by Kirchhoff for a perfect gas in 1869 and for the general case in 1894, the energy equation takes the form

$$\mathcal{L}(e) = \rho\frac{De}{Dt} - \sigma_{ij}\epsilon_{ij} - \rho s + \frac{\partial q_j}{\partial x_j} = 0 \tag{6}$$

where e is the internal energy, s is the distributed heat generation, and q_i is the heat transfer rate by diffusion across the system boundaries. The stress power, $\sigma_{ij}\,\epsilon_{ij}$, is the external power input per unit volume not contributing to the change in kinetic energy. The strain-rate tensor ϵ_{ij} is defined by

$$\epsilon_{ij} \equiv \frac{1}{2}\left(\frac{\partial u_i}{\partial x_j} + \frac{\partial u_j}{\partial x_i}\right) \tag{7}$$

A more general energy equation can be developed by adding to Eq. (6) a relation for the conservation of mechanical energy. The balance law for mechanical energy, independent of any thermodynamic considerations, is also derivable from the conservation of momentum, Eq. (5), and expresses the principle that the rate of change of kinetic and potential energy is equal to the rate at which the translation forces do work on the system.

The second law of thermodynamics, as expressed mathematically by the Clausius-Duhem inequality (Yih, 1969), plays an important role in imposing restrictions upon the constitutive relations for the conservation law system.

2.5 CONSTITUTIVE RELATIONS

Cauchy's equation of motion, Eq. (5), holds for any continuum no matter how the stress tensor σ_{ij} is related to the strain rate. The relationship between the stress field and the corresponding motion is defined by the constitutive equations selected for the particular material to be modeled. The Navier-Stokes equations are derived for a class of fluids called Newtonian fluids, where a Newtonian fluid is a linear Stokesian fluid. The fundamental behavior of a linear Stokesian fluid is based upon the following assumptions (Aris, 1962):

(1) The Cauchy stress tensor σ_{ij} is a linear function only of the strain-rate tensor ε_{ij} and the local thermodynamic state.
(2) The fluid is homogeneous. The spatial distribution of the stress field is a function only of the positional variation of the strain rate and does not explicitly depend on x_i.
(3) The fluid is isotropic. There are no preferred directions, implying that the principal directions of σ_{ij} and ε_{ij} are the same.
(4) When the fluid is at rest, $\varepsilon_{ij} = 0$, and the state of stress is hydrostatic, $\sigma_{ij} = -p\delta_{ij}$, where δ_{ij} is the Kronecker delta.

The Navier-Poisson law (also called the Stokes viscosity law) for a Newtonian fluid, satisfying the above assumptions, is

$$\sigma_{ij} = -p\,\delta_{ij} + \lambda\,\epsilon_{kk}\,\delta_{ij} + 2\mu\,\epsilon_{ij} \tag{8}$$

where μ and λ are the first and second coefficients of viscosity, respectively. Note that the trace of the strain-rate tensor, ε_{kk}, is just the dilatation rate $\partial u_k/\partial x_k$. The simplest case for 1-dimensional shear flow is due to Newton (1687). The 3-dimensional cases were obtained by Navier (1822) for incompressible fluids using molecular models and by Poisson (1831) for the generalized form. The continuum theory is due to St.-Venant (1843) and Stokes (1845), (Malvern, 1969).

For compressible fluids, the variable p in Eq. (8) can be readily set equal to the thermodynamic pressure as defined by a suitable kinetic equation of state. The definition of p is more problematic for incompressible fluids. As a result of the incompressibility condition, the kinetic equation of state does not include the pressure; therefore, the pressure can be defined in the thermodynamic sense only as the limit point for a sequence of increasingly less compressible fluids. One, therefore, must view the pressure p in Eq. (8) as a dynamical (kinetic) variable (Aris, 1962). Some insight into the nature of p can be found by recasting Eq. (8) in terms of the stress and strain-rate deviators, defined by

$$\sigma'_{ij} \equiv \sigma_{ij} - \frac{\sigma_{kk}}{3}\delta_{ij} \quad ; \quad \epsilon'_{ij} \equiv \epsilon_{ij} - \frac{\epsilon_{kk}}{3}\delta_{ij} \tag{9}$$

Inserting Eqs. (9) into Eq. (8), one obtains

$$\sigma'_{ij} = -\left(p + \frac{\sigma_{kk}}{3}\right)\delta_{ij} + \left(\lambda + \frac{2}{3}\mu\right)\epsilon_{kk}\delta_{ij} + 2\mu\,\epsilon'_{ij} \tag{10}$$

Noting that for an incompressible fluid, $\varepsilon_{kk}=0$, and by definition the trace of the deviatoric stress and deviatoric strain-rate tensors is zero, one finds upon contraction of Eq. (10) that

$$p = -\frac{\sigma_{kk}}{3} \tag{11}$$

For an incompressible fluid, the pressure is a kinetic state-variable, dependent upon the flow and equal to the mean of the normal stresses at a point. Batchelor (1967) defines p as the *modified pressure* p_m, equal to the absolute pressure minus the pressure variation due to gravity and position (relative to some datum elevation). This modified pressure (also referred to as the *motion* pressure, Gebhart et al., 1988) arises strictly from the effect of the motion of the fluid.

In Eq. (10), the grouping $(\lambda + \frac{2}{3}\mu)$ is called the *bulk viscosity*, κ. For compressible fluids, it is a common practice (with important exceptions) to adopt the Stokes assumption and assume $\kappa=0$, primarily because κ is extremely difficult to determine (Yih, 1969). For incompressible fluids, the question is moot, since $\varepsilon_{kk}=0$, obviating the need to determine the second coefficient of viscosity, λ.

Collecting ideas, the Navier-Poisson stress-strain law for an incompressible Newtonian fluid can be stated as

$$\sigma_{ij} = -p\,\delta_{ij} + \mu\left(\frac{\partial u_i}{\partial x_j} + \frac{\partial u_j}{\partial x_i}\right) \tag{12}$$

Applying Eq. (12) to the diffusion term in the momentum equation gives, assuming constant μ,

$$\frac{\partial \sigma_{ij}}{\partial x_j} = \frac{\partial p}{\partial x_j}\delta_{ij} - \frac{\partial}{\partial x_j}\left(\mu\left(\frac{\partial u_i}{\partial x_j} + \frac{\partial u_j}{\partial x_i}\right)\right) = \frac{\partial p}{\partial x_i} - \mu\,\frac{\partial}{\partial x_j}\left(\frac{\partial u_i}{\partial x_j} + \frac{\partial u_j}{\partial x_i}\right) \tag{13}$$

The stress power term in the energy equation can also be transformed using Eq. (12).

$$\begin{aligned}\sigma_{ij}\epsilon_{ij} &= \left(-p\,\delta_{ij} + \mu\left(\frac{\partial u_i}{\partial x_j} + \frac{\partial u_j}{\partial x_i}\right)\right)\frac{1}{2}\left(\frac{\partial u_i}{\partial x_j} + \frac{\partial u_j}{\partial x_i}\right) \\ &= -p\,\epsilon_{ij}\delta_{ij} + 2\mu\,\epsilon_{ij}\epsilon_{ij}\end{aligned} \tag{14}$$

Replacing the strain rate in Eq. (14) with its unique deviatoric decomposition, i.e., the sum of a spherical (isotropic) tensor and the deviatoric strain-rate tensor,

$$\epsilon_{ij} = \frac{1}{3}\epsilon_{kk}\delta_{ij} + \epsilon'_{ij} \tag{15}$$

produces

$$\sigma_{ij}\,\epsilon_{ij} = -p\epsilon_{kk} + \frac{2}{3}\,\mu\,\epsilon_{kk}^2 + 2\,\mu\,\epsilon'_{ij}\,\epsilon'_{ij} = 2\,\mu\,\epsilon'_{ij}\,\epsilon'_{ij}$$
$$= \mu\,\frac{\partial u_i}{\partial x_j}\left(\frac{\partial u_i}{\partial x_j} + \frac{\partial u_j}{\partial x_i}\right) = \mu\,\Phi \qquad (16)$$

In Equation (16), it has been recognized that ϵ_{kk}, as the dilatation rate, is zero for an incompressible fluid. The term $\mu\Phi$ is the dissipation function (Yih, 1969) and represents the irreversible rate of transformation of mechanical energy into thermal energy due to viscous effects. A scaling analysis (Schlichting, 1979) shows that for small values of the dimensionless grouping Ec/Re, where Ec is the Eckert number ($= U_r^2/c_p\Delta T_r$), Re is the Reynolds number ($= U_r L_r/\nu$), and subscript "r" denotes a suitable reference or scale value, viscous dissipation may be neglected.

Focusing on the body force term, ρb_i, in Eq. (5), a commonly occurring body force is due to small local variations of density, caused typically by temperature and/or species-concentration gradients in a gravity field. Limiting consideration to temperature gradients, the density $\rho(T)$ is assumed to be a linear function of temperature T, obtaining

$$\rho(T) = \rho_r[\,1 - \beta(T - T_r)\,] \qquad (17)$$

where subscript "r" denotes a suitable reference state, and β is the coefficient of isobaric volume expansion, defined by

$$\beta = -\frac{1}{\rho}\left(\frac{\partial \rho}{\partial T}\right)_p \qquad (18)$$

For an ideal gas, $p=\rho RT$, and $\beta=1/T$. From Eq. (17), the body force ρb_i due to local density perturbations becomes

$$\rho\, b_i = -(\rho_r - \rho)\,g_i = -\rho_r\,\beta\,(T - T_r)\,g\,\hat{\mathbf{g}}_i \qquad (19)$$

where $g = |g_i|$ is the magnitude of the gravity vector and $\mathbf{g}_i$ is a unit vector in the direction of gravitational acceleration. Equation (19) is due to Oberbeck (1879) and Boussinesq (1903) and is typically referred to as the Boussinesq buoyancy approximation.

Using Eq. (17) to approximate the buoyancy body force appears to violate the incompressibility condition of constant density. This violation is considered acceptable if the density variations are sufficiently small to induce only buoyancy forces. Gebhart et al. (1988) present a scaling analysis, based upon a Taylor series expansion of $\rho_r(T_r) - \rho(T)$, that provides insight into the conditions for which the Boussinesq approximation is valid. They identified two dimensionless parameters that should be small relative to unity,

$$R_0 = \frac{g L_r}{g_c}\left(\frac{\partial \rho}{\partial p}\right)_T \qquad R_1 = \frac{\Delta \rho}{\rho_r} \qquad (20)$$

where g_c is a conversion constant. To ignore the modified-pressure effect on density, the parameter R_0 must be small. As an extreme case, pressure effects cannot be neglected for liquids near the

thermodynamic critical point of a vapor-liquid system. If the density variation is sufficiently linear in T for the temperature region of interest and the parameter R_l is small, then the Boussinesq approximation is valid. An interesting example for which the Boussinesq approximation is not appropriate is the case of a buoyancy-driven flow in cold water near 4°C, the point at which a density extremum occurs. Slightly above 4°C, β is positive, and slightly below 4°C, β is negative. The density variation near this temperature is significantly nonlinear, and the Boussinesq approximation should not be applied. A more extensive analysis into the suitability of the Boussinesq approximation for liquids and gases has been carried out by Gray and Giorgini (1976) in which they allowed all relevant properties to be linear functions of temperature. They identified eleven dimensionless parameters which must be small to validate the approximation.

The final term in the energy equation requiring a constitutive relation is the divergence of the conduction heat flux, q_i. Fourier's law of heat conduction (Yih, 1969) can be applied, introducing the transport property k, the thermal conductivity. Fourier's law states that

$$q_i = -k \frac{\partial T}{\partial x_i} \tag{21}$$

The divergence of the heat flux vector is, therefore,

$$\frac{\partial q_j}{\partial x_j} = -\frac{\partial}{\partial x_j}\left(k \frac{\partial T}{\partial x_j} \right) \tag{22}$$

Finally, the material derivative of the internal energy can be transformed into a term involving the fluid temperature (Batchelor, 1967) by

$$\rho \frac{De}{Dt} = \rho c_p \frac{DT}{Dt} \tag{23}$$

where c_p is the mass-specific heat capacity.

Applying the above constitutive relations and imposing the incompressibility condition, the Navier-Stokes equations are, upon expansion of the material derivative operators,

$$\mathfrak{L}(\rho_0) = \frac{\partial u_j}{\partial x_j} = 0 \tag{24}$$

$$\mathfrak{L}(u_i) = \frac{\partial u_i}{\partial t} + \frac{\partial}{\partial x_j}\left[u_j u_i - \nu\left(\frac{\partial u_i}{\partial x_j} + \frac{\partial u_j}{\partial x_i} \right) + \frac{p_m}{\rho}\delta_{ij} \right] + \left[\beta (T - T_r) g \right] \hat{\mathbf{g}}_i = 0 \tag{25}$$

$$\mathfrak{L}(T) = \frac{\partial T}{\partial t} + \frac{\partial}{\partial x_j}\left(u_j T - \alpha \frac{\partial T}{\partial x_j} \right) - \frac{\nu}{c_p}\Phi - \frac{1}{\rho c_p} s = 0 \tag{26}$$

where ν is the kinematic viscosity and α is the thermal diffusivity. Equations (25)-(26) are in *divergence* form where the incompressibility condition has been applied to allow the grouping of the advection and diffusion terms.

2.6 REYNOLDS-AVERAGED NAVIER-STOKES EQUATIONS

Most flows of engineering interest are turbulent. Turbulent flows are inherently 3-dimensional, nonlinear, and unsteady, exactly the conditions for which the Navier-Stokes equations have been derived. Equations (24)-(26) should in theory be able to predict the physics of turbulence for incompressible fluids. The difficulty arises due to the fact that turbulent motion is characterized by a large number of 3-dimensional vortex elements (eddies) varying in size and fluctuating over a range of frequencies (Haroutunian, 1988). Turbulence, therefore, involves a wide spectrum of length and time scales. This spectrum is so wide that it presents a computationally intractable problem. In order to attain approximate solutions for turbulent flows using CFD algorithms based upon Eqs. (24)-(26), spatial and time discretizations would need to be fine enough to capture the characteristics of the smallest dissipating eddies. For practical engineering analysis, the capacity of today's computers is unable to meet these requirements using a direct solution approach to turbulence. Such a direct approach, called direct numerical simulation (DNS) (Moin, 1992), is classified as one of the *Grand Challenges* of scientific computing, requiring the best available supercomputing capability.

The response to this dilemma has been a statistical approach in which the instantaneous state-variables are decomposed into mean and fluctuating parts. For the general state-variable q, this Reynolds decomposition can be represented mathematically as

$$q = \bar{q} + q' \tag{27}$$

where the overbar and superscript (′) denote mean and fluctuating values, respectively. Two statistical averaging procedures employed in incompressible turbulence theory are time-averaging and ensemble averaging. Time-averaging is expressed by

$$\bar{q} = \frac{1}{\Delta t_s} \int_{t_0}^{t_0 + \Delta t_s} q(\xi)\, d\xi \tag{28}$$

where t_0 is a reference point in time and Δt_s is a sampling interval. Ensemble averaging involves calculating the arithmetic average of the results of a series of N experiments (realizations) obtained under identical conditions. The ensemble average is

$$\bar{q} = \frac{1}{N} \sum_{k=1}^{N} q^k(t_n) \tag{29}$$

where $q^k(t_n)$ is the kth value of the state-variable obtained from a single realization t_n seconds after the beginning of the experiment. If the turbulence field is statistically stationary, then the ergodic hypothesis states that the two averaging methods produce identical results (Hinze, 1975). For nonstationary turbulence in which the time scales of the mean flow and the turbulent fluctuations are sufficiently different, then time-averaging is still a valid technique. If the nonstationary time scales overlap, then ensemble averaging must be used.

When a Reynolds decomposition is executed for the state-variables in Eqs. (24)-(26), specifically u_i, p_m, and T, and when the appropriate averaging technique is carried out, the resulting partial differential equations are the Reynolds-averaged Navier-Stokes conservation law system.

$$\mathfrak{L}(\rho_0) = \frac{\partial \bar{u}_j}{\partial x_j} = 0 \tag{30}$$

$$\mathfrak{L}(\bar{u}_i) = \frac{\partial \bar{u}_i}{\partial t} + \frac{\partial}{\partial x_j}\left[\bar{u}_j \bar{u}_i - \nu\left(\frac{\partial \bar{u}_i}{\partial x_j} + \frac{\partial \bar{u}_j}{\partial x_i}\right) + \overline{u_i' u_j'} + \frac{\overline{p_m}}{\rho_0}\delta_{ij}\right] + \left[\beta(\bar{T} - T_r)g\right]\hat{g}_i = 0 \tag{31}$$

$$\mathfrak{L}(\bar{T}) = \frac{\partial \bar{T}}{\partial t} + \frac{\partial}{\partial x_j}\left(\bar{u}_j \bar{T} - \alpha \frac{\partial \bar{T}}{\partial x_j} + \overline{u_j' T'}\right) - \frac{\nu}{c_p}\bar{\Phi} - \frac{1}{\rho_0 c_p}\bar{s} = 0 \tag{32}$$

The two second-moment statistical correlations, $\overline{u_i' u_j'}$ and $\overline{u_i' T'}$ in Eqs. (31) and (32), come from the nonlinear advection terms in the momentum and energy equations. These two double correlations are the turbulent Reynolds stresses ($-\rho \overline{u_i' u_j'}$) and the turbulent heat flux vector ($-\rho c_p \overline{u_i' T'}$). The inability to calculate them directly is the *turbulence closure problem*. Turbulence modeling consists of developing techniques to calculate approximations for the Reynolds stresses, thus providing an approximate closure for the Reynolds-averaged Navier-Stokes equations.

Excellent general reviews of turbulence modeling can be found in the books by Anderson et al. (1984) and Baker (1983), the monograph by Rodi (1980), and the review papers by Ferziger (1987), Nallasamy (1985), and Speziale (1991). Various methods of turbulence model classification have been used in the literature. One method depends upon the number of partial differential equations that must be solved, and another method focuses attention on the "order" of closure, referring to the order of the correlations that must be modeled through approximations and empirical data.

Transport equations for the Reynolds stresses can be derived from the Navier-Stokes equations (cf. Tennekes and Lumley, 1972; and Rodi, 1980) with the following result,

$$\begin{aligned}\mathfrak{L}(\overline{u_i' u_j'}) = {} & \frac{\partial \overline{u_i' u_j'}}{\partial t} + \frac{\partial u_k \overline{u_i' u_j'}}{\partial x_k} + \left(\overline{u_j' u_k'}\frac{\partial u_i}{\partial x_k} + \overline{u_i' u_k'}\frac{\partial u_j}{\partial x_k}\right) + 2\nu \frac{\overline{\partial u_i' \partial u_j'}}{\partial x_k \partial x_k} \\ & + \overline{\frac{p_m'}{\rho_0}\left(\frac{\partial u_i'}{\partial x_j} + \frac{\partial u_j'}{\partial x_i}\right)} + \frac{\partial}{\partial x_k}\left[\overline{u_i' u_j' u_k'} - \nu \frac{\overline{\partial u_i' \partial u_j'}}{\partial x_k} + \overline{\frac{p_m'}{\rho_0}(\delta_{jk} u_i' + \delta_{ik} u_j')}\right] \\ & + \beta\left(g_i \overline{u_j' T'} + g_j \overline{u_i' T'}\right) = 0\end{aligned} \tag{33}$$

The Reynolds-stress transport equations, Eq. (33), are a highly nonlinear PDE system containing even higher-order unknown correlations. The CFD group in Los Alamos (Daly and Harlow, 1970) and the

Imperial College group in London (Launder et al., 1975) were among the early researchers to develop second-order closure models based upon modeled forms of the transport equations for the Reynolds stresses.

At present, the most common methods of approximate turbulence closure are based upon the concept of a turbulent kinematic *eddy viscosity*, ν', due to Boussinesq (1877). The eddy viscosity approach uses a modeled constitutive equation relating the Reynolds-stress tensor and the mean flow strain-rate tensor. Accounting for invariance, the simplest (linearized) form, modeled after the Navier-Poisson constitutive relation, Eq. (12) , is

$$\overline{u_i' u_j'} = -\nu' \left(\frac{\partial \bar{u}_i}{\partial x_j} + \frac{\partial \bar{u}_j}{\partial x_i} \right) + \frac{2}{3} k \delta_{ij} \tag{34}$$

where k is the turbulent kinetic energy, equal to one-half of the trace of the Reynolds stress tensor. Equation (34) is known as the Boussinesq approximation for turbulence closure.

Based upon Reynolds-analogy arguments, the eddy viscosity can also be employed to produce closure for the Reynolds-averaged energy equation by introducing the turbulent Prandtl number, Pr' (≈ 1 for most turbulent flows). The modeled constitutive relation for the turbulent heat flux vector is

$$\overline{u_i' T'} = -\frac{\nu'}{Pr'} \frac{\partial \bar{T}}{\partial x_i} \tag{35}$$

With Eqs.(34) and (35), the momentum and energy equations become

$$\mathcal{L}(u_i) = \frac{\partial u_i}{\partial t} + \frac{\partial}{\partial x_j} \left[u_j u_i - (\nu + \nu') \left(\frac{\partial u_i}{\partial x_j} + \frac{\partial u_j}{\partial x_i} \right) + \left(\frac{p_m}{\rho_0} + \frac{2}{3} k \right) \delta_{ij} \right] + [\beta (T - T_r) g] \delta_i = 0 \tag{36}$$

$$\mathcal{L}(T) = \frac{\partial T}{\partial t} + \frac{\partial}{\partial x_j} \left[u_j T - \left(\alpha + \frac{\nu'}{Pr'} \right) \frac{\partial T}{\partial x_j} \right] - \frac{\nu}{c_p} \Phi - \frac{1}{\rho_0 c_p} S = 0 \tag{37}$$

For notational convenience, the overbars denoting mean-flow variables have been left off Eqs. (36) and (37). Unless stated otherwise, all state-variables in the sequel are for the mean flow.

Boussinesq-based turbulence models view the eddy viscosity as the product of a characteristic turbulent velocity and length scale. The modeling problem then becomes one of selecting methods for calculating these two scaling parameters. One of the simplest turbulence models (the zero-equation model) is based upon Prandtl's mixing-length theory (Prandtl, 1925), where the eddy viscosity is calculated by

$$\nu' = l^2 \left| \frac{\partial u_1}{\partial x_2} \right| \tag{38}$$

The length scale is l, Prandtl's mixing-length, described in the theory as the transverse distance over which fluid particles maintain their original momentum. Mixing-length models remain very popular, especially in external aerodynamics applications. The text by Cebici and Smith (1974) presents a detailed review of the method as it applies to compressible Navier-Stokes flows.

One-equation models continue to use the mixing-length as their length scale, but the velocity scale is related to the square root of the turbulent kinetic energy k, calculated by a transport equation derived from the Navier-Stokes equations. The one-equation models have not gained wide acceptance since their dependence on the mixing-length limits their application primarily to turbulent flows already adequately modeled by the simpler zero-equation models (Anderson et al., 1984). The additional effort in calculating k has produced results, when compared to mixing-length models, that have not proven to be computationally "cost-effective."

For internal flows, the two-equation models are among the more popular methods for turbulence closure. Among this class of methods, the k-ε (TKE) model, originally derived by Harlow and Nakayama (1967 and 1968), uses two transport equations to calculate both k and the isotropic dissipation rate ε. The velocity scale is again related to the square root of the turbulent kinetic energy, and the length scale is proportional to $k^{3/2}/\varepsilon$. Once both k and ε distributions have been calculated, the eddy viscosity is determined by the Prandtl-Kolmogorov relation,

$$\nu' = C_\mu \frac{k^2}{\varepsilon} \tag{39}$$

where C_μ is an empirically derived constant.

TKE systems can be categorized by the range of turbulence intensity they have been designed to model. The parameter characterizing turbulence level (distribution) is the turbulence Reynolds number (Re^t) defined by

$$Re^t = \frac{\nu'}{\nu} \tag{40}$$

For a laminar flow, $\nu'=0$ by definition; therefore, Re^t is also zero. For a fully turbulent incompressible boundary layer flow, Re^t will range smoothly from zero at a solid wall up to the order of 100-500 in the fully turbulent region.

High Reynolds number TKE models (Launder and Spalding, 1974) do not attempt to resolve the low Re^t regions near wall boundaries. To bridge the region containing the viscous sublayer, from the wall out to the fully turbulent boundary layer, high Reynolds number TKE models employ *wall functions* based upon logarithmic *law-of-the-wall* velocity profiles (White, 1974).

Low Reynolds number TKE models have been developed by several researchers (cf. Jones and Launder, 1972) to include the viscous sublayer in the computational domain through the use of special wall-proximity functions. Patel et al. (1985) published a review of a number of low Reynolds number TKE models. One of the more promising for nonisothermal flows is that of Lam and Bremhorst (1981). The TKE system of equations is

$$\nu' = C_\mu f_\mu \frac{k^2}{\epsilon} \tag{41}$$

$$\mathcal{L}(k) = \frac{\partial k}{\partial t} + \frac{\partial}{\partial x_j}\left[u_j k - \left(\nu + \frac{\nu'}{\sigma_k} \right) \frac{\partial k}{\partial x_j} \right] - \nu' \Phi + \epsilon = 0 \tag{42}$$

$$\mathcal{L}(\epsilon) = \frac{\partial \epsilon}{\partial t} + \frac{\partial}{\partial x_j}\left[u_j \epsilon - \left(\nu + \frac{\nu'}{\sigma_\epsilon} \right) \frac{\partial \epsilon}{\partial x_j} \right] - C_1 f_1 \frac{\epsilon}{k} \nu' \Phi + C_2 f_2 \frac{\epsilon}{k} \epsilon = 0 \tag{43}$$

The model parameters f_μ, f_1, and f_2 are wall-proximity functions dependent upon the local distribution of turbulence Reynolds number Re^t and a wall-proximity Reynolds number Re^* with definitions

$$\begin{aligned}
C_\mu &= 0.09 \\
C_1 &= 1.44 \\
C_2 &= 1.92 \\
\sigma_k &= 1.0 \\
\sigma_\epsilon &= 1.3 \\
f_\mu &= (1 - \exp(-0.0165 Re^*))^2 (1 + (20.5 C_\mu f_\mu / Re^t)) \\
f_1 &= 1 + (0.05/f_\mu)^3 \\
f_2 &= 1 - \exp(-(Re^t / C_\mu f_\mu)^2) \\
Re^t &= \nu' / \nu \\
Re^* &= \sqrt{k}\, y / \nu
\end{aligned} \tag{44}$$

where y is the normal distance from the wall. The positive-definite function Φ is identical to the kinematic term in the molecular viscous dissipation function, Eq (16), and acts as a production (source) term for both k and ϵ.

2.7 NONDIMENSIONAL FORMS

The nondimensionalization of the conservation law system is important for both theoretical and computational reasons. Nondimensional scaling provides one method of developing nondimensional groups that can provide physical insight into the importance of various terms in the PDE system. Computationally, nondimensional forms have the added benefit of providing numerical scaling of the discrete equations when producing the terminal linear algebra statement, thus providing a physically-linked technique for improving the ill conditioning of the equation system. Typical scaling rules for the Navier-Stokes equations are

$$x_j^* = \frac{x_j}{L_r} \qquad u_j^* = \frac{u_j}{U_r} \qquad t^* = \frac{t\,U_r}{L_r}$$

$$\Theta^* = \frac{T - T_r}{\Delta T_r} \qquad P^* = \frac{\left(\frac{p_m}{\rho_0} - \frac{2}{3}k\right)}{U_r^2} \qquad \mathrm{Pr}^t = \frac{\mu^t c_p}{k^t} \tag{45}$$

where k^t is the turbulent thermal conductivity and superscript "*" denotes a nondimensional variable. Applying the above scaling rules to Eqs. (24), (36), and (37), results in

$$\mathcal{L}(p_0) = \frac{\partial u_j^*}{\partial x_j^*} = 0 \tag{46}$$

$$\mathcal{L}(u_i^*) = \frac{\partial u_i^*}{\partial t^*} + \frac{\partial}{\partial x_j^*}\left[u_j^* u_i^* - \left(\frac{1 + \mathrm{Re}^t}{\mathrm{Re}}\right)\left(\frac{\partial u_i^*}{\partial x_j^*} + \frac{\partial u_j^*}{\partial x_i^*}\right) + P^* \delta_{ij}\right] + \mathrm{Ar}\,\Theta^* \hat{g}_i = 0 \tag{47}$$

$$\mathcal{L}(\Theta^*) = \frac{\partial \Theta^*}{\partial t^*} + \frac{\partial}{\partial x_j^*}\left[u_j^* \Theta^* - \frac{1}{\mathrm{Re}}\left(\frac{1}{\mathrm{Pr}} + \frac{\mathrm{Re}^t}{\mathrm{Pr}^t}\right)\frac{\partial \Theta^*}{\partial x_j^*}\right] - \frac{\mathrm{Ec}}{\mathrm{Re}}\Phi^* = 0 \tag{48}$$

where the nondimensional moduli are the Reynolds number (Re), Prandtl number (Pr), Archimedes number (Ar), Grashof number (Gr), Eckert number (Ec), and turbulent Reynolds number (Re^t), defined by

$$\mathrm{Re} = \frac{U_r L_r}{\nu} \qquad \mathrm{Pr} = \frac{\nu}{\alpha} \qquad \mathrm{Ar} = \frac{\mathrm{Gr}}{\mathrm{Re}^2}$$

$$\mathrm{Gr} = \frac{\beta g \Delta T_r L_r^3}{\nu^2} \qquad \mathrm{Ec} = \frac{U_r^2}{c_p \Delta T_r} \qquad \mathrm{Re}^t = \frac{\nu^t}{\nu}$$

In the sequel, the superscript "*" will be dropped, and all state-variables will be assumed nondimensional.

2.8 INITIAL AND BOUNDARY CONDITIONS

Equations (46)-(48) are a coupled set of mixed parabolic/hyperbolic nonlinear partial differential equations defining an initial-/boundary-value problem. The problem is well-posed upon definition of appropriate initial and boundary conditions. Assume that Ω is an open set of $\mathbb{R}^3$ with boundary closure Γ, where Ω is located locally on one side of a Lipschitzian Γ (Temam, 1983). For the velocity and pressure field, the boundary Γ is subdivided into Γ_g and Γ_h, where $\Gamma = \Gamma_g \cup \Gamma_h$ and $\Gamma_g \cap \Gamma_h = \emptyset$. A similar partitioning of Γ is required for the energy equation where $\Gamma_{g\theta}$ and $\Gamma_{h\theta}$ do not

necessarily coincide with Γ_f and Γ_s. Mathematically, the problem is to find $u_i(x_j,t)$, $P(x_j,t)$, and $\Theta(x_j,t)$ that satisfy Eqs. (47) and (48) in Ω and $\partial u_i/\partial x_i=0$ in Ω and on Γ (a kinematic constraint) subject to the boundary conditions for $t > 0$ of

$$\left.\begin{aligned} u_i(x_j,t) &= w_i(x_j,t) && x_j \in \Gamma_D \\ -P + \left(\frac{1+\mathrm{Re}^{\dagger}}{\mathrm{Re}}\right)\frac{\partial u_n}{\partial n} &= F_n(x_j,t) \\ \left(\frac{1+\mathrm{Re}^{\dagger}}{\mathrm{Re}}\right)\frac{\partial u_{t1}}{\partial n} &= F_{t1}(x_j,t) && x_j \in \Gamma_N \\ \left(\frac{1+\mathrm{Re}^{\dagger}}{\mathrm{Re}}\right)\frac{\partial u_{t2}}{\partial n} &= F_{t2}(x_j,t) \end{aligned}\right\} \tag{49}$$

$$\begin{aligned} \Theta(x_j,t) &= \Theta_0(x_j,t) && x_j \in \Gamma_{D\Theta} \\ \frac{1}{\mathrm{Re}}\left(\frac{1}{\mathrm{Pr}} + \frac{\mathrm{Re}^{\dagger}}{\mathrm{Pr}^{\dagger}}\right)\frac{\partial \Theta}{\partial x_j} n_j &= Q_0(x_i,t) && x_i \in \Gamma_{N\Theta} \end{aligned}$$

where u_n is the normal component of velocity (outward pointing n) and u_{t1} and u_{t2} are the two tangential velocity components on Γ_s (Gresho,1991). Given boundary data include w_i, F_n, F_{t1}, F_{t2}, Θ_0, and Q_0. For the special case of $\Gamma=\Gamma_f$ and $\Gamma_s=\emptyset$, no Dirichlet data exist for the pressure. The pressure is known only to within an arbitrary constant. Also, for this special case of $\Gamma=\Gamma_f$ and $\Gamma_s=\emptyset$, a solvability condition requires the global conservation of mass, i.e.,

$$\oint_{\Gamma} w_i n_i \, d\Gamma = 0 \quad \text{for } t > 0 \tag{50}$$

A more general definition for no-slip boundaries allows no relative tangential velocity between the fluid and the wall, i.e., $\varepsilon_{ijk} u_j w_k = 0$ ($u \times w = 0$) (Tritton, 1988).

The initial conditions are

$$\frac{\partial u_j(x_i,0)}{\partial x_j} = 0 \qquad x_i \in \Omega$$

$$\frac{\partial u_j(x_i,0)}{\partial x_j} = 0 \qquad x_i \in \Gamma$$

$$u_j(x_i,0)\, n_j = w_j\, n_j \qquad x_i \in \Gamma_D$$

$$-P + \left(\frac{1 + \mathrm{Re}^{\dagger}}{\mathrm{Re}} \right) \frac{\partial u_n}{\partial n} = F_n(x_i,0) \qquad x_i \in \Gamma_n \tag{51}$$

$$\Theta(x_i,0) = \Theta_0(x_i,0) \qquad x_i \in \Gamma_{D\Theta}$$

$$\frac{1}{\mathrm{Re}} \left(\frac{1}{\mathrm{Pr}} + \frac{\mathrm{Re}^{\dagger}}{\mathrm{Pr}^{\dagger}} \right) \frac{\partial \Theta}{\partial x_j}\, n_j = Q_0(x_i,0) \qquad x_i \in \Gamma_{N\Theta}$$

The above mathematical initial and boundary conditions must eventually be translated into the various physical conditions addressed by CFD. Boundaries on which velocities may be fully defined (Γ_D) include no-slip walls and prescribed inflow planes. Partial specification of velocities occurs at tangency, symmetry, and entrainment boundaries. Neumann boundaries can occur at outflow planes.

2.9 PRESSURE POISSON EQUATION

Even though the modified pressure does not appear in the kinetic equation of state, a Poisson equation for the pressure may be derived from the momentum equations. Assuming the necessary smoothness, the divergence operator is applied to the momentum equations to produce

$$\mathcal{L}(P) = \frac{\partial}{\partial x_i} (\mathcal{L}(u_i)) =$$

$$\frac{\partial}{\partial x_i} \left(\frac{\partial u_i}{\partial t} - \frac{1}{\mathrm{Re}} \frac{\partial^2 u_i}{\partial x_j \partial x_j} \right) + \tag{52}$$

$$\frac{\partial}{\partial x_i} \left\{ \frac{\partial P}{\partial x_i} + u_j \frac{\partial u_i}{\partial x_j} - \frac{\partial}{\partial x_j} \left[\frac{\mathrm{Re}^{\dagger}}{\mathrm{Re}} \left(\frac{\partial u_i}{\partial x_j} + \frac{\partial u_j}{\partial x_i} \right) \right] + \mathrm{Ar}\, \Theta\, \hat{g}_i \right\} = 0$$

Equation (52) can be further simplified, assuming the continuity constraint is satisfied to obtain

$$\mathcal{L}(P) = \frac{\partial^2 P}{\partial x_i \partial x_i} + \frac{\partial u_j}{\partial x_i} \frac{\partial u_i}{\partial x_j} - \frac{\partial^2}{\partial x_i \partial x_j} \left[\frac{\mathrm{Re}^{\dagger}}{\mathrm{Re}} \left(\frac{\partial u_i}{\partial x_j} + \frac{\partial u_j}{\partial x_i} \right) \right] + \mathrm{Ar} \frac{\partial \Theta}{\partial x_i} \hat{g}_i = 0 \tag{53}$$

The fundamental assumptions implied by Eq. (53) are that both the velocity and the acceleration vector fields are solenoidal.

Physically-motivated boundary conditions for the pressure Poisson equation can be derived (Orszag et al., 1986 and Gresho and Sani, 1987) by projecting the momentum equations onto Γ_D. Two basic options for this projection are available, the normal direction (outward-pointing) and two tangential directions. Projection onto the normal direction produces a Neumann boundary condition for Eq. (53):

$$\frac{\partial P}{\partial n} = \frac{\partial}{\partial x_j}\left[\left(\frac{1 + \mathrm{Re}^{-1}}{\mathrm{Re}}\right)\frac{\partial u_n}{\partial x_j}\right] - \frac{\partial u_n}{\partial t} - u_j\frac{\partial u_n}{\partial x_j} - \mathrm{Ar}\,\Theta\,\hat{g}_n \qquad (54)$$

The tangential projection with subsequent integration over the boundary surface results in a Dirichlet pressure boundary. Gresho and Sani (1987) demonstrate that the Neumann boundary condition will produce solutions for the pressure field that also satisfy the tangential boundary conditions. In addition, the Neumann boundary condition applies for both $t = 0$ and $t > 0$ and maintains a solenoidal acceleration.

3. REVIEW OF INCOMPRESSIBLE CFD ALGORITHMS

The robust enforcement of the conservation of mass is the primary challenge for incompressible CFD algorithms. All admissible solutions to the momentum equations must satisfy the solenoidal kinematic constraint, $\partial u_i/\partial x_i=0$. This constraint is so critical that a taxonomy for incompressible algorithms, presented in Table 1, can be developed based upon the method chosen for conserving mass. The two broad classifications are *exact* enforcement and *inexact* (or approximate) enforcement of the continuity constraint. This chapter presents a brief sketch of the incompressibility problem and a summary of some of the more popular methods that have been developed over the last thirty years.

3.1 INCOMPRESSIBILITY – THE PROBLEM

Enforcing the kinematic constraint of a divergence-free (solenoidal) vector field poses special problems for any discrete approximation method. The problem, called the *div-stability* condition (Boland and Nicolaides, 1983), is independent of any nonlinearities in the Navier-Stokes equations; for example, it manifests itself in the linear Stokes problem in fluid mechanics and the incompressible elasticity problem in solid mechanics. If one attempts to produce approximate solutions (independent of the method, e.g., finite difference, finite volume, or finite element) for the incompressible Navier-Stokes equations without satisfying or in some way circumventing the div-stability condition, the results can be unstable and/or nonphysical velocity vector fields and spurious pressure solutions. Various approaches have been developed to understand and explain the nature of the problem, ranging from detailed mathematical descriptions using the tools of functional analysis to physical intuition.

Gunzburger (1989a) presents a readable description of the div-stability problem as it relates to the method of weighted residuals in its finite element Galerkin weak statement form for the isothermal Navier-Stokes equations. Following Gunzburger, one begins with a few mathematical preliminaries by defining some functional spaces.

For a domain Ω in $\mathbb{R}^1$ with boundary closure $\partial\Omega=\Gamma$, $L^2(\Omega)$ is the linear space of functions that are square-integrable (in the Lebesgue sense) over Ω, defined by

$$L^2(\Omega) = \{q: \int_\Omega q^2\, d\Omega < \infty\} \tag{55}$$

$L^2(\Omega)$ comes equipped with the usual inner product and norm,

$$(p,q) = \int_\Omega pq\, d\Omega \quad ; \quad \|q\|_0 = (q,q)^{1/2} \tag{56}$$

The subspace $L_0^2(\Omega)$ is constrained to include functions with zero mean over Ω.

Table 1. Taxonomy of Incompressible Navier-Stokes CFD Algorithms

CONTINUITY ENFORCEMENT	METHOD	ORIGINS	ISSUES/ DETRACTIONS
EXACT WITH VORTICITY	VORTICITY/ STREAMFUNCTION	Fromm, 1963 (FDM) Baker, 1973 (FEM)	Practical for 2D only Vorticity BC at walls
	VORTICITY/ VECTOR POTENTIAL	Aziz and Hellums, 1967	BC's for vector potential vorticity BC
	VORTICITY/VECTOR SCALAR POTENTIALS	Aregbesola and Burley, 1977	6 DOF/node in 3D vorticity BC
	VORTICITY/ VELOCITY	Fasel, 1976 (2D) Dennis et al., 1979 (3D)	6 DOF/node in 3D vorticity BC
EXACT	*u-P* Direct (mixed finite elements)	Ladyzhenskaya, 1969 Babuska, 1973 Brezzi,1974	Ill-conditioned numerical diffusion
INEXACT-ALGEBRAIC	PENALTY	Temam, 1968 Zienkiewicz et al., 1975	Ill-conditioned Reduced integrations
INEXACT-INITIAL VALUE	PSEUDO-COMPRESSIBILITY	Chorin, 1967	Steady-state only Numerical diffusion
INEXACT-BOUNDARY VALUE PROBLEM	MAC/SMAC	Harlow and Welch, 1965	Staggered mesh Velocity BC
	PROJECTION	Chorin, 1968 Temam, 1969	Staggered or non-staggered meshes BC implementation
	SIMPLE, SIMPLER, SIMPLEC, SIMPLEST	Patankar and Spalding, 1972	Staggered mesh, slow convergence, BC implementation
	VELOCITY CORRECTION	Schneider et al., 1978	Equal-order finite element, explicit with lumped mass matrix
	PISO	Issa, 1985 and 1986	2-step predictor corrector, staggered mesh, BC, pressure
	OPERATOR SPLITTING	Glowinski, 1985	decouples nonlinearity from incompressibility
	PRESENT	Williams, Noronha, Baker, 1990-	Implicit, equal-order, time-accurate, finite element Galerkin weak statement

$$L_0^2(\Omega) \equiv \{ q \in L^2(\Omega) : \int_\Omega q \, d\Omega = 0 \} \tag{57}$$

The Sobolev space $H^k(\Omega)$ is defined as

$$H^k(\Omega) \equiv \{ q \in L^2(\Omega) : D^s q \in L^2(\Omega) \text{for } s = 1, \ldots, k \} \tag{58}$$

where k is a non-negative integer and D^s denotes all generalized derivatives up to and including order s. The Sobolev norm is

$$\| q \|_k \equiv \left(\| q \|_0^2 + \sum_{s=1}^{k} \| D^s q \|_0^2 \right)^{1/2} \tag{59}$$

The constrained subspace $H_0^1(\Omega)$ requires q=0 on the boundary Γ, such that

$$H_0^1(\Omega) \equiv \{ q \in H^1(\Omega) : q = 0 \text{ on } \Gamma \} \tag{60}$$

where $H_0^1(\Omega)$ is equipped with the norm

$$\| q \|_1 \equiv \left(\| q \|_0^2 + \sum_{i=1}^{n} \left\| \frac{\partial q}{\partial x_i} \right\|_0^2 \right)^{1/2} \tag{61}$$

and the norm-equivalent energy semi-norm

$$| q |_1 \equiv \left(\sum_{i=1}^{n} \left\| \frac{\partial q}{\partial x_i} \right\|_0^2 \right)^{1/2} \tag{62}$$

The classic Galerkin weak statement for the isothermal Navier-Stokes equations is as follows. One seeks the functions $u_i(x_j, t) \in H_0^1(\Omega)$ and $P(x_j, t) \in L_0^2(\Omega)$ such that

$$\int_\Omega v_j \mathcal{L}(u_i) \, d\Omega = 0 \qquad \forall \, v_j \in H_0^1(\Omega) \tag{63}$$

$$\int_\Omega q \, \frac{\partial u_j}{\partial x_j} \, d\Omega = 0 \qquad \forall \, q \in L_0^2(\Omega) \tag{64}$$

where $\mathcal{L}(u_i)$ are the momentum equations in the canonical form as given by Eq.47. Equation (64) requires that all admissible velocity solutions, $u_i(x_j, t) \in H_0^1(\Omega)$, must also reside in the constrained (solenoidal) subspace Z, defined by

$$Z \equiv \{ v_i \in H_0^1(\Omega) : \; b(v_i, q) = 0 \quad \forall \, q \in L_0^2(\Omega) \} \tag{65}$$

where $b(v_i, q)$ is a bilinear form describing the *weak* satisfaction of the solenoidal constraint on v_i defined by

$$b(v_i,q) \equiv -\int_\Omega q \frac{\partial v_i}{\partial x_i}\, d\Omega \qquad \forall\, v_i \in H^1(\Omega), q \in L^2(\Omega) \tag{66}$$

Up to this point, all functional spaces have been infinite-dimensional, and the Galerkin weak statement, Eqs. (63) and (64), is expressed for the continuum Navier-Stokes equations. Assume that by some method, e.g., the finite-element method, approximate solutions (u_i^h) to the discrete Galerkin weak statement have been obtained, where $u_i^h \in V_0^h$ and $P^h \in S_0^h$ satisfy

$$\begin{aligned} &\int_\Omega v_j^h \mathfrak{L}^h(u_i^h)\, d\Omega = 0 \quad \forall\, v_j^h \in V_0^h \\ &\int_\Omega q^h \frac{\partial u_i^h}{\partial x_i^h}\, d\Omega = 0 \quad \forall\, q^h \in S_0^h \end{aligned} \tag{67}$$

The superscript "h" denotes a dependence on some measure of the mesh, the discrete approximation to the domain Ω. The finite-dimensional spaces V_0^h and S_0^h are the subspaces from which admissible approximating functions are selected for u_i^h and P^h.

The fundamental problem for the incompressible Navier-Stokes equations is that $V_0^h \subset H_0^1$ and $S_0^h \subset L_0^2$ alone are not sufficient conditions to produce stable approximate solutions. Define Z^h to be the subspace of discretely divergence-free functions, such that

$$Z^h = \{ v_i^h \in V_0^h : \quad b(v_i^h, q^h) = 0 \quad \forall\, q^h \in S_0^h \} \tag{68}$$

The dilemma arises from the fact that, in general, $Z^h \not\subset Z$, i.e., discretely solenoidal functions are not necessarily solenoidal in the limit as $h \to 0$. Based upon the theoretical work of Ladyzhenskaya (1969), Babuska (1973), Babuska and Aziz (1972), and Brezzi (1974), a stability condition has been developed ensuring, as $h \to 0$, that discretely divergence-free functions tend to solenoidal functions in Z.

The div-stability condition, also known as the LBB or *inf-sup* condition, states that, for a given pair of approximating functional spaces S_0^h and V_0^h, if there exists a positive real number $\gamma > 0$ such that

$$\inf_{0 \neq q^h \in S_0^h} \sup_{0 \neq v_i^h \in V_0^h} \left(\frac{b(v_i^h, q^h)}{|v_i^h|_1 \, \|q^h\|_0} \right) \geq \gamma \tag{69}$$

then the discrete solutions $u_i^h \in V_0^h$ and $P^h \in S_0^h$ to Eqs. (63) and (64) will be stable. The selection of interpolation functions for the velocity and pressure approximations that satisfy the div-stability condition is the basis for the *mixed finite-elements* methods (Stenberg, 1987). An analogous div-stability condition also exists for finite-difference methods, of course, and the well-known staggered-mesh technique is one method of producing a stable solution (Gunzburger, 1989a).

Zienkiewicz (1977) and Schneider and Raithby (1980) present the div-stability problem in terms of an over-constraint condition caused by the lack of an independent equation for the pressure. As an illustration, a Galerkin-type discretization of Eqs. (67) for a steady, isothermal flow produces a Newton linear algebra statement as

$$\begin{bmatrix} [JUU]_{3n\times 3n}, & [JUP]_{3n\times n} \\ [JUU*]_{n\times 3n}, & [0]_{n\times n} \end{bmatrix} \begin{Bmatrix} \{\delta U\}_{3n\times 1} \\ \{\delta P\}_{n\times 1} \end{Bmatrix} = - \begin{Bmatrix} \{FU\}_{3n\times 1} \\ \{FU*\}_{n\times 1} \end{Bmatrix} \tag{70}$$

where $[JUU]$ and $[JUP]$ are the Jacobian submatrices arising from the momentum equations. The submatrix $[JUU^*]$ is the contribution to the Jacobian produced by the continuity constraint. Before the application of boundary conditions, there are the same number of equations as unknowns. For a problem in $\mathbb{R}^3$ and assuming an equal-order interpolation of the velocity and pressure, there are $3n$ equations from the momentum equations and n equations from the continuity equation, where n is the total number of nodes in the mesh. With equal-order interpolation, the velocity components and the pressures are evaluated at the same locations for all nodes. Before any Dirichlet boundary conditions are applied, the number of equations ($4n$) is, therefore, equal to the number of unknowns, 3 velocity components and the pressure per node.

Typically, one considers the equations produced by the momentum conservation law to be associated with the velocity-component degrees-of-freedom, and the equations produced by the continuity constraint to be associated with the pressure degree-of-freedom. One procedure for invoking Dirichlet velocity or pressure data is to delete the corresponding degree-of-freedom from the Jacobian and to adjust the right-hand-side residual to reflect the specified values for the velocities and pressures. Let m_u be the number of fixed-velocity degrees-of-freedom, and m_p be the number of fixed-pressure degrees-of-freedom. The number of velocity equations to be solved is now $n_u = 3n-m_u$, and the number of pressure (continuity) equations to be solved is $n_p=n-m_p$. The resulting linear algebra statement is

$$\begin{bmatrix} [JUU]_{n_u\times n_u}, & [JUP]_{n_u\times n_p} \\ [JUU*]_{n_p\times n_u}, & [0]_{n_p\times n_p} \end{bmatrix} \begin{Bmatrix} \{\delta U\}_{n_u\times 1} \\ \{\delta P\}_{n_p\times 1} \end{Bmatrix} = - \begin{Bmatrix} \{FU\}_{n_u\times 1} \\ \{FU*\}_{n_p\times 1} \end{Bmatrix} \tag{71}$$

To prevent the system, Eq. (71), from being overdetermined, the following conditions must be met.

$$\begin{aligned} n_u + n_p &\geq n_u \\ n_u &\geq n_p \end{aligned} \tag{72}$$

Satisfaction of $n_u+n_p\geq n_u$ is of course trivial; however, satisfaction of the condition $n_u\geq n_p$ is dependent upon the degree of interpolation for the velocity and the pressure. Equal-order interpolation for the coupled system of Eq. (71) will in general produce an overdetermined (singular) system of equations, i.e., more equations than unknowns. The singularity can be removed by using an interpolation degree for the pressure that is less than the velocity interpolation. Let r be the total number of degrees-of-freedom for the pressure using a lower degree interpolation such that $r<n$; therefore, n_p is now $r-m_p$, and the condition $n_u\geq n_p$ can be met. Similar reasoning is used to explain the need for reduced integration techniques in the penalty method (Zienkiewicz, 1977), to be discussed in the sequel.

3.2 EXACT CONTINUITY ENFORCEMENT WITH VORTICITY

Vorticity, as a derived state-variable, plays a major role in many incompressible CFD formulations. By taking the curl of the momentum equations and applying a vector identity, $\nabla\times\nabla P=0$,

the pressure can be removed from the conservation law system, thus allowing the automatic enforcement of the continuity constraint. The following sections describe the primary ways in which vorticity has been used to obtain solutions for the incompressible Navier-Stokes equations in 2- and 3-dimensions.

3.2.1 Vorticity-Streamfunction

The vorticity-streamfunction formulation was among the first unsteady, incompressible Navier-Stokes CFD algorithms. The original finite-difference algorithm was developed at Los Alamos (Fromm, 1963 and 1964), and the first finite-element implementation is due to Baker (1973). By eliminating the pressure as a state-variable and enforcing continuity with a vector potential, the method automatically produces an exact mass-conserving velocity field. Arakawa (1966) employed the vorticity-streamfunction method to carry out an early investigation into instabilities associated with dispersive errors (which he termed "noodling") arising from the advection terms. A thorough review of boundary condition issues can be found in Roache (1972), Gupta and Manohar (1979), Baker (1983), Quartapelle and Napolitano (1984), Gunzburger (1989a), and Gresho (1991). The formulation is not limited to incompressible fluids as demonstrated by the compressible implementation of Leonardi and Reizes (1981).

For a 2-dimensional domain (three-dimensional extensions are presented in the next section), assume the flow is isothermal, $Re^{-1}=0$, and μ is constant. Taking the curl of Eq. 47 in $\mathbb{R}^2$, dropping the buoyancy term, and applying the continuity constraint produces the Helmholtz vorticity transport equation in conservative form, as

$$\mathcal{L}(\omega) = \frac{\partial \omega}{\partial t} + \frac{\partial}{\partial x_j}\left(u_j \omega - \frac{1}{Re}\frac{\partial \omega}{\partial x_j} \right) = 0 \tag{73}$$

where ω is the x_3-component of vorticity, defined in $\mathbb{R}^2$ by

$$\omega = \nabla \times \boldsymbol{u} \cdot \mathbf{k} = \epsilon_{ij3} \frac{\partial u_j}{\partial x_i} = \frac{\partial u_2}{\partial x_1} - \frac{\partial u_1}{\partial x_2} \tag{74}$$

where ϵ_{ijk} is the permutation tensor.

The pressure is eliminated from Eq. (73) due to the vector identity

$$\nabla \times \nabla P = \epsilon_{ij3} \frac{\partial}{\partial x_i}\left(\frac{\partial P}{\partial x_j} \right) = \frac{\partial^2 P}{\partial x_1 \partial x_2} - \frac{\partial^2 P}{\partial x_2 \partial x_1} = 0 \quad \text{in } \mathbb{R}^2 \tag{75}$$

Continuity is automatically enforced by defining the vector potential, $\psi\mathbf{k}$, as

$$\begin{gathered} \boldsymbol{u} = \nabla \times \psi \mathbf{k} \\ u_i = \epsilon_{ij3} \frac{\partial \psi}{\partial x_j} = \epsilon_{i23} \frac{\partial \psi}{\partial x_2} + \epsilon_{i13} \frac{\partial \psi}{\partial x_1} \\ u_1 = \frac{\partial \psi}{\partial x_2} \; ; \quad u_2 = -\frac{\partial \psi}{\partial x_1} \end{gathered} \tag{76}$$

Both the vector potential (streamfunction) and the vorticity are automatically solenoidal in 2-dimensions since the only non-zero scalar components lie perpendicular to the flow plane. With the vector identity

$$\begin{aligned} \nabla \times (\nabla \times \psi \mathbf{k}) &= \nabla(\nabla \cdot \psi \mathbf{k}) - \nabla^2 \psi \mathbf{k} \\ &= -\nabla^2 \psi \mathbf{k} \qquad \text{for } \nabla \cdot \psi \mathbf{k} = 0 \end{aligned} \tag{77}$$

the curl of Eq. (76) produces the kinematic compatibility equation tying the streamfunction ψ (and thus the continuity constraint) to the vorticity.

$$\mathcal{L}(\psi) = \nabla^2 \psi + \omega = 0 \qquad \text{in } \mathbf{R}^2 \tag{78}$$

Equation (73), with the velocity replaced by its vector potential, becomes

$$\mathcal{L}(\omega) = \frac{\partial \omega}{\partial t} + \frac{\partial}{\partial x_j}\left(\epsilon_{ji} \frac{\partial \psi}{\partial x_i} \omega - \frac{1}{\mathrm{Re}} \frac{\partial \omega}{\partial x_j} \right) = 0 \qquad \text{in } \mathbf{R}^2 \tag{79}$$

Closure has, therefore, been obtained with a Poisson equation, Eq. (78), coupled to a nonlinear transport equation for the vorticity, Eq. (79). Completion of the initial-/boundary-value problem requires the specification of well-posed initial and boundary conditions. The primary difficulties are due to the required specification of the vorticity at no-slip walls (Baker, 1983) and of the streamfunction at interior no-slip boundaries in multi-connected domains (Gunzburger, 1989a). In both instances, the boundaries require Dirichlet data that are known only as the solution evolves.

Recently, investigators have had success in not specifying any vorticity boundary conditions at all (Gresho, 1991). The idea is that the streamfunction alone carries all the necessary boundary information and that there are no boundary conditions for the vorticity. An early paper describing this method is by Campion-Renson and Crochet (1978). As an example, assume the vorticity-streamfunction equations are to be solved as a coupled system for a domain Ω with boundary closure $\Gamma = \Gamma_1 \cup \Gamma_2$, where Γ_1 is the union of all boundary segments on which both ψ and $\partial\psi/\partial n$ are known but ω is not, e.g., wall boundaries, and Γ_2 is the union of all boundary segments on which both ψ and ω are known, e.g., inflow and outflow planes. Let N be the total number of nodes in the mesh with p nodes on Γ_1 and q nodes on Γ_2. The total number of degrees-of-freedom on the interior of the domain is $2(N-p-q)$, and the total number on the boundary is p unknown vorticities on Γ_1. The total degrees-of-freedom is, therefore, $2N-p-2q$. Campion-Renson and Crochet cast Eqs. (78) and (79) into a finite element Galerkin weak statement formulation. When the Green-Gauss theorem is applied to the Galerkin weak statement for Eq. (78), the natural boundary condition is related to the normal derivative of ψ. This natural boundary condition, $\partial\psi/\partial n$, is employed as a forcing function for the equations from Eq. (78) that are associated with the p nodes on Γ_1. For the q nodes on Γ_2, the known ψ data can be applied, leaving $N-q$ independent equations from Eq. (78). Values for ω and the normal derivative of ω are unknown on Γ_2. The Galerkin weak statement for Eq. (79) produces $N-p-q$ independent equations with Dirichlet data for ψ being applied on the $p+q$ nodes on Γ_1 and Γ_2. There are, therefore, $2N-p-2q$ independent equations and $2N-p-2q$ unknowns; therefore, the problem is closed. Campion-Renson and Crochet present solutions for flow in a lid-driven cavity up to a Re=400 and flow in a channel with a step.

It is possible to eliminate the vorticity from the formulation by applying the kinematic compatibility equation, Eq. (78), to Eq. (79), producing

$$L(\psi) = \frac{\partial}{\partial t}\left(\frac{\partial^2 \psi}{\partial x_k \partial x_k}\right) + \frac{\partial}{\partial x_j}\left(\epsilon_{ijk}\frac{\partial \psi_k}{\partial x_i}\frac{\partial^2 \psi}{\partial x_k \partial x_k}\right) - \frac{1}{Re}\frac{\partial^4 \psi}{\partial x_j \partial x_i \partial x_k \partial x_k} = 0 \quad in \ R^3 \tag{80}$$

Equation (80) is an initial-value, biharmonic equation for the streamfunction. The difficulty posed by a fourth-order partial differential equation for finite element algorithms is that conforming elements must be C^1 continuous at interelement boundaries, e.g., triangular elements using incomplete quintic polynomial basis functions (Huang and Olson, 1978), and the approximation subspace must be $\Psi^h \subset H_0^2(\Omega)$. Gunzburger (1989a) presents a review of both conforming and nonconforming algorithms for the biharmonic streamfunction equation.

3.2.2 Vorticity with a Vector Potential

The natural extension of the vorticity-streamfunction method into 3-dimensions is the vorticity with a vector potential (Aziz and Hellums, 1967). The vector potential (streamvector, Ψ) is defined as

$$\begin{aligned} u &= \nabla \times \Psi \\ u_i &= \epsilon_{ijk}\frac{\partial \Psi_k}{\partial x_j} \end{aligned} \tag{81}$$

In R^3, the vorticity is a vector field defined by

$$\begin{aligned} \omega &= \nabla \times u \\ \omega_i &= \epsilon_{ijk}\frac{\partial u_k}{\partial x_j} \end{aligned} \tag{82}$$

The vorticity transport equation in R^3 is, therefore,

$$L(\omega_i) = \frac{\partial \omega_i}{\partial t} - \omega_j\frac{\partial u_i}{\partial x_j} + \frac{\partial}{\partial x_j}\left(u_j\omega_i - \frac{1}{Re}\frac{\partial \omega_i}{\partial x_j}\right) = 0 \tag{83}$$

where the new second term in Eq. (83) represents 3-dimensional "vortex stretching". Vortex stretching serves as a redistribution mechanism between the three components of vorticity. Taking the curl of Eq. (81)

$$\begin{aligned} \omega &= \nabla \times u = \nabla \times (\nabla \times \Psi) \\ \omega_i &= \epsilon_{imn}\frac{\partial u_n}{\partial x_m} = \epsilon_{imn}\frac{\partial}{\partial x_m}\left(\epsilon_{njk}\frac{\partial \Psi_k}{\partial x_j}\right) \end{aligned} \tag{84}$$

and employing the vector identity $\nabla \times (\nabla \times \Psi) = \nabla(\nabla \cdot \Psi) - \nabla^2 \Psi$ with Ψ required to be solenoidal, the Poisson equations relating the vector potential to the vorticity are

$$\nabla^2 \Psi = -\omega$$
$$\frac{\partial^2 \Psi_i}{\partial x_k \partial x_k} = -\omega_i \qquad (85)$$

Equations (81), (83), and (85) are the basis for the vorticity-vector potential method.

Aziz and Hellums (1967) used an alternating-direction-implicit (ADI) method to solve the vorticity transport equations and the successive over-relaxation (SOR) iterative method to solve the Poisson equations. Their validation case was a 3-dimensional, fully-confined cavity natural convection problem.

The *method of false transient* (Mallinson and de Vahl Davis, 1973, and de Vahl Davis and Mallinson, 1976) is a modification of the vorticity-vector potential formulation where false transient terms are added to Eqs. (85), resulting in a completely parabolic system of equations that can be solved by marching through a nonphysical transient. Upon convergence, the transient terms become negligible, and the true steady-state solution is obtained. The method is related to Chorin's *pseudocompressibility* formulation (to be discussed) in that it provides an iterative technique for steady-state solutions.

3.2.3 Vorticity with Vector and Scalar Potentials

Difficulties in specifying boundary conditions for the vector potential led to the development of the vorticity with vector and scalar potentials formulation (Aregbesola and Burley, 1977, and Richardson and Cornish, 1977), which is based upon the Helmholtz decomposition of the velocity vector field into potential and divergence-free components. Specifically,

$$\mathbf{u} = -\nabla\Phi + \nabla \times \Psi$$
$$u_i = -\frac{\partial \Phi}{\partial x_i} + \epsilon_{ijk} \frac{\partial \Psi_k}{\partial x_j} \qquad (86)$$

where Φ and Ψ are the velocity scalar and vector potentials, respectively. Existence proofs for both the scalar and vector potentials are provided by Hirasaki and Hellums (1970). The vector potential is again required to be solenoidal, and, by the vector identity $\nabla \cdot \nabla\Phi = 0$, the scalar potential is irrotational. Taking the divergence of Eq. (86) for a solenoidal velocity field and noting the vector identity $\nabla(\nabla \cdot \Psi) = 0$ produces Laplace's equation for $\mathcal{L}(\Phi)$. The curl of the defining relation for the vorticity again produces $\mathcal{L}(\Psi_i)$. The governing equations for the vorticity-vector and scalar potential method are, therefore,

$$\mathcal{L}(\Phi) = \frac{\partial^2 \Phi}{\partial x_k \partial x_k} = 0 \qquad (87)$$

$$\mathcal{L}(\omega_i) = \frac{\partial \omega_i}{\partial t} + \frac{\partial}{\partial x_j}\left(u_j \omega_i - \frac{1}{\mathrm{Re}} \frac{\partial \omega_i}{\partial x_j} \right) - \omega_j \frac{\partial u_i}{\partial x_j} = 0 \qquad (88)$$

$$\nabla^2(\Psi_i) = \frac{\partial^2 \Psi_i}{\partial x_k \partial x_k} + \omega_i = 0 \tag{89}$$

The continuity constraint is thus satisfied automatically by the scalar potential.

Aregbesola and Burley (1977) assumed that the normal velocities at all boundaries are known. The boundary condition for Φ is

$$\frac{\partial \Phi}{\partial n} = u_i n_i = u_n \tag{90}$$

where n is the outward-pointing normal. The boundary conditions for the vector potential are chosen such that the tangential components of Ψ for a planar boundary are zero. Since Ψ is required to be solenoidal, the resulting boundary conditions are

$$\Psi_t = \frac{\partial \Psi_n}{\partial n} = 0 \tag{91}$$

Values for vorticity at boundaries are calculated during the iterative cycle using the current velocity data and the defining relation for the vorticity, Eq (82). Tangential velocities at the boundaries are calculated from the scalar and vector potentials by Eq (86).

The vorticity-vector and scalar potential method continues to be the subject of research. Yang and Camarero (1991) investigated the problem of boundary conditions for general curved duct flow using a body-fitted curvilinear coordinate system. Their outflow boundary conditions were

$$\frac{\partial \Phi}{\partial n} = v_0 \qquad \frac{\partial^2 \omega_t}{\partial n^2} = 0 \qquad \frac{\partial^2 \Psi_t}{\partial n^2} = 0 \tag{92}$$

where v_0 is the mean velocity at the outlet.

3.2.4 Vorticity with Velocity

The vorticity-velocity formulation dispenses with all scalar and vector potential functions. Fasel (1976) first introduced the algorithm for 2-dimensional flows, and Dennis et al. (1979) extended it to three dimensions. Taking the curl of the defining relation for the vorticity and imposing the continuity constraint produces

$$\begin{aligned} \nabla \times \boldsymbol{\omega} &= \nabla \times (\nabla \times \boldsymbol{u}) = \nabla(\nabla \cdot \boldsymbol{u}) - \nabla^2 \boldsymbol{u} = -\nabla^2 \boldsymbol{u} \\ \epsilon_{ijk} \frac{\partial \omega_k}{\partial x_j} &= \epsilon_{ijk} \frac{\partial}{\partial x_j}\left(\epsilon_{kmn} \frac{\partial u_n}{\partial x_m}\right) = \frac{\partial}{\partial x_i}\left(\frac{\partial u_j}{\partial x_j}\right) - \frac{\partial^2 u_i}{\partial x_j \partial x_j} = -\frac{\partial^2 u_i}{\partial x_j \partial x_j} \end{aligned} \tag{93}$$

For three dimensions, therefore, the vorticity-velocity method requires six equations to be solved, three transport equations for the vorticity vector and three Poisson equations for the velocity components.

$$\mathcal{L}(\omega_i) = \frac{\partial \omega_i}{\partial t} - \omega_j \frac{\partial u_i}{\partial x_j} + \frac{\partial}{\partial x_j}\left(u_j \omega_i - \frac{1}{Re} \frac{\partial \omega_i}{\partial x_j} \right) = 0 \qquad \text{in } R^1 \tag{94}$$

$$\mathcal{L}(u_i) = \frac{\partial^2 u_i}{\partial x_j \partial x_j} + \epsilon_{ijk} \frac{\partial \omega_k}{\partial x_j} = 0 \qquad \text{in } R^1 \tag{95}$$

Boundary conditions are considerably simplified relative to vorticity-potential methods. The vorticities at the boundaries are calculated by the boundary velocity data using the defining relation for the vorticity, $\omega = \nabla \times \mathbf{u}$.

There has been a continuing interest in the vorticity-velocity method. Using a non-staggered mesh, Agarwal (1981) investigated a third-order accurate upwind scheme for the advection terms and calculated the flow in a 1-dimensional lid-driven cavity for Re=400. Farouk and Fusegi (1985) studied natural and forced convection heat transfer in a 2-dimensional annulus. Giu and Stella (1988) employed a staggered mesh and an ADI iterative method to calculate 2-dimensional flows for a lid-driven cavity and a step-wall diffuser. Gatski et al. (1989) developed a novel formulation in which a Cauchy-Riemann-type system of first-order partial differential equations is solved simultaneously for the velocity field. Guevremont et al. (1990) presented a finite-element implementation for 2- and 3-dimensional isochoric and near-isochoric (compressible subsonic) flow problems. Napolitano and Pascazio (1991) used a staggered mesh in their finite difference formulation in which the Poisson equations were parabolized to accelerate convergence to steady-state at the sacrifice of time-accuracy.

3.3 EXACT CONTINUITY ENFORCEMENT – *u-P* DIRECT METHOD

The *u-P* Direct method requires the simultaneous solution of the Navier-Stokes and continuity equations as a directly coupled system (Gresho, 1991). Primarily used with a finite-element method in the form of a Galerkin weak statement, it will be demonstrated here with the steady Navier-Stokes equations with no body forces. Mathematically, the problem statement is to find the discrete velocity vector function $\mathbf{u}^h \in \mathbf{V}_0^h$ and the discrete kinematic pressure scalar function $P^h \in S_0^h$ such that

$$\begin{aligned} &\int_\Omega v_i^h \frac{\partial}{\partial x_j}\left(u_i^h u_j^h - \frac{1}{Re} \frac{\partial u_i^h}{\partial x_j^h} + P^h \delta_{ij} \right) d\Omega = 0 \quad \forall\, v_i^h \in V_0^h \\ &\int_\Omega q^h \left(\frac{\partial u_j}{\partial x_j} \right) d\Omega = 0 \quad \forall\, q^h \in S_0^h \end{aligned} \tag{96}$$

where $\mathbf{V}_0^h \subset \mathbf{H}_0^1$ and $S_0^h \subset L_0^2$ are the functional spaces defined at the beginning of this chapter. Upon discretization, Eqs. (96) produce a system of coupled nonlinear algebraic equations. Gunzburger (1989a) describes a number of iterative techniques that can be applied to nonlinear systems such as Newton's method, the fixed Jacobian (or chord) method, and quasi-Newton algorithms such as Broyden's update method. These solution techniques for nonlinear systems are designed to produce a sequence of linear algebra problems that typically have the form

$$\begin{bmatrix} A & B^T \\ B & 0 \end{bmatrix} \begin{Bmatrix} U \\ P \end{Bmatrix} = \begin{Bmatrix} F \\ G \end{Bmatrix} \tag{97}$$

where F and G hold the nonhomogeneous data. The coefficient matrix in Eq (97) is indefinite nonsymmetric with a large number of zeros on the diagonal corresponding to the pressure degrees-of-freedom.

Due to ill-conditioning, it is common practice to solve these linear algebra problems using direct methods, e.g., Gaussian elimination. Partial pivoting can generally be avoided if the ordering of the equations places the pressure unknowns after the velocities (Gunzburger, 1989a). This ill-conditioning has tended to limit the u-P direct method to 2-dimensional applications. The use of direct solvers for 3-dimensional problems can produce prohibitively high computational costs.

As discussed at the beginning of this chapter, a critical requirement for the subspaces V_h^* and S_h^* is that they satisfy the div-stability condition, thus placing the u-P method within the broader class of mixed finite-element methods (Stenberg, 1984). Gunzburger (1989a) presents a review of finite-element pairs that satisfy div-stability, e.g., (1) using the same degree polynomials but overlaying different grids for the velocity and pressure, (2) using restrictions on the pressure space (e.g., the Taylor-Hood biquadratic velocity-bilinear pressure pair), and (3) using bubble elements in which the velocity space is enlarged through the use of "bubble" functions embedded in the basis sets for the velocity. An analysis of 3-dimensional counterparts to the Taylor-Hood element pairs is presented by Stenberg (1987).

Another approach is to use element pairs that do not satisfy div-stability (e.g., equal-order bilinear velocity and bilinear pressure elements on the same grid), but circumvention of div-stability is accomplished by making modifications to the continuity equation. An example of such a circumvention scheme is given by Hughes et al. (1986c) for the Stokes problem. Another method of circumvention is the penalty method, to be discussed.

3.4 INEXACT CONTINUITY ENFORCEMENT – PENALTY METHOD

The penalty method has had widespread application in solid mechanics, specifically incompressible elasticity problems (Zienkiewicz, 1977). Applications to Stokes and Navier-Stokes flows go back as far as Temam (1968). The penalty formulation in solid mechanics corresponds to classical, isotropic, compressible elasticity; therefore, for incompressible elasticity problems, an incompressible medium approximates a slightly compressible one. Applying the penalty method to Stokes flow, an incompressible fluid is approximated by a slightly compressible fluid resulting in an inexact enforcement of the conservation of mass.

There are a number of ways one can view the penalty method (cf. Hughes et al., 1979, and Baker, 1983). For a linear Stokes flow, it can be considered an application of a constrained minimization problem in which the penalty term is an approximation to a Lagrange multiplier. Penalty solutions are proven to converge to the exact Stokes flow solution (Temam, 1968). A physical interpretation is provided by Hughes et al. (1979). The incompressibility condition is dropped, and the constitutive relation for the Cauchy stress tensor is replaced by

$$\sigma_{ij} = -p_m^{(\lambda)}\delta_{ij} + \mu\left(\frac{\partial u_i}{\partial x_j} + \frac{\partial u_j}{\partial x_i}\right) \tag{98}$$

where

$$p_m^{(\lambda)} = -\lambda\frac{\partial u_j}{\partial x_j} \tag{99}$$

As $\lambda \to \infty$, the solution to the momentum equations, "penalized" by the large penalty term, must compensate by driving $\partial u_j/\partial x_j \to 0$.

One of the positive features of the penalty method is the computational decoupling of the pressure from the velocity determination. Since the incompressibility constraint is also dropped, the div-stability condition is apparently circumvented, hence can be ignored (Gunzburger, 1989a). If one intends to use Eq. (99) in a post-processing step to recover the pressure field, however, then the div-stability condition must be satisfied, thus leading to the key requirement of "selective reduced integration" of the penalty term in the penalized momentum equations and in the post-processing of the pressure (Baker, 1983). Reduced integration places the penalty method in the class of mixed finite-element methods. For certain combinations of velocity/pressure interpolation-function pairs, the resulting pressure field approximation is piecewise discontinuous. This discontinuous pressure field can exhibit a rank deficiency in the assembled pressure equations producing "checkerboard" oscillations. However, least squares type pressure-smoothing techniques have been successfully applied to remove such checkerboarding and other analogous pathologies (Hughes et al., 1979).

The major computational problem with the penalty method is that the dominating penalty term introduces severe ill-conditioning into the terminal linear algebra statement. The already limited diagonal dominance, produced by the momentum equations, is further weakened, and the asymmetry due to the advection terms is reinforced by the asymmetry of the penalty term. Such ill-conditioning limits the algorithm designer's choices for linear algebra solvers. Typically, direct solvers with ill-conditioning countermeasures such as partial pivoting are required. For 3-dimensional applications, direct solvers introduce a very compute-intensive aspect (relative to iterative solvers) into the algorithm. Recently, researchers have reported some progress on an *iterated penalty method* (cf. Gunzburger, 1989b, and Reddy et al., 1992) in which iterative solvers can be used with iterative cycling within a time step. A smaller penalty parameter (equal to the square root of the direct penalty term) is used to reduce the ill-conditioning normally associated with the direct penalty method. The iterated penalty method is similar to the formulation proposed by Fortin and Fortin (1985) in which Uzawa's algorithm for the Stokes problem is combined with a Newton-Raphson scheme to solve the incompressible Navier-Stokes equations.

3.5 INEXACT CONTINUITY ENFORCEMENT – PSEUDOCOMPRESSIBILITY

The pseudocompressibility (or artificial compressibility) formulation (Chorin, 1967) was originally designed and is primarily used as a method to produce an iterative procedure for converging to a steady-state solution. The solution converges to a steady condition by progressing through a non-physical transient. The continuity equation is modified by adding a temporal term yielding

$$\frac{1}{c^2}\frac{\partial P}{\partial t} + \frac{\partial u_j}{\partial x_j} = 0 \tag{100}$$

where c can be considered an artificial sound speed or, alternatively, $1/c^2$ is an artificial compressibility. When Eq. (100) is solved in conjunction with the momentum equations, Eqs. 47, the problem becomes hyperbolic in form. The hyperbolic nature of the method can be demonstrated by taking the time derivative of Eq. (100), obtaining

$$\frac{1}{c^2}\frac{\partial^2 P}{\partial t^2} = \frac{\partial}{\partial x_j}\left(\frac{\partial u_j}{\partial t}\right) \tag{101}$$

The right-hand side of Eq. (101) can be replaced by the divergence of the momentum equations resulting in

$$\frac{1}{c^2}\frac{\partial^2 P}{\partial t^2} = \frac{\partial^2 P}{\partial x_i^2} - \frac{\partial^2}{\partial x_i \partial x_j}\left[u_i u_j - \left(\frac{1}{\mathrm{Re}}\right)\left(\frac{\partial u_i}{\partial x_j} + \frac{\partial u_j}{\partial x_i}\right)\right] \tag{102}$$

Equation (102) is a generalized wave equation with wave speed c. The selection of the parameter c is critical to achieving optimal convergence and to maintaining stability. Chorin (1967) used a non-staggered mesh with leap-frog time integration for his original implementation. Peyret and Taylor (1983) suggest that a staggered-mesh implementation gives more accurate results.

Peyret and Taylor (1983) demonstrate that the iterative cycle produced by the pseudocompressibility method is, in some sense, also an iterative method for solving the pressure Poisson equation. The velocity field is represented by a Taylor series expansion over time, such that

$$u_i^{n+1} = u_i^n + \Delta t \frac{\partial u_i^n}{\partial t} + \text{(H.O.T.)} \tag{103}$$

Using the momentum equations to replace the first-order time derivative in Eq. (103) yields,

$$u_i^{n+1} = u_i^n - \Delta t \frac{\partial}{\partial x_j}\left[u_i u_j - \left(\frac{1}{\mathrm{Re}}\right)\frac{\partial u_i}{\partial x_j}\right]^n - \Delta t \frac{\partial P^n}{\partial x_i} + \text{(H.O.T.)} \tag{104}$$

A backward expansion of the pressure produces

$$P^n = P^{n+1} - \Delta t \frac{\partial P^{n+1}}{\partial t} + \text{(H.O.T.)} = P^{n+1} + \Delta t\left(c^2 \frac{\partial u_j}{\partial x_j}\right)^{n+1} \tag{105}$$

Taking the divergence of Eq. (104) and substituting the result into Eq. (105) gives, after some rearrangement of terms

$$P^{n+1} - P^n - c^2 \Delta t^2 \frac{\partial^2 P^n}{\partial x_i^2} =$$

$$- c^2 \Delta t \left[\frac{\partial u_i}{\partial x_i} - \Delta t \frac{\partial^2}{\partial x_i \partial x_j} \left(u_j u_i - \left(\frac{1 + \mathrm{Re}^{-1}}{\mathrm{Re}} \right) \left(\frac{\partial u_i}{\partial x_j} + \frac{\partial u_j}{\partial x_i} \right) \right) \right]^n \tag{106}$$

At convergence as $t \to \infty$, $P^{n+1} \to P^n$, $\partial u_i / \partial x_i \to 0$, and Eq. (106) converges to the pressure Poisson equation, Eq. (102).

Turkel (1987) suggested a modification to the pseudocompressibility method in which artificial time derivatives are introduced in both the continuity equation and the momentum equations, with the result

$$\mathcal{L}^{PC}(p_0) = \frac{1}{c^2} \frac{\partial P}{\partial t} + \frac{\partial u_j}{\partial x_j} = 0$$

$$\mathcal{L}^{PC}(u_i) = \frac{(\gamma + 1)}{c^2} u_i \frac{\partial P}{\partial t} + \frac{\partial u_i}{\partial t} + \frac{\partial}{\partial x_j} \left[u_j u_i - \left(\frac{1 + \mathrm{Re}^{-1}}{\mathrm{Re}} \right) \left(\frac{\partial u_i}{\partial x_j} + \frac{\partial u_j}{\partial x_i} \right) \right] + \frac{\partial P}{\partial x_i} = 0 \tag{107}$$

Equations (107) are called the *preconditioned* Navier-Stokes equations. For $\gamma = -1$, the preconditioned matrix method returns to the pure pseudocompressibility method. One attempts to choose the two parameters γ and c to compensate for the difference in wave speeds experienced during the nonphysical transient. The parameters act to scale the hyperbolic preconditioned system such that all of its eigenvalues are approximately the same order of magnitude. Hsu et al. (1992) tested a method for adaptive refinement of c^2 and found it led to inferior convergence. Constant values of $-3 \le \gamma \le 1$ and $c = 1$ gave them the best results for 3-dimensional simulations of fully developed flow in a straight duct of square cross-section. Cabuk et al. (1992) employed the preconditioned matrix method with local time-stepping and implicit residual smoothing for 3-dimensional flows in a 90-deg bend and a backward-facing step. A four-stage explicit Runge-Kutta scheme was used to advance the system of equations through pseudo-time.

Attempts have also been reported in the literature to apply the pseudocompressibility method to unsteady flows. Rogers and Kwak (1991) present solutions for steady-state flow through a 3-dimensional 90-deg bend and for unsteady 2-dimensional flow over a circular cylinder. Time accuracy is obtained (claimed) by subiterating the equations in pseudo-time during the physical time-step.

Ramshaw and Mesina (1991) discuss a hybrid penalty-pseudocompressibility method for performing time-accurate transient incompressible flow calculations. They combine the two methods by computing the pressure from

$$\frac{\partial P}{\partial t} = - c^2 \frac{\partial u_j}{\partial x_j} - \lambda \frac{\partial}{\partial t} \left(\frac{\partial u_j}{\partial x_j} \right) \tag{108}$$

The intent of the formulation is to introduce a diffusional character into the hyperbolic pseudocompressibility equation system. The pseudocompressibility term (first term on the right-hand side) in Eq. (108) introduces artificial pressure (acoustic) waves that are dissipated by the second

penalty-related term. Ramshaw and Mesina (1991) caution that care should be taken in the specification of both the initial velocity and pressure fields, since any errors in these initial solutions may persist for some period of time after start-up. Solutions were reported for the 2-dimensional driven-cavity problem and for flow past a rectangular obstacle.

Generalizations of the pseudocompressibility method for compressible flows at low Mach numbers have also been developed. Ramshaw and Mousseau (1991) report on a technique to increase convergence of the compressible flow equations to steady-state by adding to the conservation law system an evolution equation of the form

$$\frac{\partial q}{\partial t} - \beta^2 \frac{\partial p}{\partial t} = \left(\frac{\beta^2}{\tau} \right) (q - p) - \rho D \frac{\partial (\nabla \cdot \boldsymbol{u})}{\partial t} \tag{109}$$

In Eq. (109), β is a factor used to reduce the effective sound speed, τ is a relaxation time, and ρD is a damping term with the effect of an artificial bulk viscosity. The pseudopressure q replaces the pressure p in the momentum equations only. The true thermodynamic pressure is still used in the energy equation. At steady state, the time derivatives in Eq. (109) go to zero; thus $q = p$.

3.6 INEXACT CONTINUITY ENFORCEMENT – PRESSURE RELAXATION

Pressure-relaxation methods represent the largest class of incompressible CFD algorithms for solving the primitive-variable form of the Navier-Stokes equations. All these methods produce an inexact enforcement of the continuity constraint, but they share the advantage of being extensible to 3-dimensional implementations.

3.6.1 MAC

The Marker and Cell (MAC) method is the oldest of the incompressible pressure relaxation methods (Harlow and Welch, 1965), having been developed (at Los Alamos Scientific Laboratory) initially for free-surface flow simulations. The MAC method can also be used for general incompressible Navier-Stokes problems. The "markers" are massless Lagrangian particles that track the location of the free-surface. They do not participate in the calculation for subsurface nodes. In the original implementation, the velocity vector field is advanced by an explicit time integration (forward Euler). A modified pressure Poisson equation is designed to insure an approximate enforcement of continuity after the velocity update.

At the beginning of time step $n+1$, the velocity field is initialized with an approximate solution, typically the converged solution from the previous time-step n. The pressure field is then estimated from the initial velocity data by the modified pressure Poisson equation.

$$\frac{\partial^2 p^*}{\partial x_i \partial x_i} = \frac{\partial^2 (u_i u_j)^n}{\partial x_i \partial x_j} + \frac{1}{\mathrm{Re}} \frac{\partial^2 D^n}{\partial x_j \partial x_j} - \frac{\partial D^n}{\partial t} \tag{110}$$

where D is the discrete dilatation rate ("discrepancy term", Welch et al., 1966), $\partial u_j / \partial x_j$. These discrepancy terms are included in the pressure Poisson equation to control nonlinear numerical instabilities which may develop over a series of time steps (Hirt and Harlow, 1967).

A significant feature of the MAC method is the introduction of a *staggered mesh* in which the pressures, the discrepancy terms, and the residuals for the right-hand side of Eq. (110) are computed at cell centroids, and the velocities are computed at cell faces. Figure 1 presents the general layout for a staggered mesh surrounding an interior node (i,j) in a 2-dimensional domain, and Fig. 2 shows a typical boundary node. The finite difference discretization is based upon central differences for all spatial derivatives. To compute the residuals for the pressure Poisson equation, velocities are required at cell centers and cell corners. These velocities are calculated as simple arithmetic averages, e.g.,

$$u_{i,j} = \frac{u_{i+1/2,j} + u_{i-1/2,j}}{2}$$

$$u_{i+1/2,j+1/2} = \frac{u_{i+1/2,j} + u_{i+1/2,j+1}}{2} \tag{111}$$

$$(uv)_{i-1/2,j-1/2} = \left(\frac{u_{i-1/2,j} + u_{i-1/2,j-1}}{2} \right) \left(\frac{v_{i,j-1/2} + v_{i-1,j-1/2}}{2} \right)$$

where the subscripts (i, j), $(i+\frac{1}{2}, j)$, etc. refer to positions in the mesh.

After the pressure field has been calculated, the velocities are advanced explicitly using a central difference discretization of spatial derivatives in the momentum equations. For example, the $u_{i+1/2,j}$ difference equation is

$$u^{n+1}_{i+1/2,j} = u^{n}_{i+1/2,j} + \delta t \left[\frac{(u^2_{i,j})^n - (u^2_{i+1,j})^n}{\delta x} + \frac{(uv)^n_{i+1/2,j-1/2} - (uv)^n_{i+1/2,j+1/2}}{\delta y} + \right.$$

$$\left. \frac{P^n_{i,j} - P^n_{i+1,j}}{\delta x} + \frac{1}{\mathrm{Re}} \left(\frac{u^n_{i+3/2,j} + u^n_{i-1/2,j} - 2u^n_{i+1/2,j}}{\delta x^2} + \frac{u^n_{i+1/2,j+1} + u^n_{i+1/2,j-1} - 2u^n_{i+1/2,j}}{\delta y^2} \right) \right] \tag{112}$$

where δt is the discrete time-step and δx and δy are mesh intervals.

One of the difficulties with the staggered mesh involves the imposition of tangential velocity boundary conditions at free-slip and no-slip walls. A typical wall boundary for a staggered mesh is shown in Fig. 2. Note that whereas the normal velocity u_Γ is explicitly defined on the mesh, the tangential velocity at the wall, v_Γ, is not. To deal with this problem, a "belt" of *image* nodes are positioned along the boundary Γ, just outside of the domain Ω. The boundary condition is then approximated as $v_{0,j+1/2} = v_{1,j+1/2} = v_\Gamma$ for a free-slip wall. For a no-slip boundary, the tangential velocity in the image node is set at $v_{0,j+1/2} = -v_{1,j+1/2}$. A linear interpolation of the velocity between the boundary and image nodes produces a zero tangential velocity at the wall. This technique is called the *reflection method* for free-slip and no-slip boundaries on a staggered mesh. The local truncation error for the approximation of second derivatives at point $(1, j-\frac{1}{2})$ is shown by Peyret and Taylor (1983) to be $O(1)$ when the reflection method is used, i.e., the difference equation at $(1, j-\frac{1}{2})$ is *not consistent* with the differential equation. Higher-order consistent methods for establishing velocity boundary conditions are also discussed by Peyret and Taylor (1983).

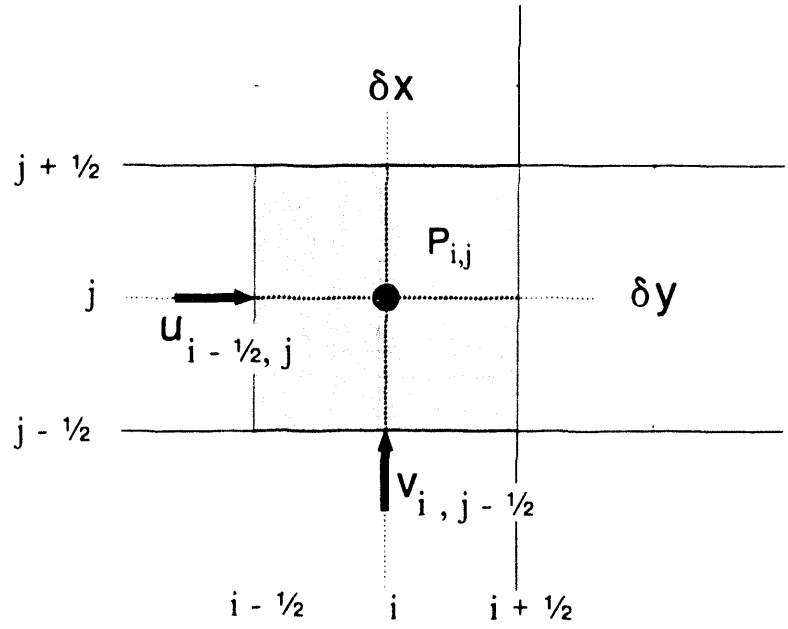

Figure 1. Layout of staggered mesh at interior cells.

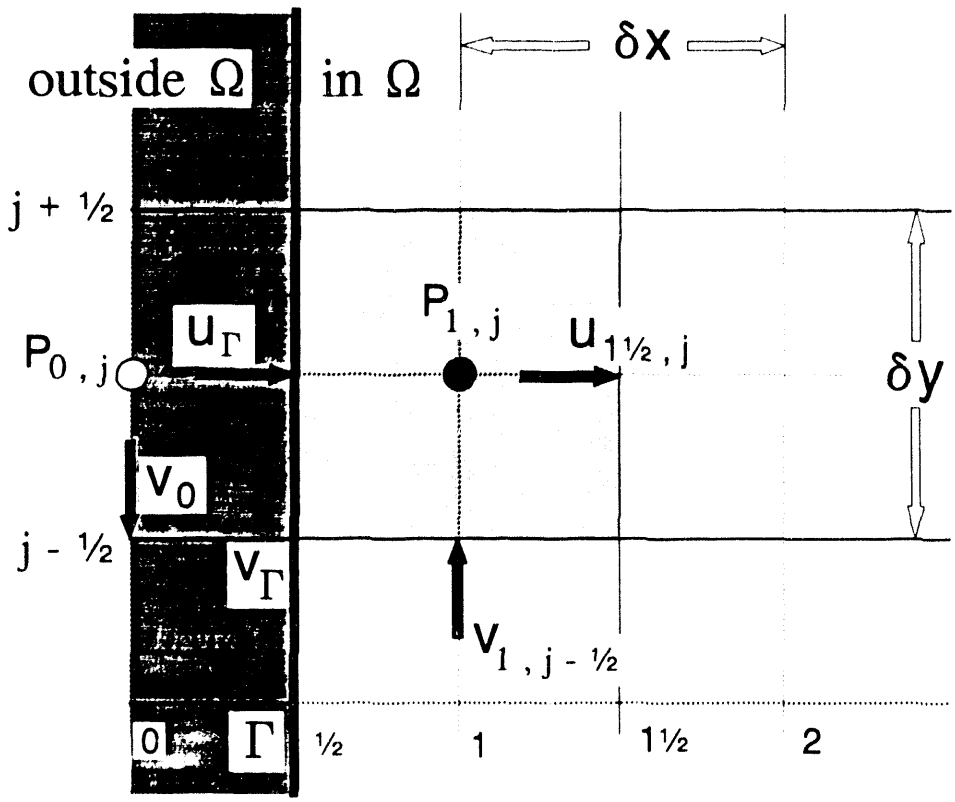

Figure 2. Layout of staggered mesh at boundary.

For the pressure at a free-slip wall, the finite-difference equivalent of a homogeneous Neumann boundary condition is applied ($P_{0,j}=P_{1,j}$). At a no-slip wall, the pressure boundary condition is a non-homogeneous Neumann condition produced by projecting the momentum equations onto the outward normal unit vector at the boundary. The result is

$$P_{0,j} = P_{1,j} - \frac{2}{\mathrm{Re}} \frac{(u_{3/2,j} - u_{\Gamma,j})}{\delta x} \tag{113}$$

It can be shown that the velocity solution produced by the MAC method is independent of the actual normal pressure gradient at the boundary when the reflection method is applied. This result has led various researchers to use the more easily implemented homogeneous boundary condition for the normal pressure gradient at wall boundaries. One should not lose sight of the fact, however, that this homogenous Neumann boundary condition is a numerical convenience only for applying velocity boundary conditions on a staggered mesh, and it does not reflect the actual physics of the pressure field.

The difficulty with applying nonhomogeneous Neumann boundary conditions, required by the true pressure Poisson equation, is that a compatibility condition must be met by the discrete equations in order to attain convergent solutions. This compatibility condition can be derived by integrating the pressure Poisson equation and then applying the Green-Gauss theorem to the pressure term to produce the following integral relation:

$$\oint_\Gamma \frac{\partial P}{\partial n} d\Gamma = \int_\Omega F d\Omega \tag{114}$$

where F is the forcing function (right-hand side) for the Poisson equation and n is the outward pointing normal on Γ. It can be shown that this compatibility condition is not automatically satisfied on either staggered (Peyret and Taylor, 1983) or nonstaggered grids (Abdallah, 1987).

Abdallah (1987) has proposed a modified MAC method based on nonstaggered grids. To satisfy the compatibility condition for the pressure Poisson equation, consistent finite-difference approximations for the velocity derivatives in the forcing function F in Eq. (114) were developed. Abdallah also notes that, even though the viscous terms from the momentum equations do not appear in F, they do appear in the nonhomogeneous boundary conditions for the pressure. The integral of the viscous terms over the boundary Γ should be consistent with the compatibility condition. Abdallah achieved compatibility by writing the viscous terms as the curl of the vorticity vector.

3.6.2 SMAC

Difficulties with applying nonhomogeneous Neumann boundary conditions for the pressure calculation led the CFD group at Los Alamos to develop a modified version of MAC called the Simplified Marker and Cell (SMAC) method (Amsden and Harlow, 1970). In SMAC, the true pressure field is never calculated. Since the vorticity transport equation does not contain the pressure, any pressure field (or the gradient of a scalar function in the position of the pressure) inserted into the Navier-Stokes equations will not prevent the subsequent time-advanced velocity solutions from carrying the correct vorticity at interior points. It is important to note that vorticity production and diffusion at a rigid wall will not be correct if the intermediate velocity field is not mass-conserving at the wall. Assuming that the velocities from the previous time step are divergence-free, then vorticity production at a wall will be correct only for an explicit time-integration scheme. If implicit

time-integration is used, however, iterative cycling within the time step is necessary. Continuing with the development of SMAC, if the inserted pseudopressure is constructed such that the resulting velocities are mass-conserving (or can be corrected to be mass-conserving), then the new velocities will be the unique and correct velocity field. The advantage of using a scalar potential function rather than the true pressure is that homogeneous Neumann boundary conditions can be used with the potential function.

The SMAC algorithm begins at the top of a time step by initializing the pseudopressure field, P^*. In the original implementation of SMAC (Amsden and Harlow, 1970), P^* is set to zero except at free-surface boundaries where appropriate Dirichlet data are applied. A staggered mesh, as in MAC, is used. An intermediate velocity field $\boldsymbol{u}^{*n+1}$ is then generated by an explicit advancement of the discrete momentum equations from the previous time step solution, $\boldsymbol{u}^n$. The finite difference equation for the $u^*_{i+1/2,j}$ velocity component in $\mathbb{R}^2$ is

$$u^*_{i+1/2,j} = u^n_{i+1/2,j} + \delta t \left[\frac{(u^2_{i,j})^n - (u^2_{i+1,j})^n}{\delta x} + \frac{(uv)^n_{i+1/2,j-1/2} - (uv)^n_{i+1/2,j+1/2}}{\delta y} + \right.$$
$$\left. \frac{P^*_{i,j} - P^*_{i+1,j}}{\delta x} + \frac{1}{\mathrm{Re}} \left(\frac{u^n_{i+3/2,j} + u^n_{i-1/2,j} - 2u^n_{i+1/2,j}}{\delta x^2} + \frac{u^n_{i+1/2,j+1} + u^n_{i+1/2,j-1} - 2u^n_{i+1/2,j}}{\delta y^2} \right) \right] \tag{115}$$

SMAC also introduced the ZIP method of differencing the node-centered momentum advection terms in order to remove the destabilizing truncation error term that occurred in the original MAC method. An example of ZIP differencing is

$$(u_{i,j})^2 = u_{i-1/2,j}\, u_{i+1/2,j} \tag{116}$$

The discrepancy term $D_{i,j}$ from the MAC method is calculated at node centers by the central difference relation

$$D_{i,j} = \frac{1}{\delta x}(u^*_{i+1/2,j} - u^*_{i-1/2,j}) + \frac{1}{\delta y}(v^*_{i,j+1/2} - v^*_{i,j-1/2}) \tag{117}$$

A mass-conserving potential function ϕ is next computed at node centers from the Poisson equation

$$\nabla^2 \phi_{i,j} = -D_{i,j} \tag{118}$$

The final step is to annihilate the divergence error by correcting the intermediate velocity field using the potential function ϕ.

$$u^{n+1}_{i+1/2,j} = u^*_{i+1/2,j} - \frac{1}{\delta x}(\phi_{i+1,j} - \phi_{i,j})$$
$$v^{n+1}_{i,j+1/2} = v^*_{i,j+1/2} - \frac{1}{\delta y}(\phi_{i,j+1} - \phi_{i,j}) \tag{119}$$

After the velocities have been corrected, the solution is advanced to the next time step. Some typical boundary condition specifications in SMAC are presented in Table 2. The subscripts on the velocities and pressures refer to locations on a staggered mesh near a left-boundary plane as shown in Fig. 2. The reflection method is used to specify tangential velocities at free-slip and no-slip boundaries. The continuative outflow condition is equivalent to applying a vanishing normal derivative on both

velocity components. For the pseudo-pressure, a homogeneous Neumann boundary condition is enforced for free-slip, no-slip, and prescribed inflow planes. The pseudo-pressure in the image cell just outside the boundary is set to zero at a continuative outflow boundary.

Ikohagi and Shin (1991) have extended the SMAC method to generalized 2-dimensional curvilinear coordinates where the momentum of the contravariant velocities are solved in transform space, and the viscous (diffusion) terms in the momentum equations are recast as contravariant vorticities. A 3-dimensional implementation of the generalized-coordinate SMAC method is proposed by Ikohagi et al. (1992). Continuing with the staggered mesh, as in the original SMAC, the contravariant velocities are defined at the centers of the computational cell faces; the contravariant vorticities are located at centers of the cell edges; and the pressure is at the cell center. Their test case was a 3-dimensional step-wall diffuser, to be discussed further in Chapter 7.

Table 2. Boundary Condition Specifications for SMAC

Boundary Type	Normal Velocity	Tangential Velocity	Pseudo-pressure
Free-slip	$u_1 = 0$	$v_0 = v_{I+1/2}$	$P_0 = P_{I+1}$
No-slip	$u_1 = 0$	$v_0 = -v_{I+1/2}$	$P_0 = P_{I+1}$
Prescribed Inflow	$u_1 = \text{Data}$	$v_0 = -v_{I+1/2}$	$P_0 = P_{I+1}$
Continuative Outflow	$u^*_I = u^*_{I-1/2}$ $u_1 = u^*_1$	$v_0 = v_{I+1/2}$	$P_0 = 0$

3.6.3 Projection Methods

The projection (or fractional step) method was independently developed by Chorin (1968) and Temam (1969). In his original description of the method, Chorin used a nonstaggered mesh and an implicit ADI time-integration of the modified momentum equations. For finite difference applications, however, it has become more commonly implemented with an explicit time-integration and a staggered mesh.

Chorin (1968) casts the momentum equations in the following operator form:

$$\frac{\partial u_i}{\partial t} + \frac{\partial P}{\partial x_i} = \mathcal{F}(u_i, b_i, \mathrm{Re}) \tag{120}$$

where $\mathcal{F}$ is a differential operator (vector function) that depends on the velocity field, the body force field, and fluid properties, but not on the pressure, P. The vector field $\mathcal{F}$ can be decomposed into the sum of a rotational (thus solenoidal) vector field and an irrotational vector field.

$$\mathcal{F}(u_i) = \nabla \times A + \nabla\phi$$
$$\nabla \cdot (\nabla \times A) = 0 \qquad \nabla \times \nabla\phi = 0 \tag{121}$$

This Helmholtz decomposition exists and is unique whenever the initial value problem for the Navier-Stokes equations is well-posed. By the continuity constraint, the divergence of the acceleration

$(\partial u_i/\partial t)$ is zero, and the curl of the gradient of the scalar pressure field is identically zero (for a sufficiently smooth pressure). One, therefore, can identify the rotational component of $\mathcal{F}(u_i)$ with the acceleration and the irrotational component with the pressure. Eqs. (120) and (121) can also be interpreted in terms of the orthogonal projection operators $\mathcal{P}$ and $\mathcal{Q}$, where $\mathcal{P}$ projects a vector onto the null space of the divergence operator and $\mathcal{Q}$ projects a vector onto the null space of the curl operator (Gresho, 1990). Therefore, one obtains

$$\frac{\partial u_i}{\partial t} = \mathcal{P}\,\mathcal{F}(u_i) \qquad \nabla P = \mathcal{Q}\,\mathcal{F}(u_i)$$
$$\mathcal{P}^2 = \mathcal{P},\ \mathcal{Q}^2 = \mathcal{Q},\ \mathcal{P}\mathcal{Q} = \mathcal{Q}\mathcal{P} = 0 \tag{122}$$

and the resulting acceleration is divergence-free as required by the continuity constraint.

Based on the above projections, Chorin proposed that the velocity field be advanced in two steps. In the first step, an auxiliary velocity field is computed from a discrete approximation to $\mathcal{F}$ by

$$\frac{u_i^* - u_i^n}{\delta t} = \mathcal{F}^h(u_i^n) \tag{123}$$

A distinguishing feature of Chorin's method is the absence of the pressure during the solution for the auxiliary velocity. In the SMAC method the initial estimate for the pressure was set to zero as an optional computational convenience; however, in the projection method the zero pressure field during this step is a fundamental part of the development. In the second step, the auxiliary velocity field is projected onto a nearby solenoidal manifold. The necessary Poisson equation is derived from

$$\frac{u_i^{n+1} - u_i^*}{\delta t} + \nabla P^{n+1} = 0$$
$$\nabla \cdot u^{n+1} = 0 \tag{124}$$
$$\Rightarrow \nabla^2 P^{n+1} = \frac{1}{\delta t}\nabla \cdot u^*$$

The boundary condition for the Poisson equation is obtained by a normal projection of the first relation in Eqs. (124) onto the boundary Γ.

$$\left(\frac{\partial P}{\partial n}\right)_\Gamma^{n+1} = -\frac{1}{\delta t}\left(u_\Gamma^{n+1} - u_\Gamma^*\right)\cdot n \tag{125}$$

For a staggered mesh and an explicit time integration, it can be shown that the velocity solution is independent of u^*_Γ since (1) u^* is a function of u_i^n only in an explicit scheme, and (2) u^*_Γ appears in both the right-hand side and in the Neumann boundary condition of the Poisson problem where it identically cancels for a staggered mesh (Peyret and Taylor, 1983). If u^*_Γ is arbitrary, it can be chosen to be u_Γ^{n+1}, producing a homogeneous boundary condition for the Poisson problem in Eq. (124). After P^{n+1} has been calculated, the final step in the projection is to correct the auxiliary velocity field by

$$u^{n+1} = u^* - \delta t \nabla p^{n+1} \tag{126}$$

Notice that for the above implementation, the projection method is identical to SMAC, although the development of the two methods followed different lines of reasoning. It is, however, important to note that the designers of SMAC did not associate the potential function (used to correct the auxiliary velocity field) with the true pressure. They recognized that the use of homogeneous Neumann boundary conditions was a computational convenience and did not reflect the physically correct boundary conditions for the pressure.

Donea et al. (1982) have proposed a finite-element implementation of the projection method. By diagonalizing the mass matrix using the standard row-sum lumping technique, they are able to use a purely explicit time-integration. The div-stability condition is satisfied with either the bilinear velocity and element-constant pressure or the biquadratic velocity and bilinear pressure interpolation functions. During the momentum advancement step, the complete velocity Dirichlet boundary conditions are applied. For the projection step, the Neumann velocity boundary conditions are imposed, but only the normal component of the velocity Dirichlet boundary data is enforced. The tangential velocity boundary conditions are satisfied only in the weak sense in order to be consistent with the pressure boundary conditions. The fractional step method was tested on an unsteady driven cavity, axisymmetric flow through a sudden enlargement, flow around a stationary sphere, and natural convection in a closed vertical cylinder.

Shimura and Kawahara (1988), using an equal-order finite-element projection method, investigated a procedure for applying a computed nonhomogeneous Dirichlet outflow boundary condition for the pressure equation. This Dirichlet pressure condition is calculated by integrating a boundary pressure Poisson equation along a layer of elements adjacent to the outflow plane. The boundary pressure equation is constructed with velocity data from either the previous time step or a previous iterate. The resulting pressures computed on the outflow plane are applied as Dirichlet pressure data during a subsequent global Poisson solve for the mass-conserving potential function.

Continuing with the development of both the projection and SMAC methods, researchers have investigated various semi-implicit techniques in which the advection terms are advanced explicitly and the diffusion terms implicitly. Gresho (1990) presents an extensive theoretical discussion of boundary condition issues for a number of proposed semi-implicit projection methods. A finite element implementation of a semi-implicit technique is given by Gresho and Chan (1990).

3.6.4 Velocity Correction

Schneider and Raithby (1978) proposed a finite-element pressure relaxation technique based primarily on the SMAC method. They were able to circumvent the div-stability condition while using equal-order interpolation functions for the velocity and pressure by maintaining a "strict enforcement of the continuity constraint at every stage of the iterative process." The first step in their *velocity correction* method involves an explicit time-advancement of the momentum equations using a guessed solenoidal velocity field (from the previous time step) and a pressure field calculated from the genuine pressure Poisson equation. The new velocity field does not satisfy the continuity constraint, so a mass-conserving potential function (see Eq. (118)) is computed via a Poisson equation and the discrete divergence error. The potential function is then used to correct the velocity field. Schneider and Raithby note that the corrected velocity field will no longer satisfy the momentum

equations, so the final step of the iterative cycle is to recalculate the pressure using the true pressure Poisson equation. Time-marching with biquadratic finite elements was used to calculate steady-state solutions for the lid-driven and natural convection cavities. Kawahara and Ohmiya (1985) used the velocity correction method to calculate density flow in a tank with a sloping bottom. Indicative of its roots in the SMAC method, Kawahara and Ohmiya also used Lagrangian marker particles for flow visualization, and they dropped the pressure Poisson solve at the end of the time step.

Rice and Schnipke (1986, see also Schnipke and Rice, 1987) discuss an equal-order velocity correction method very similar to the one proposed by Schneider and Raithby (1980). In fact the distinctions are not obvious. The momentum equations are solved for an intermediate velocity field which is then corrected with a potential function computed from a Poisson equation. The forcing terms for the Poisson equation are the discrete divergence error, and homogeneous Neumann boundary conditions are applied at wall and inflow boundaries. "Natural boundary conditions" for the potential function are applied at outflow planes; however, the nature of these boundary conditions is not discussed. A streamline upwind method for controlling dispersion error is also presented (Rice and Schnipke, 1985).

3.6.5 SIMPLE/SIMPLER/SIMPLEC

Developed by the Imperial College CFD group in the late 1960s (Patankar and Spalding, 1972), the Semi-Implicit Method for Pressure-Linked Equations (SIMPLE) is a widely used pressure relaxation CFD technique. Employing a staggered grid, Fig. 3, SIMPLE uses the finite-volume method for discretizing the incompressible Navier-Stokes equations. A review of the finite-volume method, as applied to heat transfer and fluid flow problems, is given in the book by Patankar (1980). An early SIMPLE-like algorithm using finite-differences is discussed by Roscoe (1976).

A generic finite-volume with typical SIMPLE notation is shown in Fig. 3. Velocities are evaluated at the faces of the volume, and the pressure and any other scalar variable such as temperature are assigned at the element center. As an example of SIMPLE algorithm notation, the implicit advancement of the u_i^{n+1} velocity component (neglecting body forces) at the **east** face of node **P** is calculated as

$$a_e u_e = \sum a_{nb} u_{nb} + (P_P - P_E) A_e \qquad (127)$$

where the a's are coefficients produced by the finite-volume integrations over the faces of the volume, the subscript nb refers to the surrounding faces (neighbors) of node **P**, and A_i is the surface area of the east face. The a coefficients are functions of the velocity field, the mesh geometry, and the time-step. In Eq. (127), the correct pressures at the volume centers are assumed known. Since at the beginning of the iterative cycle a guessed pressure field must be used, the actual implicit velocity advancement step is written as

$$a_e u_e^* = \sum a_{nb} u_{nb}^* + (P_P^* - P_E^*) A_e \qquad (128)$$

where the superscript "*" denotes the current estimate for the velocities and pressures.

SIMPLE involves a velocity correction step and a pressure correction step. The velocity correction equations are derived by first subtracting Eq. (128) from Eq. (127), giving

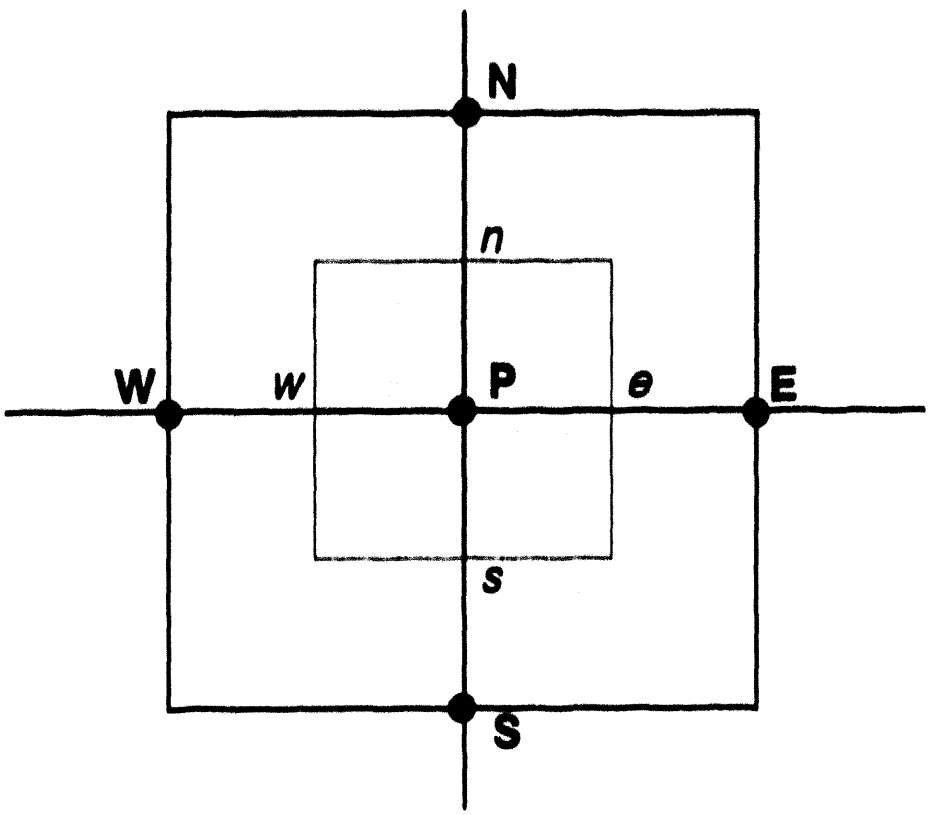

Figure 3. Generic finite-volume with SIMPLE notation.

$$a_e u_e' = \sum a_{nb} u_{nb}' + (P_P' - P_E') A_e$$
$$u = u^* + u' \quad ; \quad P = P^* + P' \tag{129}$$

Equation (129) is the fully implicit velocity correction equation. The semi-implicit velocity correction equation drops the underlined term in Eq. (129) to obtain

$$u_e' = d_e (P_P' - P_E')$$
$$d_e = A_e / a_e \tag{130}$$

An equation can be derived for the pressure correction terms by using Eq. (130) with the discrete continuity equation. The resulting Poisson equation is

$$\nabla^2 P' = -\frac{1}{\Delta t} \nabla \cdot u^* \tag{131}$$

In practice, the pressure corrections produced by Eq. (131) tend to overpredict the required adjustment to the pressure; therefore, some level of underrelaxation is required when the pressure correction is applied, e.g.,

$$P = P^* + \alpha_p P' \tag{132}$$

It is also common practice to underrelax the momentum update of the velocity field by

$$\frac{a_e}{\alpha} u_e'^m = \sum a_{nb} u_{nb}'^m + (P_P'^m - P_E'^m) A_e + \frac{(1-\alpha)}{\alpha} a_e u_e'^{m-1} \tag{133}$$

where m is an iteration index. Typical values for α_p and α are 0.8 and 0.5, respectively (Patankar, 1980).

The iterative sequence for SIMPLE is

(1) guess a pressure field P^*;

(2) solve the momentum equations, Eq. (133), to obtain u^*;

(3) solve the Poisson equation, Eq. (131), to obtain the pressure corrections, P';

(4) apply the pressure correction with underrelaxation, $P^{**(n+1)} = P^{**} + \alpha_p P'$;

(5) calculate the velocity correction, Eq. (130), and correct the velocities to obtain $u^{**(n+1)}$;

(6) repeat steps 2-5 until convergence, then

Boundary conditions for SIMPLE are very similar to those used in the SMAC method. No-slip and free-slip walls use the reflection method for the velocity and a homogeneous Neumann condition for the pressure.

There has been a continuing effort to improve the convergence and stability of the SIMPLE algorithm. It was soon recognized that even though the pressure correction term did a good job of correcting the velocities it did not produce very good estimates for the corrected pressure field. This slow convergence of the pressure correction was attributed to the dropping of the term underlined in Eq. (129). A modified algorithm called SIMPLE Revised (SIMPLER) was developed by Patankar (1980) to improve the convergence rate of the pressure field. In SIMPLER, the pressure corrections are applied to the velocities only. The pressures are updated using a Poisson equation with an improved estimate for the velocity field.

The SIMPLER algorithm proceeds as follows:

(1) guess a velocity field u^*;

(2) calculate a pseudovelocity field, u^{**}, using Eq. (133) with the pressures set to zero;

(3) use the pseudovelocities u^{**} to form the right-hand side of the Poisson equation, Eq. (131), and calculate a new estimate for the pressure field, P^*;

(4) calculate u^* with the pressures P^* from step 3 using Eq. (133);

(5) solve the Poisson equation, Eq. (131), for the pressure correction terms, P', using the u^* from step 4 to form the right-hand side;

(6) correct u^* with the P' calculated in step 5. Do not correct the pressure, P^*;

(7) repeat steps 2-6, until convergence; then

Notice that step 2 is an implicit form of the first step in Chorin's projection method.

The SIMPLEC method (van Doormal and Raithby, 1984) was also developed to improve the convergence rate for the pressure field. In SIMPLEC, the fully implicit velocity correction equation is modified by subtracting the term $\sum a_{nb} u'_e$ from both sides of Eq. (129).

$$(a_e - \sum a_{nb}) u'_e = \sum a_{nb} (u'_{nb} - u'_e) + (P'_P - P'_E) A_e \tag{134}$$

The underlined term in Eq. (134) is dropped, and the modified velocity correction equation is

$$\begin{aligned} u'_e &= d_e (P'_P - P'_E) \\ d_e &= \frac{A_e}{(a_e - \sum a_{nb})} \end{aligned} \tag{135}$$

The iterative cycle for SIMPLEC proceeds exactly as in SIMPLE with the new definition for d_e and with $\alpha_p = 1.0$.

Connell and Stow (1986) compared convergence rates of the SIMPLE algorithm to the results of two extended pressure correction equations. The extensions involved adding higher-order advection terms to the right-hand-side of the pressure correction Poisson equation. With these extensions, they found that underrelaxation of the momentum equations was not necessary; however, underrelaxation of the pressure correction was still required. Based on tests with the driven cavity problem, the extended pressure correction equations produced up to a 50% decrease in CPU time compared to SIMPLE.

A modified SIMPLEC method has been proposed for nonstaggered grids by Aksoy and Chen (1992). The Momentum Weighted Interpolation Method (MWIM) calculates velocities and pressures at element centers. MWIM is very similar to another nonstaggered variant of SIMPLE called the Pressure Weighted Interpolation Method (PWIM) due to Rhie and Chow (1983). To avoid spurious pressure solutions, the divergence error (required as the right-hand-side for the pressure-correction Poisson equation) is evaluated using velocities interpolated to element faces. Aksoy and Chen applied the finite analytic method (Chen, 1988) to discretize the momentum equations. A comparative assessment of the performance of MWIM to SIMPLER, SIMPLEC, PWIM, and a nonstaggered grid version of MAC by Abdallah (1987), was carried out by Aksoy and Chen using the lid-driven cavity problem. They found that the performance of all the algorithms deteriorated as the grid size was refined. The nonstaggered version of MAC had excellent convergence and stability properties as an explicit method; however, conservation of mass was poor in isolated areas of the mesh near flow singularities. MWIM and PWIM produced more or less the same performance characteristics. They were able to attain larger stable time-step sizes than either SIMPLER or SIMPLEC; however, SIMPLER and SIMPLEC required fewer iterations for convergence than the implicit nonstaggered grid algorithms.

3.6.6 PISO

The Pressure-Implicit with Splitting of Operators (PISO) method is a non-iterative predictor/corrector algorithm developed by Issa (1985) (see also Issa et al., 1986) for incompressible and low Mach number compressible CFD applications. Time-integration is fully implicit (backward Euler), and the spatial discretization is based on a finite-volume staggered mesh. Following Jang et al. (1986), PISO can be presented using SIMPLE-like notation for easy comparison to the SIMPLE family of algorithms. Note in the corrector step for the pressure, the genuine pressure Poisson equation is used to insure that the final pressure distribution is consistent with the momentum-equation update of the velocity field distribution in the second corrector step for the velocities.

The two-stage version of PISO is as follows:

(1) Predictor step for velocity – Advance the implicit discrete momentum equations with the pressure field from the previous time-step:

$$a_e\, u_e^{*} = \sum a_{nb}\, u_{nb}^{*} + A_e(p_P^{n} - p_I^{n}).$$

(2) Predictor step for pressure – Solve a Poisson equation for p^*:

$$\nabla^2 p^{*} = -\, 1/\Delta t\ \nabla \cdot \boldsymbol{u}^{*}.$$

(3) First corrector step for velocity – Use a SIMPLE-like velocity corrector:

$$u_e^{**} = u_e^{*} + d_e \left[(p_P^{*} - p_P^{n}) - (p_I^{*} - p_I^{n}) \right].$$

(4) Corrector step for pressure – Solve the genuine pressue Poisson equation for p^{**}:

$$\nabla^2 p^{**} = -\, \nabla \cdot \left[u^{**} \cdot \nabla u^{**} - (1/\mathrm{Re}) \nabla^2 u^{**} \right]$$

(5) Second corrector step for velocity. – Use an explicit advancement of the momentum equations with ($p^{**} - p^{*}$).

$$u_e^{***} = u_e^{**} + \left[\sum a_{nb} (u_{nb}^{**} - u_{nb}^{*}) \right] / a_e + d_e \left[(p_P^{**} - p_P^{*}) - (p_I^{**} - p_I^{*}) \right]$$

(6) Advance to the next time step – $u_e^{n+1} = u_e^{***}$ and $p^{n+1} = p^{**}$

Homogeneous Neumann boundary conditions are applied for the pressure Poisson equations. Like SIMPLER, two Poisson solves are required. However, in PISO the second velocity corrector step is accepted as the converged solution for the velocity, and the algorithm advances to the next time step. Issa (1985) performed a heuristic error analysis of the two-stage version of PISO and determined that the errors in the solution of the linearized difference equations for the pressure and velocity are of order Δt^{1} and Δt^{2}, respectively.

Jang et al. (1986) carried out a comparative assessment of the performance of PISO, SIMPLER, and SIMPLEC. They found that for isothermal laminar flows, where the momentum equations are not strongly coupled to a scalar state-variable with its own transport equation, the noniterative PISO algorithm outperformed the iterative SIMPLER and SIMPLEC methods in terms of computational effort. For problems with a strong coupling between the momentum and scalar transport equations (e.g., coupling with the energy equation through a Boussinesq buoyancy term, or with a k-ε turbulence model through the eddy viscosity ν^{t}), PISO did not exhibit good convergence rates relative to SIMPLER and SIMPLEC. PISO also required small time steps for the strongly coupled cases in order to obtain acceptable solutions.

Braaten and Shyy (1987) studied a multi-step pressure correction algorithm, similar to PISO, with extensions that included nonorthogonal curvilinear coordinates and a multi-grid solver for the Poisson equations. They found improved performance, relative to a single pressure correction step algorithm, for laminar flows and flows on nearly orthogonal meshes. However, convergence rates did not improve for more complicated flows and geometries, e.g., turbulent and reacting flows, and highly nonorthogonal meshes. Little performance gain was obtained by solving the pressure Poisson equations to a tight tolerance at each pressure correction step.

3.6.7 Operator Splitting

Glowinski and Pironneau (1992) have recently presented a review of a class of finite element methods for the incompressible Navier-Stokes problem based on *operator splitting*. These time-integration schemes produce at each time step two groups of subproblems, the advection-diffusion problem and the linear incompressible Stokes problem. A generalized form is the θ-scheme, described below for the unsteady Navier-Stokes equations with no body forces.

(1) First Stokes Problem – Solve for $\boldsymbol{u}^{n+\theta}$ and $P^{n+\theta}$.

$$\frac{\boldsymbol{u}^{n+\theta} - \boldsymbol{u}^{n}}{\theta \Delta t} - \frac{\alpha}{Re} \nabla^2 \boldsymbol{u}^{n+\theta} + \nabla P^{n+\theta} = \frac{\beta}{Re} \nabla^2 \boldsymbol{u}^{n} - (\boldsymbol{u}^{n} \cdot \nabla) \boldsymbol{u}^{n} \tag{136}$$

$$\nabla \cdot \boldsymbol{u}^{n+\theta} = 0$$

(2) Advection-Diffusion Problem – Solve for $\boldsymbol{u}^{n+1-\theta}$.

$$\frac{\boldsymbol{u}^{n+1-\theta} - \boldsymbol{u}^{n+\theta}}{(1-2\theta)\Delta t} - \frac{\beta}{Re} \nabla^2 \boldsymbol{u}^{n+1-\theta} + (\boldsymbol{u}^{n+\theta} \cdot \nabla) \boldsymbol{u}^{n+1-\theta} = \frac{\alpha}{Re} \nabla^2 \boldsymbol{u}^{n+\theta} - \nabla P^{n+\theta} \tag{137}$$

(3) Second Stokes Problem – Solve for $\boldsymbol{u}^{n+1}$ and P^{n+1}.

$$\frac{\boldsymbol{u}^{n+1} - \boldsymbol{u}^{n+1-\theta}}{\theta \Delta t} - \frac{\alpha}{Re} \nabla^2 \boldsymbol{u}^{n+1} + \nabla P^{n+1} = \frac{\beta}{Re} \nabla^2 \boldsymbol{u}^{n+1-\theta} - (\boldsymbol{u}^{n+1-\theta} \cdot \nabla) \boldsymbol{u}^{n+1-\theta} \tag{138}$$

$$\nabla \cdot \boldsymbol{u}^{n+1} = 0$$

The continuity constraint is enforced in the linear Stokes problems, Steps 1 and 3. In Step 2, the advection-diffusion problem has been linearized by lagging the coefficient of the nonlinear advection term. The splitting parameters, α and β, can be chosen such that

$$\alpha = \frac{(1-2\theta)}{(1-\theta)} \quad ; \quad \beta = \frac{\theta}{(1-\theta)} \tag{139}$$

Glowinski and Pironneau suggest an optimal value for θ is $1 - 1/\sqrt{2}$.

The operator splitting scheme succeeds in decoupling the nonlinearity in the Navier-Stokes equations from the incompressibility constraint. The algorithm designer is still faced, however, with the nontrivial tasks of solving the incompressible Stokes problem and the advection-diffusion problem. Taking advantage of the symmetric positive-definite terminal matrix statement produced for the Stokes equations, a preconditioned conjugate gradient algorithm can be used (Cahouet and Chabard, 1988). A number of methods have been developed to control the dispersive errors associated with advection-diffusion equations, e.g., Taylor-Galerkin methods (cf. Baker and Kim, 1987; and Donea, 1984), Petrov-Galerkin methods (cf. Hughes et al., 1986a and b), and Lagrangian/Eulerian schemes based on the method of characteristics (Glowinski and Pironneau, 1992).

Shen and Temam (1989) have proposed an interesting variant of the projection method in terms of an operator splitting scheme. This algorithm was designed to produce an approximation of a nonhomogeneous Neumann boundary condition for the pressure while retaining the computationally attractive properties of homogeneous Neumann boundary conditions for the intermediate pseudopressure q. The scheme proceeds in two steps as follows:

(1) Stokes Problem – Solve for $\boldsymbol{u}^{n+1/2}$ and $q^{n+1/2}$.

$$\frac{\boldsymbol{u}^{n+1/2} - \boldsymbol{u}^{n}}{(\Delta t/2)} - \frac{1}{\mathrm{Re}} \nabla^2 \boldsymbol{u}^{n+1/2} + \nabla q^{n+1/2} = 0 \qquad (140)$$

$$\nabla \cdot \boldsymbol{u}^{n+1/2} = 0$$

(2) Advection-Diffusion Problem – Solve for $\boldsymbol{u}^{n+1}$

$$\frac{\boldsymbol{u}^{n+1} - \boldsymbol{u}^{n+1/2}}{(\Delta t/2)} - \frac{1}{\mathrm{Re}} \nabla^2 \boldsymbol{u}^{n+1} + 2\boldsymbol{u}^{n+1/2} \cdot \nabla \boldsymbol{u}^{n+1} = -\nabla q^{n+1/2} \qquad (141)$$

Shen and Temam postulate that

$$P^{n} = \frac{1}{2}\left(q^{n+1/2} + q^{n-1/2}\right) \qquad (142)$$

is a good approximation for $P(t_n)$ based on the observation that, upon summing Eqs. (140) and (141) at time step n -1 and then projecting the result onto the outward normal at the boundary, one obtains

$$\frac{\partial P^{n}}{\partial n} = \left(\frac{1}{2\,\mathrm{Re}} \nabla^2 (\boldsymbol{u}^{n+1/2} + \boldsymbol{u}^{n}) - \boldsymbol{u}^{n-1/2} \cdot \nabla \boldsymbol{u}^{n} \right) \cdot \boldsymbol{n} \qquad (143)$$

which corresponds to a discrete approximation of the nonhomogeneous Neumann boundary condition for the pressure Poisson equation. Their stability and convergence study found that the new scheme is unconditionally stable and convergent. An error analysis, in which numerical results produced by the new scheme and by Chorin's projection method were compared to an analytical (exact) solution, showed the new scheme to be more accurate. They also discovered that the precision of the pressure approximation produced by the new scheme slightly improved as the Reynolds number was increased.

3.7 SUMMARY

The algorithms discussed in this chapter demonstrate the range of formulations that have been developed to enforce the continuity constraint. The pressure gradient in the momentum equations provides a mathematical linkage to the continuity equation; however, the absence of the pressure in the barotropic equation of state for an incompressible fluid presents severe computational difficulties.

Exact enforcement of continuity typically involves eliminating the pressure by recasting the problem in terms of a derived state-variable, the vorticity. Conservation of mass can then be satisfied automatically by coupling the resulting Helmholtz vorticity transport equation to a streamfunction in $\mathbb{R}^2$ or vector and/or scalar potential functions in $\mathbb{R}^3$. These potential functions can be bypassed with formulations linking the vorticity directly to the velocities. With all of these methods, the elliptic

nature of the incompressible continuity principle is manifest by the presence of one or more Poisson equations. The $\boldsymbol{u}$-P direct formulation, as a mixed-finite element method, has found some application to 2-dimensional problems; however, the ill-conditioning of the final matrix statement presents obstacles to extending it to 3-dimensions.

Formulations designed to produce inexact or approximate enforcement of the continuity constraint require a modification to the conservation law system. The conservation of mass can be transformed into either an algebraic relation (e.g., penalty methods), a hyperbolic initial-value PDE (e.g., pseudo-compressibility methods), or a boundary-value PDE (e.g., pressure relaxation methods). However, all of these formulations must eventually be implemented within a semi-discrete approximation statement, and, as a consequence, resolvability on the spatial discretization Ω^h is a key issue. The computational impact is truly significant, since every inexact theory centrally involves "measuring" the error in $\nabla^h \cdot \boldsymbol{u}^h$, and then correcting it (Baker et al., 1992c). Any code implementation can accomplish this operation only *modulo* the discrete approximation ∇^h to the gradient and divergence operators, ∇ and $\nabla\cdot$, respectively. As an example of the difficulties arising from the use of an inappropriate ∇^h, consider the discrete velocity solution shown in Fig. 4. The velocities are located at cell centers, and the solution is clearly nonphysical. However, if central differences are used to evaluate $\nabla^h \cdot \boldsymbol{u}^h{}_P$, the discrete divergence error at node P will be zero. Such difficulties led the developers of MAC to the staggered mesh.

The dominant approximation error mode for ∇^h is dispersive, and, as a result, $\nabla^h \cdot \boldsymbol{u}^h$ is not only non-smooth but usually piecewise discontinuous on Ω^h. Therefore, for any of the inexact formulations, the created discrete approximations to the theoretical pressure estimate may contain short wavelength oscillations which can become very pronounced. In fact, such oscillations appear to be critical to the numerical enforcement of approximate continuity, to be discussed, but this constraint potential function bears little relation to the genuine (smooth) pressure distribution.

The theoretical framework for the new method to be presented in Chapter 4 assumes that the continuity constraint fields ϕ^h, as computed *modulo* ∇^h, are no more than just that, i.e., they are not accurate approximations to the genuine pressure P. Assuming that one can achieve $\nabla^h \cdot \boldsymbol{u}^h \leq \varepsilon$, then a genuine pressure field can be approximated by the solution to the pressure Poisson equation with physically motivated and numerically well-posed boundary conditions.

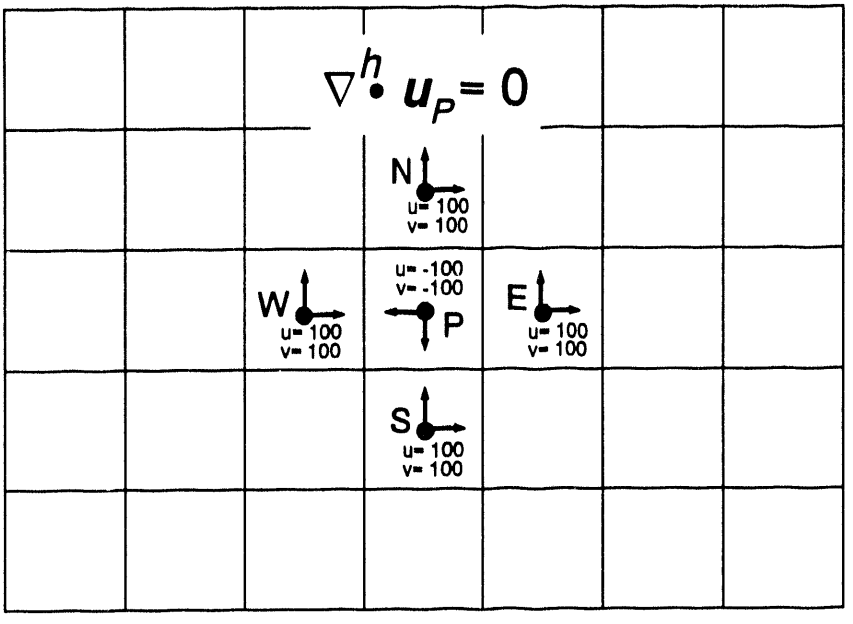

Figure 4. Example of a spurious velocity solution with $\nabla^h \cdot u_P = 0$ using central differences.

4. CONTINUITY CONSTRAINT METHOD

A new primitive-variable finite-element CFD algorithm, the Continuity Constraint Method (CCM), has been developed to produce approximate solutions for the unsteady Navier-Stokes equations in three dimensions. Falling in the general class of *pressure relaxation* algorithms, the new method has its origins in the finite-difference SMAC method (Amsden and Harlow, 1970), the finite-element velocity-correction method of Schneider and Raithby (1978), and early developments in research on incompressible algorithms at the University of Tennessee's CFD Laboratory (cf. Noronha, 1989; and Noronha et al., 1990).

Recognition of the dual role of the pressure, as both an enforcer of the continuity constraint and as a force in the mechanical balance law for the conservation of linear momentum (Gresho and Sani, 1987), has been a guiding principle in the algorithm's development. An implicit time integration with iterative cycling within the time step allows the two roles for the pressure to be completely separated. Specifically, a mass-conserving potential function is used to enforce continuity while the genuine pressure, as induced by a solenoidal velocity field, is calculated with well-posed and physically-motivated boundary conditions by the pressure Poisson equation. This separation of tasks produces a clear view of the individual and totally distinct boundary conditions required for the continuity constraint function and the pressure.

Additionally, the CCM employs a θ-implicit time-integration scheme, a consistent mass matrix, an optional Taylor Weak Statement (TWS) formulation for dispersion error control, and equal-order interpolation of all state-variables. Implicit time-integration allows larger stable time-steps compared to explicit schemes. A consistent full mass matrix, as opposed to the "lumped" mass matrix commonly used in explicit methods, exploits the cross-coupling in the inertial terms of the momentum and energy equations produced by the finite-element semi-discretization. The TWS theory has been employed by Baker and Kim (1987) to identify a multi-dimensional tensorial mechanism for hyperbolic conservation law systems. The derived stability formulation was later verified for incompressible systems as highly effective in control of third-order dispersive error mechanisms (Noronha and Baker, 1989). Equal-order interpolation of the velocity, pressure, and temperature state-variables with trilinear and bilinear (for boundary condition surface integrals) basis functions produces a continuous and more accurate pressure solution.

4.1 CONTINUITY ERROR DISTRIBUTION

Gresho (1990) presents an investigation of the continuity error distribution for semi-implicit projection methods. Expressing the solenoidal velocity solution at time-step $n+1$ in terms of a Taylor series expansion about the solution at time-step n results in

$$u_i^{n+1} = u_i^n + \Delta t \left.\frac{\partial u_i}{\partial t}\right|_n + \frac{\Delta t^2}{2} \left.\frac{\partial^2 u_i}{\partial t^2}\right|_n + O(\Delta t^3) \qquad (144)$$

Assuming any approximation to the velocity field, u_i^*, can be made with any guessed pressure field, $P^* = P^n$, the Taylor series companion to Eq. (144) is

$$u_i^* = u_i^{*n} + \Delta t \left.\frac{\partial u_i}{\partial t}\right|_{*n} + \left.\frac{\Delta t^2}{2}\frac{\partial^2 u_i}{\partial t^2}\right|_{*n} + O(\Delta t^3) \tag{145}$$

At $t=t_n$,

$$u_i^{*n} = u_i^n \rightarrow \left.\frac{\partial u_i^*}{\partial t}\right|_n = \left.\frac{\partial u_i}{\partial t}\right|_n = -\left[u_j\frac{\partial u_i}{\partial x_j} - \frac{1}{\mathrm{Re}}\frac{\partial^2 u_i}{\partial x_j^2} + \frac{\partial P}{\partial x_i}\right]_n \tag{146}$$

and Gresho specifies that the second derivatives of u_i^n and u_i^{*n} with respect to time are

$$\left.\frac{\partial^2 u_i}{\partial t^2}\right|_n = -\frac{\partial}{\partial t}\left[u_j\frac{\partial u_i}{\partial x_j} - \frac{1}{\mathrm{Re}}\frac{\partial^2 u_i}{\partial x_j^2} + \frac{\partial P}{\partial x_i}\right]_n \tag{147}$$

$$\left.\frac{\partial^2 u_i}{\partial t^2}\right|_{*n} = -\frac{\partial}{\partial t}\left[u_j\frac{\partial u_i}{\partial x_j} - \frac{1}{\mathrm{Re}}\frac{\partial^2 u_i}{\partial x_j^2}\right]_{*n} \tag{148}$$

where, apparently, for the guessed pressure field $\partial P^{*n}/\partial t=0$. Although the rationale for setting $\partial P^{*n}/\partial t=0$ is not given by Gresho, one explanation may be that the genuine pressure field, P^n, is assumed to be evolving in time with the solution, and the guessed pressure field is not. Subtracting Eq. (144) from Eq. (145), one obtains the following expression for the error in the velocity field,

$$u_i^{n+1} - u_i^* = \frac{\Delta t^2}{2}\left(\frac{\partial^2 u_i}{\partial t^2} - \frac{\partial^2 u_i^*}{\partial t^2}\right)_n + O(\Delta t^3) = -\frac{\Delta t^2}{2}\frac{\partial}{\partial x_i}\left(\frac{\partial P}{\partial t}\right)_n + O(\Delta t^3) \tag{149}$$

The curl of Eq. (149) is identically zero; hence the divergence error for explicit time integration can be expressed as the gradient of a scalar field, i.e.,

$$u_i^{n+1} - u_i^* = \frac{\partial \phi}{\partial x_i} \tag{150}$$

This divergence-error distribution, Eq. (149), is used to develop "optimal" semi-implicit projection schemes that require the estimation of $(\partial P/\partial t)^n$. These schemes are semi-implicit in the sense that the diffusion terms are advanced in time implicitly, and the advection terms are advanced explicitly.

A θ-implicit time integration scheme can be derived with the aid of two Taylor series expansions for $u_i^{n+1-\theta}$, about u_i^n and u_i^{n+1}, thus obtaining

$$u_i^{n+1-\theta} = u_i^n + (1-\theta)\Delta t \left.\frac{\partial u_i}{\partial t}\right|_n + \left.\frac{(1-\theta)^2 \Delta t^2}{2}\frac{\partial^2 u_i}{\partial t^2}\right|_n + O(\Delta t^3) \tag{151}$$

$$u_i^{n+1-\theta} = u_i^{n+1} - \theta \Delta t \left.\frac{\partial u_i}{\partial t}\right|_{n+1} + \left.\frac{\theta^2 \Delta t^2}{2}\frac{\partial^2 u_i}{\partial t^2}\right|_{n+1} + O(\Delta t^3) \tag{152}$$

Subtracting Eq. (152) from Eq. (151) and rearranging terms, the θ-implicit integration scheme is

$$u_i^{n+1} - u_i^n = \Delta t\left(\theta \left.\frac{\partial u_i}{\partial t}\right|_{n+1} + (1-\theta)\left.\frac{\partial u_i}{\partial t}\right|_n \right) + O(\Delta t^2) \tag{153}$$

Using the momentum equations to replace the time derivatives in Eq. (153) results in

$$\begin{aligned} u_i|_{n+1} - u_i|_n = &-\theta \Delta t\left[\frac{\partial (u_j u_i)}{\partial x_j} - \frac{\partial}{\partial x_j}\left(\frac{1+\mathrm{Re}^{\dagger}}{\mathrm{Re}}\left(\frac{\partial u_i}{\partial x_j} + \frac{\partial u_j}{\partial x_i} \right)\right) + \frac{\partial P}{\partial x_i} + \mathrm{Ar}\,\Theta\,\mathbf{g}_i \right]_{n+1} \\ &-(1-\theta)\Delta t\left[\frac{\partial (u_j u_i)}{\partial x_j} - \frac{\partial}{\partial x_j}\left(\frac{1+\mathrm{Re}^{\dagger}}{\mathrm{Re}}\left(\frac{\partial u_i}{\partial x_j} + \frac{\partial u_j}{\partial x_i} \right)\right) + \frac{\partial P}{\partial x_i} + \mathrm{Ar}\,\Theta\,\mathbf{g}_i \right]_n + O(\Delta t^2) \end{aligned} \tag{154}$$

Integrating the momentum equations with a guessed pressure field, P^*, results in a velocity field, u_i^*, that does not in general satisfy the continuity constraint. Equation (154) becomes

$$\begin{aligned} u_i^*|_{n+1} - u_i|_n = &-\theta \Delta t\left[u_j^* \frac{\partial u_i^*}{\partial x_j} - \frac{\partial}{\partial x_j}\left(\frac{1+\mathrm{Re}^{\dagger}}{\mathrm{Re}}\left(\frac{\partial u_i^*}{\partial x_j} + \frac{\partial u_j^*}{\partial x_i} \right)\right) + \frac{\partial P^*}{\partial x_i} + \mathrm{Ar}\,\Theta^*\,\mathbf{g}_i \right]_{n+1} \\ &-(1-\theta)\Delta t\left[\frac{\partial (u_j u_i)}{\partial x_j} - \frac{\partial}{\partial x_j}\left(\frac{1+\mathrm{Re}^{\dagger}}{\mathrm{Re}}\left(\frac{\partial u_i}{\partial x_j} + \frac{\partial u_j}{\partial x_i} \right)\right) + \frac{\partial P}{\partial x_i} + \mathrm{Ar}\,\Theta\,\mathbf{g}_i \right]_n + O(\Delta t^2) \end{aligned} \tag{155}$$

Note that the advection term for u_i^* in Eq. (155) is not in divergence form since

$$\frac{\partial u_j^*}{\partial x_j} \neq 0 \quad \rightarrow \quad u_j^* \frac{\partial u_i^*}{\partial x_j} \neq \frac{\partial (u_j^* u_i^*)}{\partial x_j}$$

Subtracting Eq. (155) from Eq. (154), the relation for the θ-implicit divergence error is

$$e_i^{n+1} \equiv \left(u_i - u_i^*\right)_{n+1} = \theta\,\Delta t \left[u_j^* \frac{\partial u_i^*}{\partial x_j} - \frac{\partial (u_j u_i)}{\partial x_j} \right]_{n+1}$$

$$+ \theta\,\Delta t \frac{\partial}{\partial x_j} \left[\left(\frac{1 + \mathrm{Re}'}{\mathrm{Re}} \right) \left(\frac{\partial u_i}{\partial x_j} + \frac{\partial u_j}{\partial x_i} \right) - \left(\frac{1 + \mathrm{Re}'}{\mathrm{Re}} \right)^* \left(\frac{\partial u_i^*}{\partial x_j} + \frac{\partial u_j^*}{\partial x_i} \right) \right]_{n+1} \tag{156}$$

$$+ \theta\,\Delta t \frac{\partial (P^* - P)}{\partial x_i}\bigg|_{n+1} + \mathrm{Ar} (\Theta^* - \Theta)_{n+1}\, g_i + O(\Delta t^2)$$

There are four modes in Eq. (156) producing errors in the velocity field, i.e., error modes due to advection, diffusion, pressure, and a nonconservative (rotational) body force. Taking the curl of Eq. (156) shows that in general the θ-implicit error is not irrotational. Only the error induced by the incorrect pressure field can be represented by the gradient of a scalar potential function. The remaining errors in Eq. (156) must be reduced by insuring that $u_i^* \Rightarrow u_i^{n+1}$ through iterative cycling with the momentum equations and, in the case of nonisothermal flow, the energy equation.

An iteration strategy can be devised to drive the divergence error to below some specified level. The first step is to assume that the divergence error at iteration $p+1$ can be approximated by the gradient of a potential function; hence,

$$\left(u_i^* - u_i\right)\Big|_{n+1}^{p+1} \approx - \frac{\partial \phi}{\partial x_i}\bigg|_{n+1}^{p+1} \tag{157}$$

The advection term in Eq. (156) can be approximated by

$$\left(u_j^* \frac{\partial u_i^*}{\partial x_j} - u_j \frac{\partial u_i}{\partial x_j} \right)_{n+1}^{p} \approx \left(u_j^* \frac{\partial (u_i^* - u_i)}{\partial x_j} \right)_{n+1}^{p} \approx - u_j^* \frac{\partial^2 \phi}{\partial x_j \partial x_i}\bigg|_{n+1}^{p} \tag{158}$$

and the diffusion term, for $\mathrm{Re}'=0$, by

$$\theta\,\Delta t \frac{1}{\mathrm{Re}} \left[\frac{\partial}{\partial x_j} \left(\frac{\partial u_i}{\partial x_j} + \frac{\partial u_j}{\partial x_i} \right) - \frac{\partial}{\partial x_j} \left(\frac{\partial u_i^*}{\partial x_j} + \frac{\partial u_j^*}{\partial x_i} \right) \right]_{n+1}^{p} \approx - \theta\,\Delta t \frac{1}{\mathrm{Re}} \frac{\partial^2 (u_i^* - u_i)}{\partial x_j^{\,2}}\bigg|_{n+1}^{p} \tag{159}$$

$$= \theta\,\Delta t \frac{1}{\mathrm{Re}} \frac{\partial^3 \phi}{\partial x_j^{\,2} \partial x_i}\bigg|_{n+1}^{p}$$

Equation (156) is, therefore, approximated by

$$\left.\frac{\partial \phi}{\partial x_i}\right|_{n+1}^{p+1} = \theta \Delta t \left(\frac{1}{\mathrm{Re}} \frac{\partial^3 \phi}{\partial x_j^2 \partial x_i} - u_j^* \frac{\partial^2 \phi}{\partial x_j \partial x_i} \right)_{n+1}^{p} + \theta \Delta t \left. \frac{\partial (P^* - P)}{\partial x_i} \right|_{n+1}^{p} + \mathrm{Ar} (\Theta^* - \Theta) g_i \Big|_{n+1}^{p} \quad (160)$$

Continuing with simplifying Eq. (160), the advection, diffusion, and body force terms are neglected to obtain

$$\left.\frac{\partial \phi}{\partial x_i}\right|_{n+1}^{p+1} = \theta \Delta t \left. \frac{\partial (P^* - P)}{\partial x_i} \right|_{n+1}^{p} \quad (161)$$

Integrating Eq. (161) and setting the constant of integration to zero result in a pseudo-pressure correction equation of the form

$$P|_{n+1}^{p} = P^*|_{n+1}^{p} + \frac{1}{\theta \Delta t} \phi|_{n+1}^{p+1} \quad (162)$$

The difficulty posed by Eq. (162) is that it requires a correction for the pressure at iteration p using the unknown ϕ solution at iteration $p+1$. A computable strategy, therefore, must rely on the accumulation of ϕ solutions, i.e.,

$$P|_{n+1}^{p} = P|_{n} + \frac{1}{\theta \Delta t} \sum_{k=1}^{p} \phi_{n+1}^{k} \quad (163)$$

where, as the iterations converge, $\| \phi \|_l \to 0$ and $\phi \to 0$.

With the above strategy, the error in the velocity field at iteration p is defined as the gradient of a scalar potential function at iteration $p+1$, giving

$$\left(u_i^{n+1} - u_i^* \right)^p = - \frac{\partial \phi}{\partial x_i}^{p+1} \quad (164)$$

Taking the divergence of Eq. (164), the resultant Poisson equation for ϕ is

$$\mathcal{L}(\phi) = \frac{\partial^2 \phi}{\partial x_j \partial x_j} - \frac{\partial u_j^*}{\partial x_j} = 0 \quad (165)$$

The Neumann boundary condition for Eq. (165) is obtained by projecting Eq. (164) onto the outward-pointing normal direction at the boundary Γ, i.e.,

$$- \frac{\partial \phi}{\partial x_i} n_i = \left(u_i^{n+1} - u_i^* \right) n_i \qquad \text{on } \Gamma \quad (166)$$

For that portion of the boundary where all the efflux velocity components are fixed with Dirichlet data, $u_n(x_i, t) = w_n(x_i, t)$ for $x_i \in \Gamma_1$, Eq. (166) becomes a homogeneous Neumann boundary condition.

Using Eq. (164) as a mechanism for a velocity correction equation of the form

$$u_i^{**} = u_i^{*} - \frac{\partial \phi}{\partial x_i} \tag{167}$$

where u_i^{**} is the "corrected" velocity, produces spurious errors near the boundary. The homogeneous Neumann boundary condition, Eq. (166), allows the normal component of u_i^{**} to satisfy the Dirichlet data, i.e., $u_i^{**} n_i = w_n$ for $x_i \in \Gamma_D$; however, in general

$$u_i^{**} \tau_i = \left(u_i^{*} - \frac{\partial \phi}{\partial x_i} \right) \tau_i = w_\tau \qquad \text{on } \Gamma_D \text{ in } \mathbb{R}^2 \tag{168}$$

where w_τ is the tangential component of the Dirichlet velocity vector at the boundary. The velocity correction (or projection) step, therefore, generates a spurious slip velocity that violates the noslip boundary condition (Gresho, 1990). If $u_i^{**} \tau_i$ is set equal to w_τ after the velocity correction, a vortex sheet is produced at Γ_D, thus discontinuously injecting additional vorticity into Ω. Again, iteration within the time step is required to minimize the amount of spurious vorticity produced on Γ_D.

4.2 POISSON EQUATION FOR ϕ

The following discussion presents a formal development of the Poisson equation for the continuity constraint potential function, ϕ, and its natural boundary conditions arising from a Galerkin weak statement.

Recall that the defining relation for ϕ is

$$-\frac{\partial \phi}{\partial x_i} = \left(u_i - u_i^{*} \right) \tag{169}$$

where u_i is the solenoidal velocity field, and u_i^{*} is the computed velocity field not satisfying the continuity condition. The Poisson equation for ϕ results from applying the divergence operator on Eq. (169).

$$-\frac{\partial}{\partial x_i}\left(\frac{\partial \phi}{\partial x_i} \right) = \frac{\partial}{\partial x_i}\left(u_i - u_i^{*} \right) = \frac{\partial u_i}{\partial x_i} - \frac{\partial u_i^{*}}{\partial x_i} = -\frac{\partial u_i^{*}}{\partial x_i}$$

$$\frac{\partial^2 \phi}{\partial x_i \partial x_i} = \frac{\partial u_i^{*}}{\partial x_i} \tag{170}$$

$$\therefore \quad \mathcal{L}(\phi) = \frac{\partial^2 \phi}{\partial x_i \partial x_i} - \frac{\partial u_i^{*}}{\partial x_i} = 0$$

A weak statement for ϕ is

$$\int_\Omega \psi \, \mathcal{L}(\phi) \, d\Omega = \int_\Omega \psi \, \frac{\partial^2 \phi}{\partial x_i \partial x_i} \, d\Omega - \int_\Omega \psi \, \frac{\partial u_i^*}{\partial x_i} \, d\Omega = 0$$
$$\forall \psi \in L_0^2(\Omega) \text{ and } \phi \in H_0^2(\Omega), \; u_i^* \in H^1(\Omega) \tag{171}$$

Applying the Green-Gauss theorem to the diffusion term in Eq. (171) gives

$$\int_\Omega \psi \, \frac{\partial^2 \phi}{\partial x_i \partial x_i} \, d\Omega = -\int_\Omega \frac{\partial \psi}{\partial x_i} \frac{\partial \phi}{\partial x_i} \, d\Omega + \oint_{\partial\Omega} \psi \, \frac{\partial \phi}{\partial x_i} n_i \, d\Gamma \tag{172}$$

where n_i is the outward-pointing normal unit vector on the boundary. Inserting Eq. (172) into Eq. (171), the resulting Galerkin weak statement is

$$\int_\Omega \psi \, \mathcal{L}(\phi) \, d\Omega = -\int_\Omega \frac{\partial \psi}{\partial x_i} \frac{\partial \phi}{\partial x_i} \, d\Omega - \int_\Omega \psi \, \frac{\partial u_i^*}{\partial x_i} \, d\Omega + \oint_{\partial\Omega} \psi \, \frac{\partial \phi}{\partial x_i} n_i \, d\Gamma = 0$$
$$\forall \psi \in H_0^1(\Omega) \text{ and } \phi \in H^1(\Omega), \; u_i^* \in H^1(\Omega) \tag{173}$$

The natural boundary condition for ϕ is the projection of the gradient of ϕ onto the outward-pointing normal of the boundary. By Eq. (169), this projection is related to the error in the velocity field at the boundary

$$-\frac{\partial \phi}{\partial x_i} n_i = (u_i - u_i^*) n_i \tag{174}$$

The six types of boundaries to be investigated are inflow, outflow, entrainment, symmetry, no-slip, and free-slip (tangency condition) boundaries.

4.2.1 Inflow Boundaries

Assume at an inflow boundary that the normal velocities are prescribed by problem data, and, therefore,

$$-\frac{\partial \phi}{\partial x_i} n_i = (u_i - u_i^*) n_i = 0 \tag{175}$$

thus producing a homogeneous Neumann boundary condition for the surface integral in Eq. (173). Using a homogeneous Neumann boundary condition, therefore, establishes a solvability constraint for the data supplied to the ϕ Poisson equation; that is, the Dirichlet velocity data must be divergence free.

4.2.2 Outflow Boundaries

For outflow boundaries, a traction force-balance (Neumann) boundary condition is typically applied for the momentum equations. Therefore, the divergence error is generally not zero at the beginning of the iterations, that is,

$$-\frac{\partial \phi}{\partial x_i} n_i = \left(u_i - u_i^*\right) n_i \neq 0 \tag{176}$$

For a local normal-tangential coordinate system, the gradient of ϕ is

$$\begin{aligned} -\frac{\partial \phi}{\partial n} &= (u_n - u_n^*) \\ -\frac{\partial \phi}{\partial s} &= (u_s - u_s^*) \end{aligned} \tag{177}$$

Assuming that the outflow boundary is positioned such that the predominant flow across the boundary is in the normal direction, one may expect, therefore, that throughout the iterative cycle, the tangential divergence error remains small, such that

$$\begin{aligned} (u_s - u_s^*) = -\frac{\partial \phi}{\partial s} &< \epsilon << 1 \\ \text{or } \frac{\partial \phi}{\partial s} &= 0 \\ \therefore \phi &= \text{constant along } s \end{aligned} \tag{178}$$

The value for ϕ at outflow boundaries is usually set to zero.

4.2.3 Entrainment Boundaries

Based on the above observations for outflow boundaries, a similar argument can be made for entrainment boundaries, specifically, that the tangential divergence error is small throughout the iterative cycle, and a good approximation for ϕ is to set it to zero. The divergence error can be made identically zero by fixing the tangential velocity at an entrainment boundary.

4.2.4 Symmetry Boundaries

For symmetry boundaries, the normal velocity components are set to zero, and, by Eq. (174), the normal component of the divergence error at these boundaries is identically zero. Therefore, the boundary condition for ϕ is homogeneous Neumann.

4.2.5 No-Slip Boundaries

For no-slip boundaries, all velocities are set to zero, and the divergence error at these boundaries is identically zero. Again, the boundary condition for ϕ is homogeneous Neumann.

4.2.6 Free-Slip (Tangency Condition) Boundaries

The tangency boundary condition is

$$u_i n_i = 0 \tag{179}$$

For a free-slip wall, Eq. (174) can, therefore, be rewritten as

$$-\frac{\partial \phi}{\partial x_i} n_i = (u_i - u_i^*) n_i = u_i n_i - u_i^* n_i = -u_i^* n_i$$
$$\text{or} \quad \frac{\partial \phi}{\partial x_i} n_i = u_i^* n_i \neq 0 \tag{180}$$

resulting in a nonhomogeneous Neumann boundary condition at free-slip boundaries. The resulting surface integral should be computed if u_n is not specified. Equation (180) provides an effective means of enforcing a tangency condition along an arbitrarily oriented surface without explicitly having to specify $u_n=0$. With the tangency boundary condition, the Galerkin weak statement for ϕ is

$$\int_\Omega \psi \, \mathcal{L}(\Phi) \, d\Omega = \int_\Omega \frac{\partial \psi}{\partial x_i} \frac{\partial \Phi}{\partial x_i} d\Omega + \int_\Omega \psi \frac{\partial u_i^*}{\partial x_i} d\Omega$$
$$- \oint_{\partial\Omega \text{ tangency}} \psi u_i^* n_i \, d\Gamma = 0 \tag{181}$$
$$\forall \psi \in H_0^1(\Omega) \text{ and } \phi \in H_0^1(\Omega), \; u_i^* \in H^1(\Omega)$$

Evaluating the surface integral in Eq. (181) will enforce an approximation to the tangency condition as the solution converges.

4.3 PRESSURE POISSON EQUATION

One difficulty in solving the pressure Poisson equation for turbulent flows is that the turbulent Reynolds number, i.e., the eddy viscosity ν', is not constant but varies significantly over the flow field. The pressure Poisson equation, therefore, has the general form

$$\mathfrak{L}(P) = \frac{\partial}{\partial x_i}(\mathfrak{L}(u_i)) =$$

$$\frac{\partial}{\partial x_i}\left(\frac{\partial u_i}{\partial t} - \frac{1}{\mathrm{Re}}\frac{\partial^2 u_i}{\partial x_j \partial x_j}\right) + \tag{182}$$

$$\frac{\partial}{\partial x_i}\left(\frac{\partial P}{\partial x_i} + u_j\frac{\partial u_i}{\partial x_j} - \frac{\partial}{\partial x_j}\left(\frac{\mathrm{Re}^t}{\mathrm{Re}}\left(\frac{\partial u_i}{\partial x_j} + \frac{\partial u_j}{\partial x_i}\right)\right) + \mathrm{Ar}\,\Theta\,\hat{g}_i\right) = 0$$

where, due to the presence of the Re^t term, third order spatial derivatives exist for the velocity field. The following analysis demonstrates how the Galerkin weak statement, after selective applications of Green's theorem, reveals the appropriateness of the classic $H^1(\Omega)$ Sobolev space for the velocity, thus producing an easily computed right-hand side for the pressure Poisson equation. The analysis also reveals the natural boundary conditions associated with the Galerkin weak statement for the pressure in laminar and turbulent flows.

Equation (182) can be further simplified by imposing the continuity constraint on the flow field. Assuming the necessary smoothness in the flow field's dependence on time allows the commutation of the temporal derivative with the divergence operator, thus implying that the acceleration is solenoidal for all time, hence

$$\frac{\partial}{\partial x_i}\left(\frac{\partial u_i}{\partial t}\right) = \frac{\partial}{\partial t}\left(\frac{\partial u_i}{\partial x_i}\right) = 0 \tag{183}$$

Next, sufficient smoothness for the spatial derivatives is assumed to allow them to commute. The reference Reynolds number, Re, by definition does not vary over the flow field, therefore,

$$\frac{\partial}{\partial x_i}\left(\frac{1}{\mathrm{Re}}\frac{\partial^2 u_i}{\partial x_j^2}\right) = \frac{1}{\mathrm{Re}}\frac{\partial^2}{\partial x_j^2}\left(\frac{\partial u_i}{\partial x_i}\right) = 0 \tag{184}$$

Applying Eqs. (183) and (184) to Eq. (182) yields the pressure Poisson equation for divergence-free flow fields as

$$\mathfrak{L}(P) = \frac{\partial}{\partial x_i}\left(\mathfrak{L}^*(u_i)\right) =$$

$$\frac{\partial}{\partial x_i}\left(\frac{\partial P}{\partial x_i} + u_j\frac{\partial u_i}{\partial x_j} - \frac{\partial}{\partial x_j}\left(\frac{\mathrm{Re}^t}{\mathrm{Re}}\left(\frac{\partial u_i}{\partial x_j} + \frac{\partial u_j}{\partial x_i}\right)\right) + \mathrm{Ar}\,\Theta\,\hat{g}_i\right) = 0 \tag{185}$$

Note that $\mathcal{L}^*(u_i)$ is defined as

$$\begin{aligned}\mathcal{L}^*(u_i) &\equiv \frac{\partial P}{\partial x_i} + u_j \frac{\partial u_i}{\partial x_j} - \frac{\partial}{\partial x_j}\left(\frac{\mathrm{Re}^{\dagger}}{\mathrm{Re}}\left(\frac{\partial u_i}{\partial x_j} + \frac{\partial u_j}{\partial x_i} \right) \right) + \mathrm{Ar}\,\Theta\,\hat{\mathbf{g}}_i \\ &= \mathcal{L}(u_i) - \frac{\partial u_i}{\partial t} + \frac{\partial}{\partial x_j}\left(\frac{1}{\mathrm{Re}} \frac{\partial u_i}{\partial x_j} \right)\end{aligned} \tag{186}$$

In Eq. (185), the continuity constraint has eliminated the diffusion term associated with the mean flow Reynolds number; however, the spatial dependence of the $\mathrm{Re}^{\dagger}$ diffusion term has forced a third-order derivative on the velocity to remain in the formulation.

A Galerkin weak statement for the pressure is now

$$\begin{aligned}&\int_\Omega \psi\, \mathcal{L}(P)\, d\Omega = \int_\Omega \psi \frac{\partial}{\partial x_i}\left(\mathcal{L}^*(u_i) \right) d\Omega = 0 \\ &\forall\ \psi \in L_0^2(\Omega) \quad \text{and } u_i \in H_0^3(\Omega),\quad P \in H_0^2(\Omega)\end{aligned} \tag{187}$$

specifically, u_i lies in $H_0^3(\Omega)$. Employing Green's theorem with Eq. (187) results in

$$\begin{aligned}&\int_\Omega \psi \frac{\partial}{\partial x_i}\left(\mathcal{L}^*(u_i) \right) d\Omega = -\int_\Omega \frac{\partial \psi}{\partial x_i} \mathcal{L}^*(u_i)\, d\Omega + \oint_{\partial\Omega} \psi\, \mathcal{L}^*(u_i)\, n_i\, d\Gamma = 0 \\ &\forall\ \psi \in H_0^1(\Omega) \text{ and } u_i \in H_0^2(\Omega),\quad P \in H_0^1(\Omega)\end{aligned} \tag{188}$$

From the momentum equations observe that

$$\begin{aligned}\mathcal{L}^*(u_i) &= \frac{\partial P}{\partial x_i} + u_j \frac{\partial u_i}{\partial x_j} - \frac{\partial}{\partial x_j}\left(\frac{\mathrm{Re}^{\dagger}}{\mathrm{Re}}\left(\frac{\partial u_i}{\partial x_j} + \frac{\partial u_j}{\partial x_i} \right) \right) + \mathrm{Ar}\,\Theta\,\hat{\mathbf{g}}_i \\ &= -\frac{\partial u_i}{\partial t} + \frac{1}{\mathrm{Re}} \frac{\partial^2 u_i}{\partial x_j^2}\end{aligned} \tag{189}$$

Therefore, Eq. (188) becomes

$$\int_\Omega \psi \frac{\partial}{\partial x_i}\left(\mathcal{L}^*(u_i)\right) d\Omega =$$

$$-\int_\Omega \frac{\partial \psi}{\partial x_i}\left[\frac{\partial P}{\partial x_i} + u_j \frac{\partial u_i}{\partial x_j} - \frac{\partial}{\partial x_j}\left(\frac{Re^t}{Re}\left(\frac{\partial u_i}{\partial x_j} + \frac{\partial u_j}{\partial x_i}\right)\right) + Ar\,\Theta\,\hat{\mathbf{g}}_i \right] d\Omega \qquad (190)$$

$$- \oint_{\partial\Omega} \psi \frac{\partial u_i}{\partial t} n_i \, d\Gamma + \oint_{\partial\Omega} \psi \frac{1}{Re} \frac{\partial^2 u_i}{\partial x_j^2} n_i \, d\Gamma = 0$$

$$\forall\ \psi \in H_0^1(\Omega) \text{ and } u_i \in H_0^2(\Omega)$$

In Eq. (190), both the turbulent diffusion term and the final surface integral act to constrain the velocity to reside in $H^2(\Omega)$. The following analysis verifies that the Sobolev space for velocity can be expanded to $H^1(\Omega)$.

4.3.1 Treatment of the Re^t Term in Eq. (190)

Focusing attention on the term in Eq. (190) involving the turbulent Reynolds number Re^t, the pressure Poisson equation, Eq. (185), can be expressed as

$$\mathcal{L}(P) = \frac{\partial}{\partial x_i}\left(\mathcal{L}^*(u_i)\right) = \frac{\partial}{\partial x_i}\left(\mathcal{L}_1^*(u_i) + \mathcal{L}_2^*(u_i)\right) \qquad (191)$$

where

$$\mathcal{L}_1^*(u_i) = \frac{\partial P}{\partial x_i} + u_j \frac{\partial u_i}{\partial x_j} + Ar\,\Theta\,\hat{\mathbf{g}}_i \qquad (192)$$

$$\mathcal{L}_2^*(u_i) = -\frac{\partial}{\partial x_j}\left(\frac{Re^t}{Re}\left(\frac{\partial u_i}{\partial x_j} + \frac{\partial u_j}{\partial x_i}\right)\right) \qquad (193)$$

From Eq. (187), the weak statement for the pressure is

$$\int_\Omega \psi\, \mathcal{L}(P) d\Omega = \int_\Omega \psi \frac{\partial}{\partial x_i}\left(\mathcal{L}_1^*(u_i) + \mathcal{L}_2^*(u_i)\right) d\Omega$$

$$= \int_\Omega \psi \frac{\partial}{\partial x_i}\left(\mathcal{L}_1^*(u_i)\right) d\Omega + \int_\Omega \psi \frac{\partial}{\partial x_i}\left(\mathcal{L}_2^*(u_i)\right) d\Omega = 0 \qquad (194)$$

The weak statement for $\mathcal{L}_2$, upon expanding terms, becomes

$$\int_\Omega \psi \frac{\partial}{\partial x_i}\left(\mathcal{L}_2^*(u_i)\right) d\Omega = \int_\Omega \psi \frac{\partial}{\partial x_i}\left[- \frac{\partial}{\partial x_j}\left(\frac{Re^t}{Re}\left(\frac{\partial u_i}{\partial x_j} + \frac{\partial u_j}{\partial x_i}\right)\right)\right] d\Omega$$

$$= - \int_\Omega \psi \frac{\partial^2}{\partial x_j \partial x_i}\left(\frac{Re^t}{Re}\left(\frac{\partial u_i}{\partial x_j} + \frac{\partial u_j}{\partial x_i}\right)\right) d\Omega$$

$$= - \int_\Omega \psi \left[\frac{\partial^2}{\partial x_j \partial x_i}\left(\frac{Re^t}{Re} \frac{\partial u_i}{\partial x_j}\right) + \frac{\partial^2}{\partial x_i \partial x_j}\left(\frac{Re^t}{Re} \frac{\partial u_j}{\partial x_i}\right)\right] d\Omega \qquad (195)$$

$$= -2 \int_\Omega \psi \frac{\partial^2}{\partial x_j \partial x_i}\left(\frac{Re^t}{Re} \frac{\partial u_i}{\partial x_j}\right) d\Omega$$

$$= -2 \int_\Omega \psi \frac{\partial}{\partial x_j}\left(\frac{\partial (Re^t/Re)}{\partial x_i} \frac{\partial u_i}{\partial x_j} + \frac{Re^t}{Re} \frac{\partial}{\partial x_j}\left(\frac{\partial u_i}{\partial x_i}\right)\right) d\Omega$$

$$= -2 \int_\Omega \psi \frac{\partial}{\partial x_j}\left(\frac{\partial (Re^t/Re)}{\partial x_i} \frac{\partial u_i}{\partial x_j}\right) d\Omega$$

Green's theorem is applied to the final form of Eq. (195), with the result

$$-2 \int_\Omega \psi \frac{\partial}{\partial x_j}\left(\frac{\partial (Re^t/Re)}{\partial x_i} \frac{\partial u_i}{\partial x_j}\right) d\Omega = \qquad (196)$$

$$2\left[\int_\Omega \frac{\partial \psi}{\partial x_j} \frac{\partial (Re^t/Re)}{\partial x_i} \frac{\partial u_i}{\partial x_j} d\Omega - \oint_{\partial\Omega} \psi \frac{\partial (Re^t/Re)}{\partial x_i} \frac{\partial u_i}{\partial x_j} n_j \, d\Gamma\right]$$

$$\therefore \int_\Omega \psi \frac{\partial}{\partial x_i}\left(\mathcal{L}_2^*(u_i)\right) d\Omega = \qquad (197)$$

$$2 \int_\Omega \frac{\partial \psi}{\partial x_j} \frac{\partial (Re^t/Re)}{\partial x_i} \frac{\partial u_i}{\partial x_j} d\Omega - 2 \oint_{\partial\Omega} \psi \frac{\partial (Re^t/Re)}{\partial x_i} \frac{\partial u_i}{\partial x_j} n_j \, d\Gamma$$

Returning to $\mathcal{L}_1$, Green's theorem gives

$$\int_\Omega \psi \frac{\partial}{\partial x_i}\left(\mathcal{L}_1^*(u_i)\right) d\Omega = - \int_\Omega \frac{\partial \psi}{\partial x_i} \mathcal{L}_1^*(u_i) \, d\Omega + \oint_{\partial\Omega} \psi \mathcal{L}_1^*(u_i) n_i \, d\Gamma \qquad (198)$$

Note that

$$\mathcal{L}^{*}_{1}(u_i) = \frac{\partial P}{\partial x_i} + u_j \frac{\partial u_i}{\partial x_j} + \mathrm{Ar}\,\Theta\,\hat{\mathbf{g}}_i = -\frac{\partial u_i}{\partial t} + \frac{1}{\mathrm{Re}}\frac{\partial^2 u_i}{\partial x_j^{\,2}} + \frac{\partial}{\partial x_j}\left(\frac{\mathrm{Re}'}{\mathrm{Re}}\left(\frac{\partial u_i}{\partial x_j} + \frac{\partial u_j}{\partial x_i}\right)\right) \tag{199}$$

$$\therefore \; -\int_\Omega \frac{\partial \psi}{\partial x_i}\,\mathcal{L}^{*}_{1}(u_i)\,d\Omega + \oint_{\partial\Omega} \psi\,\mathcal{L}^{*}_{1}(u_i)\,n_i\,d\Gamma = -\int_\Omega \frac{\partial \psi}{\partial x_i}\left(\frac{\partial P}{\partial x_i} + u_j\frac{\partial u_i}{\partial x_j} + \mathrm{Ar}\,\Theta\,\mathbf{g}_i\right)d\Omega - \oint_{\partial\Omega}\psi\frac{\partial u_i}{\partial t}n_i\,d\Gamma + \frac{1}{\mathrm{Re}}\oint_{\partial\Omega}\psi\frac{\partial^2 u_i}{\partial x_j^{\,2}}n_i\,d\Gamma + \oint_{\partial\Omega}\psi\frac{\partial}{\partial x_j}\left(\frac{\mathrm{Re}'}{\mathrm{Re}}\left(\frac{\partial u_i}{\partial x_j} + \frac{\partial u_j}{\partial x_i}\right)\right)n_i\,d\Gamma \tag{200}$$

The weak statement for the pressure is now, after multiplying through by -1,

$$\int_\Omega \psi\,\mathcal{L}(P)\,d\Omega = \int_\Omega \frac{\partial \psi}{\partial x_i}\left(\frac{\partial P}{\partial x_i} + u_j\frac{\partial u_i}{\partial x_j} + \mathrm{Ar}\,\Theta\,\hat{\mathbf{g}}_i\right)d\Omega + \oint_{\partial\Omega}\psi\frac{\partial u_i}{\partial t}n_i\,d\Gamma - \frac{1}{\mathrm{Re}}\oint_{\partial\Omega}\psi\frac{\partial^2 u_i}{\partial x_j^{\,2}}n_i\,d\Gamma - \oint_{\partial\Omega}\psi\frac{\partial}{\partial x_j}\left(\frac{\mathrm{Re}'}{\mathrm{Re}}\left(\frac{\partial u_i}{\partial x_j} + \frac{\partial u_j}{\partial x_j}\right)\right)n_i\,d\Gamma - 2\int_\Omega \frac{\partial \psi}{\partial x_j}\frac{\partial(\mathrm{Re}'/\mathrm{Re})}{\partial x_i}\frac{\partial u_i}{\partial x_j}d\Omega + 2\oint_{\partial\Omega}\psi\frac{\partial(\mathrm{Re}'/\mathrm{Re})}{\partial x_i}\frac{\partial u_i}{\partial x_j}n_j\,d\Gamma = 0 \tag{201}$$

$$\forall\ \psi \in H^1_0(\Omega)\ \text{and}\ u_i \in H^2(\Omega),\quad P \in H^1(\Omega)$$

The surface integrals in Eq. (201) involving Re' can be further simplified by

$$-\oint_{\partial\Omega}\psi\frac{\partial}{\partial x_j}\left(\frac{\mathrm{Re}'}{\mathrm{Re}}\left(\frac{\partial u_i}{\partial x_j} + \frac{\partial u_j}{\partial x_i}\right)\right)n_i\,d\Gamma + 2\oint_{\partial\Omega}\psi\frac{\partial(\mathrm{Re}'/\mathrm{Re})}{\partial x_i}\frac{\partial u_i}{\partial x_j}n_j\,d\Gamma = -\oint_{\partial\Omega}\psi\frac{\partial(\mathrm{Re}'/\mathrm{Re})}{\partial x_j}\left(\frac{\partial u_i}{\partial x_j} + \frac{\partial u_j}{\partial x_i}\right)n_i\,d\Gamma - \oint_{\partial\Omega}\psi\frac{\mathrm{Re}'}{\mathrm{Re}}\frac{\partial^2 u_i}{\partial x_j^{\,2}}n_i\,d\Gamma + 2\oint_{\partial\Omega}\psi\frac{\partial(\mathrm{Re}'/\mathrm{Re})}{\partial x_j}\frac{\partial u_j}{\partial x_i}n_i\,d\Gamma \tag{202}$$

The second term on the right-hand side of Eq. (202) can also benefit from an application of Green's theorem:

$$- \oint_{\partial\Omega} \psi \frac{\mathrm{Re}^t}{\mathrm{Re}} \frac{\partial^2 u_i}{\partial x_j^2} n_i \, d\Gamma = \oint_{\partial\Omega} \frac{\partial(\psi(\mathrm{Re}^t/\mathrm{Re}))}{\partial x_j} \frac{\partial u_i}{\partial x_j} n_i \, d\Gamma - \oint_{\partial\Omega_{1D}} \psi \frac{\mathrm{Re}^t}{\mathrm{Re}} \frac{\partial u_i}{\partial x_j} n_i n_j \, d\Gamma_{1D} =$$

$$\oint_{\partial\Omega} \psi \frac{\partial(\mathrm{Re}^t/\mathrm{Re})}{\partial x_j} \frac{\partial u_i}{\partial x_j} n_i \, d\Gamma + \oint_{\partial\Omega} \frac{\mathrm{Re}^t}{\mathrm{Re}} \frac{\partial \psi}{\partial x_j} \frac{\partial u_i}{\partial x_j} n_i \, d\Gamma - \oint_{\partial\Omega_{1D}} \psi \frac{\mathrm{Re}^t}{\mathrm{Re}} \frac{\partial u_k}{\partial x_k} d\Gamma_{1D} \tag{203}$$

In Eq. (203), the dyadic $n_i n_j$ for an orthogonal coordinate system is equal to the Kronecker delta, δ_{ij}, and, therefore, the continuity constraint will remove the final integral. Equation (202), with the use of Eq. (203), becomes

$$- \oint_{\partial\Omega} \psi \frac{\partial}{\partial x_j} \left(\frac{\mathrm{Re}^t}{\mathrm{Re}} \left(\frac{\partial u_i}{\partial x_j} + \frac{\partial u_j}{\partial x_i} \right) \right) n_i \, d\Gamma + 2 \oint_{\partial\Omega} \psi \frac{\partial(\mathrm{Re}^t/\mathrm{Re})}{\partial x_i} \frac{\partial u_i}{\partial x_j} n_j \, d\Gamma =$$

$$- \oint_{\partial\Omega} \psi \frac{\partial(\mathrm{Re}^t/\mathrm{Re})}{\partial x_j} \left(\frac{\partial u_i}{\partial x_j} + \frac{\partial u_j}{\partial x_i} \right) n_i \, d\Gamma + \oint_{\partial\Omega} \psi \frac{\partial(\mathrm{Re}^t/\mathrm{Re})}{\partial x_j} \frac{\partial u_i}{\partial x_j} n_i \, d\Gamma \tag{204}$$

$$+ \oint_{\partial\Omega} \frac{\mathrm{Re}^t}{\mathrm{Re}} \frac{\partial \psi}{\partial x_j} \frac{\partial u_i}{\partial x_j} n_i \, d\Gamma + 2 \oint_{\partial\Omega} \psi \frac{\partial(\mathrm{Re}^t/\mathrm{Re})}{\partial x_j} \frac{\partial u_j}{\partial x_i} n_i \, d\Gamma$$

or

$$- \oint_{\partial\Omega} \psi \frac{\partial}{\partial x_j} \left(\frac{\mathrm{Re}^t}{\mathrm{Re}} \left(\frac{\partial u_i}{\partial x_j} + \frac{\partial u_j}{\partial x_i} \right) \right) n_i \, d\Gamma + 2 \oint_{\partial\Omega} \psi \frac{\partial(\mathrm{Re}^t/\mathrm{Re})}{\partial x_i} \frac{\partial u_i}{\partial x_j} n_j \, d\Gamma =$$

$$+ \oint_{\partial\Omega} \frac{\mathrm{Re}^t}{\mathrm{Re}} \frac{\partial \psi}{\partial x_j} \frac{\partial u_i}{\partial x_j} n_i \, d\Gamma + \oint_{\partial\Omega} \psi \frac{\partial(\mathrm{Re}^t/\mathrm{Re})}{\partial x_j} \frac{\partial u_j}{\partial x_i} n_i \, d\Gamma \tag{205}$$

The pressure weak statement with the above considerations is

$$\int_\Omega \psi \, \mathfrak{L}(P) \, d\Omega = \int_\Omega \frac{\partial \psi}{\partial x_i} \left(\frac{\partial P}{\partial x_i} + u_j \frac{\partial u_i}{\partial x_j} + \mathrm{Ar}\,\Theta\, \mathbf{g}_i \right) d\Omega$$

$$+ \oint_{\partial\Omega} \psi \frac{\partial u_i}{\partial t} n_i \, d\Gamma - \frac{1}{\mathrm{Re}} \oint_{\partial\Omega} \psi \frac{\partial^2 u_i}{\partial x_j^2} n_i \, d\Gamma \tag{206}$$

$$+ \oint_{\partial\Omega} \frac{\mathrm{Re}^t}{\mathrm{Re}} \frac{\partial \psi}{\partial x_j} \frac{\partial u_i}{\partial x_j} n_i \, d\Gamma - 2 \int_\Omega \frac{\partial \psi}{\partial x_j} \frac{\partial(\mathrm{Re}^t/\mathrm{Re})}{\partial x_i} \frac{\partial u_i}{\partial x_j} d\Omega + \oint_{\partial\Omega} \psi \frac{\partial(\mathrm{Re}^t/\mathrm{Re})}{\partial x_j} \frac{\partial u_j}{\partial x_i} n_i \, d\Gamma = 0$$

$$\forall \; \psi \in H_0^1(\Omega) \text{ and } u_i \in H^1(\Omega)$$

To complete the analysis, two cases will be examined for the surface integral involving the second derivative of u_n.

4.3.2 Case 1: Inflow Boundaries

A second application of Green's theorem for the final surface integral in Eq. (190) results in

$$-\frac{1}{\mathrm{Re}}\oint_{\partial\Omega}\psi\,\frac{\partial^2 u_i}{\partial x_j^{\,2}}\,n_i\,\mathrm{d}\Gamma=\frac{1}{\mathrm{Re}}\oint_{\partial\Omega}\frac{\partial\psi}{\partial x_j}\,\frac{\partial u_i}{\partial x_j}\,n_i\,\mathrm{d}\Gamma-\frac{1}{\mathrm{Re}}\oint_{\partial\Omega\text{-}1D}\psi\,\frac{\partial u_i}{\partial x_j}\,n_i n_j\,\mathrm{d}\Gamma \tag{207}$$

As noted previously, for orthogonal coordinate systems the dyadic or second order tensor arising from the outer product of two unit vectors, $n_i\,n_j$, is equal to the Kronecker delta, δ_{ij}. Therefore, the final 1-dimensional integral in Eq. (207) is

$$\frac{1}{\mathrm{Re}}\oint_{\partial\Omega\text{-}1D}\psi\,\frac{\partial u_i}{\partial x_j}\,n_i n_j\,\mathrm{d}\Gamma=\frac{1}{\mathrm{Re}}\oint_{\partial\Omega\text{-}1D}\psi\,\frac{\partial u_i}{\partial x_j}\,\delta_{ij}\,\mathrm{d}\Gamma=\frac{1}{\mathrm{Re}}\oint_{\partial\Omega\text{-}1D}\psi\,\frac{\partial u_j}{\partial x_j}\,\mathrm{d}\Gamma=0 \tag{208}$$

Therefore, with Eqs. (207) and (208), the weak statement, for Case 1, is

$$\begin{aligned}\int_\Omega\psi\,\mathfrak{L}(P)\,\mathrm{d}\Omega&=\int_\Omega\frac{\partial\psi}{\partial x_i}\left(\frac{\partial P}{\partial x_i}+u_j\frac{\partial u_i}{\partial x_j}+\mathrm{Ar}\,\Theta\,\hat{\mathbf{g}}_i\right)\mathrm{d}\Omega\\&+\oint_{\partial\Omega}\psi\,\frac{\partial u_i}{\partial t}\,n_i\,\mathrm{d}\Gamma+\frac{1}{\mathrm{Re}}\oint_{\partial\Omega}\frac{\partial\psi}{\partial x_j}\,\frac{\partial u_i}{\partial x_j}\,n_i\,\mathrm{d}\Gamma\\&+\oint_{\partial\Omega}\frac{\mathrm{Re}^{\dagger}}{\mathrm{Re}}\,\frac{\partial\psi}{\partial x_j}\,\frac{\partial u_i}{\partial x}\,n_i\,\mathrm{d}\Gamma-2\int_\Omega\frac{\partial\psi}{\partial x_j}\,\frac{\partial(\mathrm{Re}^{\dagger}/\mathrm{Re})}{\partial x_i}\,\frac{\partial u_i}{\partial x_j}\,\mathrm{d}\Omega+\oint_{\partial\Omega}\psi\,\frac{\partial(\mathrm{Re}^{\dagger}/\mathrm{Re})}{\partial x_j}\,\frac{\partial u_j}{\partial x_i}\,n_i\,\mathrm{d}\Gamma=0\end{aligned} \tag{209}$$

$$\forall\ \psi\in H_0^1(\Omega)\ \text{and}\ u_i\in H^1(\Omega),\quad P\in H^1(\Omega)$$

4.3.3 Case 2: No-slip and Free-slip Boundaries

For no-slip and free-slip walls, an alternate formulation of the surface integral of the viscous flux vector can be examined. For convenience, the analysis is set in $\mathbb{R}^2$.

At the surface of a wall one can construct a local normal/tangential or *n-s* coordinate system. The proper boundary conditions for the velocity field at an impenetrable no-slip wall are, in the *n-s* coordinate system,

$$\begin{aligned}u_i\,n_i&=0\\u_i\,s_i&=0\end{aligned} \tag{210}$$

Note that the continuity equation in the *n-s* coordinate system is

$$\frac{\partial u_s}{\partial s} + \frac{\partial u_n}{\partial n} = 0 \tag{211}$$

and the Laplacian operator has the form $\frac{\partial^2}{\partial x_j^2} \Rightarrow \frac{\partial^2}{\partial n^2} + \frac{\partial^2}{\partial s^2}$. Transforming the surface integral from the global to the local *n-s* coordinate system gives

$$-\frac{1}{\mathrm{Re}} \oint_{\partial\Omega} \psi \frac{\partial^2 u_n}{\partial x_j^2} d\Gamma = -\frac{1}{\mathrm{Re}} \oint_{\partial\Omega} \psi \left(\frac{\partial^2 u_n}{\partial s^2} + \frac{\partial^2 u_n}{\partial n^2} \right) d\Gamma \quad . \tag{212}$$

At a no-slip wall, the derivative of the normal component of the velocity field with respect to the wall tangential direction is zero, since u_n is 0 along s, thus

$$\frac{\partial^2 u_n}{\partial s^2} = \frac{\partial}{\partial s}\left(\frac{\partial u_n}{\partial s} \right) = 0 \tag{213}$$

By the continuity equation, the second derivative of u_n with respect to the normal coordinate becomes

$$\frac{\mathrm{d}^2 u_n}{\mathrm{d}n^2} \rightarrow \frac{\mathrm{d}}{\mathrm{d}n}\left(\frac{\partial u_n}{\partial n} \right) = -\frac{\mathrm{d}}{\mathrm{d}n}\left(\frac{\partial u_s}{\partial s} \right) \tag{214}$$

Therefore, the surface integral along the no-slip wall is

$$-\frac{1}{\mathrm{Re}} \oint_{\partial\Omega} \psi \left(\frac{\partial^2 u_n}{\partial s^2} + \frac{\partial^2 u_n}{\partial n^2} \right) d\Gamma = -\frac{1}{\mathrm{Re}} \oint_{\partial\Omega} \psi \left(-\frac{\partial}{\partial s}\left(\frac{\mathrm{d}u_s}{\mathrm{d}n} \right) \right) d\Gamma \tag{215}$$

Applying Green's theorem results in

$$-\frac{1}{\mathrm{Re}} \oint_{\partial\Omega} \psi \left(-\frac{\partial}{\partial s}\left(\frac{\mathrm{d}u_s}{\mathrm{d}n} \right) \right) d\Gamma = -\frac{1}{\mathrm{Re}} \oint_{\partial\Omega} \frac{\partial\psi}{\partial s}\left(\frac{\mathrm{d}u_s}{\mathrm{d}n} \right)_{\mathrm{wall}} d\Gamma + \left[\psi \frac{\mathrm{d}u_s}{\mathrm{d}n} \cdot s \right] \tag{216}$$

As was true in the previous Case 1, the final term in Eq. (216) is zero since it represents the projection of a vector in the n direction onto the s direction. Since n and s are orthogonal, their inner product must be zero. Note that the derivative $\mathrm{d}u_s/\mathrm{d}n$ represents the shear strain rate (and also the vorticity) at the wall. Coupled with the viscosity in the Reynolds number pre-multiplying the surface integral, the term also represents a nondimensional shear stress at the wall.

4.3.4 Inflow Boundaries: Treatment of Advection Term

The term in the pressure residual arising from the kinematic flux vector in the momentum equations can provide natural boundary conditions for inflow planes. Applying Green's theorem,

$$\int_\Omega \frac{\partial \psi}{\partial x_i}\, u_j\, \frac{\partial u_i}{\partial x_j}\, d\Omega = -\int_\Omega \psi\, \frac{\partial u_j}{\partial x_i}\, \frac{\partial u_i}{\partial x_j}\, d\Omega + \oint_{\partial\Omega} \psi\, u_j\, \frac{\partial u_i}{\partial x_j}\, n_i\, d\Gamma \tag{217}$$

The surface integral in Eq. (217) must be computed at inflow boundaries.

4.4 CCM OVERVIEW

In a preceding section it was demonstrated that an iterative cycle within the time-step is required for an implicit integration. During these outer iterations, the CCM replaces the genuine pressure with a continuity constraint state-variable, C^p_{n+1}, where the superscript p is an iteration index. The θ-implicit semi-discrete momentum equations, therefore, have the form

$$\begin{aligned} u_i^*\big|^p_{n+1} = u_i\big|_n - \theta\Delta t\left[\frac{\partial (u_j u_i)^*}{\partial x_j} - \frac{\partial}{\partial x_j}\left(\frac{1+\mathrm{Re}^t}{\mathrm{Re}}\left(\frac{\partial u_i}{\partial x_j}+\frac{\partial u_j}{\partial x_i}\right)\right)^* + \frac{\partial C}{\partial x_i} + \mathrm{Ar}\,\Theta^*\,\hat{\mathbf{g}}_i\right]^p_{n+1} \\ -(1-\theta)\Delta t\left[\frac{\partial (u_j u_i)}{\partial x_j} - \frac{\partial}{\partial x_j}\left(\frac{1+\mathrm{Re}^t}{\mathrm{Re}}\left(\frac{\partial u_i}{\partial x_j}+\frac{\partial u_j}{\partial x_i}\right)\right) + \frac{\partial P}{\partial x_i} + \mathrm{Ar}\,\Theta\,\hat{\mathbf{g}}_i\right]_n \end{aligned} \tag{218}$$

When the genuine pressure, P, is required, it is assumed computable, as discussed in the previous section, from the pressure Poisson equation, i.e.,

$$\mathfrak{L}(P) = \frac{\partial^2 P}{\partial x_i \partial x_i} + \frac{\partial u_j}{\partial x_i}\frac{\partial u_i}{\partial x_j} - \frac{\partial^2}{\partial x_i \partial x_j}\left(\frac{\mathrm{Re}^t}{\mathrm{Re}}\left(\frac{\partial u_i}{\partial x_j}+\frac{\partial u_j}{\partial x_i}\right)\right) + \mathrm{Ar}\,\frac{\partial \Theta}{\partial x_i}\,\hat{\mathbf{g}}_i = 0 \tag{219}$$

for any $u_i\big|_{n+1}$, a converged, solenoidal velocity vector field. The genuine nonhomogeneous Neumann boundary condition for Eq. (219) is

$$\frac{\partial P}{\partial n} = \frac{\partial}{\partial x_j}\left[\left(\frac{1+\mathrm{Re}^t}{\mathrm{Re}}\right)\frac{\partial u_n}{\partial x_j}\right] - \frac{\partial u_n}{\partial t} - u_j\frac{\partial u_n}{\partial x_j} - \mathrm{Ar}\,\theta\,\hat{\mathbf{g}}_n \quad \text{on } \Gamma_D \tag{220}$$

where Γ_D is the union of all boundary segments where the velocities are fixed by Dirichlet data, e.g., walls and inflow planes.

The iterative cycle in the CCM requires the solution of a Poisson equation for a continuity constraint potential function Φ. This Poisson equation has the form

$$\nabla^2 \Phi^{p+1} = \nabla \cdot \boldsymbol{u}^{*p} \tag{221}$$

The boundary conditions for Φ on Γ_D are homogeneous Neumann.

$$\frac{\partial \Phi}{\partial n}^{p+1} = 0 \quad \text{on } \Gamma_D \tag{222}$$

The CCM iterative solution strategy is:

● TIME STEP $n+1$

(1) initialize the constraint state-variable by either $C^1{}_{n+1} = C^{p+1}_n$ or $C^1{}_{n+1} = P^n$;
(2) solve the momentum and energy equations implicitly for u^{*p} and Θ^{*p} ;
(3) solve Poisson equation for Φ^p ;
(4) update approximation for C_{n+1} by

$$C^{p+1}_{n+1} = C^1_{n+1} + \left(\frac{1}{\theta \Delta t} \right) \sum_{k=1}^{p} \Phi^k$$

(5) repeat steps (2)-(4) until

$$\| \Phi^p \|_E < \epsilon \quad , \text{ convergence tolerance}$$

(6) advance time step ; solve genuine pressure Poisson equation for P^{n+1}.

Since equal-order interpolation of all state-variables is employed, which is the finite-element equivalent of using a nonstaggered mesh, the div-stability condition is not satisfied by the CCM. As a result, there is a dominant dispersive error mode, *modulo* ∇^h, associated with Φ. One significant computational attribute of the genuine pressure Poisson solve in Step 6 is that it prevents the dispersive error from polluting the velocity and temperature solutions. Step 6 also provides the means for establishing a basis (i.e., a continuous $C^1{}_{n+1}$ based on the genuine pressure P^n) for an approximation of P^{n+1} during the iterative cycle. Experience with the CCM has shown that the pressure Poisson solve can be subcycled (e.g., solved every third, fourth, or fortieth time-step) to improve computational efficiency.

Step 5 defines the *stopping test* for the outer iteration cycle in terms of the energy semi-norm of Φ, defined as

$$\| \Phi^p \|_E = \left. \frac{\frac{1}{2} \int_\Omega \frac{\partial \Phi}{\partial x_j} \frac{\partial \Phi}{\partial x_j} \, d\Omega}{\text{Volume of } \Omega^h} \right|^p_{n+1} \tag{223}$$

where the $\| \Phi \|_E$ has been normalized by the volume of the mesh. By the definition of Φ, Eq. (164), the normalized energy norm can be seen to be a measure of the kinetic energy per unit volume of the error in the current approximation for $u_i \mid_{n+1}$.

4.5 GALERKIN WEAK STATEMENT

The conservation law system described in Chapter 2 constitutes a nonlinear coupled set of initial-value partial differential equations (PDE) whose solutions are constrained by the incompressibility condition. These PDEs can be expressed in the general form

$$\mathcal{L}(q) = \frac{\partial q}{\partial t} + \frac{\partial}{\partial x_j} \left(f_j - f_j^v \right) - s = 0 \qquad \text{on } \Omega \subset \mathbb{R}^n \, , \; t \geq t_0 \tag{224}$$

where $\mathcal{L}(q)$ is a differential equation system written on the state-variable $q(x_j,t)$. The function f_j is called the *kinematic flux vector*, and f_j^v is the *viscous flux vector*. For the Reynolds-averaged Navier-Stokes equations in $\mathbb{R}^3$ with Boussinesq buoyancy body forces and negligible viscous dissipation, q, f_j, and f_j^v have the following definitions:

$$q \equiv \begin{Bmatrix} u_1 \\ u_2 \\ u_3 \\ \Theta \end{Bmatrix} \; ; \; f_j \equiv \begin{Bmatrix} u_j u_1 + P\delta_{1j} \\ u_j u_2 + P\delta_{2j} \\ u_j u_3 + P\delta_{3j} \\ u_j \Theta \end{Bmatrix} \; ; \; f_j^v \equiv \begin{Bmatrix} \left(\frac{1 + \mathrm{Re}^t}{\mathrm{Re}}\right)\frac{\partial u_1}{\partial x_j} \\ \left(\frac{1 + \mathrm{Re}^t}{\mathrm{Re}}\right)\frac{\partial u_2}{\partial x_j} \\ \left(\frac{1 + \mathrm{Re}^t}{\mathrm{Re}}\right)\frac{\partial u_3}{\partial x_j} \\ \frac{1}{\mathrm{Re}}\left(\frac{1}{\mathrm{Pr}} + \frac{\mathrm{Re}^t}{\mathrm{Pr}^t}\right)\frac{\partial \Theta}{\partial x_j} \end{Bmatrix} \; ; \; s \equiv \begin{Bmatrix} -\mathrm{Ar}\Theta\hat{g}_1 \\ -\mathrm{Ar}\Theta\hat{g}_2 \\ -\mathrm{Ar}\Theta\hat{g}_3 \\ s_\Theta \end{Bmatrix} \tag{225}$$

The algorithm auxiliary quasi-linear Poisson PDEs have the general form

$$\mathcal{L}(q_\alpha) = \nabla^2 q_\alpha - s_\alpha(q) = 0 \quad \text{on } \Omega \subset \mathbb{R}^n \; , \; t \geq t_0 \tag{226}$$

where

$$q_\alpha \equiv \begin{Bmatrix} \phi \\ P \end{Bmatrix} \quad ; \quad s_\alpha \equiv \begin{Bmatrix} \nabla \cdot \boldsymbol{u}^* \\ -\nabla \cdot (\mathcal{L}(\boldsymbol{u}) - \nabla P) \end{Bmatrix} \tag{227}$$

Proceeding to the discrete form of Eq. (224), the state-variables q and q_α are replaced by a continuous approximation that assumes the separability of space and time, thus

$$q(x_j,t) \approx q^N(x_j,t) \equiv \sum_{i=1}^{N} \Psi_i(x_j)\, Q_i(t) \tag{228}$$

where the function set $\Psi_i(x_j)$, called the approximation "trial space," is user-selectable. The superscript N in Eq. (228) denotes *any* approximate solution produced via the inner product of the known trial function $\Psi_i(x_j)$ and the set of unknown coefficients $Q_i(t)$.

The *weak statement* is a continuum form of the *method of weighted residuals* for constraining the error in q^N. Using the functional spaces defined in Chapter 3, one seeks the vector function $u_i^N(x_j,t) \in V_0$ and the scalar functions $\Theta^N(x_j,t) \in V_0$, $\phi^N(x_j,t) \in S_0$, and $P^N(x_j,t) \in S_0$ such that

$$\int_\Omega w(x_i,t)\, \mathcal{L}(q^N)\, d\tau = 0 \quad , \; \forall\, w \in V_0 \tag{229}$$

where the velocity vector function u_i^N is also constrained to sit in Z, the space of weakly divergence-free functions. The requirement that Eq. (229) must hold for any test function $w(x_j,t) \in V_0$ is enforced by making the integral stationary with respect to any set of $W_i(t)$, where the interpolation of $w(x_j,t)$ is carried out by

$$w^M(x_j,t) \equiv \sum_{i=1}^{M} \Phi_i(x_j)\, W_i(t) \tag{230}$$

This extremum is termed a "weak statement" with the form

$$\begin{aligned} WS^N &\equiv \frac{\partial}{\partial W_i} \int_\Omega w^M(x_j,t)\, \mathfrak{L}(q^N)\, d\tau \quad , \quad \forall\, i \\ &= \int_\Omega \Phi_i(x_j)\, \mathfrak{L}(q^N)\, d\tau = 0 \quad , \quad \text{for } 1 \le i \le M \end{aligned} \tag{231}$$

The optimal choice for the test function set $\Phi_i(x_j)$ is that it be identical to the trial space $\Psi_i(x_j)$ (Baker, 1983). This decision yields a *Galerkin weak statement*

$$GWS^N \equiv \int_\Omega \Psi_i(x_j)\, \mathfrak{L}(q^N)\, d\tau = 0, \quad \text{for } 1 \le i \le N \tag{232}$$

Mathematically, the GWS^N is optimal since the approximation error in $q^N(x_j,t)$ is required to be orthogonal to the space of functions supporting q^N for any choice of trial space (cf. Baker et al., 1992b).

For *any* approximate solution, the GWS^N form for Eq. (224) is

$$\begin{aligned} GWS^N &= \int_\Omega \Psi_i \left(\frac{\partial q^N}{\partial t} + \frac{\partial}{\partial x_j}\left(f_j - f_j^v \right)^N - s^N \right) d\tau \\ &= \left(\int_\Omega \Psi_i \left(\frac{\partial q^N}{\partial t} - s^N \right) d\tau - \int_\Omega \frac{\partial \Psi_i}{\partial x_j} \left(f_j - f_j^v \right)^N d\tau + \oint_{\partial\Omega_e \cap \partial\Omega} \Psi_i \left(f_j - f_j^v \right) n_j\, d\sigma \right) = \{0\} \end{aligned} \tag{233}$$

where Green's theorem has been applied to project the divergence operator from the flux vectors, f_j and f_j^v, to the approximation trial space, Ψ_i, and to produce a surface integral in Eq. (233) that is the mathematical placeholder for all *natural* boundary conditions in the GWS^N.

The finite-element method uses a spatial semi-discretization (or partitioning) Ω^h, of the continuum domain Ω, made up of the union of a set of non-overlapping subdomains Ω_e or finite elements, such that

$$\Omega \approx \Omega^h \equiv \bigcup_e \Omega_e \tag{234}$$

The approximation q^N is then formed as q^h, the union of finite-element approximations q_e on Ω_e, i.e.,

$$q(x_j,t) \approx q^N(x_j,t) \equiv q^h(x_j,t) = \bigcup_e q_e(x_j,t) \tag{235}$$

On any finite-element domain Ω_e, the generic form for q_e is

$$q_e(x_j,t) = \{N_k(\eta_j)\}^T \{Q(t)\}_e \tag{236}$$

where each element in the row vector $\{N_k\}^T$ (called the finite-element *basis* set) is a kth degree polynomial. There are as many of these polynomials as there are nodal degrees-of-freedom in Ω_e.

The indicated integrals in Eq. (233) are evaluated at the element level, and the resulting element-rank expressions are then summed (*assembled*) into a global matrix statement of the form

$$GWS^h = [M]\frac{d\{Q\}}{dt} + \{R(Q)\} = \{0\} \tag{237}$$

In Eq. (237), $[M]$ and $\{R\}$ are a global rank square matrix and column vector, respectively, and $\{Q\}\equiv\{Q(t)\}$ is the array of the state-variable approximation coefficients at the geometric nodes of Ω^h. The residual $\{R\}$ is a nonlinear function of $\{Q\}$, and contains contributions from all terms in Eq. (233) except the time term, i.e., convection, diffusion, source, and boundary conditions.

For the present CCM implementation, the discretization of the time derivative employs the θ-implicit, one-step algorithm family (Euler/trapezoidal) derived in the previous section. The terminal algebraic statement for Eq. (237) is of the form

$$\{FQ\} = [M]\{Q_{n+1}-Q_n\} + \Delta t(\theta\{R\}_{n+1} + (1-\theta)\{R\}_n) = \{0\} \tag{238}$$

where $t_{n+1} = t_n+\Delta t$ and $0.5\le\theta\le1.0$. A GWS^N is also developed for any Poisson equation in the CCM, directly producing the algebraic system as

$$\{FQ_A\} = [D]\{Q_A\} - \{S_A(Q(t))\} \tag{239}$$

The GWS^h finite-element methodology has, therefore, produced a coupled, nonlinear system of algebraic equations that must be solved iteratively. The classic Newton method constitutes the following iterative cycle,

$$\begin{aligned}
&\{Q\}^0_{n+1} = \{Q\}_n \;\;;\;\; \{FQ\}^0_{n+1} = \{FQ\}_n \\
&\text{for } p = 0,1,2,\ldots \text{ until convergence} \\
&\left[M + \theta\Delta t\frac{\partial\{R\}}{\partial\{Q\}}\right]^p_{n+1}\{\delta Q\}^{p+1}_{n+1} = -\{FQ\}^p_{n+1} \\
&\{Q\}^{p+1}_{n+1} = \{Q\}^p_{n+1} + \{\delta Q\}^{p+1}_{n+1}
\end{aligned} \tag{240}$$

Quasi-Newton approximations amount to the use of simplified forms of the Jacobian $[M+\theta\Delta t\partial\{R\}/\partial\{Q\}]$.

The quasi-linear algebraic system Eq. (239) has the matrix statement

$$[D]\{Q_A\} = \{S_A(Q(t))\} \tag{241}$$

4.6 FINITE-ELEMENT BASIS OPERATIONS

The CCM Galerkin weak statement algorithm is cast into computable form via a finite-element semi-discretization of the domain of integration of the GWS^N, with a 0-implicit time integration procedure. The element geometry considered most appropriate for verification of the CCM is the trilinear, planar-faced hexahedron, Fig. 5. This 3-dimensional finite element can be distorted easily to fit most applicable geometries. In transform (η) space, it appears as a Cartesian unit cube. The trilinear basis functions spanning the 8-node hexahedron, in the nodal order given in Fig. 5, are

$$\{N(\eta_i)\} = \frac{1}{8}\begin{Bmatrix} (1-\eta_1)(1-\eta_2)(1-\eta_3) \\ (1+\eta_1)(1-\eta_2)(1-\eta_3) \\ (1+\eta_1)(1+\eta_2)(1-\eta_3) \\ (1-\eta_1)(1+\eta_2)(1-\eta_3) \\ (1-\eta_1)(1-\eta_2)(1+\eta_3) \\ (1+\eta_1)(1-\eta_2)(1+\eta_3) \\ (1+\eta_1)(1+\eta_2)(1+\eta_3) \\ (1-\eta_1)(1+\eta_2)(1+\eta_3) \end{Bmatrix} \tag{242}$$

A fundamental aspect of the finite-element method is the use of a *master element* where all element-data inner products and integrations are performed in generalized coordinates. The coordinate transformation (or mapping) that bridges the computational (transform) η-space and Euclidean space $\mathbb{R}^3$ is

$$\tau^e : \eta \to x_i = x_i(\eta) \tag{243}$$

The mapping τ^e is *one-to-one and onto* its range provided the transformation Jacobian J is nonsingular, where

$$[J] = \left[\frac{\partial x_j}{\partial \eta_i}\right]_{(3,3)} = \begin{Bmatrix} \frac{\partial}{\partial \eta_1} \\ \frac{\partial}{\partial \eta_2} \\ \frac{\partial}{\partial \eta_3} \end{Bmatrix} \{x_1, x_2, x_3\} = \begin{bmatrix} J_{11} & J_{12} & J_{13} \\ J_{21} & J_{22} & J_{23} \\ J_{31} & J_{32} & J_{33} \end{bmatrix} \tag{244}$$

The inverse of Eq. (244) is required to evaluate the flux vector divergence term in the GWS^N. The closed form solution is

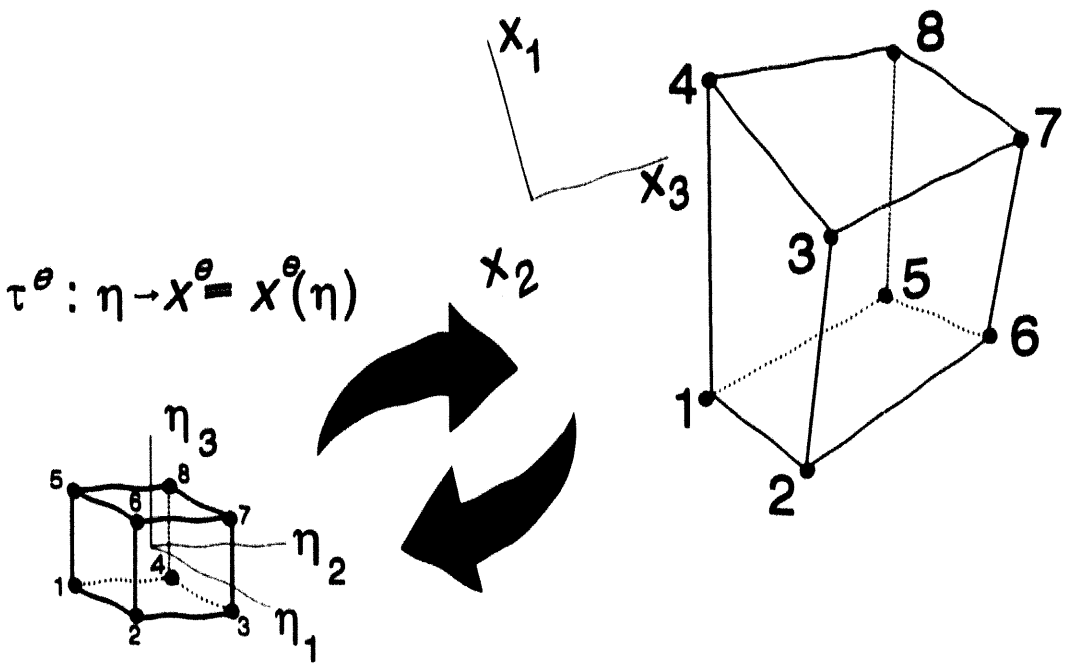

Figure 5. Trilinear hexahedron with one-to-one mapping onto R^3.

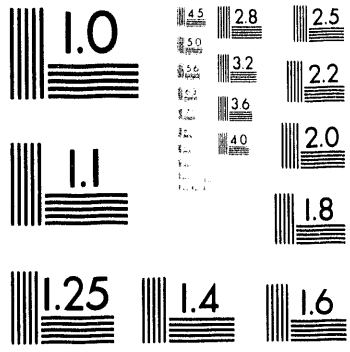
1.0
1.1
1.25
1.4
1.6
2.0
2.2
2.5
2.8
3.2
3.6
4.0
4.5
5.0
5.6

2 of 4

$$[J]^{-1} = \left[\frac{\partial \eta_j}{\partial x_i}\right] = \frac{1}{\det[J]} \begin{bmatrix} (J_{22}J_{33} - J_{32}J_{23}), & (J_{13}J_{32} - J_{12}J_{33}), & (J_{12}J_{23} - J_{13}J_{22}) \\ (J_{31}J_{23} - J_{21}J_{33}), & (J_{11}J_{33} - J_{13}J_{31}), & (J_{21}J_{13} - J_{23}J_{11}) \\ (J_{21}J_{32} - J_{31}J_{22}), & (J_{12}J_{31} - J_{32}J_{11}), & (J_{11}J_{22} - J_{12}J_{21}) \end{bmatrix} \tag{245}$$

where

$$\begin{aligned} \det[J] &= J_{11}(J_{22}J_{33} - J_{32}J_{23}) - J_{12}(J_{21}J_{33} - J_{31}J_{23}) + J_{13}(J_{21}J_{32} - J_{31}J_{22}) \\ &= \frac{\partial x_1}{\partial \eta_1}\left(\frac{\partial x_2}{\partial \eta_2}\frac{\partial x_3}{\partial \eta_3} - \frac{\partial x_2}{\partial \eta_3}\frac{\partial x_3}{\partial \eta_2}\right) - \frac{\partial x_2}{\partial \eta_1}\left(\frac{\partial x_1}{\partial \eta_2}\frac{\partial x_3}{\partial \eta_3} - \frac{\partial x_1}{\partial \eta_3}\frac{\partial x_3}{\partial \eta_2}\right) + \\ &\quad \frac{\partial x_3}{\partial \eta_1}\left(\frac{\partial x_1}{\partial \eta_2}\frac{\partial x_2}{\partial \eta_3} - \frac{\partial x_1}{\partial \eta_3}\frac{\partial x_2}{\partial \eta_2}\right) \end{aligned} \tag{246}$$

The metric tensor $\partial \eta_j / \partial x_i$ is required only on the master element Ω_e ; therefore, the specific local form for Eq. (243) uses the interpolation Eq. (242) yielding

$$x_j^e = x_j^e(\eta_i) = \{N(\eta_i)\}^T \{XJ\}_e \tag{247}$$

where the entries in $\{XJ\}_e$ are the (x_1, x_2, x_3) coordinates of the eight nodes of Ω_e . (The notational convention from here on is that capital letters denote discrete data at the nodes of Ω^h, while lower case defines the continuum forms.) Since the element transformation generates piecewise smooth data, on quality discretizations it is appropriate to evaluate the metric data $\partial \eta_j / \partial x_i$ at the centroid of Ω_e, yielding a significant DO-loop economy in the code. Using a subscript to denote node numbers on Ω_e , one obtains, for example,

$$\begin{aligned} \frac{\partial x_1}{\partial \eta_1} &= \frac{1}{8}(-XI_1 + XI_2 + XI_3 - XI_4 - XI_5 + XI_6 + XI_7 - XI_8) \\ \frac{\partial x_2}{\partial \eta_1} &= \frac{1}{8}(-X2_1 + X2_2 + X2_3 - X2_4 - X2_5 + X2_6 + X2_7 - X2_8) \\ \frac{\partial x_3}{\partial \eta_1} &= \frac{1}{8}(-X3_1 + X3_2 + X3_3 - X3_4 - X3_5 + X3_6 + X3_7 - X3_8) \\ &\vdots \\ \frac{\partial x_3}{\partial \eta_3} &= \frac{1}{8}(-X3_1 - X3_2 - X3_3 - X3_4 + X3_5 + X3_6 + X3_7 + X3_8) \end{aligned} \tag{248}$$

The final steps for the finite-element implementation are to form the basis η_i-derivatives, needed for the flux vector terms, and to complete all integrals. The derivative operation on Eq. (242) is trivial and produces

$$\left\{\frac{\partial N}{\partial \eta_1}\right\} = \frac{1}{8}\begin{Bmatrix} -(1-\eta_2)(1-\eta_3) \\ (1-\eta_2)(1-\eta_3) \\ (1+\eta_2)(1-\eta_3) \\ -(1+\eta_2)(1-\eta_3) \\ -(1-\eta_2)(1+\eta_3) \\ (1-\eta_2)(1+\eta_3) \\ (1+\eta_2)(1+\eta_3) \\ -(1+\eta_2)(1+\eta_3) \end{Bmatrix}; \left\{\frac{\partial N}{\partial \eta_2}\right\} = \frac{1}{8}\begin{Bmatrix} -(1-\eta_1)(1-\eta_3) \\ -(1+\eta_1)(1-\eta_3) \\ (1+\eta_1)(1-\eta_3) \\ (1-\eta_1)(1-\eta_3) \\ -(1-\eta_1)(1+\eta_3) \\ -(1+\eta_1)(1+\eta_3) \\ (1+\eta_1)(1+\eta_3) \\ (1-\eta_1)(1+\eta_3) \end{Bmatrix}; \left\{\frac{\partial N}{\partial \eta_3}\right\} = \frac{1}{8}\begin{Bmatrix} -(1-\eta_1)(1-\eta_2) \\ -(1+\eta_1)(1-\eta_2) \\ -(1+\eta_1)(1+\eta_2) \\ -(1-\eta_1)(1+\eta_2) \\ (1-\eta_1)(1-\eta_2) \\ (1+\eta_1)(1-\eta_2) \\ (1+\eta_1)(1+\eta_2) \\ (1-\eta_1)(1+\eta_2) \end{Bmatrix} \quad (249)$$

Products of $\{N(\eta_i)\}$ with itself, and/or $\partial\{N\}/\partial\eta_i$, are required to be integrated over Ω_e to form the *master matrix library* for the selected basis. A compact notation, (cf. Baker and Pepper, 1991, Ch. 5), for any 1-, 2-, or 3-dimensional matrix is [*Mabcd*], where

M: prefix denoting the dimensionality of the element master matrix, *M*= *A* for 1D, *B* for 2D, and *C* for 3D

a: an integer indicating how many bases occur in the integral

b,c,d: integers 1,2, or 3, denoting the η_i-direction of the derivatives in the matrix, or 0 for no derivative

The master element matrices appearing in Eq. (238) are of the form [*B2bc*] for boundary condition 2-dimensional surface elements, [*C*200] for the mass matrix and source terms, and [*C2bc*] or [*C3bcd*] for the kinematic and viscous flux vector terms. Since the summation convention operates therein, (*b,c,d*) can also become (*I,J,K*) in compact notation for inner products on EJK_e, where "EJK_e," is the name in compact notation for $(\partial\eta_k/\partial x_j)_e$.

As an example, the kinematic flux vector term is nonlinear and, with *P* extracted via the CCM continuity theory, yields the finite-element matrix equivalent as

$$\begin{aligned} \int_{\Omega_e} \frac{\partial\{N\}}{\partial\eta_k}\frac{\partial\eta_k}{\partial x_j} f_j^{\,e}\, d\Omega &= \int_{\Omega_e} \frac{\partial\{N\}}{\partial\eta_k}\frac{\partial\eta_k}{\partial x_j}(qu_j)_e \det[J]\; d\Omega \\ &\approx \left(\frac{\partial\eta_k}{\partial x_j}\right)_e DET_e \int_{\Omega_e} \{UJ\}_e^T\{N\}\frac{\partial\{N\}}{\partial\eta_k}\{N\}^T\{Q\}_e\, d\eta \\ &= \left(\frac{\partial\eta_k}{\partial x_j}\right)_e DET_e\, \{UJ\}_e^T\left(\int_{\Omega_e}\{N\}\frac{\partial\{N\}}{\partial\eta_k}\{N\}^T d\eta\right)\{Q\}_e \\ &\equiv EJK_e\, DET_e\, \{UJ\}_e^T[C30K0]\{Q\}_e \end{aligned} \quad (250)$$

The three master hypermatrices [*C*30K0], K=1,2,3 , each consist of nine 8×1 column arrays of

integers normalized by an integer, since $1 \le (J,K) \le n = 3$ is a summation index. The formulation of its contribution into $\{R\}_e$ of the Newton statement, Eq. (240), involves a DO-loop to multiply the various element-dependent data (with subscript e) as inner products.

The actual construction of any [C30K0] employs a Gaussian quadrature rule, e.g.,

$$[C3010] = \int_{-1}^{1}\int_{-1}^{1}\int_{-1}^{1} f(\eta_1,\eta_2,\eta_3)\, d\eta_1\, d\eta_2\, d\eta_3$$
$$= \sum_{i=1}^{n}\sum_{j=1}^{n}\sum_{k=1}^{n} w_i w_j w_k\, f(\eta_{1i},\eta_{2j},\eta_{3k}) \qquad (251)$$

where the function in the integrand is

$$f(\eta_{1i},\eta_{2j},\eta_{3k}) = \{N(\eta_{1i},\eta_{2j},\eta_{3k})\}\frac{\partial\{N(\eta_{1i},\eta_{2j},\eta_{3k})\}}{\partial\eta_1}\{N(\eta_{1i},\eta_{2j},\eta_{3k})\}^T \qquad (252)$$

4.7 FINITE-ELEMENT RESIDUAL STATEMENTS

The construction of finite-element residuals $\{FQ\}$ (as specified by Eq. (238)) for the velocity components is representative of data base operations for the CCM. The lead term in Eq. (238), from the time derivative in Eq. (224), becomes

$$\int_{\Omega_e} \{N\}\{N\}^T \det[J]\, d\Omega\, (\{UI\}^{n+1} - \{UI\}^n) \approx DET_e\, [C200](\{UI\}^{n+1} - \{UI\}^n)_e \qquad (253)$$

since no derivatives are involved, and DET_e is evaluated at the centroid of Ω_e. The kinematic flux vector term yields, after application of Green's theorem (Baker, 1983),

$$-\Delta t\, \{UJ\}^T \int_{\Omega_e} \{N\}\frac{\partial\eta_k}{\partial x_j}\frac{\partial\{N\}}{\partial\eta_k}\{N\}^T \det[J]\, d\Omega\, \{UI\} \approx$$
$$-\Delta t\, DET_e\ \ EJK_e\ \ \{UJ\}_e^T\, [C30K0]\, \{UI\}_e \qquad (254)$$

The viscous flux vector term, with effective diffusion coefficient $1/Re^E \equiv (1+Re^t)/Re$ evaluated at the centroid, yields

$$\Delta t \int_{\Omega_e} \frac{1}{Re^E}\frac{\partial\eta_k}{\partial x_j}\frac{\partial\{N\}}{\partial\eta_k}\frac{\partial\eta_m}{\partial x_j}\frac{\partial\{N\}^T}{\partial\eta_m} \det[J]\, d\Omega\, \{UI\} \approx$$
$$\Delta t\, DET_e\, \frac{1}{Re^E}\, EJK_e\, EJM_e\, [C2KM]\, \{UI\}_e \qquad (255)$$

The Boussinesq body-force term is

$$\Delta t\, \mathrm{Ar} \int_{\Omega_e} \{N\}\{N\}^T g_i \det[J]\, d\Omega \{\Theta\}_e \approx$$
$$\Delta t\, DET_e\ \mathrm{Ar}\ GI\ [C200]\{\Theta\}_e \tag{256}$$

where GI is a unit vector in the direction of gravity. Finally, the continuity constraint function is applied via the directional derivative

$$\Delta t \int_{\Omega_e} \frac{\partial \eta_k}{\partial x_i} \{N\} \frac{\partial \{N\}^T}{\partial \eta_k} \det[J]\, d\Omega \{CNP1\}_e \approx \Delta t\ DET_e\ EIJ_e\ [C20J]\{CNP1\}_e =$$
$$\Delta t\, DET_e (EI1\,[C201] + EI2\,[C202] + EI3\,[C203])\{CNP1\}_e \tag{257}$$

where $\{CNP1\}$ contains the current evaluation of $C^1_{n+1} + \sum_{k=2}^{p+1} \frac{\Phi^k}{\theta\, \Delta t}$.

The residual statement for all other members of the initial-valued state variable is similarly formed. For example, the residual for the energy equation in compact form is

$$\{F\Theta\} = DET_e [C200](\{\Theta\}^{n+1} - \{\Theta\}^n)_e$$
$$- \Delta t\, DET_e\ EJK_e \{UJ\}^T_e [C30K0]\{\Theta\}_e$$
$$+ \Delta t \frac{1}{\mathrm{Re}} \left(\frac{1}{\mathrm{Pr}} + \frac{\mathrm{Re}^t}{\mathrm{Pr}^t} \right) DET_e\ EJK_e\ EJM_e\ [C2KM]\{\Theta\}_e \tag{258}$$
$$- \Delta t\ DET_e\ [C200]\ \{S\Theta\}$$

Two Poisson discrete weak statements for the auxiliary variables close the CCM algorithm. For the continuity constraint, the GWS^h yields the residual

$$\{F\Phi\} = DET_e\ EJK_e\ EJM_e\ [C2KM]\{\Phi\}_e$$
$$+ DET_e\ EJK_e\ [C20K]\{UJ\}^{n+1}_e \tag{259}$$
$$+ DET2_e [B200]\ NJ_e \{UJ\}^{n+1}_e = \{0\}$$

The last term in Eq.(259) is the Neumann boundary condition resulting from the application of Green's theorem to the residual for Φ. Since this boundary condition is imposed on a 2-dimensional boundary segment $\partial\Omega_e$, it produces a $[B\ \ldots\ ]$ master matrix and the corresponding determinant $DET2_e$ as indicated.

The discretized residual for the pressure is, using Eq. (209) as a guide,

$$\{FP\} = \int_\Omega \frac{\partial\{N\}}{\partial x_i}\left[\frac{\partial(\{N\}^T\{P\})}{\partial x_i} + \{N\}^T\{UJ\}\frac{\partial(\{N\}^T\{UI\})}{\partial x_j} + \mathrm{Ar}\,\{N\}^T\{\Theta\}\,\mathbf{g}_i\right]d\Omega$$

$$- 2\int_\Omega \frac{\partial(\{RETURB\}^T\{N\})}{\partial x_i}\,\frac{\partial\{N\}}{\partial x_j}\,\frac{\partial(\{N\}^T\{UI\})}{\partial x_j}\,d\Omega$$

$$+ \oint_{\partial\Omega}\{N\}\{N\}^T\{DUIDt\}\,n_i\,d\Gamma + \frac{1}{\mathrm{Re}}\oint_{\partial\Omega}\frac{\partial\{N\}}{\partial x_j}\,\frac{\partial(\{N\}^T\{UI\})}{\partial x_j}\,n_i\,d\Gamma \qquad (260)$$

$$+ \oint_{\partial\Omega}\{RETURB\}^T\{N\}\,\frac{\partial(\{N\})}{\partial x_j}\,\frac{\partial(\{N\}^T\{UI\})}{\partial x_j}\,n_i\,d\Gamma$$

$$+ \oint_{\partial\Omega}\frac{\partial(\{RETURB\}^T\{N\})}{\partial x_j}\{N\}\,\frac{\partial(\{N\}^T\{UJ\})}{\partial x_i}\,n_i\,d\Gamma = \{0\}$$

In compact notation, the 3-dimensional residual for the pressure is

$$\{FP\}_e = DET_e\,EJK_e\,EJM_e\,[C2KM]\,\{P\}_e$$

$$+ DET_e\,EIK_e\,EJM_e\,\{UJ\}_e^T\,[C30KM]\,\{UI\}_e$$

$$+ DET_e\,GI\,\mathrm{Ar}_e\,EIK_e\,[C2K0]\,\{\Theta\}_e$$

$$- 2\,DET_e\,EIM_e\,EJK_e\,EJL_e\,\{RETURB\}_e^T\,[C3MKL]\,\{UI\}_e$$

$$+ DET2_e\,[B200]\,\{DUIDt\}_e\,NI \qquad (261)$$

$$+ DET2_e\,\frac{1}{\mathrm{Re}}\,EJK_e\,EJM_e\,[B2KM]\,\{UI\}_e\,NI$$

$$+ DET2_e\,EJK_e\,EJM_e\,\{RETURB\}_e^T\,[B30KM]\,\{UI\}_e\,NI$$

$$+ DET2_e\,EJK_e\,EIM_e\,\{RETURB\}_e^T\,[B3K0M]\,\{UJ\}_e\,NI = \{0\}$$

4.8 A QUASI-NEWTON ITERATION PROCEDURE

Any linear algebra matrix iteration approximation starts with the formation of the Newton Jacobian. For Eq. (240), the developed finite-element residual statements are readily differentiated to produce the necessary *master matrix* expressions. The element contribution to the Newton Jacobian from the residual time term for $\{FUI\}_e$ is

$$\frac{\partial\{FUI\}}{\partial\{UI\}} = DET_e\,[C200] \tag{262}$$

Similarly,

$$\frac{\partial\{FUI\}}{\partial\{UI\}} = -\Delta t\,\theta\; DET_e \Big[\{UJ\}_e^T EJK_e\,[C30K0] + \{UI\}_e^T \left(EI1_e\,[C3010] + EI2_e\,[C3020] + EI3_e\,[C3030] \right) \Big] \tag{263}$$

is the velocity self-coupling contribution from $\theta\Delta t\{R\}$. The non-self-coupling momentum contributions, from Eq. (254), are

$$\frac{\partial\{FUI\}}{\partial\{UJ\}} = -\Delta t\,\theta\, DET_e\,\{UI\}_e^T \left(EJ1_e\,[C3010] + EJ2_e\,[C3020] + EJ3_e\,[C3030] \right) \tag{264}$$

for the restriction J≠I. The dissipative flux vector term in $\theta\Delta t\{R\}$ yields

$$\frac{\partial\{FUI\}}{\partial\{UI\}} = \Delta t\, DET_e \frac{1}{\mathrm{Re}} \left(1 + \mathrm{Re}^t \right) EJK_e\; EJM_e\,[C2KM] \tag{265}$$

and the temperature coupling term is

$$\frac{\partial\{FUI\}}{\partial\{\Theta\}} = \Delta t\,\theta\; DET_e\; \mathrm{Ar}\,[C200]\,GI \tag{266}$$

Expressions similar to Eqs. (262)-(266) are readily derived for all other state variable contributions to the Newton Jacobian. The segregated Jacobians for the two Poisson equation discrete statements are identical and of the form

$$\frac{\partial\{F\Phi\}}{\partial\{\Phi\}} = DET_e\; EJK_e\; EJM_e\,[C2KM] \tag{267}$$

4.9 BOUNDARY CONDITIONS

Four common boundary types that must be addressed by any incompressible Navier-Stokes CFD algorithm are: (1) no-slip impenetrable boundaries, (2) free-slip and drag-slip tangential boundaries, (3) inflow boundaries, and (4) outflow boundaries. The following discussion details the treatment of these boundaries by the CCM.

No-slip impenetrable boundaries require that the flow velocity at the boundary equal the velocity of the boundary; therefore, all velocity components are fixed at the no-slip boundary velocity, $w_i(x_j,t)$. For a fully-contained flow, $\Gamma_N=\varnothing$, a solvability condition exists for the Dirichlet data, such that

$$\oint_{\Gamma} w_i n_i \, d\Gamma = 0 \tag{268}$$

which is a requirement for global conservation of mass.

Free-slip boundaries require the satisfaction of a tangency condition, i.e., $u_i n_i = w_n$. If the wall is parallel to a coordinate axis, then the tangency condition can be easily enforced by setting $u_i n_i = w_n$. For stationary boundaries at arbitrary angles with respect to the coordinate system, an approximate tangency condition may be applied using a nonhomogeneous Neumann boundary condition with Poisson equation for the continuity constraint potential function.

A tangential traction or drag is imposed on the flow-field through the evaluation of the natural boundary condition produced by applying Green's theorem to the viscous flux vector for the momentum equations. For example, for laminar flow,

$$-\frac{1}{\mathrm{Re}}\int_{\Omega}\psi\,\frac{\partial^2 u_i}{\partial x_i\,\partial x_j}\,d\Omega = \frac{1}{\mathrm{Re}}\int_{\Omega}\frac{\partial\psi}{\partial x_j}\,\frac{\partial u_i}{\partial x_j}\,d\Omega - \frac{1}{\mathrm{Re}}\oint_{\partial\Omega}\psi\,\frac{\partial u_i}{\partial n}\,d\Gamma \tag{269}$$

Focusing on the surface integral in Eq. (269), the integrand can be related to the shear stress at a slip wall by

$$-\frac{1}{\mathrm{Re}^{E}}\left(\frac{\mu\,U_{ref}}{g_c\,L_{ref}}\right)\left(\frac{g_c\,L_{ref}}{\mu\,U_{ref}}\right)\oint_{\partial\Omega}\psi\,\frac{\partial u_i}{\partial n}\,d\Gamma = \frac{1}{\mathrm{Re}^{E}}\oint_{\partial\Omega}\psi\,\tau_{i\text{-}wall}\,d\Gamma \tag{270}$$

where $\tau_{i\text{-}wall}$ is the dimensionless traction at the wall in the *ith* direction. The dimensional traction, τ_i^* has been scaled by $(g_c\,L_{ref}/\mu\,U_{ref})$ such that

$$\frac{\partial u_i}{\partial n} = -\tau_{i\text{-}wall} \tag{271}$$

The traction at the wall can be expressed by a general function, e.g.,

$$\tau_{i\text{-}wall} = \left| a + b\,U_{i\text{-}s} + c\left(U_{i\text{-}s} - U_{b\text{-}s}\right)^{d} \right| \tag{272}$$

where $U_{i\text{-}s}$ is the tangential velocity of the fluid near the wall, and $U_{b\text{-}s}$ is the velocity of the wall boundary itself. By Eq. (272), the boundary condition in $\mathbb{R}^3$ is applied to the residuals for each momentum equation by

$$+\Delta t\;\theta\;\frac{1}{\mathrm{Re}}\,[B200]\,\{TAUIW\}_e\,DET2_e \tag{273}$$

For the energy equation at wall boundaries, the temperature or the heat flux may be fixed. The heat flux may be applied as a constant or as a linear or nonlinear function of boundary and near-wall fluid temperatures. The heat flux boundary condition arises from the diffusion term in the weak statement for the energy equation. Applying Green's theorem results in

$$\frac{1}{\mathrm{Re\,Pr}}\int_{\Omega}\frac{\partial\psi}{\partial x_j}\frac{\partial\Theta}{\partial x_j}\,d\Omega \;-\; \frac{1}{\mathrm{Re\,Pr}}\oint_{\Gamma}\psi\frac{\partial\Theta}{\partial x_j}n_j\,d\Gamma \tag{274}$$

The surface integral in Eq. (274) can be related to the dimensional heat flux at the boundary by Fourier's Law of Conduction

$$q_{wall} = -k\frac{\partial T}{\partial n} \tag{275}$$

Eq. (275) can be non-dimensionalized such that

$$-\frac{\partial\Theta}{\partial n} = \left(\frac{L_{ref}}{\Delta T_{ref}\,k}\right) q_{wall} = QFLUX \tag{276}$$

In Eq. (276), *QFLUX* is the non-dimensional heat flux at the boundary where a positive value indicates that heat is being removed from the flow. The residual for the energy equation is now, using compact notation for the 3-dimensional case,

$$\{F\Theta\} = \{\text{other terms}\} + DET2_e\frac{1}{\mathrm{Re\,Pr}}[B200]\{QFLUX\}_e \tag{277}$$

The contribution to the Jacobian for the energy equation is

$$\frac{\partial\{F\Theta\}}{\partial\{\Theta\}} = \theta\Delta t\,\frac{DET2_e}{\mathrm{Re\,Pr}}\,\overline{\frac{\partial QFLUX}{\partial\Theta}}\,[B200] \tag{278}$$

The overbar in Eq. (278) indicates that any explicit appearance of Θ in the derivative term will be replaced by an average value for the 2-dimensional boundary element.

A general function describing three possible methods of imposing a heat flux at a boundary is

$$q_{wall} = a + bT + c(T-T_b)^d \tag{279}$$

The constants a, b, c, d, and T_b are data. Note that Eq. (279) is a dimensional equation, and a, b, c, and T_b must, therefore, have dimensions consistent with any other dimensional data in the problem. The temperature T_b is a prescribed boundary temperature located outside of the computational domain. The three positionally dependent boundary conditions that can be applied using Eq. (279) are a prescribed heat flux, forced convection, and natural convection.

4.9.1 Case 1 - Prescribed Heat Flux

The heat flux q_{wall} is imposed by some external means and is independent of any solution variables. This boundary condition is applied by setting

$$a = Q_{wall} \quad ; \quad b = c = d = 0$$

4.9.2 Case 2 - Forced Convection

For a forced convection boundary condition, Newton's Law of Cooling has the form

$$q_{wall} = h\,(T - T_b) \tag{280}$$

where h is a user-prescribed heat transfer coefficient (film coefficient). Eq. (279) requires that

$$a = -h\,T_b \quad ; \quad b = h \quad ; \quad c = d = 0$$

In terms of a , b , and θ, the result is

$$q_{wall} = b\,[\,\theta\,\Delta T_{ref} + T_{ref}\,] + a$$

4.9.3 Case 3 - Natural Convection

In the case of natural convection from a surface, there are a number of empirical correlations expressing the film coefficient for natural convection as a nonlinear function of the difference between the fluid temperature, T , and the surface temperature, T_b . (Recall that T_b is located outside of the computational domain.) These correlations typically can be cast in the dimensional form

$$h = C_1\,(T - T_b)^{C_2} \quad . \tag{281}$$

The relation for the boundary heat flux is now

$$q_{wall} = h\,(T - T_b) = C_1\,(T - T_b)^{1+C_2} \tag{282}$$

In terms of the general function,

$$a = b = 0 \quad ; \quad c = C_1 \quad ; \quad d = 1 + C_2 \quad ; \quad \text{specify } T_b$$

The complete nondimensional form for Eq. (279) is

$$QFLUX = \left(\frac{a\,L_{ref}}{\Delta T_{ref}\,k}\right) + \left(\frac{b\,L_{ref}}{k}\right)\left[\Theta + \frac{T_{ref}}{\Delta T_{ref}}\right] + \left(\frac{c\,L_{ref}}{\Delta T_{ref}\,k}\right)\left[\Theta\,\Delta T_{ref} + T_{ref} - T_b\right]^d \tag{283}$$

and the required derivative for the Jacobian is

$$\frac{\partial\{QFLUX\}}{\partial\{\Theta\}} = \left(\frac{b\,L_{ref}}{k}\right) + \left(\frac{c\,d\,L_{ref}}{k}\right)\left(\Theta_m\,\Delta T_{ref} + T_{ref} - T_b\right)^{d-1} \tag{284}$$

The explicit appearance of Θ in Eq. (284) has been replaced by the arithmetic average Θ_m of the temperatures of the four points defining the surface element over which the integration is taking place.

An alternative would be to interpolate the Θ and change the $[B200]$ to a $[B3000]$ for the Jacobian only.

Outflow boundaries present a unique problem for CFD algorithms. Their location is typically arbitrary and somewhat artificial, arising from the need to truncate the domain at some point in order to establish a finite domain, thus a tractable problem. The physics of the flow field generally offers little guidance. Application of Green's theorem to the kinematic and viscous flux vectors, however, does produce mathematically well-posed natural boundary conditions for outflow planes. The advection term in divergence form in the GWS^N for the momentum equations is

$$\int_\Omega \psi \frac{\partial(u_i u_j)}{\partial x_j} \, d\Omega = - \int_\Omega \frac{\partial \psi}{\partial x_j} u_i u_j \, d\Omega + \oint_\Gamma \psi \, u_i u_j n_j \, d\Gamma \quad . \tag{285}$$

The volume integral on the right-hand side of Eq. (285) has been discussed in a previous section, and its formulation in compact notation for the residual $\{FUI\}$ is

$$- \Delta t \; DET_e \; \{UJ\}_e^T \; EJK_e \; [C30K0] \; \{UI\}_e \tag{286}$$

The contribution of the surface integral to the residual $\{FUI\}$ is

$$+ \Delta t \; DET2_e \; \{UN\}_e^T [B3000] \; \{UI\}_e \tag{287}$$

where $\{UN\}$ is the projection of u_i onto the outward-pointing normal at each node in the surface element. The surface integral represented by Eq. (287) is evaluated at an outflow boundary using the latest estimate for the velocity solution. A similar boundary condition for the energy equation can be developed.

The viscous flux vector or diffusion term in the momentum equations produces the following volume integral for $\{FUI\}$

$$\begin{aligned} \Delta t \; \frac{1}{\mathrm{Re}} \int_\Omega \frac{\partial \eta_k}{\partial x_j} \frac{\partial \{N\}}{\partial \eta_k} \frac{\partial \eta_m}{\partial x_j} \frac{\partial \{N\}^T}{\partial \eta_m} \det[J] \, d\Omega \; \{UI\}_e = \\ + \Delta t \; DET_e \; \frac{1}{\mathrm{Re}} \; EJK_e \; EJM_e \; [C2KM] \; \{UI\}_e \end{aligned} \tag{288}$$

and the corresponding surface integral is

$$\begin{aligned} - \Delta t \; \frac{1}{\mathrm{Re}} \oint_\Gamma \{N\} \; \frac{\partial \eta_k}{\partial x_j} \frac{\partial \{N\}}{\partial \eta_k} \det[J]_{2D} \, d\Gamma \; \{UI\}_e \, nJ = \\ - \Delta t \; DET2_e \; \frac{1}{\mathrm{Re}} \; EJK_e \; [B20K] \; \{UI\}_e \, nJ \end{aligned} \tag{289}$$

The surface integral in Eq. (289) requires the evaluation of the normal gradient of the velocity at the outflow plane. This gradient is in general unknown in the absence of specific data on downstream conditions. A common approach is to assume a vanishing normal derivative (a "continuative" outflow boundary). A more accurate technique is the one proposed by Freels (1992) in which it is assumed

that the gradient at the element adjacent to the boundary is equal to the gradient at the boundary. Implementation of this boundary condition involves setting to zero the row of the diffusion matrix associated with the boundary node during assembly of the global system matrix. This approximation improves in accuracy as the mesh is refined near the outflow plane. The continuative assumption cannot be improved through mesh refinement.

4.10 DISPERSION ERROR CONTROL

In the development of any CFD algorithm, a key theoretical issue is stability in convection -dominated flows. With increasing Reynolds and Peclet numbers, the natural dissipation mechanisms, associated with the physical diffusion terms in the momentum and energy conservation laws, begin to lose their ability to moderate a dominant dispersive error mode. The spatial discretization of the hyperbolic advection terms is the source of this numerical dispersive error which manifests itself as characteristic "2-Δx waves" in the velocity and temperature distributions (Baker, 1983). To address the issue of dispersion error control, a *Taylor Weak Statement* is employed wherein a temporal Taylor-series-derived modification to the conservation law statement is added to the momentum and energy equations.

In finite-difference/finite-volume CFD applications, various *upwind* differencing schemes are employed for dispersion error control, ranging from donor-cell upwinding (Gentry et al., 1966) to high-order upwind operators such as QUICK/QUICKEST schemes (Leonard, 1979). Upwind differencing involves approximating convective derivatives with upstream and cell-centered solution values. As discussed by Roache (1972), upwinding methods inherently introduce some level of artificial diffusion into the flow field. A particularly troublesome manifestation of this error mechanism is "cross-wind" diffusion in which velocity fields experience a dissipation error normal to the flow direction.

Finite-element upwinded convective terms can be developed in several ways, including modified weighting functions (Christie et al., 1976), modified quadrature rules (Hughes, 1978), stream-line-upwind Petrov-Galerkin (SUPG) methods (Brooks and Hughes, 1982), multi-dimensional "tensor viscosity" schemes (Dukowicz and Ramshaw, 1979), "balancing tensor diffusivity" (BTD) methods (Gresho et al., 1984), and Taylor-Galerkin methods (Donea, 1984; and Baker and Kim, 1987).

The theoretical treatment of dispersive error instability has relied typically upon the linear, 1-dimensional, scalar advection equation as a hyperbolic model problem,

$$\frac{\partial q}{\partial t} = a \frac{\partial q}{\partial x} \tag{290}$$

where a is a scalar constant. Equation (290) describes an evolutionary process for which existence of the Taylor series

$$q^{n+1} = q^n + \Delta t \left.\frac{\partial q}{\partial t}\right|_n + \frac{\Delta t^2}{2} \left.\frac{\partial^2 q}{\partial t^2}\right|_n + \frac{\Delta t^3}{6} \left.\frac{\partial^3 q}{\partial t^3}\right|_n + \cdots \tag{291}$$

is guaranteed. Baker and Kim (1987) present a generalization of the Taylor Weak Statement algorithm for Eq. (290) which permits selective control of both time accuracy and stability. As noted by Noronha and Baker (1989), "the Taylor Weak Statement (TWS) procedure provides the broader generalized perspective for nonlinear stability mechanisms for hyperbolic and/or partially parabolic conservation law systems."

The TWS formulation for the incompressible Navier-Stokes equations was derived and verified by Noronha and Baker (1989). In the limit of large Re (and neglecting source terms), the multidimensional form of the conservation laws can be restated as

$$\mathcal{L}(q) = \frac{\partial q}{\partial t} + \frac{\partial f_j}{\partial x_j} = \frac{\partial q}{\partial t} + A_j \frac{\partial q}{\partial x_j} = 0 \tag{292}$$

where A_j is the Jacobian of the kinematic flux vector ($\partial f_j / \partial q$). Following Baker and Kim (1987), the higher order time derivatives in Eq. (291) are replaced with spatial derivatives obtained from Eq. (292). For example, it can be shown that the second derivative of q with respect to time is

$$\frac{\partial^2 q}{\partial t^2} = \frac{\partial}{\partial x_j}\left(\alpha^* A_j \frac{\partial q}{\partial t} + \beta^* A_j A_k \frac{\partial q}{\partial x_k} \right) \tag{293}$$

subject to the convexity constraint $\alpha^* - \beta^* = 1$. Similar manipulations can produce an expression for the third-order temporal derivative in Eq. (291) in terms of spatial derivatives. Substitution of the revised Taylor series into Eq. (290) results in the Taylor-modified conservation law statement,

$$\begin{aligned} \mathcal{L}_m(q) = \frac{\partial q}{\partial t^*} + A_j \frac{\partial q}{\partial x_j} - \frac{\Delta t}{2}\frac{\partial}{\partial x_j}\left[\alpha^* A_j \frac{\partial q}{\partial t} + \gamma^* \frac{\Delta t}{3}\frac{\partial}{\partial x_k}\left(A_j A_k \frac{\partial q}{\partial t} \right) \right] \\ - \frac{\Delta t}{2}\frac{\partial}{\partial x_j}\left[\beta^* A_j A_k \frac{\partial q}{\partial x_k} + \mu^* \frac{\Delta t}{3}\frac{\partial}{\partial x_k}\left(A_j A_k A_l \frac{\partial q}{\partial x_l} \right) \right] = 0 \end{aligned} \tag{294}$$

where $\partial q/\partial t^* \rightarrow \partial q/\partial t$ as $\Delta t \rightarrow 0$. A Galerkin weak statement can be formed with Eq. (294) that, based upon the specification of the parameter set α^*, β^*, γ^*, and μ^*, contains over a dozen independently derived dissipative CFD algorithms (Baker and Kim, 1987).

For the current application, dispersion error control is based upon the use of the β^*-term in Eq. (294). Noronha and Baker (1989) show that the required TWS form for the momentum conservation law involves adding

$$-\beta^* \frac{\Delta t}{2}\frac{\partial}{\partial x_j}\left(u_j u_k \frac{\partial u_i}{\partial x_k} + u_i u_k \frac{\partial u_j}{\partial x_k} \right) \tag{295}$$

to the momentum equations. The β*-modified energy equation includes the term

$$- \beta_\Theta^* \frac{\Delta t}{2} \frac{\partial}{\partial x_j} \left(u_j u_k \frac{\partial \Theta}{\partial x_k} \right) \tag{296}$$

As a computational convenience, (295) can be approximated by neglecting $u_i u_k \frac{\partial u_j}{\partial x_k}$.

This approximation produces a β-term similar in form to (296), i.e.,

$$- \beta^* \frac{\Delta t}{2} \frac{\partial}{\partial x_j} \left(u_j u_k \frac{\partial u_i}{\partial x_k} \right) \tag{297}$$

Equation (297) is identical in form to a "balancing tensor diffusivity"or BTD term (cf. Gresho et al.,1984; and Dukowicz and Ramshaw, 1979). Following Raymond and Garder (1976), an approximate element-level Courant number replaces the time-step Δt in (296) and (297), thus,

$$\beta^* \frac{\Delta t}{2} \approx \frac{\beta h_e^{1/n}}{|u|_e} \quad ; \quad \beta_\Theta^* \frac{\Delta t}{2} \approx \frac{\beta_\Theta h_e^{1/n}}{|u|_e} \tag{298}$$

where β and β_Θ are user-selectable parameters (≥0), n is the problem dimension, h_e is an appropriate local mesh measure (with the dimensions of area for n=2 and volume for n=3), and $|\mathbf{u}|_e$ is an element-based reference speed.

The Taylor weak statement for the momentum equations is, therefore,

$$TWS = \int_\Omega \psi \, \mathcal{L}_m(u_i) \, d\Omega = \int_\Omega \psi \, \mathcal{L}(u_i) \, d\Omega - \frac{\beta h_e^{1/n}}{|u|_e} \int_\Omega \psi \frac{\partial}{\partial x_j} \left(u_j u_k \frac{\partial u_i}{\partial x_k} \right) d\Omega = 0 \tag{299}$$

$$\forall \, \psi \in L_0^2(\Omega) \; , \; u_i \in H^2(\Omega)$$

Applying Green's theorem to the β-term in Eq. (299) gives

$$TWS = \int_\Omega \psi \, \mathcal{L}_m(u_i) \, d\Omega = \int_\Omega \psi \, \mathcal{L}(u_i) \, d\Omega$$

$$+ \frac{\beta h_e^{1/n}}{|u|_e} \int_\Omega \frac{\partial \psi}{\partial x_j} u_j u_k \frac{\partial u_i}{\partial x_k} \, d\Omega - \frac{\beta h_e^{1/n}}{|u|_e} \oint_{\partial\Omega} \psi \; u_k \frac{\partial u_i}{\partial x_k} u_j n_j \, d\Gamma = 0 \tag{300}$$

$$\forall \, \psi \in H_0^1(\Omega) \; , \; u_i \in H^1(\Omega)$$

The discrete form of the β-terms in Eq. (300) is, therefore,

$$\frac{\beta\, h_e^{1/n}}{|u|_e}\int_\Omega \{UJ\}^T\{N\}\,\{UK\}^T\{N\}\,\frac{\partial\eta_l}{\partial x_j}\,\frac{\partial\{N\}}{\partial\eta_l}\,\frac{\partial\eta_m}{\partial x_k}\,\frac{\partial\{N\}^T}{\partial\eta_m}\{UI\}\det[J]_e\,d\eta$$
$$-\frac{\beta\, h_e^{1/n}}{|u|_e}\oint_{\partial\Omega}\{UK\}^T\{N\}\,\{N\}\,\frac{\partial\eta_m}{\partial x_k}\,\frac{\partial\{N\}^T}{\partial\eta_m}\{UI\}\,\{N\}^T\{UN\}\det[J]_{2D}\,d\eta_2 \qquad (301)$$

where $\{UN\}$ are the boundary velocities projected onto the outward-pointing normal. In compact form, one obtains the TWS contribution to the $\{FUI\}_e$ residual

$$\frac{\beta\, h_e^{1/3}}{|u|_e}\,EJL_e\,EKM_e\,DET_e\,\{UJ\}_e^T\left(\{UK\}_e^T[C400LM]\{UI\}_e\right)$$
$$-\frac{\beta\, h_{2e}^{1/2}}{|u|_e}\,EKM_e\,DET2_e\{UN\}_e^T\left(\{UK\}_e^T[B4000M]\{UI\}_e\right) \qquad (302)$$

The assembly of the [C400LM] and [B4000M] hypermatrices into the global residuals and Newton Jacobian matrix is a prohibitively compute-intensive operation for large problems. As an approximation, the order of these terms can be reduced through the formation of element-averaged velocity components, hence,

$$\frac{\beta\, h_e^{1/3}}{|u|_e}\,EJL_e\,EKM_e\,DET_e\,\overline{UJ}_e\,\{UK\}_e^T[C30LM]\{UI\}_e$$
$$-\frac{\beta\, h_{2e}^{1/2}}{|u|_e}\,EKM_e\,DET2_e\,\overline{UN}_e\{UK\}_e^T[B300M]\{UI\}_e \qquad (303)$$

Similar terms can be developed for the energy equation residual $\{F\Theta\}$ with the result

$$\frac{\beta_\Theta\, h_e^{1/3}}{|u|_e}\,EJL_e\,EKM_e\,DET_e\,\overline{UJ}_e\,\{UK\}_e^T[C30LM]\{\Theta\}_e$$
$$-\frac{\beta_\Theta\, h_{2e}^{1/2}}{|u|_e}\,EKM_e\,DET2_e\,\overline{UN}_e\{UK\}_e^T[B300M]\{\Theta\}_e \qquad (304)$$

The surface integrals in (303) and (304) should be evaluated for those boundaries at which the normal velocities are not fixed by Dirichlet data, e.g., outflow boundaries.

The β-terms can be differentiated to obtain their contributions to the element-level Newton Jacobians. For the momentum equations, the self-coupling term is

$$\frac{\partial\{FUI\}}{\partial\{UI\}} = \frac{\beta h_e^{1/3}}{|u|_e} EJL_e\, EKM_e\, DET_e\, \overline{UJ}_e\, \{UK\}_e^T\, [C30LM]$$

$$+ \frac{\beta h_e^{1/3}}{|u|_e} EJL_e\, EIM_e\, DET_e\, \overline{UJ}_e\, \{UI\}_e^T\, [C3ML0]$$

$$+ \frac{\beta h_e^{1/3}}{|u|_e} EIL_e\, EKM_e\, DET_e\, \overline{UK}_e\, \{UI\}_e^T\, [C3ML0] \qquad (305)$$

$$- \frac{\beta h_{2e}^{1/2}}{|u|_e} EKM_e\, DET2_e\, \overline{UN}_e\, \{UK\}_e^T\, [B300M]$$

$$- \frac{\beta h_{2e}^{1/2}}{|u|_e} EIM_e\, DET2_e\, \overline{UN}_e\, \{UI\}_e^T\, [B3M00]$$

and the cross-coupling term is

$$\left.\begin{aligned} \frac{\partial\{FUI\}}{\partial\{UK\}} &= \frac{\beta h_e^{1/3}}{|u|_e} EJL_e\, EKM_e\, DET_e\, \overline{UJ}_e\, \{UI\}_e^T\, [C3ML0] \\ &+ \frac{\beta h_e^{1/3}}{|u|_e} EJL_e\, EJM_e\, DET_e\, \overline{UK}_e\, \{UI\}_e^T\, [C3ML0] \\ &- \frac{\beta h_{2e}^{1/2}}{|u|_e} EKM_e\, DET2_e\, \overline{UN}_e\, \{UI\}_e^T\, [B3M00] \end{aligned}\right\} \quad I \neq K \qquad (306)$$

For the energy equation, the self-coupling term in the Jacobian is

$$\frac{\partial\{F\Theta\}}{\partial\{\Theta\}} = \frac{\beta_\Theta h_e^{1/3}}{|u|_e} EJL_e\, EKM_e\, DET_e\, \overline{UJ}_e\, \{UK\}_e^T\, [C30LM]$$

$$- \frac{\beta_\Theta h_{2e}^{1/2}}{|u|_e} EKM_e\, DET2_e\, \overline{UN}_e\, \{UK\}_e^T\, [B300M] \qquad (307)$$

and the cross-coupling term is

$$\frac{\partial\{F\Theta\}}{\partial\{UI\}} = \frac{\beta_\Theta h_e^{1/3}}{|u|_e} EJL_e\, EIM_e\, DET_e\, \overline{UJ}_e\, \{\Theta\}_e^T\, [C3ML0]$$

$$+ \frac{\beta_\Theta h_e^{1/3}}{|u|_e} EIL_e\, EKM_e\, DET_e\, \overline{UK}_e\, \{\Theta\}_e^T\, [C3ML0] \qquad (308)$$

$$- \frac{\beta_\Theta h_{2e}^{1/2}}{|u|_e} EIM_e\, DET2_e\, \overline{UN}_e\, \{\Theta\}_e^T\, [B3M00]$$

It remains to select an appropriate measure for the mesh h_e. For rectangular hexahedra, the determinant of the transformation Jacobian, det $[J_e]$, is equal to one-eighth of the volume of the element; therefore, one choice for h_e is to set it equal to 8×det $[J_e]$. The cube root of h_e will, therefore, be dimensionally correct. The boundary conditions are evaluated with bilinear quadrilateral elements. For rectangular quadrilaterals, det $[J_e]$ is equal to one-fourth of the element area; therefore, an appropriate choice for h_{2e} is 4×det $[J_{2D}]$.

5. NUMERICAL LINEAR ALGEBRA

In the translation from algorithmic theory to practical computer code, the CFD practitioner is ultimately presented with the task of solving a sequence of linear algebra problems of the form

$$A x = b \tag{309}$$

where the square matrix A and the vector b are known, and x is the vector of unknowns. For many incompressible formulations, the ellipticity associated with the continuity constraint produces one or more Poisson equations. The resulting terminal matrix statements have A matrices that are symmetric positive semi-definite (SPSD), an important property in the design of numerical linear algebra procedures. When implicit time-integration techniques are used for the momentum and energy equations, the A matrices are nonsymmetric, indefinite, and ill-conditioned. In both instances, however, A is characteristically large and sparse. Golub and Van Loan (1989) note that two important measures of efficiency for linear algebra algorithms are exploitation of matrix data structures and economy of computational effort. This chapter presents a review of some of the latest methods in data management and linear algebra solution techniques, hence identification of those feasible for CFD implementation in a workstation computing environment.

The matrix shown in Eq. (310) is an example of the type of matrices produced by the Laplacian operator for the Φ and pressure Poisson equations. The model problem consists of a unitcube with a M= 2×2×2 discretization. No boundary conditions have been applied. The matrix A is symmetric with positive diagonal elements and nonpositive off-diagonals. Since A is symmetric, its spectrum (set of eigenvalues) are real, as shown in Eq. (311). The presence of the zero eigenvalue indicates that the matrix is singular, i.e., det $(A) = 0$, and A^{-1} does not exist. However, since the remaining eigenvalues are positive, A is classified as *symmetric positive semi-definite.* The singularity can be removed by applying a Dirichlet boundary condition on one node. One method of imposing Dirichlet boundary data is (on the row of the corresponding Dirichlet node) to replace the diagonal element with a large number. For example, when the element in the (1,1) position in A is replaced by 10^6, the resulting set of eigenvalues are shown in Eq. (312). Examination of the matrix spectrum in Eq. (312) shows that all the eigenvalues are now positive. The modified A is an example of a class-M matrix, where the diagonals are all positive, the off-diagonals are nonpositive, and A is *irreducibly diagonally dominant* (Ortega, 1972). The definition of irreducible diagonal dominance is given in a subsequent section. A symmetric M-matrix is called a *Stieltjes* matrix, and it can be shown (cf. Ortega, 1972; and Horn and Johnson, 1985) that a Stieltjes matrix is symmetric positive definite (SPD). A more formal definition of positive definiteness is (Wachspress, 1966):

> Given the square matrix A, if the quadratic form $x^T A x > 0$ for all $x \neq 0$, then A is *positive definite*. If $x^T A x \geq 0$ for all $x \neq 0$, then A is *positive semi-definite*.

One property of a SPD matrix is that its spectrum consists of all positive eigenvalues.

$$
A = \begin{bmatrix}
.167 & 0 & 0 & 0 & -.042 & 0 & 0 & 0 & 0 & 0 & -.042 & 0 & -.042 & -.042 & 0 & 0 & 0 & 0 & 0 & 0 & 0 & 0 & 0 & 0 & 0 & 0 & 0 \\
 & .333 & 0 & -.042 & 0 & -.042 & 0 & 0 & 0 & -.042 & 0 & -.042 & -.042 & -.083 & -.042 & 0 & 0 & 0 & 0 & 0 & 0 & 0 & 0 & 0 & 0 & 0 & 0 \\
 & & .167 & 0 & -.042 & 0 & 0 & 0 & 0 & 0 & -.042 & 0 & 0 & -.042 & -.042 & 0 & 0 & 0 & 0 & 0 & 0 & 0 & 0 & 0 & 0 & 0 & 0 \\
 & & & .333 & 0 & 0 & 0 & -.042 & 0 & -.042 & -.042 & 0 & 0 & -.083 & 0 & -.042 & -.042 & 0 & 0 & 0 & 0 & 0 & 0 & 0 & 0 & 0 & 0 \\
 & & & & .667 & 0 & -.042 & 0 & -.042 & -.042 & -.083 & -.042 & -.083 & 0 & -.083 & -.042 & -.083 & -.042 & 0 & 0 & 0 & 0 & 0 & 0 & 0 & 0 & 0 \\
 & & & & & .333 & 0 & -.042 & 0 & 0 & -.042 & -.042 & 0 & -.083 & 0 & 0 & -.042 & -.042 & 0 & 0 & 0 & 0 & 0 & 0 & 0 & 0 & 0 \\
 & & & & & & .167 & 0 & 0 & 0 & 0 & 0 & -.042 & -.042 & 0 & 0 & -.042 & 0 & 0 & 0 & 0 & 0 & 0 & 0 & 0 & 0 & 0 \\
 & & & & & & & .333 & 0 & 0 & 0 & 0 & -.042 & -.083 & -.042 & -.042 & 0 & -.042 & 0 & 0 & 0 & 0 & 0 & 0 & 0 & 0 & 0 \\
 & & & & & & & & .167 & 0 & 0 & 0 & 0 & -.042 & -.042 & 0 & -.042 & 0 & 0 & 0 & 0 & 0 & 0 & 0 & 0 & 0 & 0 \\
 & & & & & & & & & .333 & 0 & 0 & 0 & -.083 & 0 & 0 & 0 & 0 & 0 & -.042 & 0 & -.042 & -.042 & 0 & 0 & 0 & 0 \\
 & & & & & & & & & & .667 & 0 & -.083 & 0 & -.083 & 0 & 0 & 0 & -.042 & 0 & -.042 & -.042 & -.083 & -.042 & 0 & 0 & 0 \\
 & & & & & & & & & & & .333 & 0 & -.083 & 0 & 0 & 0 & 0 & 0 & -.042 & 0 & 0 & -.042 & -.042 & 0 & 0 & 0 \\
 & & & & & & & & & & & & .667 & 0 & 0 & 0 & -.083 & 0 & -.042 & -.042 & 0 & 0 & -.083 & 0 & -.042 & -.042 & 0 \\
 & & & & & & & & & & & & & 1.33 & 0 & -.083 & 0 & -.083 & -.042 & -.083 & -.042 & -.083 & 0 & -.083 & -.042 & -.083 & -.042 \\
 & & & & & & & & & & & & & & .667 & 0 & -.083 & 0 & 0 & -.042 & -.042 & 0 & -.083 & 0 & 0 & -.042 & -.042 \\
 & & & & & & & & & & & & & & & .333 & 0 & 0 & 0 & 0 & 0 & -.042 & -.042 & 0 & 0 & -.042 & 0 \\
 & & & & & & & & & & & & & & & & .667 & 0 & 0 & 0 & 0 & -.042 & -.083 & -.042 & -.042 & 0 & -.042 \\
 & & & & & & & & & & & & & & & & & .333 & 0 & 0 & 0 & 0 & -.042 & -.042 & 0 & -.042 & 0 \\
 & & & & & & & & & & & & & & & & & & .167 & 0 & 0 & 0 & -.042 & 0 & 0 & 0 & 0 \\
 & & & & & & & & & & & & & & & & & & & .333 & 0 & -.042 & 0 & -.042 & 0 & 0 & 0 \\
 & & & & & & & & & & & & & & & & & & & & .167 & 0 & -.042 & 0 & 0 & 0 & 0 \\
 & & & & & & & & & & & & & & & & & & & & & .333 & 0 & 0 & 0 & -.042 & 0 \\
 & & & & & & & & & & & & & & & & & & & & & & .667 & 0 & -.042 & 0 & -.042 \\
 & & & & & & & & & & & & & & & & & & & & & & & .333 & 0 & -.042 & 0 \\
 & & & & & & & & & & & & & & & & & & & & & & & & .167 & 0 & 0 \\
 & & & & & & & & & & & & & & & & & & & & & & & & & .333 & 0 \\
 & & & & & & & & & & & & & & & & & & & & & & & & & & .167
\end{bmatrix} \tag{310}
$$

$$\lambda_i = \begin{bmatrix} 1.413 \\ 0 \\ 0.435 \\ 0.680 \\ 0.864 \\ 0.864 \\ 0.680 \\ 0.153 \\ 0.680 \\ 0.153 \\ 0.386 \\ 0.386 \\ 0.417 \\ 0.153 \\ 0.153 \\ 0.417 \\ 0.417 \\ 0.250 \\ 0.250 \\ 0.333 \\ 0.250 \\ 0.333 \\ 0.333 \\ 0.167 \\ 0.167 \\ 0.167 \\ 0.167 \end{bmatrix} \tag{311}$$

$$\lambda_i = \begin{bmatrix} 10^6 \\ 1.411 \\ 0.006 \\ 0.675 \\ 0.429 \\ 0.159 \\ 0.153 \\ 0.864 \\ 0.680 \\ 0.864 \\ 0.680 \\ 0.153 \\ 0.386 \\ 0.386 \\ 0.153 \\ 0.417 \\ 0.417 \\ 0.250 \\ 0.250 \\ 0.417 \\ 0.250 \\ 0.167 \\ 0.333 \\ 0.167 \\ 0.333 \\ 0.167 \\ 0.333 \end{bmatrix} \tag{312}$$

5.1 MATRIX DATA STRUCTURES

Symmetry, *bandedness*, and *sparsity* are among the matrix structural properties that have a potential for exploitation in the design of linear algebra solvers (Golub and Van Loan, 1989). The obvious advantage of symmetry is that only the upper (or lower) triangular part and the main diagonal of the matrix need be stored. The term bandedness includes the properties of *bandwidth*, *profile*, and root-mean-square (rms) *wavefront*, all of which depend solely on the ordering of the unknowns in Eq. (309). Sparsity is the property of a matrix that is *sparsely populated* with nonzero elements.

To produce "optimal" orderings, various heuristic resequencing strategies have been developed to minimize bandwidth, profile, or rms wavefront (Everstine, 1979). For a symmetric square matrix A of order n, the bandwidth w_i for row i is defined as the number of columns from the first to the last nonzero in the row. The matrix bandwidth BW and profile PR are defined as

$$BW \equiv \max_{i \le n} w_i$$

$$PR \equiv \sum_{i=1}^{n} \frac{(w_i + 1)}{2} \tag{313}$$

The wavefront f_i is the number of active columns in row i, where a column j is *active* in row i if $j \ge i$ and there is a nonzero in that column in any row with index $k \le i$. The matrix rms wavefront WF is defined as

$$WF \equiv \sqrt{\left(\frac{1}{n} \sum_{i=1}^{n} f_i^2 \right)} \tag{314}$$

Everstine (1979) presents a comparative study of three popular resequencing algorithms, testing the performance of the Cuthill-McKee, Gibbs-Poole-Stockmeyer, and Levy methods. For the test problems that Everstine examined, the Gibbs-Poole-Stockmeyer method was found to be the fastest and best able to reduce profile and rms wavefront. Schwarz (1988) gives a description of the Rosen, Cuthill-Mckee, and reverse Cuthill-Mckee methods in terms of graph theory. The Cuthill-Mckee algorithm has the advantage of reducing both the bandwidth and the profile, simultaneously.

Assuming an approximate "optimal" ordering has been accomplished, a number of compact storage techniques are available. The *band storage* method in the general linear algebra package LINPACK (Coleman and Van Loan, 1988) is an example of how the banded structure of a matrix can be exploited. The lower bandwidth is defined as that positive integer p such that $a_{ij}=0$ whenever $i>j+p$, and the upper bandwidth q implies that $a_{ij}=0$ whenever $i<j-q$. As before, the matrix bandwidth is $BW=p+q+1$. In LINPACK's band storage technique, a square $n \times n$ matrix is mapped to a $(2p+q+1)\times n$ matrix, e.g.,

$$A(i,j) \rightarrow A_{band}(i-j+q+1,j)$$

$$A = \begin{bmatrix} a_{11} & a_{12} & a_{13} & 0 & 0 \\ a_{21} & a_{22} & a_{23} & a_{24} & 0 \\ 0 & a_{32} & a_{33} & a_{34} & a_{35} \\ 0 & 0 & a_{43} & a_{44} & a_{45} \\ 0 & 0 & 0 & a_{54} & a_{55} \end{bmatrix} \rightarrow A_{band} = \begin{bmatrix} 0 & 0 & a_{13} & a_{24} & a_{35} \\ 0 & a_{12} & a_{23} & a_{34} & a_{45} \\ a_{11} & a_{22} & a_{33} & a_{44} & a_{55} \\ a_{21} & a_{32} & a_{43} & a_{54} & 0 \end{bmatrix} \tag{315}$$

For the above storage scheme to be effective, it is necessary that $p,q << n$.

The *NSPCG* linear algebra package (Oppe et al., 1988) uses a *primary storage* technique for unstructured matrices. The method is efficient for matrices that have a relatively constant number of nonzeros on each row. The $n \times n$ matrix A is represented by two $n \times maxnz$ matrices, a real-valued matrix $COEF$ and an integer matrix $JCOEF$, where each row in $COEF$ holds the nonzeros of the corresponding row in the full matrix A, and $JCOEF$ contains the respective column numbers. The positive integer $maxnz$ is the maximum number of nonzeros per row over all the rows of A. An example of primary storage is

$$A = \begin{bmatrix} a_{11} & 0 & 0 & a_{14} & a_{15} \\ 0 & a_{22} & 0 & 0 & 0 \\ 0 & 0 & a_{33} & 0 & 0 \\ a_{41} & 0 & 0 & a_{44} & a_{45} \\ a_{51} & 0 & 0 & a_{54} & a_{55} \end{bmatrix} \rightarrow COEF = \begin{bmatrix} a_{11} & a_{14} & a_{15} \\ a_{22} & 0 & 0 \\ a_{33} & 0 & 0 \\ a_{44} & a_{41} & a_{45} \\ a_{55} & a_{51} & a_{54} \end{bmatrix}; \; JCOEF = \begin{bmatrix} 1 & 4 & 5 \\ 2 & 0 & 0 \\ 3 & 0 & 0 \\ 4 & 1 & 5 \\ 5 & 1 & 4 \end{bmatrix} \tag{316}$$

For the above example, n=5 and $maxnz$=3. If a row in A has fewer than $maxnz$ nonzeros, then the corresponding row in $COEF$ is padded with zeros.

The *diagonal storage* technique is effective for matrices with a block or diagonal structure. The diagonals of A are stored in the columns of the compressed matrix $COEF$, and the offsets from the main diagonal are stored in the integer vector $JCOEF$. An example of diagonal storage is

$$A = \begin{bmatrix} a_{11} & a_{12} & 0 & a_{14} & 0 \\ a_{21} & a_{22} & a_{23} & 0 & a_{25} \\ 0 & a_{32} & a_{33} & a_{34} & 0 \\ 0 & 0 & a_{43} & a_{44} & a_{45} \\ 0 & 0 & 0 & a_{54} & a_{55} \end{bmatrix} \rightarrow COEF = \begin{bmatrix} a_{11} & a_{12} & a_{14} & 0 \\ a_{22} & a_{23} & a_{25} & a_{21} \\ a_{33} & a_{34} & 0 & a_{32} \\ a_{44} & a_{45} & 0 & a_{43} \\ a_{55} & 0 & 0 & a_{54} \end{bmatrix}; \; JCOEF = \begin{bmatrix} 0 \\ 1 \\ 3 \\ -1 \end{bmatrix} \tag{317}$$

The superdiagonals in A are top-justified, i.e., short superdiagonals are padded with zeros from below, and subdiagonals are bottom-justified. Positive integers in $JCOEF$ indicate a superdiagonal, and subdiagonals have negative offsets.

For more general unstructured sparse matrices, diagonal storage can result in a large number of zeros being stored and computed on. *Coordinate storage* (also known as *triad storage*) is effective for general sparsity structures at the cost of additional integer overhead. In coordinate storage, only the *nnz* nonzeros of A are stored in the vector *COEF*. Two *nnz* length integer vectors or one *nnz*×2 integer matrix hold the row and column indices of the corresponding elements in *COEF* . For the following example, *nnz*=17.

$$A = \begin{bmatrix} a_{11} & a_{12} & 0 & a_{14} & 0 \\ a_{21} & a_{22} & a_{23} & 0 & a_{25} \\ 0 & a_{32} & a_{33} & a_{34} & 0 \\ a_{41} & 0 & a_{43} & a_{44} & a_{45} \\ 0 & a_{52} & 0 & a_{54} & a_{55} \end{bmatrix} \rightarrow COEF = \begin{bmatrix} a_{11} \\ a_{12} \\ a_{14} \\ a_{21} \\ a_{22} \\ a_{23} \\ a_{25} \\ a_{32} \\ a_{33} \\ a_{34} \\ a_{41} \\ a_{43} \\ a_{44} \\ a_{45} \\ a_{52} \\ a_{54} \\ a_{55} \end{bmatrix} ; \; JCOEF = \begin{bmatrix} 1 & 1 \\ 1 & 2 \\ 1 & 4 \\ 2 & 1 \\ 2 & 2 \\ 2 & 3 \\ 2 & 5 \\ 3 & 2 \\ 3 & 3 \\ 3 & 4 \\ 4 & 1 \\ 4 & 3 \\ 4 & 4 \\ 4 & 5 \\ 5 & 2 \\ 5 & 4 \\ 5 & 5 \end{bmatrix} \tag{318}$$

In Eq. (318), the nonzeros of A are stored by row, but they can also be stored by column.

The *Yale Sparse Matrix Package* (Eisenstat et al., 1977b) has an even more compact storage format in which only the nonzeros of A are stored in the vector *COEF*, either by column or row, and two integer vectors, *IA* of length $n+1$ and *JA* of length *nnz*, hold the structural data. The integer vector *JA* stores the row (or column) indices of the corresponding elements in *COEF*, and *IA* contains pointers to positions in *JA* and *COEF* where each new column (or row) begins. The following example uses Yale Sparse Matrix (YSM) column storage with the main diagonal positioned at the beginning of each new column.

$$A = \begin{bmatrix} a_{11} & a_{12} & 0 & a_{14} & 0 \\ a_{21} & a_{22} & a_{23} & 0 & a_{25} \\ 0 & a_{32} & a_{33} & a_{34} & 0 \\ a_{41} & 0 & a_{43} & a_{44} & a_{45} \\ 0 & a_{52} & 0 & a_{54} & a_{55} \end{bmatrix} \rightarrow COEF = \begin{bmatrix} a_{11} \\ a_{21} \\ a_{41} \\ a_{22} \\ a_{12} \\ a_{32} \\ a_{52} \\ a_{33} \\ a_{23} \\ a_{43} \\ a_{44} \\ a_{14} \\ a_{34} \\ a_{54} \\ a_{55} \\ a_{25} \\ a_{45} \end{bmatrix}; \; JA = \begin{bmatrix} 1 \\ 2 \\ 4 \\ 2 \\ 1 \\ 3 \\ 5 \\ 3 \\ 2 \\ 4 \\ 4 \\ 1 \\ 3 \\ 5 \\ 5 \\ 2 \\ 5 \end{bmatrix}; \; IA = \begin{bmatrix} 1 \\ 4 \\ 8 \\ 11 \\ 15 \\ 18 \end{bmatrix} \tag{319}$$

An advantage of the both the coordinate and YSM techniques is that the storage requirements are independent of the *bandedness* of the matrix, since only the nonzeros of A are included in its sparse representation. The disadvantage is that some integer overhead is incurred to decode the sparsity structure.

5.2 SPARSE SOLUTION TECHNIQUES

Linear algebra solution techniques for Eq. (309) can be classified into two main groups, direct methods and iterative methods. Direct methods involve a factorization of A into triangular (and easily solvable) systems. Iterative methods are designed to generate a convergent sequence of vectors x^p where $A^{-1} b$ is the limit point of the sequence. The data management techniques discussed in the previous section can be incorporated into many direct and iterative linear algebra algorithms. The following discussion gives a brief overview of some of the more popular sparse linear algebra algorithms currently employed in finite-element applications.

5.2.1 Direct Methods

For any nonsingular square matrix A, a basic theorem of linear algebra (Horn and Johnson, 1985) states that a permutation matrix P exists such that the factorization

$$PA = LU \tag{320}$$

exists, where L is a unit lower triangular matrix (ones on the diagonal) and U is upper triangular. The matrix P acts to reorder the rows of A before factorization. The vector of unknowns x is obtained by the solution of two triangular systems,

$$\begin{aligned} Ly &= Pb \\ Ux &= y \end{aligned} \tag{321}$$

The factorization described by Eq. (320) is called gaussian elimination with partial pivoting. Complete pivoting requires a second permutation matrix Q, such that

$$\begin{aligned} PAQ = LU \rightarrow (PAQ)(Q^T x) &= Pb \\ Ly &= Pb \\ U(Q^T x) &= y \end{aligned} \tag{322}$$

The factorization in Eq. (322) takes advantage of the fact that permutation matrices are orthogonal, thus

$$Q^T = Q^{-1} \rightarrow QQ^T = Q^T Q = I \tag{323}$$

where I is the identity matrix.

If A is symmetric, then the permutation matrices in Eq. (322) are related by $Q=P^T$ resulting in the factorization, i.e.,

$$\begin{aligned} PAP^T = LL^T \rightarrow (PAP^T)(Px) &= Pb \\ Ly &= Pb \\ L^T(Px) &= y \end{aligned} \tag{324}$$

If A is SPD, then $P=I$, and no pivoting is required, resulting in the well-known Cholesky factorization. The solve steps (called forward and back substitution) for the triangular systems in Eqs. (321), (322), and (324) require a small computational effort relative to the factorization steps. For banded matrices, direct methods have the advantage of preserving the bandwidth during the factorization; however, the original sparsity structure within the bandwidth is lost due to a process called "fill-in." Banded direct solvers are, therefore, most efficient when the matrix is dense within the bandwidth and the ordering of the unknowns is "optimal," i.e., the bandwidth is as small as possible relative to the order of the matrix. If the matrix is sparse within the bandwidth, then special sparse direct methods may be required.

Dongarra et al. (1991) group sparse direct methods into three main categories: frontal methods, multifrontal methods, and general sparse techniques. Frontal schemes were originally designed for symmetric positive definite matrices produced by finite-element structural analysis

codes; however, they can also be applied to nonsymmetric matrices. Performing well on systems whose bandwidth or profile is small, frontal methods can be interpreted as extensions of band or variable-band schemes. For symmetric systems, the frontal method consists of setting up a subset of the equation system while simultaneously carrying out a Cholesky factorization and forward substitution. The method exploits the fact that, for a banded matrix of bandwidth BW, it is necessary to store only $BW+1$ successive rows of the matrix in core memory (Schwarz, 1988). This submatrix, called the "frontal" matrix, is used as a "window" that runs down the band as the elimination progresses (Dongarra et al., 1991). The results of each elimination step are stored in "out-of-core" memory (also called "backing" or auxiliary storage). After a complete sweep of the band, the unknowns can be obtained by back substitution. A small bandwidth/profile is critical, since, for large bandwidth matrices, frontal methods can require more storage and many more floating point operations than general methods. Multifrontal methods are an attempt to improve computational efficiency while maintaining some of the benefits of frontal methods. The details of both frontal and multifrontal methods are discussed in the book by Duff et al. (1986).

An example of a general sparse direct solver is Harwell's MA28 code (Duff, 1980). MA28 is composed of a suite of Fortran subroutines for the solution of sparse nonsymmetric linear algebra systems using a variant of Gaussian elimination and employing sparsity pivoting to minimize fill-in as well as complete numerical pivoting for round-off error control. The rows and columns of A are first reordered so that the coefficient matrix is block triangular, i.e.,

$$PAQ = \begin{bmatrix} A_{11} & [0] & \cdots & \cdots & [0] \\ A_{21} & A_{22} & [0] & \vdots & \vdots \\ A_{31} & A_{32} & A_{33} & [0] & \vdots \\ \vdots & \vdots & \vdots & \ddots & [0] \\ A_{N1} & \cdots & \cdots & \cdots & A_{NN} \end{bmatrix} \tag{325}$$

where P and Q are permutation matrices. The diagonal blocks, A_{ii}, are square matrices, and the off-diagonal blocks, A_{ij} ($j<i$), are rectangular. The block triangular system is then solved by block forward substitution, where each block is solved with its own LU factorization with complete numerical pivoting. Information gained during the initial permutation and factorization of A can be saved in order to reduce the computational effort for subsequent factorizations of new matrices that have the same sparsity structure as A. MA28 uses the coordinate scheme for top-level (input) storage of A; however, several linked lists are employed as dynamic storage for the internal representation of the permuted and factored blocks.

Finally, Gunzburger (1989) notes that "although for two-dimensional problems direct solution techniques have proven to be popular and successful, it seems that they cannot be used for solving realistic three-dimensional problems on today's super-computers." For 3-dimensional problems in CFD, therefore, the current methods of choice fall in the broad class of iterative algorithms.

5.2.2 Iterative Methods

Iterative methods have two main advantages over direct schemes for large sparse linear algebra problems; they preserve the original sparsity structure of the matrix, and the accuracy of the iterated solution can be estimated and, thereby, controlled. Since sparsity is preserved, memory and storage requirements for iterative methods are significantly less than direct methods. For many

applications, a machine-precision direct solution is not necessary; therefore, the ability to apply a stopping-test during the iteration cycle can result in significant reductions in computational cost.

In general, iterative methods may be broadly categorized as either stationary or accelerated (nonstationary) procedures (cf. Hageman and Young, 1981; and Wachspress, 1966). Within these classes, the diagonal or non-diagonal structure of the iterative matrices is also a delimiting characteristic. The basic stationary methods such as Jacobi, Gauss-Seidel, and successive overrelaxation (SOR) can be formulated both as point-iterative (diagonal structures) schemes or as line-iterative (non-diagonal block structures) schemes. The stationary Alternating Direction Implicit (ADI) and approximate factorization (AF) methods use non-diagonal matrices exclusively. Accelerated methods involve applying techniques such as Chebyshev or conjugate gradient acceleration to the basic iterative methods.

Hageman and Young (1981) define linear stationary iterative methods of the first degree as having the general form

$$x^{p+1} = Gx^{p} + k, \quad p = 0,1,2, \ldots \tag{326}$$

where G is called the *iteration matrix*. The specific iterative procedure is uniquely defined by the form of its *splitting matrix* Q, where

$$G = I - Q^{-1}A \quad ; \quad k = Q^{-1}b \tag{327}$$

The known matrix A and vector b are the original system coefficient matrix and right-hand-side "load" vector as given in Eq. (309). If the sequence $x^0, x^1, x^2, \ldots$ converges to $A^{-1}b$ for an arbitrary x^0, then the iterative method is defined to be *convergent* (Young and Gregory, 1972). It is a fundamental theorem of linear algebra (Ortega, 1972) that a necessary and sufficient condition for Eq. (326) to be convergent is

$$S(G) < 1 \tag{328}$$

where $S(G)$ is the spectral radius of the matrix G. The *spectral radius* is the maximum in modulus of the eigenvalues of a matrix. $S(G)$ is also a measure of the efficiency of an iterative procedure since the asymptotic rate of convergence is defined as

$$R_{\infty}(G) \equiv -\log S(G) \tag{329}$$

The convergence rate, therefore, increases as $S(G)$ decreases.

Five stationary procedures are designated by Hageman and Young (1981) as *basic iterative methods*: the Richardson (RF), Jacobi, Gauss-Seidel, successive overrelaxation (SOR), and symmetric SOR (SSOR) methods. These basic methods can be described in matrix form with the following decomposition:

$$A = D - L - U \tag{330}$$

where D holds the diagonals of A, and L and U are strictly lower and upper triangular, respectively.

RF iteration is a variant of Richardson's method where $Q=I$, and

$$x^{p+1} = (I - A)x^p + b \tag{331}$$

Conjugate gradient methods can be categorized as acceleration techniques applied to the RF method. Without acceleration, the RF method has little utility since line-iterative forms cannot be accommodated (Hageman and Young, 1981).

The Jacobi method has the splitting matrix $Q=D^{-1}$ such that

$$x^{p+1} = Bx^p + k$$
$$B \equiv I - D^{-1}A \quad ; \quad k \equiv D^{-1}b \tag{332}$$

where B is the Jacobi iteration matrix. In its point-iterative form, Jacobi iteration solves for each unknown on the diagonal of A in terms of the corresponding off-diagonals using values obtained from the previous iteration, i.e.,

$$x_i^{p+1} = \frac{1}{a_{ii}}\left(b_i - \sum_{j \neq i} a_{ij} x_j^p \right), \quad i = 1, \ldots, n \tag{333}$$

Gauss-Seidel improves upon the convergence rate of the Jacobi method by using current values for the lower off-diagonal terms as they are updated. The splitting matrix for Gauss-Seidel is $Q = D - L$, and

$$x^{p+1} = \mathcal{L} x^p + k$$
$$\mathcal{L} \equiv (I - D^{-1}L)^{-1} D^{-1} U \quad ; \quad k \equiv (I - D^{-1}L)^{-1} D^{-1} b \tag{334}$$

where $\mathcal{L}$ is the Gauss-Seidel iteration matrix.

A fundamental property of A that ensures convergence of both the Jacobi and Gauss-Seidel iterations is given by the *Diagonal Dominance Theorem* (Ortega, 1972).

> If A is either strictly diagonally dominant or irreducibly diagonally dominant, then $S(B) < 1$ and $S(\mathcal{L}) < 1$, and both the Jacobi iterates, Eq. (332), and the Gauss-Seidel iterates, Eq. (334), converge to $A^{-1}b$ for any x^0.

Diagonal dominance requires that the absolute values of the diagonal terms in a matrix be greater than or equal to the sum of the absolute values of their respective off-diagonals, i.e.,

$$|a_{ii}| \geq \sum_{j \neq i} |a_{ij}|, \quad i = 1, \ldots, n \tag{335}$$

If strict inequality holds in Eq. (335) for all the rows of A, then the matrix is *strictly diagonally dominant*. *Irreducible diagonal dominance* requires the matrix to be irreducible and diagonally dominant, and strict inequality must hold for at least one row. Definitions of irreducibility in terms of either directed-graph structure or canonical forms can be found in the books by Ortega (1972) and Horn and Johnson (1985). Note that the Diagonal Dominance Theorem does not require that A be symmetric; therefore, Jacobi and Gauss-Seidel iterative schemes have a potential application for nonsymmetric problems.

The SOR method is a modification of the Gauss-Seidel method; however, unlike Gauss-Seidel, its primary convergence theorem assumes that A is symmetric positive definite (SPD). SOR overrelaxes the Gauss-Seidel iterate and, as a point-iterative scheme, can be expressed as

$$x_i^{p+1} = x_i^p + \omega\left(x_i^{*\,p+1} - x_i^p\right) \tag{336}$$

where $x_i^{*\,p+1}$ is the Gauss-Seidel iterate. In matrix form, the SOR method is

$$\begin{gathered} x^{p+1} = \mathcal{L}_\omega\, x^p + k_\omega \\ \mathcal{L}_\omega \equiv (D - \omega L)^{-1}[(1-\omega)D + \omega U] \quad ; \quad k_\omega \equiv \omega (D - \omega L)^{-1} b \end{gathered} \tag{337}$$

The Ostrowski-Reich theorem is a fundamental convergence theorem for SOR.

> If A is SPD and $0<\omega<2$, then $S(\mathcal{L}_\omega) < 1$, and the SOR iterates, Eq. (337), converge to $A^{-1}b$ for any x^0.

The splitting matrix for SOR is $(\omega^{-1}D - L)$, where for $\omega=1$ the Gauss-Seidel method is recovered. In order to fully exploit the high convergence rates of SOR, an "optimal" value for the iteration parameter ω should be used. Wachspress (1966) and Hageman and Young (1981) describe adaptive techniques for estimating an optimal ω by monitoring the convergence history of the iterative cycle. An SSOR iteration is a two-step procedure consisting of a forward SOR and a backward SOR sweep.

Increased convergence rates are possible as a result of applying acceleration schemes for those basic iterative methods that can be classified as *symmetrizable* (Hageman and Young, 1981). An iteration method is symmetrizable if, for some nonsingular matrix W, the matrix $W(Q^{-1}A)W$ is SPD. For example, if both A and Q are SPD, then the method is symmetrizable. The Jacobi and SSOR methods are symmetrizable and suitable candidates for acceleration if A is SPD.

Polynomial acceleration is a semi-iterative procedure involving a new vector sequence v^p produced by a linear combination of the basic iterates, x^p. One chooses the coefficients $\alpha_{p,0}, \alpha_{p,1}, \ldots, \alpha_{p,p}$ such that

$$\sum_{k=0}^{p} \alpha_{p,k} = 1 \quad , \quad p = 0,1,2,\ldots \tag{338}$$

and determines the accelerated iterates v^0, v^1, ... by

$$v^p = \sum_{k=0}^{p} \alpha_{p,k} x^k \tag{339}$$

With suitable choices of $\alpha_{p,k}$, it is theoretically possible to substantially improve the convergence rate of the basic method. A popular technique for accelerating Jacobi iteration is based on the use of Chebyshev polynomials of the first kind (Young and Gregory, 1972). In Chebyshev acceleration, the iterates v^1, v^2, ... are calculated by the three-term recurrence relation

$$v^{p+1} = \frac{\rho_{p+1}}{2 - (\alpha + \beta)} \left[(2B - (\beta + \alpha) I) v^p + 2k \right] + (1 - \rho_{p-1}) v^{p-1}, \quad p = 0,1,2, \tag{340}$$

where

$$\left.\begin{aligned} &\rho_1 = 1, \ \rho_2 = \frac{2z^2}{2z^2 - 1}, \\ &\rho_{p+1} = \left(1 - \frac{1}{4z^2} \rho_p \right)^{-1}, \ p = 2,3, \end{aligned}\right| \quad \begin{aligned} z &= \frac{2 - (\alpha + \beta)}{\beta - \alpha} \quad \text{if } \alpha \neq \beta \\ \rho_1 &= 1 \quad \text{if } \alpha = \beta \end{aligned}$$

The matrix B is the iteration matrix for Jacobi iteration, Eq. (332), the vector k is $D^{-1} b$, and the parameters α and β are the upper and lower bounds of the eigenvalues of B. As Hageman and Young (1981) note, in order for Chebyshev acceleration to be effective on slowly convergent problems, it is important that nearly optimum iteration parameters be used, specifically the typically unknown minimum and maximum eigenvalues of B. Assuming a SPD coefficient matrix A, adaptive procedures have been developed to provide estimates for α and β during the iterative cycle.

A difficulty with iterative procedures like SOR and Chebyshev acceleration is that, in order to obtain optimal convergence rates, the user is required to choose or in some way calculate good estimates for various iteration parameters. In general, these parameters are unknown and in many cases may be difficult to determine (Golub and Van Loan, 1989). A family of iterative procedures having competitive convergence rates and no user-specified iteration parameters have gained much popularity in recent years. Included in this family are the preconditioned conjugate gradient, biconjugate gradient, conjugate gradient squared, and generalized minimal residual (GMRES) methods.

The conjugate gradient method falls in a class of algorithms that are sometimes called *Krylov-subspace* or *projection* methods (Dongarra et al., 1991). One can recast Eq. (326) in terms of the splitting matrix Q, thus

$$x^{p+1} = x^p + Q^{-1}(b - A x^p), \quad p = 0,1,2, \tag{341}$$

Defining the initial residual vector $r^0 = b - Ax^0$, it can be proven by mathematical induction that the iterate x^l is determined by a linear combination of vectors of the form

$$x^p = x^0 + \alpha_0 r^0 + \alpha_1 A r^0 + \alpha_2 A^{(2)} r^0 + \quad + \alpha_p A^{(p-1)} r^0 \tag{342}$$

where a superscript in parentheses denotes a matrix raised to a power. The iterate x^p is, therefore, seen to be equal to x^0 plus a vector taken from the subspace defined by the spanning set

$$\text{span}\{ r^0, Ar^0, A^{(2)} r^0, \quad , A^{(p-1)} r^0 \} \tag{343}$$

This vector space is called a p-dimensional *Krylov* subspace, $K_p(A; r^0)$. The basic iterative methods involve selecting special elements from this subspace; however, projection methods are devised to search for more optimal elements. Upon construction of a suitable basis for $K_p(A; r^0)$, one solves the system $Ax=b$ *projected* onto this Krylov subspace. Projection methods can also be formulated as acceleration techniques for the basic iterative algorithms (Young and Mai, 1987).

Following Golub and Van Loan (1989), the conjugate gradient method is viewed as a minimization technique. Specifically, given the SPD matrix A, find the value of x such that the quadratic form

$$\phi(x) = \frac{1}{2} x^T A x - x^T b \tag{344}$$

is a minimum. Differentiating $\phi(x)$ with respect to x and setting the result to zero, one finds that the functional $\phi(x)$ is stationary at $x=A^{-1}b$. Since A is SPD, this stationary point is an absolute minimum, therefore, the original linear algebra problem, Eq. (309), is equivalent to the minimization problem Eq. (344). The *method of steepest descent* (also known as Richardson's method) is a simple approach to minimizing $\phi(x)$ based on the recurrence relation

$$x^k = x^{k-1} + \alpha_k r^{k-1} \tag{345}$$

where $r^k = b - A x^k$ is the residual vector. The iterate x^k is equal to the vector sum of the previous iterate and a search *direction* vector. The direction vectors in Eq. (345) are just $-\nabla\phi$, and the parameters α_k are determined such that $\phi(x^{k-1} + \alpha r^{k-1})$ is minimized, via

$$\alpha_k = \frac{(r^{k-1}, r^{k-1})}{(r^{k-1}, Ar^{k-1})} \tag{346}$$

where (x, y) denotes the inner product $x^T y$. The method of steepest descent generally converges very slowly when the condition number of A is very large.

Other direction vectors may be selected that do not experience the convergence problems of the gradient directions, $-\nabla\phi$. The *conjugate gradient* method, *CG*, is an efficient way of generating a set of direction vectors p^k such that

$$(p^i, Ap^j) = 0 \quad , \quad i \neq j \tag{347}$$

The criteria in Eq. (347) state that the p^k vectors must be mutually A-conjugate, i.e., they are orthogonal with respect to the inner product (x, Ay) as defined by A.

The basic CG algorithm is

CONJUGATE GRADIENT ALGORITHM

Choose x^0, set $p^0=r^0=b-Ax^0$, calculate (r^0, r^0)

For $k=0, 1, \ldots$

$$\alpha_k = (r^k, r^k)/(p^k, Ap^k)$$

$$x^{k+1} = x^k + \alpha_k p^k$$

$$r^{k+1} = r^k - \alpha_k Ap^k$$

if $(\| r^{k+1} \|_2 / \| b \|_2) \geq \varepsilon$, continue

$$\beta_k = (r^{k+1}, r^{k+1})/(r^k, r^k)$$

$$p^{k+1} = r^{k+1} + \beta_k p^k$$

The coefficients β_k ensure that p^{k+1} is A-conjugate to p^k, and the stopping test is based on the 2-norm of the current residual. The conjugate gradient algorithm was originally presented as a direct method in a paper by Hestenes and Stieffel (1952). In theory, the direct solution should be obtained in exact arithmetic in, at most, n steps, where n is the order of A (Ortega and Poole, 1981). However, the conjugate gradient method is not practicable as a direct method, since, for large systems, n steps of the procedure incurs an unacceptably large computational cost. In addition, rounding errors lead to a loss of orthogonality among the residuals resulting in a breakdown of the procedure (Hageman and Young, 1981). However, its convergence properties indicate that the CG method can be a very effective iteration procedure if A is close to a rank r correction to the identity matrix. The following convergence theorem is presented and proven in Golub and Van Loan (1989).

If $A=I+B$ is an $n \times n$ SPD matrix and the rank of B is equal to r, then the conjugate gradient method will converge to the direct solution in at most r steps.

The above theorem points to the potential of a preconditioned conjugate gradient, PCG.

Preconditioning is carried out by a congruence transformation of the form

$$A' = SAS^T \tag{348}$$

where S is a nonsingular matrix chosen so that the condition number of A' is less than A. The CG method, in theory, is applied to the preconditioned system

$$\begin{aligned} (SAS^T)(S^{-T}x) &= Sb \\ \Downarrow & \\ A'x' &= b' \end{aligned} \tag{349}$$

Since the congruence transformation destroys the sparsity structure of A, PCG is designed to work with A and a preconditioner matrix $M = (S^T S)^{-1}$ rather than explicitly constructing A'. It is desired to choose M such that the condition number of A' is as small as possible. The relationship between the spectral condition number of A' and the preconditioner M is

$$\text{cond}_2(A') = \frac{\lambda_{max}(M^{-1}A)}{\lambda_{min}(M^{-1}A)} \tag{350}$$

where λ_{max} and λ_{min} are the maximum and minimum eigenvalues of $M^{-1}A$ (Ortega, 1987). The ideal (but impractical) preconditioner is $M=A$, since $M^{-1}A=I$, and $\text{cond}_2(A')=1$. Preconditioning procedures, therefore, have the goal of producing an M matrix that is as close to A as is computationally feasible.

The derivation of the following PCG procedure is given by Ortega (1987).

PRECONDITIONED CONJUGATE GRADIENT ALGORITHM

Choose x^0, set $r^0 = b - Ax^0$, solve $Mw^0 = r^0$, set $p^0 = w^0$

For $k=0, 1, \ldots$

$$\alpha_k = (w^k, r^k)/(p^k, Ap^k)$$

$$x^{k+1} = x^k + \alpha_k p^k$$

$$r^{k+1} = r^k - \alpha_k Ap^k$$

test for convergence

solve for $w^{k+1} \Rightarrow Mw^{k+1} = r^{k+1}$

$$\beta_k = (w^{k+1}, r^{k+1})/(w^k, r^k)$$

$$p^{k+1} = w^{k+1} + \beta_k p^k$$

One can see that another requirement for M is that the preconditioning step $Mw=r$ be easily computable.

A number of schemes have been developed that attempt to satisfy, in varying degrees, the generally conflicting criteria for a good preconditioner. Perhaps the simplest preconditioner is *diagonal scaling* where $M = \mathrm{diag}(A)$; however, the improvement in convergence rate is fairly minimal. *Truncated series* preconditioning involves a preset number of passes by a basic iterative method operating on the system $Aw=r$ to produce the auxiliary vector w. The basic method must have a SPD iteration matrix which excludes Gauss-Seidel and SOR. Examples of this approach include the *m-step Jacobi* and *m-step SSOR* preconditioners. Diagonal scaling can, therefore, be considered a 1-step Jacobi preconditioner. Ortega (1987) also discusses a form of *polynomial* preconditioning.

Perhaps the most important and effective preconditioning technique is based on the notion of *incomplete factorization* of A. Cholesky factorization can be viewed as

$$A = LL^T = HH^T + R \tag{351}$$

where A is assumed SPD, and H is lower triangular. The SPD matrix HH^T has the same sparsity structure as A, and the matrix R contains all of the "fill-in" produced by the factorization. In incomplete factorization, R is ignored, and HH^T is the preconditioning matrix M. Various strategies, called *no-fill* schemes, have been developed to avoid the computation of any elements of R. The no-fill principle can be relaxed, however, to make HH^T a better approximation of A, if necessary. The incomplete Cholesky conjugate gradient (ICCG) procedure has become one of the more widely used iterative methods for large sparse SPD problems.

The conjugate gradient method requires both A and the preconditioner M to be SPD in order to achieve mutually orthogonal residual vectors r^i using a simple three-term recurrence relation. In general, therefore, *PCG* cannot be applied to nonsymmetric indefinite matrices. Krylov-subspace methods have been developed, however, for the more general problem. Included in this class of methods are *biconjugate gradients* (BCG), *conjugate gradient squared* (CGS), and *generalized minimal residual* (GMRES).

In the BCG method, two sequences of mutually orthogonal residuals, r and r^*, are generated using simple relations similar to CG schemes. Also, two sets of direction vectors, p and p^*, are chosen to be mutually A-conjugate. As in CG, a number of preconditioning techniques are available to improve convergence. The following BCG method is due to Fletcher (1976).

PRECONDITIONED BICONJUGATE GRADIENT

Choose $x^{(0)}$; set $r^{(0)} = b - Ax^{(0)}$; solve $Mw^{(0)} = r^{(0)}$
Choose $r^{*(0)} = r^{(0)}$ or $r^{*(0)} = w^{(0)}$; set $\beta_0 = 0$
For $k = 0, 1, 2, \ldots$
$p^{(k)} = w^{(k)} + \beta_k p^{(k-1)}$
$p^{*(k)} = r^{*(k)} + \beta_k p^{*(k-1)}$
$\alpha_k = (r^{*(k)}, w^{(k)}) / (p^{*(k)}, Ap^{(k)})$
$r^{(k+1)} = r^{(k)} - \alpha_k Ap^{(k)}$
solve for $y \Rightarrow M^{-1}y = p^{*(k)}$
$r^{*(k+1)} = r^{*(k)} - \alpha_k A^{-1}y$
solve for $w^{(k+1)} \Rightarrow Mw^{(k+1)} = r^{(k+1)}$
$x^{(k+1)} = x^{(k)} + \alpha_k p^{(k)}$
test for convergence
$\beta_{k+1} = (r^{*(k+1)}, w^{(k+1)}) / (r^{*(k)}, w^{(k)})$

Note that the auxiliary vectors r^* and p^* are used only in the calculation of α_k and β_k. The preconditioning matrix M can be generated, for example, by diagonal scaling or incomplete LU factorization.

The conjugate gradient squared, CGS, method is a modification of BCG. Dongarra et al. (1991) observe that the residuals $r^{(k)}$ and $r^{*(k)}$ in the BCG method satisfy the relations $r^{(k)} = P^{(k)}(A)r^{(0)}$ and $r^{*(k)} = P^{(k)}(A^{-1})r^{*(0)}$, where $P^{(k)}(A)$ is a kth degree polynomial in A. The idea behind the *conjugate gradient squared* (CGS) method is that applying the operator $P^{(k)}(A)$ a second time, such that $r^{(k)} = P^{(k)}(A)^2 r^{(0)}$, will result in the residual $r^{(k)}$ being doubly reduced. A preconditioned form for CGS is the following:

PRECONDITIONED CONJUGATE GRADIENT SQUARED

Choose $x^{(0)}$; set $r^{(0)} = b - Ax^{(0)}$; $r^{*(0)} = r^{(0)}$;
$\beta_0 = (r^{(0)}, r^{*(0)})$; $q^{(0)} = p^{(-1)} = 0$
For $k = 0, 1, 2, \ldots$
$u^{(k)} = r^{(k)} + \beta_k q^{(k)}$
$p^{(k)} = u^{(k)} + \beta_k (q^{(k)} + \beta_k p^{(k-1)})$
solve for $y \Rightarrow My = p^{(k)}$
$\alpha_k = (r^{*(0)}, r^{(k)}) / (r^{*(0)}, Ay)$
$q^{(k+1)} = u^{(k)} - \alpha_k Ay$
solve for $u^* \Rightarrow Mu^* = u^{(k)} + q^{(k+1)}$
$x^{(k+1)} = x^{(k)} + \alpha_k u^*$
test for convergence
$r^{(k+1)} = r^{(k)} - \alpha_k Au^*$
if $(r^{*(0)}, r^{(k+1)}) = 0$ then the method fails
$\beta_{k+1} = (r^{*(0)}, r^{(k+1)}) / (r^{*(0)}, r^{(k)})$

In the above description of CGS, M is a suitable preconditioner such as diagonal scaling or incomplete LU factorization. The CGS algorithm typically converges twice as fast as BCG.

When A is SPD, the projection of $Ax=b$ onto the Krylov subspace $K_j(A; r^0)$ results in an easily solvable tridiagonal matrix formed by a simple three-term recurrence relation (Dongarra et al., 1991). For nonsymmetric indefinite systems, the projected system is an upper Hessenberg matrix. A family of algorithms including ORTHOMIN, ORTHODIR, ORTHORES, and GCR (Generalized Conjugate Residual) have been developed to construct this Hessenberg system (cf. Hageman and Young, 1981; and Chandra et al., 1977). The Generalized Minimal Residual (GMRES), due to Saad and Schultz (1986), is one of the more popular algorithms in this group. GMRES(m) as presented by Saad and Schultz (1986) is:

GENERALIZED MINIMAL RESIDUAL - GMRES(m)

Choose x^0 ; set $r^0 = b - Ax^0$; $v^1 = r^0/\|r^0\|$

For $j = 1,2, \ldots, m$

compute the l_2-orthonormal basis v^j

$h_{i,j} = (Av^j, v^i)$, $i = 1,2, \ldots, j$

$v^{*(j+1)} = Av^j - \sum_{i=1,2,\ldots,j} h_{i,j} v^i$

construct elements of upper Hessenberg matrix H

$h_{j+1,j} = \|v^{*(j+1)}\|$

$v^{(j+1)} = v^{*(j+1)}/h_{j+1,j}$

Form the approximate solution:

V^m matrix consists of the Arnoldi vectors v^j

$x^m = x^0 + V^m y^m$ where y^m minimizes $\|\beta e_1 - H_m y\|$

Restart:

set $r^m = b - Ax^m$

test for convergence

reset $x^0 = x^m$, $v^1 = r^m/\|r^m\|$

The construction of the upper Hessenberg system typically involves techniques developed for the algebraic eigenvalue problem such as Householder transformations or a modified Gram-Schmidt orthogonalization. A practical implementation of the method is GMRES(m) in which the iterations are restarted every m steps, thus avoiding the disadvantage of having to store all of the residual vectors up to convergence.

A comparative study of a number of Krylov subspace methods, specifically BCG, CGS, and CGR, and a direct nonsymmetric frontal solver is presented by Howard et al. (1990) for 2- and 3-dimensional FEM semi-discretizations of the Navier-Stokes equations. The model problem is natural convection in a unit-square box solved with the mixed finite-element u-P direct method. Both unpreconditioned and ILU preconditioned forms of the iterative methods were tested on a Cray XMP/48 and a Cray 2. The results of the study indicate that the unpreconditioned BCG method is robust for moderately nonlinear problems, and the ILU-BCG method is very robust and more economic than a nonsymmetric frontal solver on a Cray 2. The direct method had advantages over the iterative methods in the ability to vectorize significant CPU-intensive portions of the coding. Optimal implementations of the iterative methods on vector supercomputers were more difficult to attain since performance (i.e., convergence rate) is dependent upon the spectral (eigenvalue) properties of the specific matrix being solved, and there is no single portion of the code that dominates the CPU usage.

6. IMPLEMENTATION ON A UNIX WORKSTATION

The Continuity Constraint Method (CCM), described in Chapter 4, has been implemented in the Fortran 77 computer code **CFDL.PHI3D**. The target computer for CFDL.PHI3D was an engineering workstation running under the UNIX operating system, specifically an IBM Risc/6000-UNIX(AIX) Model 320 with a 20 mHz clock speed and 32 mbytes of random-access-memory (RAM). This machine is typical of the "UNIX-X Windows" systems that are emerging as the dominant platforms for modern CFD and general scientific computing. A summary of the methods, approximations, and decisions required to implement the CCM for this computing environment is presented in this chapter.

6.1 LINEAR ALGEBRA PROCEDURES

As discussed in Chapter 5, iterative methods appear to hold the greatest promise as efficient solution techniques for 3-dimensional CFD implementations. In a workstation environment, where internal memory capacity represents a significant capital investment, the efficient management of sparse linear algebra data structures is of critical importance.

After a survey of the literature, a library of sparse solver routines was assembled. The main source for the library was public-domain software, available through the *netlib* service based at the Oak Ridge National Laboratory (Dongarra et al., 1991). A number of Krylov-subspace solvers for SPD and general nonsymmetric problems developed at the Courant Institute and Lawrence Livermore National Laboratory for the Sparse Linear Algebra Package (SLAP) project, and the MA28 general sparse direct solver from Harwell were selected. The assembled library also includes a Gauss-Seidel sparse solver developed by the author.

To solve the linear algebra problem $Ax = b$, CFDL.PHI3D accesses the sparse solver library by a single call to an interface subroutine called *sparse*. The call format for *sparse* is:

call sparse (norder, nnz, lenw, leniw, itrmax, m, isym, tol, solve, lldiag, inj, smat, xp, b, iwork, work)

Input:		
norder	=	order of the matrix A
nnz	=	number of nonzeros in A (dimension of *smat*)
lenw	=	dimension of *work*
leniw	=	dimension of *iwork*
itrmax	=	maximum number of iterations allowed
m	=	number of vectors saved in **GMRES(m)** and **ORTHOMIN(m)**
isym	=	0, all nonzeros of A are stored in *smat*
	=	1, A is symmetric and only diagonal and strictly upper/lower triangle nonzeros are stored in *smat*
tol	=	convergence tolerance for stopping test
solve	=	keyword specifying the solver and preconditioner, see Table 3
lldiag	=	integer list of pointers to diagonals in *inj* and *smat*
inj	=	integer of row numbers for nonzeros in *smat*
smat	=	sparse representation of A using YSM column storage
b	=	vector holding right-hand-side data
iwork	=	integer workspace for solver
work	=	double precision workspace for solver
Output:		
xp	=	vector holding the solution x

The call list for *sparse* requires that the amount of integer and double precision work space (*leniw* and *lenw*) be input for the specific solver designated by the keyword *solve*. A subroutine called *worksp* is available in the solver library to calculate these dimensions. The *solve* keywords are given in Table 3.

The sparse solver library uses the YSM column format representation of the matrix A. In this format the nonzeros are stored counting down columns (except for the diagonal entry, which must appear first in each "column") and are stored in the double precision vector *smat*. In other words, for each column in the matrix one stores the diagonal entry in *smat*. Then the other nonzero elements are stored going down the column (except the diagonal) in order. The *inj* integer vector holds the row index for each nonzero. The *lldiag* integer vector holds the offsets into the *inj* and *smat* vectors for the beginning of each column. That is, *inj*(*lldiag*(*icol*)) and *smat*(*lldiag*(*icol*)) point to the beginning of the icol-th column in *inj* and *smat*, and *inj*(*lldiag*(*icol*+1)-1) and *smat*(*lldiag*(*icol*+1)-1) point to the end of the icol-th column in *inj* and *smat*. The information necessary to calculate the sparsity structure of the A matrix and generate the *lldiag* and *inj* vectors is available in the element connectivity table. This table is constructed as a part of the finite-element mesh generation and consists of a list of node numbers for each element. As pointers to the global coordinate data base, the node numbers provide the complete geometric definition of the element. By carrying out a symbolic assembly of the global system matrix using the connectivity table, the sparsity structure of A can be determined. A Fortran listing of a subroutine that executes this symbolic assembly is given in Fig. 6 The subroutine *llist* was

Table 3. Sparse Solver Library Keywords

Keyword	Solver	Preconditioner
gseidel	Gauss-Seidel	none
dsgmres	GMRES	diagonal scaling
lugmres	GMRES	incomplete LU factorization
dsbcgrd	biconjugate gradient	diagonal scaling
lubcgrd	biconjugate gradient	incomplete LU factorization
dsbcgs	conjugate gradient squared	diagonal scaling
lubcgs	conjugate gradient squared	incomplete LU factorization
dsormin	ORTHOMIN	diagonal scaling
luormin	ORTHOMIN	incomplete LU factorization
dscgrad	conjugate gradient	diagonal scaling
iccgrad	conjugate gradient	incomplete Cholesky factorization
direct	MA28	none

designed for YSM row storage, but it is also applicable for YSM column storage since the sparsity structure of A is symmetric, even though A itself may be nonsymmetric.

The global coefficient matrix A is never actually formed by CFDL.PHI3D. As a part of the construction of the Newton residuals for each state variable, the sparse representation of A, represented by the double precision vector *smat*, is assembled on an *element-by-element* basis in a *DO*-loop over all of the elements in the mesh. The information necessary to build the YSM formatted vector *smat* is contained in the integer vectors *ildiag* and *inj*.

6.2 FINITE-ELEMENT MESH GENERATION

The generation of the finite-element mesh is carried out as a preprocessing step using the public-domain code INGRID (Stillman and Hallquist, 1985). Work on INGRID began in 1979 at the University of Tennessee with the acquisition of the Los Alamos program INGEN. A preprocessor was added to INGEN along with a simple graphics program to produce INGRID. Subsequently, the work on INGRID shifted to Lawrence Livermore National Laboratory (LLNL). Perhaps the most important new capability added to the code is associated with the ease of application of boundary conditions, loads, and material properties required by nonlinear mechanics programs. The current version of INGRID is designed to produce complete input files for a suite of 3-dimensional finite-element solid mechanics and heat transfer codes developed at LLNL. The author has written an interface program that takes an input file generated by INGRID for the 3-dimensional heat conduction code TOPAZ3D and produces the necessary input files for CFDL.PHI3D. INGRID is capable of producing general

3-dimensional finite-element meshes using 8-node hexahedra. Various boundary conditions are applied by *paving* the required surfaces with general 4-node quadrilateral elements. The ordering of the nodes in the connectivity table for these 2-dimensional elements is used to specify the direction of the outward-pointing normal unit vectors for each boundary surface. Multi-connected domains can be generated with the INGRID *delete* commands, and mesh grading is available in any of the coordinate directions.

6.3 MEMORY MANAGEMENT

In a workstation environment, the ability to control the allocation of internal memory during job execution is of critical importance for the efficient use of computing resources. The Fortran 77 language (ANSI Standard X3.9–1978) makes no provision for dynamic memory allocation; however, the *C* programming language supplies, as a part of its standard implementation (Kernighan and Ritchie, 1988), the functions *malloc* and *realloc* which can be used in a Fortran-callable *C* function. The *C* function *malloc* (defined as *void *malloc (size);*) sets aside a block of contiguous memory for an object of size "*size*" in bytes and returns a pointer to the starting address of the block. If the memory is unavailable, the pointer is set to *NULL*. The *C* function *realloc* (defined as *void *realloc (void *ptr, newsize);*) resizes to "*newsize*" the contiguous memory block set aside by a previous call to *malloc*( ). The contents of the memory are not corrupted. If space is not available (when more is needed) at the present location, then a new location is selected, the contents copied there, and a new pointer returned. The variable *ptr* is a pointer to the original memory location allocated by the previous call to *malloc*( ). The *void* pointer for *realloc*( ) points to the starting address of the reallocated contiguous memory block if the operation is successful. If unsuccessful, then the *void* pointer is set to *NULL*. Listings of two Fortran-callable *C* functions that carry out these operations are given in Fig. 7.

6.4 SOLUTION STRATEGIES

An initial study of memory requirements indicated the need for a sequential segregated solution strategy in which the required sequence of linear algebra problems is limited to a single degree-of-freedom per node. Segregated formulations are discussed by Benim and Zinser (1986) and Shaw (1991). For the present work, two segregated quasi-Newton iterative solution strategies were investigated. Both schemes employ quasi-Newton Jacobians completed for self-coupling only, neglecting cross-coupling terms such as $\partial\{FU\}/\partial\{U\}$, $\partial\{FU\}/\partial\{\Theta\}$, and $\partial\{F\Theta\}/\partial\{U\}$.

The first solution strategy is presented in Table 4. This scheme uses a standard segregated sequence of system matrix and residual **FORM** steps followed by state-variable **SOLVE** and **UPDATE** steps. The sparse representation of each state-variable Jacobian matrix (denoted by the vector *smat*) is formed exactly for all self-coupling terms and boundary conditions in Steps 1, 4, 7, 10, and 13. The residuals $\{FU\}$, $\{F\Theta\}$, and $\{R\Phi\}$ are also formed in these same sequential **FORM** steps where they are able to use the most recently updated solutions for the other state-variables. Timing studies showed that the most compute-intensive components of the iterative cycle for Strategy No. 1 were the **FORM** steps and the **SOLVE** step for the Φ-Poisson equation, Step 14.

```
c*****************************************************************************c
c***                        subroutine llist                                ***c
c*****************************************************************************c
c***   Determine YSM sparse data structure for global system matrix.         ***c
c***   input:                                                                ***c
c***     n=       order of system matrix                                     ***c
c***     isym=    logical symmetry flag                                      ***c
c***     mel(8,nmel)= element connectivity table                             ***c
c***   workspace: (must be input)                                            ***c
c***     iwork(27,n)                                                         ***c
c***     nnz(n)                                                              ***c
c***   output:                                                               ***c
c***     lldiag(n+1)= list of pointers to diagonals in inj                   ***c
c***     inj(nz)= integer list of column pointers                            ***c
c***     nz= number of non-zeros in smat                                     ***c
c*****************************************************************************c
      subroutine llist (lldiag,inj,mel,nnz,iwork,n,nmel,nz,isym)
      implicit double precision (a-h , o-z)
      logical isym
      integer mel(8,nmel),lldiag(n+1),inj(27*n),iwork(27,n),nnz(n)
c****************** first executable line of llist ***********************
c     initialize work space
      do 10 i=1,n
        nnz(i)= 1
        iwork(1,i)= i
        do 10 j=2,27
         iwork(j,i)= 0
 10   continue
c************************ begin loop over elements ***********************
      do 60 jel=1,nmel
        do 50 i=1,8
c         get row number
          irow= mel(i,jel)
          do 40 j=1,8
c           get column number
            jcol= mel(j,jel)
c           skip over diagonal position. it has already been counted.
            if (irow.eq.jcol) goto  40
c           for symmetric matrices store only the upper triangular block
            if(isym .and. jcol.lt.irow) goto  40
c           check to see if jcol has already been counted
            do 20 ii=1,nnz(irow)
              if (iwork(ii,irow).eq.jcol) goto  40
 20         continue
            nnz(irow)= nnz(irow) + 1
            iwork(nnz(irow),irow)= jcol
 40       continue
 50     continue
 60    continue
c********************** end of element loop ********************************
c     construct integer-lists and compute total number of non-zeros
      lldiag(1)= 1
      nz= 0
      do 70 i=2,n+1
        nz= nz + nnz(i-1)
        lldiag(i)= lldiag(i-1) + nnz(i-1)
 70    continue
      do 100 irow=1,n
        il= 0
        do 100 j=lldiag(irow),lldiag(irow+1)-1
          il= il + 1
          inj(j)= iwork(il,irow)
 100  continue
      return
c************* last line of subroutine llist ******************************
      end
```

Figure 6. Listing of Fortran subroutine to construct YSM data lists.

```
#include <sys/types.h>
#include <sys/times.h>
#include <time.h>
#include <stdio.h>
#include <stdlib.h>
/* ************************************************************ */
/* ***                      falloc                              *** */
/* ***  dynamically allocate contiguous memory (number*size)    *** */
/* ************************************************************ */
/* ***                                                          *** */
/* ***  input:                                                  *** */
/* ***    int *number = the number of words to be allocated     *** */
/* ***    int *size   = number of bytes per word                *** */
/* ***    int *array  = pointer to allocated array              *** */
/* ***                                                          *** */
/* ***  output:                                                 *** */
/* ***    int *addr   = address of allocated memory             *** */
/* ***    int *offset = offset of allocated memory              *** */
/* ************************************************************ */
void falloc(int *number,int *size,int *array,int *addr,int *offset)
{
/*  int *malloc();  */
  int *addrp;
  addrp = malloc((*number)*(*size));
  if (addrp == NULL )  {
     printf( " Memory allocation unsuccessful \n");
     printf( " Execution aborted \n");
     exit(1);
   }
  *offset = (int)(addrp-array)*sizeof(int)/(*size);
  *addr = (int)addrp;
  printf( " Memory allocation successful  address= %d \n",*addr);
}
/* ************************************************************ */
/* ***                      reloc                               *** */
/* *** reallocate contiguous memory (number*size) at *addr      *** */
/* ************************************************************ */
/* ***                                                          *** */
/* ***  input:                                                  *** */
/* ***    int *number = the number of words to be allocated     *** */
/* ***    int *size   = number of bytes per word                *** */
/* ***    int *array  = pointer to allocated array              *** */
/* ***    int *addr   = address of original allocation          *** */
/* ***                                                          *** */
/* ***  output:                                                 *** */
/* ***    int *addr   = address of reallocated memory           *** */
/* ***    int *offset = offset of reallocated memory            *** */
/* ************************************************************ */

void reloc(int *number,int *size,int *array,int *addr,int *offset)
{
/*  int *realloc();  */
  int *addrp;
  addrp = realloc( *addr, (*number)*(*size));
  if ( addrp == NULL )  {
     printf( " Memory reallocation unsuccessful \n");
     printf( " Execution aborted \n");
     exit(1);
   }
  *offset = (int)(addrp-array)*sizeof(int)/(*size);
  *addr = (int)addrp;
  printf( " Memory reallocation successful  address= %d \n",*addr);
}
```

Figure 7. Listing of Fortran-callable C functions for dynamic memory allocation.

Table 4. Segregated Solution Strategy No. 1.

Step	Operation	Description
1	FORM-Θ	form Θ-*smat*, apply boundary conditions, and construct $\{R\Theta\}$
2	SOLVE-Θ	solve for $\delta\Theta^{(p+1)}$: $[SMAT]\{\delta\Theta\} = \{R\Theta\}$
3	UPDATE-Θ	update $\Theta^{(p+1)}$ for iteration $p+1$: $\Theta^{(p+1)} = \Theta^{(p)} + \{\delta\Theta\}^{(p+1)}$
4	FORM-$U1$	form $U1$-*smat*, apply boundary conditions, construct $\{RU1\}$
5	SOLVE-$U1$	solve for $\delta U1^{(p+1)}$: $[SMAT]\{\delta U1\} = \{RU1\}$
6	UPDATE-$U1$	update $U1^{(p+1)}$ for iteration $p+1$: $U1^{(p+1)} = U1^{(p)} + \{\delta U1\}^{(p+1)}$
7	FORM-$U2$	form $U2$-*smat*, apply boundary conditions, construct $\{RU2\}$
8	SOLVE-$U2$	solve for $\delta U2^{(p+1)}$: $[SMAT]\{\delta U2\} = \{RU2\}$
9	UPDATE-$U2$	update $U2^{(p+1)}$ for iteration $p+1$: $U2^{(p+1)} = U2^{(p)} + \{\delta U2\}^{(p+1)}$
10	FORM-$U3$	form $U3$-*smat*, apply boundary conditions, construct $\{RU3\}$
11	SOLVE-$U3$	solve for $\delta U3^{(p+1)}$: $[SMAT]\{\delta U3\} = \{RU3\}$
12	UPDATE-$U3$	update $U3^{(p+1)}$ for iteration $p+1$: $U3^{(p+1)} = U3^{(p)} + \{\delta U3\}^{(p+1)}$
13	FORM-Φ	form Φ-*smat*, apply boundary conditions, and construct $\{R\Phi\}$
14	SOLVE-Φ	solve for $\Phi^{(p+1)}$: $[SMAT]\{\Phi\} = \{R\Phi\}$
15	UPDATE-C	update $C^{(p+1)}$ for iteration $p+1$: $C^{(p+1)} = P^{(p)} + \sum_{m=1}^{M} \Phi^{m}$
16	TEST STOP	test for convergence: IF $\|\Phi\|_{\infty} < \varepsilon$ THEN go to STEP 18
17	GOTO STEP 1	increment iteration index p and repeat outer iteration
18	FORM-P	form P-*smat*, apply boundary conditions, and construct $\{RP\}$
19	SOLVE-P	solve for $P^{(p+1)}$: $[SMAT]\{P\} = \{RP\}$
20	ADVANCE	update state-variables $\{Q^{n}\} = \{Q^{(p+1)}\}$, go to next time station

For the momentum equations, the self-coupling quasi-Newton Jacobian (excluding boundary conditions) in Strategy No. 1 is, in compact notation,

$$\frac{\partial\{FU1\}}{\partial\{U1\}} = DET_1[C200]$$

$$+ \Delta t\,0\ DET_1\ EJK_1\ \{U1\}^T_1[C30K0]$$

$$+ \Delta t\,0\ DET_1\{U1\}^T_1(E11_1[C3010] + E12_1[C3020] + E13_1[C3030]) \tag{352}$$

$$+ \Delta t\,0\ DET_1\ \frac{1}{Re}(1 + Re^{-1})\ EJK_1\ EJM_1[C2KM]$$

where the repeated "1" index is not summed. The corresponding Jacobian for the energy equation is

$$\frac{\partial\{F\Theta\}}{\partial\{\Theta\}} = DET_1[C200]$$

$$+ \Delta t\,0\ DET_1\ EJK_1\ \{U1\}^T_1[C30K0] \tag{353}$$

$$+ \Delta t\,0\ DET_1\ \frac{1}{Re}\left(\frac{1}{Pr} + \frac{Re^{-1}}{Pr^{-1}}\right) EJK_1\ EJM_1[C2KM]$$

A revised solution strategy was developed to reduce the computational cost of the **FORM** steps. Strategy No. 2 is presented in Table 5. It was noted that by modifying the convection term contributions to *smat* in the momentum equations, a base level approximation for *smat* (not including boundary conditions) could be assembled that would be identical for all three momentum equations and the energy equation. This approximate *smat* is formed only once for each outer iteration. The **FORM** steps for the energy and momentum equations consist of adding the required boundary conditions to *smat*, resulting in a significant computational savings since the application of boundary conditions does not typically require a complete loop over all mesh elements. After the each **SOLVE** step, the boundary conditions are **REMOVE**d from *smat* in preparation for the next equation system. Since the residuals for each state-variable continue to be formed exactly, the modified quasi-Newton Jacobians affect only solution convergence rates and not solution accuracy.

If the third term on the right-hand side of Eq. (352) is neglected, then the resulting approximation to the quasi-Newton Jacobian for the momentum equations will be similar in form to Eq. (353).

$$\frac{\partial\{FU1\}}{\partial\{U1\}} = DET_1[C200]$$

$$+ \Delta t\,0\ DET_1\ EJK_1\ \{U1\}^T_1[C30K0] \tag{354}$$

$$+ \Delta t\,0\ DET_1\ \frac{1}{Re}(1 + Re^{-1})\ EJK_1\ EJM_1[C2KM]$$

Table 8. Segregated Solution Strategy No. 2.

Step	Operation	Description
1	BASRES	form base level *smat* and all residuals $\{R1\}$ and $\{R\Theta\}$ with boundary conditions applied to residuals only
2	FORM-Θ	add boundary conditions to *smat* for Θ solution
3	SOLVE-Θ	solve for $\delta\Theta^{(p+1)}$: $[SMAT]\{\delta\Theta\} = \{R\Theta\}$
4	REMOVE-Θ	subtract Θ boundary conditions from *smat*
5	UPDATE-Θ	update $\Theta^{(p+1)}$ for iteration $p+1$: $\Theta^{(p+1)} = \Theta^{(p)} + \{\delta\Theta\}^{(p+1)}$
6	FORM-$U1$	add boundary conditions to *smat* for $U1$ solution
7	SOLVE-$U1$	solve for $\delta U1^{(p+1)}$: $[SMAT]\{\delta U1\} = \{RU1\}$
8	REMOVE-$U1$	subtract $U2$ boundary conditions from *smat*
9	UPDATE-$U1$	update $U1^{(p+1)}$ for iteration $p+1$: $U1^{(p+1)} = U1^{(p)} + \{\delta U1\}^{(p+1)}$
10	FORM-$U2$	add boundary conditions to *smat* for $U2$ solution
11	SOLVE-$U2$	solve for $\delta U2^{(p+1)}$: $[SMAT]\{\delta U2\} = \{RU2\}$
12	REMOVE-$U2$	subtract $U2$ boundary conditions from *smat*
13	UPDATE-$U2$	update $U2^{(p+1)}$ for iteration $p+1$: $U2^{(p+1)} = U2^{(p)} + \{\delta U2\}^{(p+1)}$
14	FORM-$U3$	add boundary conditions to *smat* for $U3$ solution
15	SOLVE-$U3$	solve for $\delta U3^{(p+1)}$: $[SMAT]\{\delta U3\} = \{RU3\}$
16	REMOVE-$U3$	subtract $U3$ boundary conditions from *smat*
17	UPDATE-$U3$	update $U3^{(p+1)}$ for iteration $p+1$: $U3^{(p+1)} = U3^{(p)} + \{\delta U3\}^{(p+1)}$
18	FORM-Φ	form Φ-*smat*, apply boundary conditions, and construct $\{R\Phi\}$
19	SOLVE-Φ	solve for $\Phi^{(p+1)}$: $[SMAT]\{\Phi\} = \{R\Phi\}$
20	UPDATE-C	update $C^{(p+1)}$ for iteration $p+1$: $C^{(p+1)} = P^{(p)} + \sum_{i=1,p+1} \Phi^{i}$
21	TEST STOP	test for convergence: IF $\|\Phi\| <$ TOLN go to STEP 23
22	GOTO STEP 1	increment iteration index p and repeat outer iteration
23	FORM-P	form P-*smat*, apply boundary conditions, and construct $\{RP\}$
24	SOLVE-P	solve for $P^{(p+1)}$: $[SMAT]\{P\} = \{RP\}$
25	ADVANCE	update state-variables $Q^{n} = Q^{(p+1)}$, go to next time station

Equation (154) is the template for the base level *vmat* in Step 1 of Strategy No 2 Two approximations are being made for the base level *vmat* (1) the convection term contribution to the global system Newton Jacobian for the momentum equations is compromised and (2) the influence of the Prandtl number on the diffusion term in the energy equation is neglected As noted above, these modifications are applied only to the formation of the base level *vmat* The calculation of the state-variable residuals are not compromised, i e , solution convergence is affected only, not solution accuracy

An additional impact on the convergence rate for Strategy No 2 arises from the fact that the state-variable residuals {7 1} and {7 9} are calculated only in Step 1, therefore, the individual **UPDATE** steps (Steps 5, 9, 13, and 17) do not influence the residual calculations until a full pass through the iterative cycle has been completed The boundary condition updates for *vmat* (Steps 6, 10, and 14) do use the latest updated solutions In Strategy No 1, however, the effect of the **UPDATE** steps is immediately felt by all subsequent residual and global *vmat* calculations

Even with the above disadvantages, however, preliminary testing has indicated that Strategy No 2 is effective in reducing the overall CPU costs (in terms of compute cycles per time step) relative to Strategy No 1 The minimal reduction in convergence rates was more than offset by the savings realized in reduced floating point operations Therefore, all of the solutions to be presented in Chapter 7 were obtained with Strategy No 2

6.5 PROGRAM OPERATION

Even though the UNIX operating system does not formally include a *batch* operating mode, as a multi-tasking system it does support *background* processing, which allows the user to initiate a task and then proceed to other activities while the system continues to work on the original background task (Groff and Weinberg, 1988) The CFDI PHIID program is, therefore, normally executed as a background process through the *nohup* ("no hangup") utility The *nohup* utility allows the user to log off of the computer without killing the background process

Three-dimensional CFD problems can require execution times on the order of several hundred hours or more to produce a steady-state solution In order to sustain such long residence times on the computer, any large application program should have an internal *checkpointing* capability if it is not provided by the operating system CFDI PHIID has its own system of checkpointing by temporarily suspending computations at preselected intervals, called checkpoints, and writing a binary *restart* file to out-of-core memory (e g , a hard disk) These checkpoints provide a means of protecting long-running jobs from system failures or intentional shutdowns If the computer should be shutdown for some reason, CFDI PHIID execution can be subsequently restarted from the most recent *restart* file

The system matrices for the Φ and pressure Poisson equations are functions of the mesh geometry only and do not change during execution It is, therefore, more computationally efficient to calculate these matrices once and then store them for subsequent retrieval in the **FORM** steps (Step 18 and 23) for Φ and the pressure If incomplete factorization is used as a preconditioner for any of the Krylov-subspace iterative solvers listed in Table 1, the preconditioning factors need only be computed once and then stored for future **SOLVE** steps CFDI PHIID makes use of binary *swap files* to carry out these store and retrieval operations A swap file is a temporary file (typically residing on a medium such as a hard disk) that is accessed by an unformatted binary "read" where the required

data are *swapped* into and out of a shared block of internal memory. Swap files are, in effect, a user-controllable form of virtual memory.

Solution Strategy No. 2 indicates that the pressure solution is required in Steps 23-24 at the end of each time step. It was determined, however, that these steps could be subcycled without a significant loss in stability or solution accuracy. Subcycling the pressure solution involves executing Steps 23-24 at selected time stations (e.g., every 10th time station).

The progress of program execution is monitored by tracking the iteration history of the evolution of each of the state-variables in the system as measured by appropriate energy norms. At the end of each outer iteration in the cycle (Step 22 in Table 5), the global energy norms for the three velocity components, the temperature, and the potential function Φ are computed and written to a file. This file can be accessed at any time by the user to generate iteration-history plots which can be used as a diagnostic tool for determining the status of the calculations. Large excursions by any of the energy norms are indicative of a pending breakdown in the solution process. Attainment of an approximate steady-state solution can be determined by a comparison of the relative rates of change of the energy norms.

6.6 POST-PROCESSING

The visualization of 3-dimensional data is becoming an important subfield of modern scientific computing. As with any CFD code, CFDL-PHOD produces a large amount of information, and the ability to present this information in an effective and clear graphical format is a critical requirement for a successful implementation.

As a part of its checkpointing function, CFDL-PHOD generates, at selected intervals, a binary plot file containing a number of solution variables. Included in this file are the mesh definition, the velocity vector field distribution, scalar field distributions for the temperature and pressure, a node-based distribution of the divergence error as measured by the energy norm of the Φ potential function, and a vorticity vector field distribution. A post-processing program was specifically developed to translate the data in the plot file into an input file for the commercial graphics program TECPLOT®, an interactive code for visualizing engineering and scientific data (TECPLOT, Version 5 User's Guide, 1992). TECPLOT integrates XY plotting with 2- and 3-dimensional surface contouring, scatter field plots, vector plotting, streamlining, and surface visualization into a single program. One can use the program to display, manipulate, and examine data, and then create high-quality color or grey-scale hardcopy plots on various output devices including laser printers, film recorders, and pen plotters.

7. RESULTS AND DISCUSSION

Test cases, designed to investigate the accuracy and limitations of algorithm implementations, can be grouped into three classes of problems: *verification*, *benchmarking*, and *validation* (Williams et al., 1989). *Verification* involves the comparison of computational to analytical results for problems in which a "closed-form" solution exists. *Benchmarking* is the comparison of results to those produced by an independent computational model, i.e., "code-to-code" comparisons. Code *validation* requires the comparison of computer simulations to experimental data. The results of test cases, selected from all three categories, are presented in this chapter with the intent of exploring the accuracy, convergence, and stability of the CCM as implemented in CFDL-PHIII. Preliminary testing of CFDL-PHIII focused on 2-dimensional flows generated via vanishing normal derivative boundary conditions on a two-element wide mesh in the third direction (Williams et al., 1992). The test cases discussed herein complete the verification, benchmarking, and validation studies by exploring 3-dimensional flows, including fully developed flow in a square duct, developing flow near the entrance of a square duct, natural convection in a thermal-driven cavity, isothermal separated flow in a 2- and 3-dimensional step-wall diffuser, combined forced- and natural-convection in the University of Illinois test facility for full-scale room ventilation experiments, and natural convection in a partitioned thermal cavity based on scale model experiments carried out at Colorado State University.

7.1 PRELIMINARY STUDIES

As a key element in the development and implementation of the CCM, studies were performed to investigate (1) the fully-discrete performance of the algorithm's pseudo-pressure distribution during iterative cycling and (2) the computational performance of the sparse solvers available in the linear algebra library discussed in Chapter 6.

7.1.1 Smoothing of Pseudo-Pressure

Due to equal-order interpolation in the CCM of all state variables including the continuity constraint function, Φ, there is a dominant dispersive-error mode present in the pseudo-pressure distribution accumulated during iterative cycling within the time step and over time steps. Several researchers have investigated the application of recursive and non-recursive digital filters to remove these high-frequency "2-Δx" signals (cf. Pepper et al., 1979; Lee et al., 1979; Hughes et al., 1979; and Gresho et al., 1984) from pressure and velocity distributions. Tests were carried out to determine the effect of smoothing the pseudo-pressure distribution during cycling with the genuine pressure solution as it is modified by the continuity constraint function.

The test problem was fully-developed flow through a channel, Re=100, to be discussed in detail in the following section. A simple 5-term nonrecursive, low-pass filter (Hamming, 1971) was applied to the pseudo-pressure distribution (referred to as $C^{(k)}$ in Chapter 6) after each update in the outer iteration of the solution strategy (see Step 20 in Table 5, Chapter 6). A visual inspection of the pseudo-pressure before and after the filtering operation showed a definite smoothing of the solution, however, comparisons with control tests also showed a decrease in convergence upon smoothing with an eventual divergence after approximately 10 time steps. The conclusions drawn from these tests were (1) filtering out the dispersive error mode in the continuity constraint distribution is not effective in improving convergence rates, and (2) the dispersive error mode definitely plays an important role

in the ability of the continuity constraint function to remove the divergence error in the discrete velocity distribution. These results confirmed the decision to use the genuine pressure, calculated from a smooth solenoidal velocity distribution, as a replacement for the pseudo-pressure [7], to prevent the contamination of the velocity and temperature fields by the inherent dispersive error mode present in [7].

7.1.2 Sparse-Solver Linear Algebra Study

Test cases were run on a 3-dimensional natural convection cavity, $M = 17 \times 17 \times 10$, to measure the performance of different combinations of solvers available in the Sparse Iterative Solver Library, developed as a part of this research. The results of 8 cases are reported in Table 6. The thermal-driven cavity problem is discussed in detail in a later section. For these tests at $Ra = 10^4$ $Pr = 0.7$, the initial conditions were the steady-state solution at $Ra = 10^3$. The energy norm traces for all state-variables were examined and found to be essentially the same for each test case; therefore, the number of outer iterations executed over the 10 time steps used in the test were the same, and the solutions produced by each solver were equivalent. The solver designations are the *keywords* defined in Table 3 of Chapter 6. Also reported in Table 6, *memory* is the workspace memory required by the solver, *time* is the CPU execution time for the specified solve step for 10 time stations, and *total time* is the total CPU execution time for all operations. The most effective combinations appear to be Cases 6, 1, and 4, in that order. The final memory requirements for Cases 1 and 4 are the same. Since workspace is shared by the solvers, it is the maximum memory among the solve steps, rather than the sum, that determines the workspace requirements for an execution. The configuration in Case 6 was later eliminated after subsequent testing on more ill-conditioned problems, because diagonal scaling proved

Table 6. Memory and CPU Timing Data for 3-dimensional Test Problem

Case No	u,v,w-Solutions			ϕ- and Pressure Solutions			Total Time s
	solver	memory kbytes	time s	solver	memory kbytes	time s	
1	dsgmres	471.8	100.8	iccgrad	643.8	188.7	965
2	dsormm	941.3	130.4	iccgrad	643.8	194.4	1031
3	dsbcgrd	216.4	141.2	iccgrad	643.8	184.6	1007
4	dsbcgs	203.7	116.6	iccgrad	643.8	188.8	967
5	dsbcgs	203.7	122.4	dsbcgs	203.7	301.9	1122
6	dsbcgs	203.7	120.6	dscgrad	216.4	111.7	904
7	lubcgs	1122.0	224.2	iccgrad	643.8	168.0	1072
8	lugmres	2296.0	223.0	iccgrad	643.8	168.7	1072

to be an ineffective preconditioner. For all solutions reported in the remainder of this chapter, the Case 1 configuration was used, i.e., the momentum and energy solutions were obtained with the diagonally-scaled GMRES sparse solver, and the Φ and pressure Poisson solutions used the conjugate gradient solver with incomplete Cholesky preconditioning.

7.2 FULLY-DEVELOPED FLOW IN A SQUARE DUCT

Steady-state, isothermal, laminar flow in a straight duct of square cross-section is a common first-verification case for incompressible Navier-Stokes CFD algorithms (cf. Pelletier et al., 1989; and Hsu et al., 1992). For the x_1-coordinate direction aligned with the duct axis, Fig. 8, the axial velocity fully-developed profile at any x_1-station, with $-a \le x_2 \le a$ and $-b \le x_3 \le b$, is

$$u_1(x_2, x_3, a, b) = \frac{16a^2}{\mu \pi^3}\left(-\frac{dp}{dx_1}\right)\xi(x_2, x_3, a, b) \quad ; \quad u_2 = u_3 = 0$$

$$\xi(x_2, x_3, a, b) = \sum_{n=1,3,5,\ldots} (-1)^{\frac{(n-1)}{2}}\left[1 - \frac{\cosh(n\pi x_3/2a)}{\cosh(n\pi b/2a)}\right]\frac{\cos(n\pi x_2/2a)}{n^3} \tag{355}$$

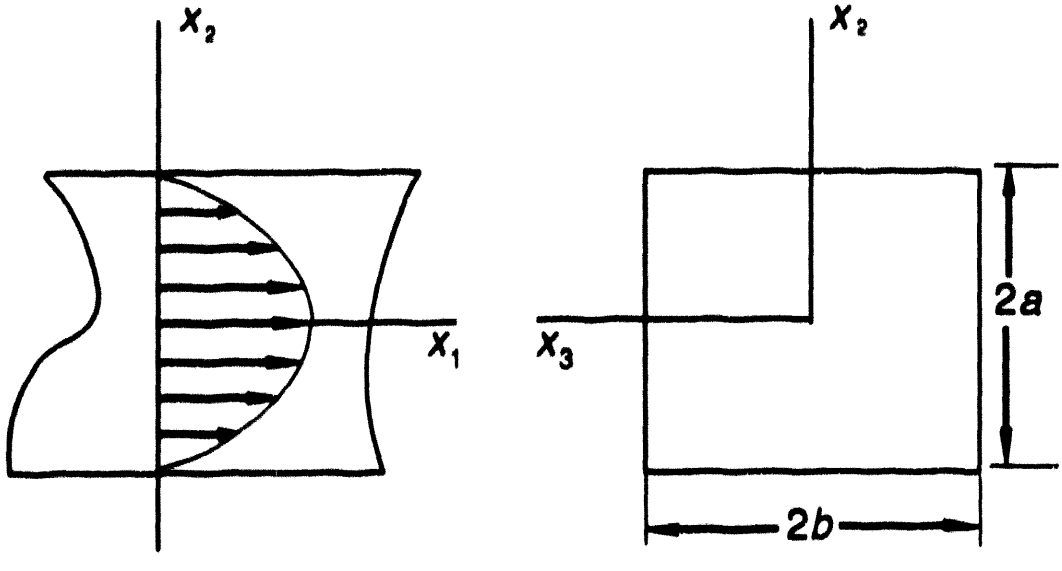

Figure 8. Fully-developed flow in a rectangular duct.

The associated axial pressure gradient dp/dx_1 is a uniform constant, and the corresponding volumetric flowrate Q through the duct is (White, 1974)

$$Q(a,b) = u_{1\,avg}(2a \times 2b) = \frac{4ba^3}{3\mu}\left(-\frac{dp}{dx_1}\right)\zeta(a,b)$$
$$\zeta(a,b) = 1 - \frac{192a}{\pi^5 b}\sum_{n=1,3,5}^{\infty}\frac{\tanh(n\pi b/2a)}{n^5} \tag{356}$$

The nondimensional velocity profile, scaled by the average duct velocity $u_{1\text{-}avg}$, is obtained by dividing Eq. (355) by Eq. (356), yielding

$$u_1^* = \frac{u_1}{u_{1\,avg}} = \frac{48}{\pi^3}\frac{\xi(x_2,x_3,a,b)}{\zeta(a,b)} \tag{357}$$

where superscript "star" denotes a nondimensional variable. At the centerline of the duct ($x_2 = x_3 = 0$), the maximum velocities are

$$u_{1\,max}^* = 1.5 \text{ for a two-dimensional duct, } b \to \infty$$
$$u_{1\,max}^* = 2.096 \text{ for a square duct, } a = b \tag{358}$$

which are independent of the flowrate and pressure drop in the duct. Using Eq. (356), the constant nondimensional axial pressure gradient is a function of the bulk-flow Reynolds number and the geometry of the duct.

$$-\frac{dP^*}{dx_1^*} = \frac{3}{\mathrm{Re}}\left(\frac{4b}{a+b}\right)^2\frac{1}{\zeta(a,b)} \tag{359}$$

where

$$\mathrm{Re} = \frac{u_{1\,avg}D_h}{\nu};\quad D_h = \frac{4ab}{a+b};\quad P^* = \frac{p}{\rho u_{1\,avg}^2};\quad x_1^* = \frac{x_1}{D_h} \tag{360}$$

where D_h is the *hydraulic diameter* of the channel (White, 1974). For a 2-dimensional channel

$$\zeta(a,b) = 1 \quad \text{and} \quad -\frac{dP^*}{dx_1^*} = \frac{48}{\mathrm{Re}} \quad \text{as } b \to \infty \tag{361}$$

and for a square duct

$$\zeta(a,b) = 0.42173 \quad \text{and} \quad -\frac{dP^*}{dx_1^*} = \frac{28.45}{\mathrm{Re}} \quad \text{for } a = b \tag{362}$$

Steady-state laminar flow in a straight duct of square cross-section was simulated using the modestly nonuniform mesh shown in Fig. 9. Exploiting the symmetry of the flow field, only half the duct was included in the model domain. The mesh discretization is M=24×20×10 consisting of 5775

nodes and 4800 hexahedra elements. The boundary conditions for the six surfaces of the model are given in Table 7. As initial conditions, the velocity components and pressure were set to zero for all interior points and on all boundaries where Neumann boundary conditions were applied. For Re=100, the steady-state velocity solution is shown in Fig. 10 where selected cutting planes have been extracted from the complete solution to enhance visualization. Figures 11 and 12 present quantitative comparisons for the analytical and computed solutions. In Fig. 11, spanwise velocity profiles at the middle of the channel height (x_2=0, $0 \le x_1 \le 0.5$) are compared to the analytical solution, Eq. (357), for selected locations along the length of the channel at Re=100 and Re=25. All the data are in essentially exact agreement with the analytical solution. A check of the vertical span (x_1=0, $-0.5 \le x_2 \le 0.5$) shows the same level of agreement.

Equation (362) confirms that the constant axial pressure gradient is inversely proportional to the duct flow Reynolds number. Estimates for the pressure gradient were calculated at the mid-point of the channel, x_i=(1,0,0), for a range of Re with the pressure set to zero uniformly across the outflow plane. The computed gradients, Fig. 12, consistently underpredicted the analytical solution by an average of 6.8%. The pressure Dirichlet boundary was switched from the outflow plane to inflow plane, and a case was rerun for Re=75. No significant differences were observed in the solution. The grid was refined by increasing the number of cross-stream elements in the x_2- and x_3-coordinate directions to give a mesh of M=24×30×15, thus increasing the number of nodes to 12,400. Pressure gradients were calculated with the refined-mesh solution for Re=10, 25, 50, 75, and 100, with the pressure fixed across the outflow plane. The resulting nondimensional pressure gradients, calculated at the center of the channel using a central difference formula, are now in close agreement (approximately 0.1% error) with the analytical values, Fig. 12. For Re=100, the pressure distribution on cutting planes in the channel is presented in Fig. 13 as nine equally-spaced contour levels with a minimum contour of 0.06 and a maximum of 0.53. The analytical solution predicts a uniform pressure distribution for a constant x_1-plane. No significant span-wise pressure gradients were observed in the computed solution as indicated in Fig. 13. The distribution of the energy norm of the Φ constraint

Table 7. Boundary Conditions for Fully-Developed Channel Flow

	Velocity	Φ Potential Function	Pressure
3 walls	no-slip ($u_1=u_2=u_3=0$)	$\partial\Phi/\partial n=0$	nonhomogeneous Neumann
inflow	fully-developed profile using Eq. (357)	$\partial\Phi/\partial n=0$	nonhomogeneous Neumann
outflow	homogeneous Neumann	$\Phi=0$	$P=P_0$
symmetry	$u_1=0$ $\partial u_2/\partial n=\partial u_3/\partial n=0$	$\partial\Phi/\partial n=0$	nonhomogeneous Neumann

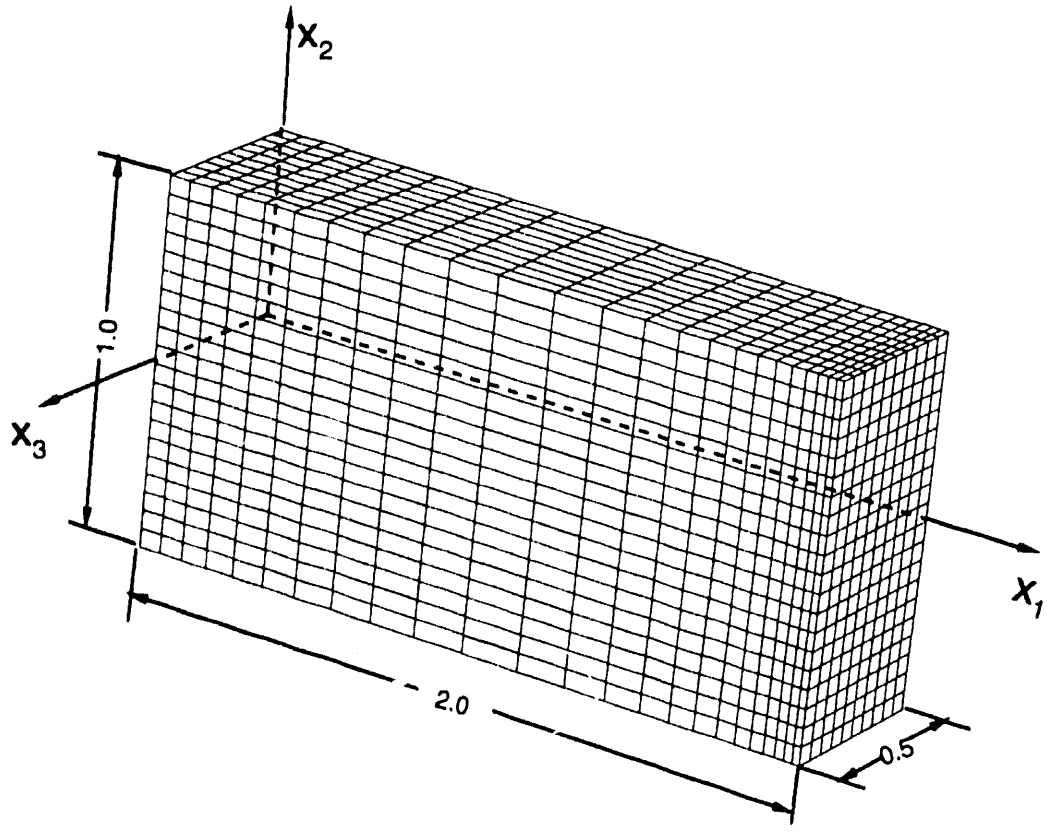

Figure 9. Fully-developed channel flow: mesh layout for $M=24\times20\times10$.

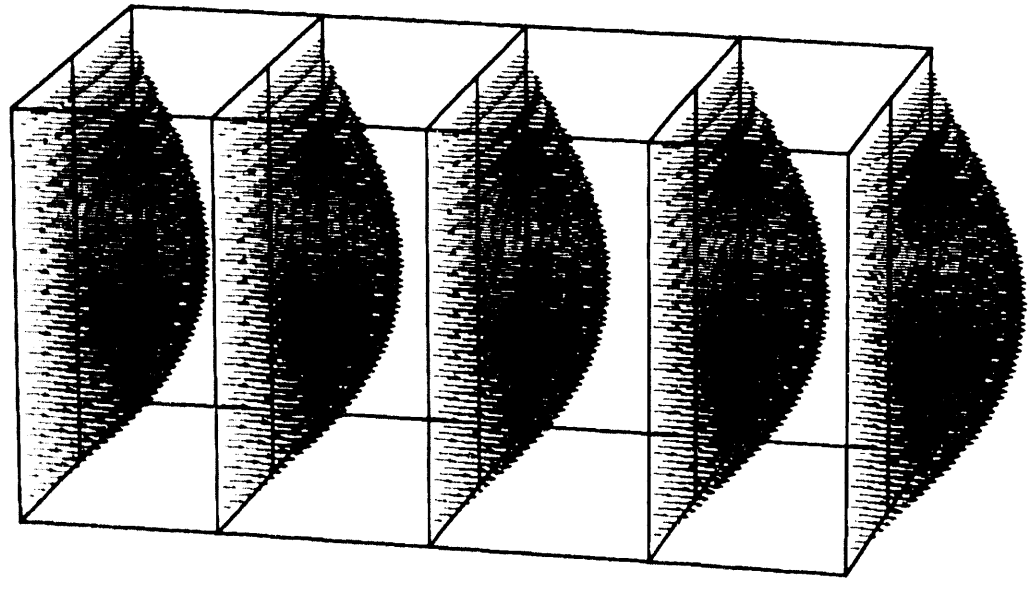

Figure 10. Fully-developed channel flow: velocity vector field at Re=100.

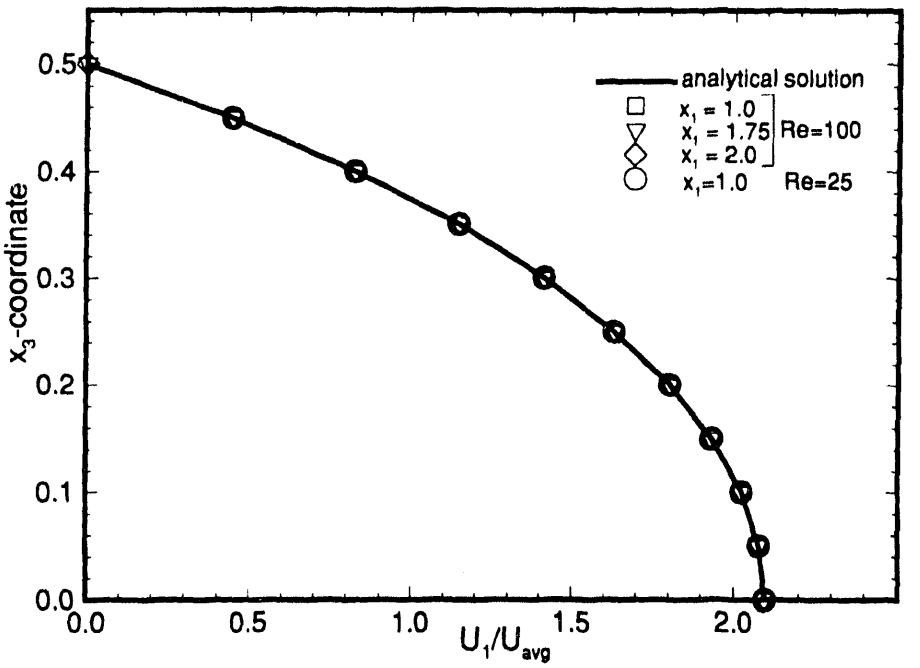

Figure 11. Fully-developed channel flow: spanwise velocity profiles at x_2=0.

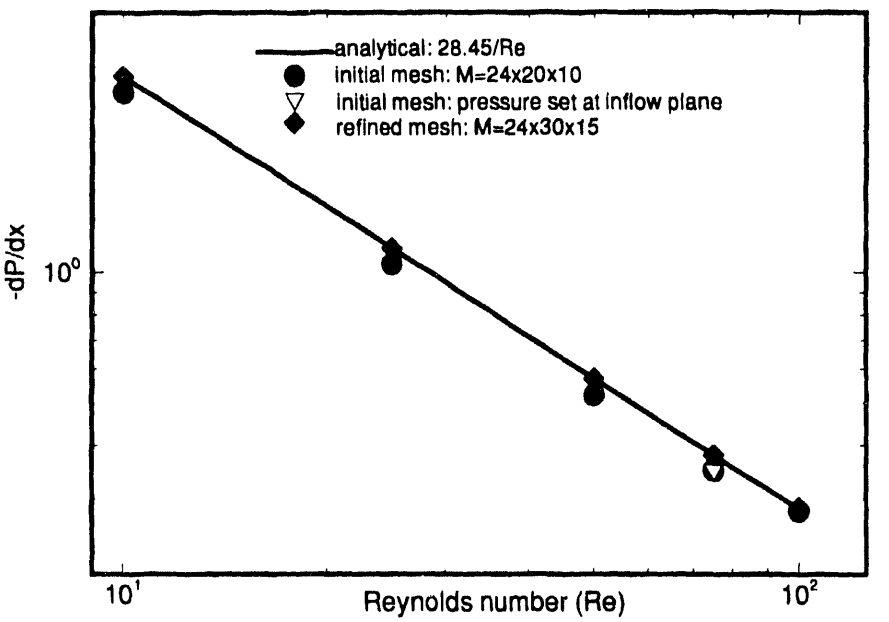

Figure 12. Fully-developed channel flow: pressure gradients v. Re.

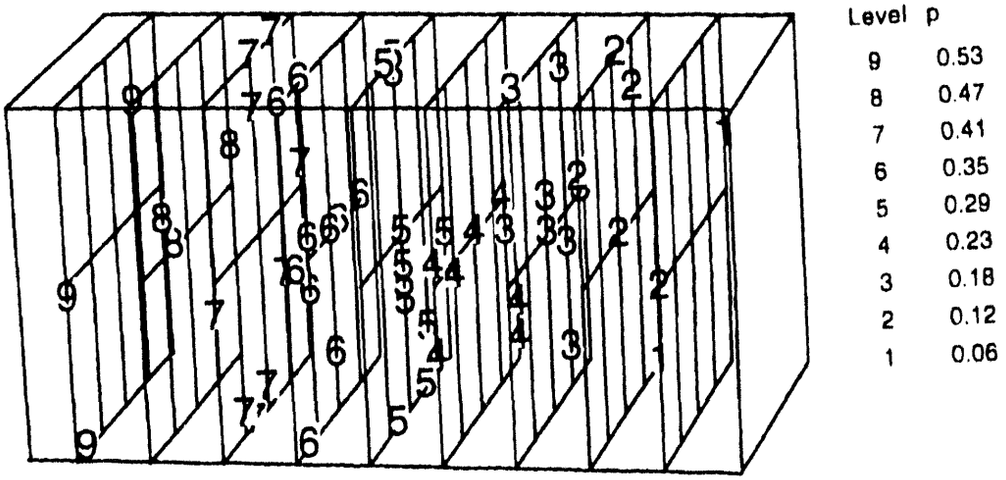

Figure 13. Fully-developed channel flow: pressure contours at Re=100.

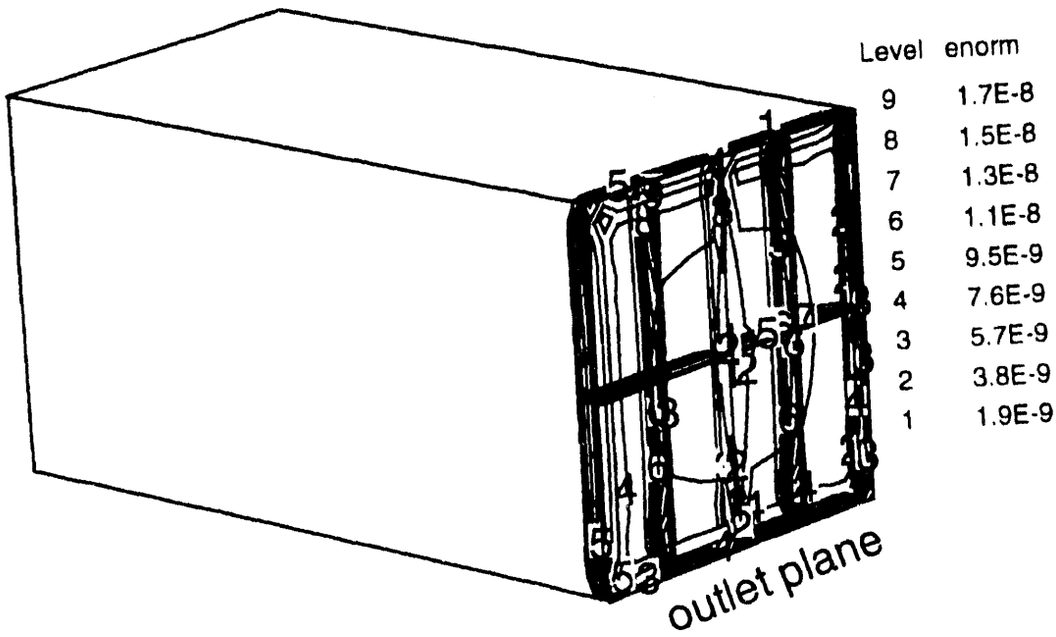

Figure 14. Fully-developed channel flow: $\|\Phi\|_E$ distribution at Re=100.

function is plotted in Fig. 14, where the nine equally-spaced contours have a minimum level of 1.9×10^{-9} and a maximum of 1.7×10^{-8}. The non-zero, but very small, divergence error exists at the outflow plane where the Dirichlet boundary condition is applied, as anticipated.

7.3 DEVELOPING FLOW IN A SQUARE DUCT

Developing flow in the entrance region of a straight rectangular cross-section duct has been the subject of extensive study. Han (1960) calculated analytical velocity profiles based upon boundary layer linearization approximations to the Navier-Stokes equations. For the duct axis aligned with the x_1-coordinate axis and the coordinate system origin located at the centroid of the duct entrance plane, Fig. 15, the analytical axial velocity profile is

$$u_1^* \equiv \frac{u_1}{u_{1\,avg}} = \frac{\pi^2}{4} \frac{\sum_{m,n=1,3,5}^{\infty} (-1)^{\frac{m+n}{2}-1} \frac{\cos(m\pi x_2/2a)\cos(n\pi x_3/2b)}{mn[m^2+n^2\gamma^2+(2\beta a/\pi)^2]}}{\sum_{m,n=1,3,5}^{\infty} [m^2n^2(m^2+n^2\gamma^2+(2\beta a/\pi)^2)]^{-1}} \tag{363}$$

where $\gamma=a/b$ is the duct aspect ratio, and β is a parameter evaluated via numerical integration as a function of x_1. Entrance lengths, defined as the axial distance from the duct entrance plane to the point at which the centerline velocity reaches 99% of the fully-developed value, are calculated by Han for

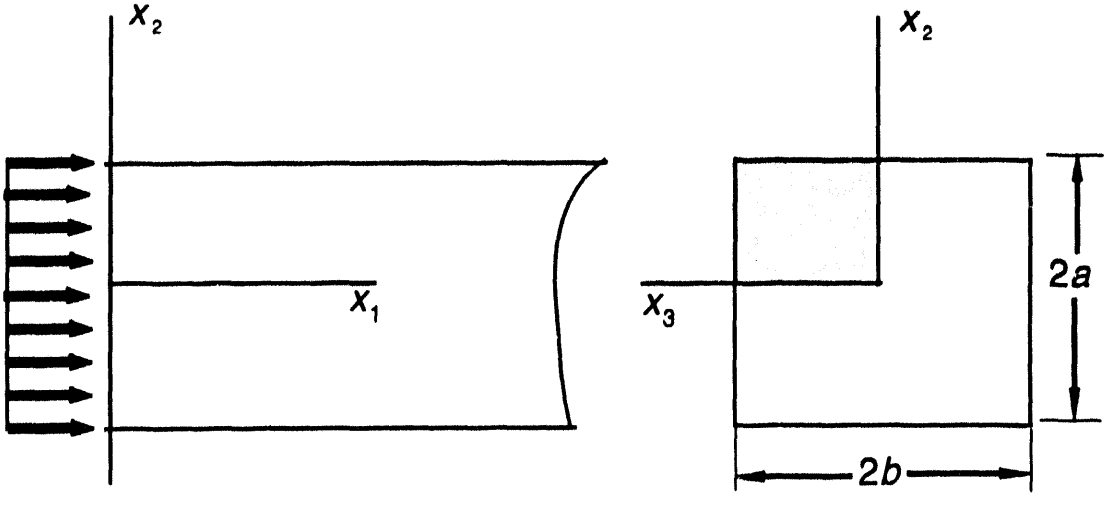

Figure 15. Developing flow at the entrance of a rectangular duct.

rectangular channels of six aspect ratios. For a given aspect ratio, the analysis shows that the entrance length, x_{fl}, when correlated by the dimensionless modulus $x_{fl}/(D_h \cdot \mathrm{Re})$, is independent of Re. The Reynolds number, Re, is evaluated using the area-weighted average flow velocity, u_{1_avg}, and the hydraulic diameter, D_h, of the duct. Han calculates a value of $x_{fl}/(D_h \cdot \mathrm{Re}) = 0.0752$ for a square duct.

Goldstein and Kreid (1967) present experimental data for developing laminar flow in a square duct obtained with a laser-Doppler anemometer. They compared their data to Han's predictions and found close agreement in the fully-developed region. In the developing region, Han's approximate analysis tended to overpredict the centerline velocities as compared to the measured velocities. Goldstein and Kreid measured a value of $x_{fl}/(D_h \cdot \mathrm{Re})$ of 0.090 for their square duct, but they noted that "the slope of the curve is very small when the center-line velocity approaches the fully developed value. Thus, when using the foregoing definition of x_{fl}, the difference between the measurement and prediction is perhaps magnified out of the true proportion."

Using a space-marching integration technique, Briley (1974) presents solutions to the parabolized Navier-Stokes equations for flow at the entrance to a rectangular straight duct for two aspect ratios and at Re=1000 and 1333. Comparisons between Briley's computed centerline velocity profiles and the experimental data of Goldstein and Kreid (1967) showed better agreement than did Han's results; however, the growth of the wall boundary layer near the inlet plane continued to be overpredicted.

Aregbesola and Burley (1977) used the vorticity, vector-scalar potential method to calculate approximate solutions for the full Navier-Stokes equations for developing flow in a square duct at Re=1, 50, and 100. Their calculated values for $x_{fl}/(D_h \cdot \mathrm{Re})$ are approximately constant at 0.086 for $\mathrm{Re} > 50$. Centerline velocity profiles at Re=50 are compared to the analytical results of Han (1960) and the computational results of Briley (1974). These solutions show better agreement with the available experimental data in the developing flow region than either of the two parabolized Navier-Stokes solutions. All three solutions converge to the fully-developed profile beyond the duct entrance length region.

Mizukami and Tsuchiya (1984) present solutions for entrance flow in a square duct at Re=20 using a finite element implementation of Chorin's projection method (Chorin, 1968). Finally, Yang and Camarero (1991) combine the vorticity and vector-scalar potential algorithm with a new rotated upwind difference scheme to solve the developing duct flow problem for Re=100, 400, and 800. Using an M=15×15×31 grid, their solutions show excellent agreement with the experimental data of Goldstein and Kreid (1967).

The laminar, isothermal flow near the entrance to a straight square duct of unit cross-sectional area was simulated with a quarter-duct model, 15 units in length and a=b=0.5. As depicted in Fig. 18, the mesh discretization is M=100×15×15 with 25,856 nodes and 22,500 elements. The mesh is graded slightly near the two solid-wall boundaries and the outflow plane. The boundary conditions are as given in Table 7, except there are now two symmetry planes, and the prescribed inflow velocity profile is slug flow, i.e., $u_1 = 1.03$, $u_2 = u_3 = 0$. The inlet u_1 velocities were set to 1.03 (except at the no-slip walls) to give an effective $u_{1\text{-}avg} \approx 1.0$ at the inlet. The velocity field was initialized with a slug-flow profile throughout the length of the duct.

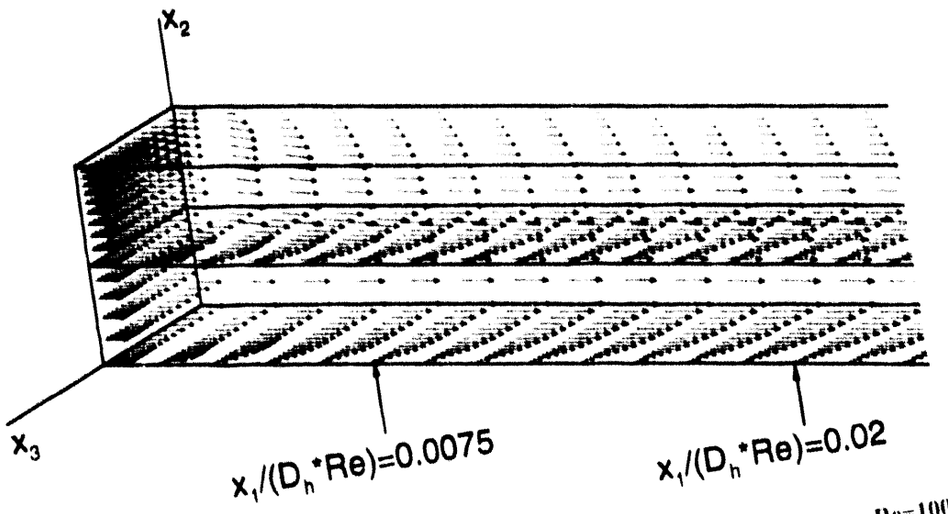

Figure 16. Developing flow in a channel: velocity vector field near entrance, Re=100.

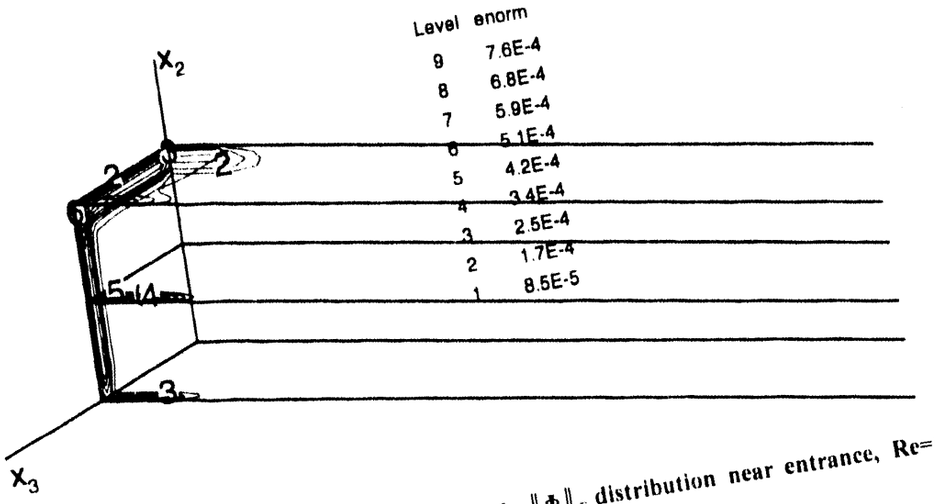

Figure 17. Developing flow in a square channel: $\|\Phi\|_E$ distribution near entrance, Re=100.

The steady-state velocity vector and $\|\Phi\|_e$ distributions for Re=100 are presented in Figs. 16 and 17 on selected cutting planes near the inflow plane. The computed centerline velocity at the outlet is 2.096, indicating the establishment of a fully-developed profile with negligible loss of mass (<0.01%). The essential steady-state solution was obtained after 250 time steps using a nondimensional time step of 0.01. The associated maximum local Courant number was approximately 0.7. The distribution of the energy norm of the continuity constraint function Φ is shown in Fig. 17 for 9 equally-spaced contours with minimum 8.5×10^{-5} and maximum 7.6×10^{-4}. The maximum divergence error level is now located near the inflow plane, which is surrounded by homogeneous Neumann boundary conditions. The constraint algorithm is attempting to enforce conservation of mass between the inflow plane and the first plane of interior nodes, but the Dirichlet data for u_1, u_2, and u_3 across the inlet plane do not provide any solution-adjustable degrees-of-freedom, hence the localized continuity error is a maximum (as expected).

The distribution of the axial centerline u_1 velocity is plotted in Fig. 19 as a function of x_1/Re. Near the entrance plane, the selected inflow boundary condition (with data designated as the *base case*) appears to retard the growth of the wall boundary layers near the inlet plane (x_1=0), as compared to the analytical results of Han (1960) and the experimental data of Goldstein and Kreid (1967). Aregbesola and Burley (1977) also underpredicted the experimental data in this region, and they commented that "in experimental work it is difficult to reproduce the sharply singular inlet profiles used in the theoretical calculations so that comparisons very close to the inlet are not particularly reliable." Near x_1/Re=0.05, the solutions of Briley (1974), Aregbesola and Burley (1977), and the present study converge to the analytical solution of Han (1960), which slightly overpredicts the experimental data until the fully-developed region is attained. For a second experiment, the mesh was refined in the axial direction by reducing the length of the model from 15 units to 10 units, while keeping the same number of nodes. The results for mesh 2 showed no significant difference compared to the base case. Spanwise u_1 velocity profiles at three x_1 stations are plotted in Fig. 20, and the locations of the first two x_1 stations (x_1*/Re=0.0075 and 0.02) are noted in Fig. 16. Except near the entrance plane at x_1*/Re=0.0075, the present base case results show good agreement with the experimental data. The results for the refined mesh solution are not significantly different from the base case.

These data prompted design of a refined CFD experiment to improve the simulation near the inlet plane. The slug profile specification across the inlet plane requires all three velocity components fixed as Dirichlet data. As was the case with the fully-developed channel flow problem, the algorithm will attempt to satisfy the continuity constraint; however, these Dirichlet boundary data do not provide required solution-adjustable degrees-of-freedom between the inlet plane and the first plane of interior nodes. The result is a localized error in the divergence-free requirement for the velocity flow field. To assess a correction for this problem, the inlet of the channel was extended upstream 0.25 units, with free-slip velocity boundary conditions applied on all walls and the symmetry planes. Then, Dirichlet data across the inlet plane of the inviscid entrance region provides a strict slug-flow profile (i.e., u_1=1.0, u_2=u_3=0), and Neumann boundary conditions for the pressure and continuity constraint function, Φ, remain appropriate.

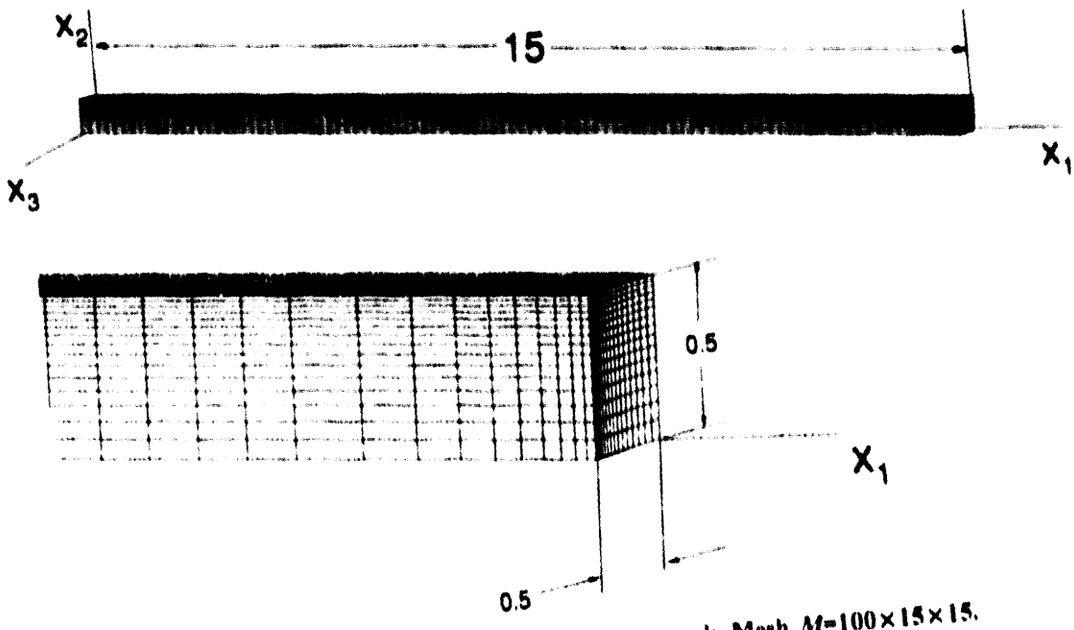

Figure 18. Developing flow in a square channel: Mesh M=100×15×15.

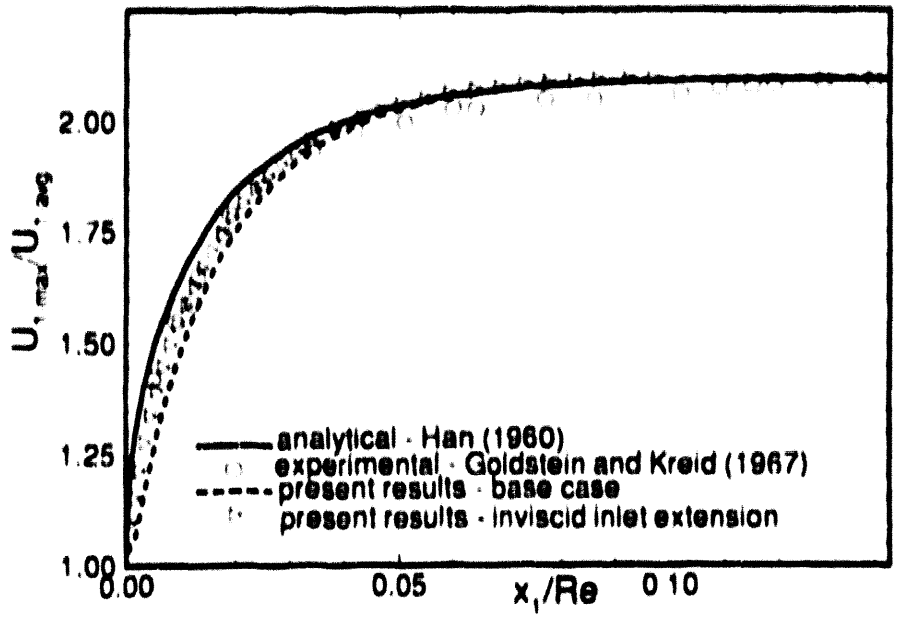

Figure 19. Developing flow in a square channel: centerline u_1 profiles, Re=100.

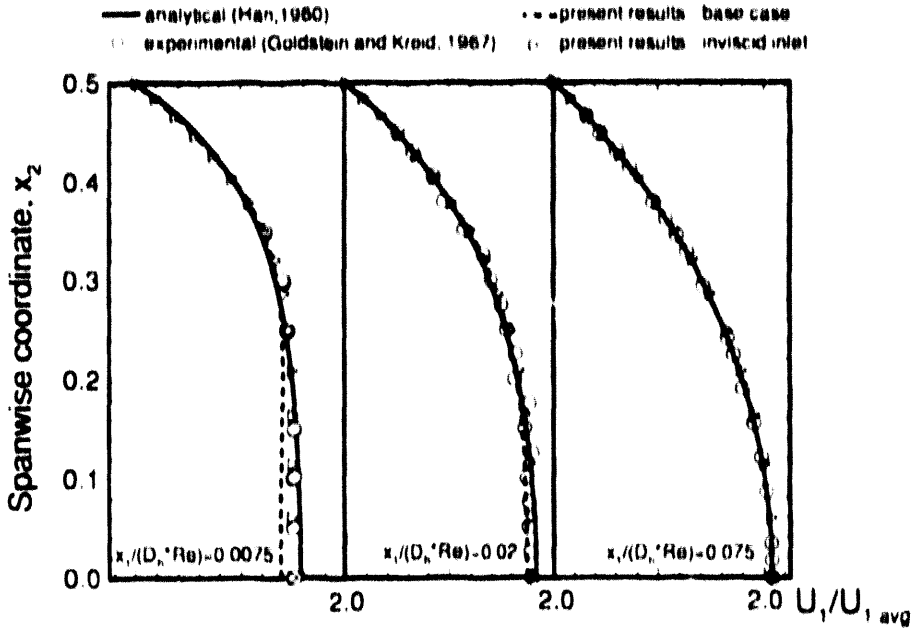

Figure 20. Developing flow in a square channel: spanwise u_1 profiles, Re=100.

The problem specification was run now with zero velocity data at all interior nodes as the initial condition. The results for Re=100 with this *inviscid inlet extension* are given in Figs. 19 and 20. The modified inlet boundary condition resulted in significant improvement in the agreement with the experimental data of Goldstein and Kreid (1967). The entrance lengths reported by Han (1960), Goldstein and Kreid (1967), and Aregbesola and Burley (1977) are compared with the base case and inviscid inlet present results in Table 8. The distribution of the energy norm of the continuity constraint function Φ decreased to a minimum of 9.2×10^{-7} and a maximum of 9.2×10^{-6} near the new inlet plane.

Table 8. Entrance Lengths for Developing Flow in a Square Duct

Source	x^*_{fd}/Re
Han (1960)	0.075
Goldstein and Kreid (1967)	0.090
Aregbesola and Burley (1977)	0.086
present results: base case	0.072
present results: inviscid inlet	0.078

7.4 NATURAL CONVECTION IN AN ENCLOSED CAVITY

Buoyancy-driven flow, resulting from natural convection in an enclosed cavity, represents a suitable benchmark for incompressible CFD codes. This problem also has many practical applications including nuclear reactor insulation, energy conservation, ventilation of rooms, solar energy collection, cooling of electronic equipment, dispersion of waste heat in estuaries, and crystal growth in liquids.

For many years, research on natural convection in enclosures has concentrated on two basic modes of convection, specifically flows induced by a density gradient oriented either normal or parallel to the body-force vector (Ostrach, 1982). If the density gradient is normal to the body force, the flow starts immediately; however, if the gradient is aligned with the body force, then no flow starts until a critical value of the density gradient is exceeded (e.g., Bénard convection). The two modes can occur simultaneously as in the case of tilted enclosures. Density gradients can result from temperature gradients, species-concentration gradients, or a combination of both.

A number of experimental studies have been carried out for natural convection in enclosures. The early investigations focused on collecting quantitative heat transfer data with only limited qualitative observations of flow field structures. An excellent review of the experimental work done in this area up to 1965 is given by Elder (1965). The heat transfer data were used to develop correlations for the Nusselt number, Nu, as a function of the Grashof number, Gr, and nondimensional parameters related to the enclosure geometry. Among the earliest of such correlations is due to Jakob

(1949), based upon his analysis of the experimental data of Mull and Reiher (1930). Much of the experimental work since then (e.g., Eckert and Carlson, 1961) has been concerned primarily with improving and extending the range of these heat transfer correlations.

Only limited experimental data are available for validation of computer codes. The first detailed velocity measurements of natural convection in enclosures were reported by Elder (1965) who used medicinal paraffin and silicone oil as the working fluids. Streak-line photographs were used to measure velocities for Rayleigh numbers up to 10^5, with cavity height-to-width ratios from 1 to 60 and Prandtl numbers from 1100 to 2600. Vertical velocity profiles, obtained in the central core of the cavities, were not symmetrical about the center line. Higher velocities and smaller wall-layer thicknesses were observed in the flow field near the hot wall. The theoretical study by Gill (1966) concurred with Elder's results that for given Rayleigh and Prandtl numbers the core streamfunction and temperature depended only on the vertical coordinate. Using laser-Doppler anemometry, Morrison and Tran (1978) investigated 3-dimensional laminar flow structures in a vertical rectangular cavity with a height-to-width ratio of 5. Velocity profiles were measured at a Rayleigh number of $5 \cdot 10^4$, and the effect of end-wall conduction on the flow structure was studied by varying the degree of insulation applied to the unheated walls. Morrison and Tran show that heat loss through the vertical end-walls is a major factor in the breakdown of 2-dimensional flow. Cheesewright et al. (1986) present experimental turbulent velocity data for natural convection in a cavity with a height-to-width ratio of 5. The Rayleigh number of approximately 10^{10} is based upon the cavity height. All of the experimental cases reported by Cheesewright et al. show evidence of 3-dimensional effects. Accordingly, they present a correction method to make the data suitable for validation of 2-dimensional computer codes.

Early computational studies of natural convection in cavities include the work of Wilkes and Churchill (1966), Elder (1966), Aziz and Hellums (1967), and Newell and Schmidt (1970). With the exception of Aziz and Hellums, these investigations were concerned primarily with predicting heat transfer rates. Aziz and Hellums were the first to attempt a 3-dimensional solution; although, the limited computing capacity available in 1967 restricted simulations to very coarse meshes (M 11 · 11 · 11), so few details of the 3-dimensional flow structure could be determined. Recent notable numerical studies of turbulent flows in 2-dimensional cavities are reported by Fraikin et al. (1982), Markatos and Pericleous (1984), and Thompson et al. (1987).

7.4.1 Two-Dimensional Natural Convection Cavity Benchmark

Since quality laminar experimental data for the validation of computer codes has yet to be obtained, benchmarking (i.e., code-to-code comparisons) is at present the most widely used method for testing computer codes for natural convection flows in enclosures. A 2-dimensional benchmark problem for this purpose was suggested by Jones (1979), and the commonly accepted benchmark solution was published by de Vahl Davis (1983). The problem, referred to as the "double-glazing" problem, is that of 2-dimensional flow of an incompressible fluid of Prandtl number 0.71 in an upright square cavity of side L. The buoyancy body force is modeled by the Boussinesq approximation. The upper and lower horizontal walls are adiabatic, and the vertical sidewalls are set at the constant uniform temperatures T_{hot} and T_{cold}. The velocity boundary condition is no-slip on the four walls. Solutions for this problem, including velocity and temperature distributions and rates of heat transfer, are presented by de Vahl Davis for Rayleigh numbers of 10^3, 10^4, 10^5, and 10^6. The vorticity/streamfunction formulation was used with a finite-difference implementation to obtain solutions on uniform meshes from M 11 · 11 to 41 · 41 for Rayleigh numbers of 10^3 and 10^4; at the

higher Rayleigh values, finer meshes up to 81×81 were required. The results from several meshes were then applied with a Richardson extrapolation scheme to produce the benchmark solution.

A number of dimensionless accuracy measures are reported by de Vahl Davis to provide a means for quantitative comparisons between computer solutions. Of the original nine, the first two measures involved the streamfunction which is not computed by CFDL.PHI3D. The remaining seven are defined as follows:

$u_{1,max}$	the maximum horizontal (dimensionless) velocity component on the vertical mid-plane of the cavity (together with its location on the x_2 coordinate);
$u_{2,max}$	the maximum vertical (dimensionless) velocity component on the horizontal mid-plane of the cavity (together with its location on the x_1 coordinate);
Nu_{avg}	the average Nusselt number throughout the cavity;
Nu_{x_2}	the average Nusselt number on the vertical mid-plane of the cavity;
Nu_{0}	the average Nusselt number on the vertical boundary ($x_1 = 0$) of the cavity;
Nu_{max}	the maximum value of the local Nusselt number on the vertical boundary ($x_1 = 0$) of the cavity (together with its location on the x_2 coordinate);
Nu_{min}	the minimum value of the local Nusselt number on the vertical boundary ($x_1 = 0$) of the cavity (together with its location on the x_2 coordinate);

The velocity components are nondimensionalized via a reference velocity scale which is not uniquely available for this problem. Since the domain is fully confined (i.e. no inlets or outlets), the selection of a suitable velocity scale is somewhat problematic. de Vahl Davis chose the *thermal diffusion velocity*, α/L, as a reference velocity, where α ($=k/\rho c_p$) is the thermal diffusivity. Ostrach (1982) reviews several velocity scales that have appeared in the literature for natural convection flows and comments on the implied flow and heat transfer conditions for which these velocity scales are appropriate. The *thermal diffusion velocity* implies a balance between convection and conduction in the energy equation. The *viscous diffusion velocity*, ν/L, implies that the inertial and viscous terms in the momentum equations are of the same order of magnitude. A *hybrid velocity scale*, $(\alpha\nu)^{1/2}/L$, has also been used; however, no physical implications are clear. The velocity scale, $\beta g \Delta T L^2/\nu$, implies that buoyancy and viscous forces are of equal magnitude and is generally appropriate only for small values of Grashof (Gr) and Rayleigh (Ra) numbers (i.e., $Gr < 1$ and $Ra < 1$). Ostrach demonstrates how improper selection of the reference velocity for problems involving natural convection in enclosures can be the cause of considerable numerical problems and errors. Such problems can be avoided, he notes, by properly normalizing the governing partial differential equations with the goal of making the state-variables not only nondimensional but also of *unit order of magnitude*.

The present study developed a velocity scale related to the intensity of the buoyant motion as described by the free-fall velocity of a thermal (Gray and Giorgini, 1976). This velocity scale is derived by assuming the kinetic energy of the buoyancy-induced flow is balanced by the work done by the buoyancy force (as represented by the Bousinnesq approximation) acting over the reference length scale, hence,

$$\frac{\rho U_{ref}^2}{2g_c} = F_{buoy} \cdot L_{ref} \propto \frac{\rho g \beta \Delta T_{ref} L_{ref}}{g_c} \tag{364}$$

The *free-fall velocity* is, therefore, proportional to $(g \beta \Delta T_{ref} L_{ref})^{1/2}$, as

$$U_{ref} = \frac{1}{C} (g \beta L_{ref} \Delta T_{ref})^{1/2} \tag{365}$$

where C' is a problem-dependent constant that can be adjusted to reduce computational conditioning, e.g., round-off problems. One consequence of Eq. (365) is that the square root of the Grashof number assumes the role of the Reynolds number in the scaling of the Navier-Stokes equations (Jaluria, 1980, and Gebhart et al., 1988), i.e.,

$$\mathrm{Re} = \frac{U_{ref} L_{ref}}{\nu} = \frac{1}{C} (g \beta \Delta T_{ref} L_{ref})^{1/2} \frac{L_{ref}}{\nu} = \frac{1}{C} \left(\frac{g \beta \Delta T_{ref} L_{ref}^3}{\nu^2} \right)^{1/2} = \frac{(\mathrm{Gr})^{1/2}}{C} \tag{366}$$

The Archimedes number, Ar, becomes

$$\mathrm{Ar} = \frac{\mathrm{Gr}}{\mathrm{Re}^2} = C^2 \frac{\mathrm{Gr}}{\mathrm{Gr}} = C^2 \tag{367}$$

thus giving some physical guidance for the selection of an appropriate value for C'. For the thermal-driven cavity solutions developed in the present study and following numerical experimentation, C'=1 was determined to minimize computational ill-conditioning problems over the Rayleigh number range for the benchmark. With the nondimensionalization of the conservation law system described in Chapter 2, the selection of C' provides a measure of control over the scaling of the diffusion terms in the momentum and energy equations (thus affecting computational stability) through the Reynolds and Peclet numbers. For C'=1, Ar=1, and the Reynolds (Re) and Peclet (Pe) numbers are

$$\begin{aligned} \mathrm{Re} &= \left(\frac{\mathrm{Gr}}{C} \right)^{1/2} = \{ (\mathrm{Ra}/\mathrm{Pr})^{1/2} \}_{C=1} \\ \mathrm{Pe} &= \mathrm{Re}\ \mathrm{Pr} = \left(\frac{\mathrm{Gr}}{C} \right)^{1/2} \mathrm{Pr} = \{ (\mathrm{Ra}\ \mathrm{Pr})^{1/2} \}_{C=1} \end{aligned} \tag{368}$$

In a post-processing operation, the nondimensional velocities computed by CFDL.PHI3D are multiplied by $(\mathrm{Ra}\ \mathrm{Pr}/\ \mathrm{Ar})^{1/2}$ for comparison to the benchmark solution of de Vahl Davis.

The benchmark Nusselt number is defined as the x_1- or horizontal component of the dimensionless local heat flux vector (de Vahl Davis, 1983).

$$\mathrm{Nu}(x_1^*, x_2^*) = u_1^* \Theta - \frac{\partial \Theta}{\partial x_1^*} \tag{369}$$

where

$$\Theta(x_1, x_2) = \frac{(T(x_1, x_2) - T_{cold})}{(T_{hot} - T_{cold})} \quad ; \quad u_1^* = \frac{u_1(x_1, x_2)}{L_{ref}} \quad ; \quad x_1^* = \frac{x_1}{L_{ref}} \quad ; \quad L_{ref} = L \tag{370}$$

Except for the vertical sidewalls, the local first derivative of the potential temperature with respect to x_1^* is approximated in the present results by a three-point second-order central-difference formula (Hoffmann, 1989).

$$\left.\frac{\partial \Theta}{\partial x_1^*}\right|_{(x_1, x_2)} = \frac{\Theta_{i+1} + (\gamma^2 - 1)\Theta_i - \gamma^2 \Theta_{i-1}}{\gamma(\gamma + 1)(\Delta x_i)} + O(\Delta x)^2$$

$$\gamma = \frac{\Delta x_{i+1}}{\Delta x_i} \quad ; \quad \Delta x_i = (x_1^*)_i - (x_1^*)_{i-1} \tag{371}$$

where i is a node-column index. Dimensionless temperature gradients at the vertical sidewalls were calculated using a two-point first-order difference ratio. The five benchmark Nusselt numbers are defined as

$$\mathrm{Nu}_0 = \int_0^1 \mathrm{Nu}(0, x_2^*)\, dx_2^*$$

$$\mathrm{Nu}_{1/2} = \int_0^1 \mathrm{Nu}(1/2, x_2^*)\, dx_2^*$$

$$\mathrm{Nu}_{avg} = \int_0^1 \int_0^1 \mathrm{Nu}(x_1^*, x_2^*)\, dx_2^*\, dx_1^* \tag{372}$$

$$\mathrm{Nu}_{max} = \max_{0 \le x_2^* \le 1} (\mathrm{Nu}(0, x_2^*))$$

$$\mathrm{Nu}_{min} = \min_{0 \le x_2^* \le 1} (\mathrm{Nu}(0, x_2^*))$$

For the present study, the integrations required for evaluating Nu_0, $\mathrm{Nu}_{1/2}$, and Nu_{avg} are calculated numerically using the trapezoidal rule.

Table 9 presents a comparison of the seven benchmark parameters as calculated by de Vahl Davis (1983), Upson et al. (1980), Markatos and Pericleous (1984), and the present study, for Ra = 10^3, 10^4, 10^5, and 10^6. Figure 21 gives a comparison of the solutions for four accuracy measures

in terms of their percent deviation from the benchmark solution by de Vahl Davis (1983). The agreement among the solutions is generally good. The most significant disagreement occurs in the values for Nu_{min} and Nu_{max}. Markatos and Pericleous found these accuracy measures to be very sensitive to small differences in the temperature solution.

Upson et al. solved the benchmark problem using a finite-element penalty method code, implemented with 9-node biquadratic elements for u_i and Θ and a bilinear discontinuous approximation for pressure P. They chose the *free-fall velocity*, $(g\,\beta\,\Delta T_{ref}\,L_{ref})^{1/2}$ with $C = 1$, as their reference velocity scale because "it results in dimensionless velocities and pressures that are of order unity, and secondly, it allows simulation at larger Ra since the penalty method is more accurate in this form ... " (Upson et al., 1980). The nonuniform finite-element mesh consisted of 745 nodes and 168 isoparametric elements with refinement near the walls and in the four corners. The reported Nusselt numbers were calculated using the "consistent flux method" which gives an integral relation for the heat flux distribution at the boundaries. The two Nusselt numbers that require interior heat flux data, $Nu_{1/2}$ and Nu_{avg}, are not reported by Upson et al.

Markatos and Pericleous (1984) employ the finite-volume algorithm SIMPLEST (Patankar, 1980) with a nonuniform M=40×40 mesh. Three- and five-point finite-difference formulae are used to resolve the temperature gradients required for the Nusselt number calculations. For Ra up to 10^6, solutions were obtained using "normalized variables, in such a way that dimensionless velocities were of the order of unity, in order to improve the accuracy of the results." The specific velocity scale is not reported.

For the present results, an M=32×32 nonuniform mesh, shown in Fig. 22a, was used for solutions at Ra = 10^3, 10^4, and 10^5, and an M=80×80 mesh, in Fig. 22b, was used for Ra = 10^6. At each Rayleigh number, the solution was run for approximately 1000 time steps. The benchmark variables were then calculated, and the solution restarted and run an additional 500 time steps. If the benchmark measures remained stationary to three significant figures, then the solution was accepted as converged. This solution was then used as the initial condition for the next higher Rayleigh number execution.

The results of de Vahl Davis (1983) and the present solutions are summarized as contour plots of streamline, temperature, and the u_1 and u_2 velocity components in Figs. 23-30, respectively. Qualitative agreement with the companion plots presented in the de Vahl Davis's benchmark solution is good. The contour values for each plot are presented using a common format, i.e., *cmin* (*interval*) *cmax*, where *cmin* and *cmax* are the minimum and maximum contours and *interval* is the interval between each contour line. As noted by Upson et al. (1980), the flow fields are similar at Ra = 10^3 and 10^4, with a primary vortex roll completely filling the domain. Significant vertical temperature stratification in the central core has already developed, however, by Ra = 10^4. Secondary vortex rolls, embedded in the primary roll, appear by Ra = 10^5, and definite thermal boundary layers are evident along the vertical walls. These secondary rolls do not result from an instability of the base flow but are caused by the flow-induced distortion of the temperature field (Mallinson and de Vahl Davis, 1977). As the Rayleigh number increases to 10^6, the secondary rolls strengthen and become distorted in shape, and their centers move closer to the vertical walls. There is also evidence of a weak tertiary vortex roll, rotating in the same direction as the base flow, developing in the central core.

Table 9. Benchmark Measures for 2D Natural Convection of Air in a Square Cavity

	Ra=10^3				Ra=10^4			
	(1)*	(2)	(3)	(4)	(1)	(2)	(3)	(4)
$u_{1\text{-}max}$	3.649	3.656	3.544	3.668	16.18	16.19	16.18	16.26
at x_2	0.813	0.812	0.832	0.811	0.823	0.822	0.832	0.841
$u_{2\text{-}max}$	3.697	3.704	3.593	3.709	19.62	19.68	19.44	20.22
at x_1	0.178	0.166	0.168	0.189	0.119	0.119	0.113	0.107
Nu_{avg}	1.118	–	1.108	1.111	2.243	–	2.201	2.212
$Nu_{1/2}$	1.118	–	–	1.124	2.243	–	–	2.205
Nu_0	1.117	1.118	–	1.117	2.238	2.245	–	2.221
Nu_{max}	1.505	1.506	1.496	1.507	3.528	3.535	3.482	3.460
at x_2	0.092	0.075	0.082	0.107	0.143	0.132	0.142	0.159
Nu_{min}	0.692	0.691	0.720	0.685	0.586	0.585	0.643	0.511
at x_2	1	1	0.992	0.954	1	1	0.992	0.971

	Ra=10^5				Ra=10^6			
	(1)	(2)	(3)	(4)	(1)	(2)	(3)	(5)
$u_{1\text{-}max}$	34.73	34.62	35.73	31.72	64.63	64.59	68.81	61.84
at x_2	0.855	0.856	0.857	0.868	0.850	0.850	0.872	0.841
$u_{2\text{-}max}$	68.59	68.90	69.08	70.82	219.4	220.6	221.8	225.7
at x_1	0.066	0.066	0.067	0.064	0.037	0.032	0.038	0.040
Nu_{avg}	4.519	–	4.430	4.454	8.800	–	8.754	8.802
$Nu_{1/2}$	4.519	–	–	4.496	8.799	–	–	8.750
Nu_0	4.509	4.521	–	4.482	8.817	8.817	–	8.863
Nu_{max}	7.717	7.731	7.626	7.510	17.92	17.29	17.87	17.08
at x_2	0.081	0.075	0.082	0.107	0.038	0.045	0.038	0.052
Nu_{min}	0.729	0.728	0.824	0.279	0.989	0.980	1.232	0.115
at x_2	1	1	0.992	0.954	1	1	0.992	0.966

***Solution Source Key**

(1) de Vahl Davis (1983)

(2) Upson et al. (1980)

(3) Markatos and Pericleous (1984)

(4) Present results M=32×32

(5) Present results M=80×80

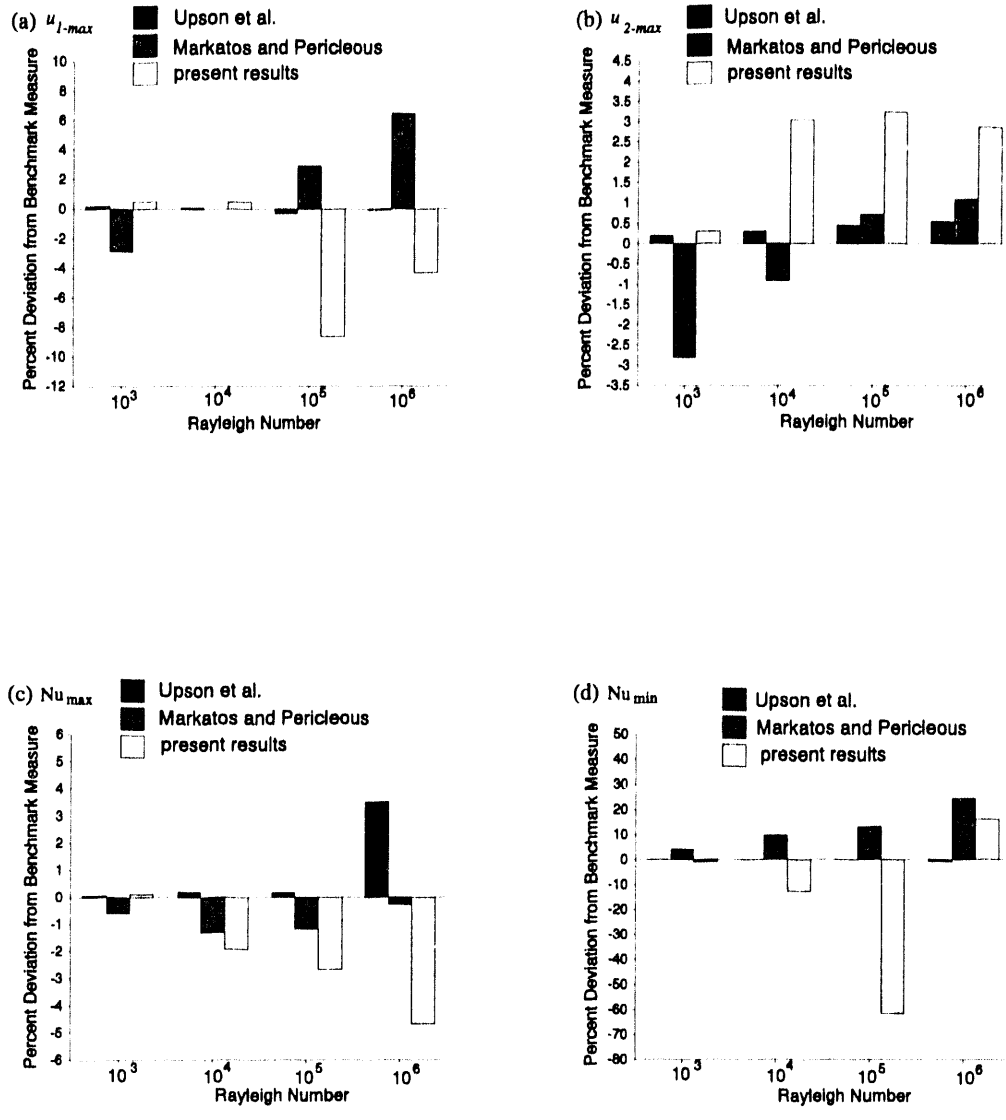

Figure 21. Comparisons to deVahl Davis (1983) benchmark for four accuracy measures.

(a) M=32x32

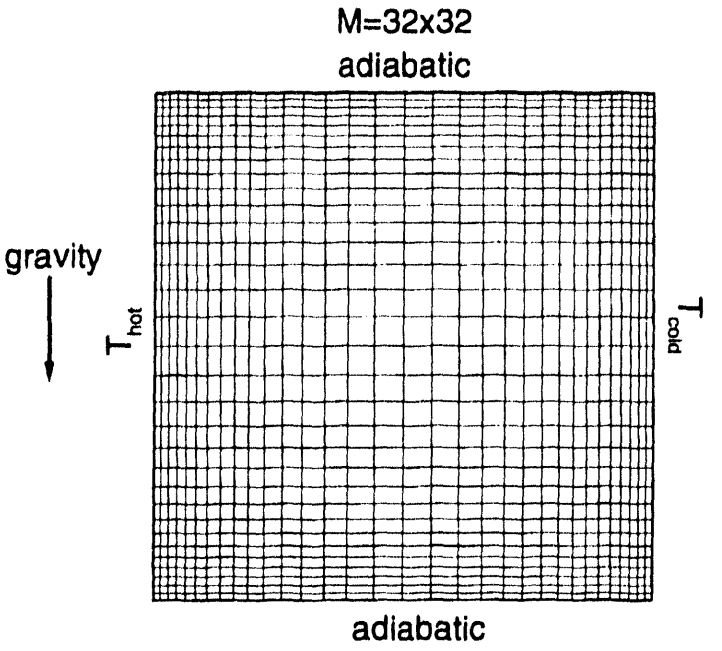

(b) M=80x80

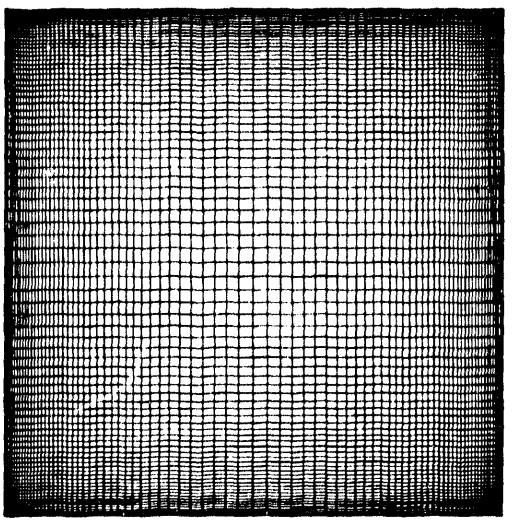

Figure 22. Natural convection in a cavity.

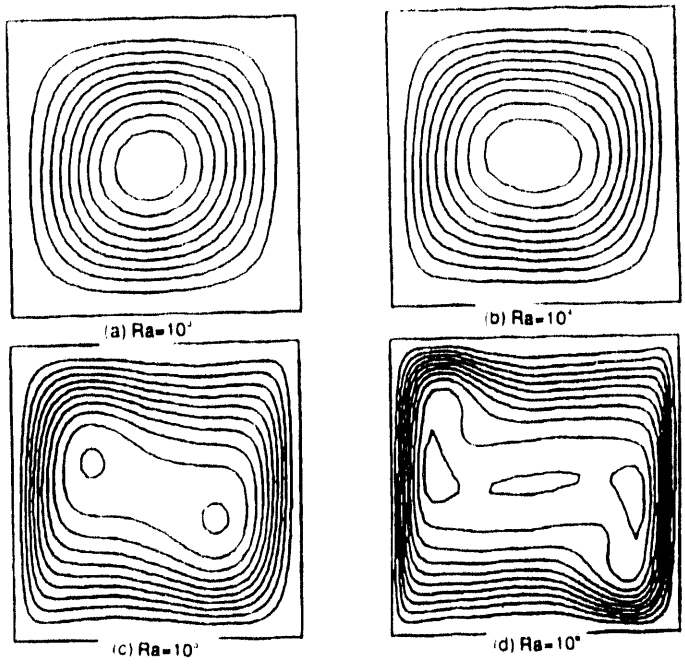

Figure 23. Contour maps of streamfunction, de Vahl Davis (1983).

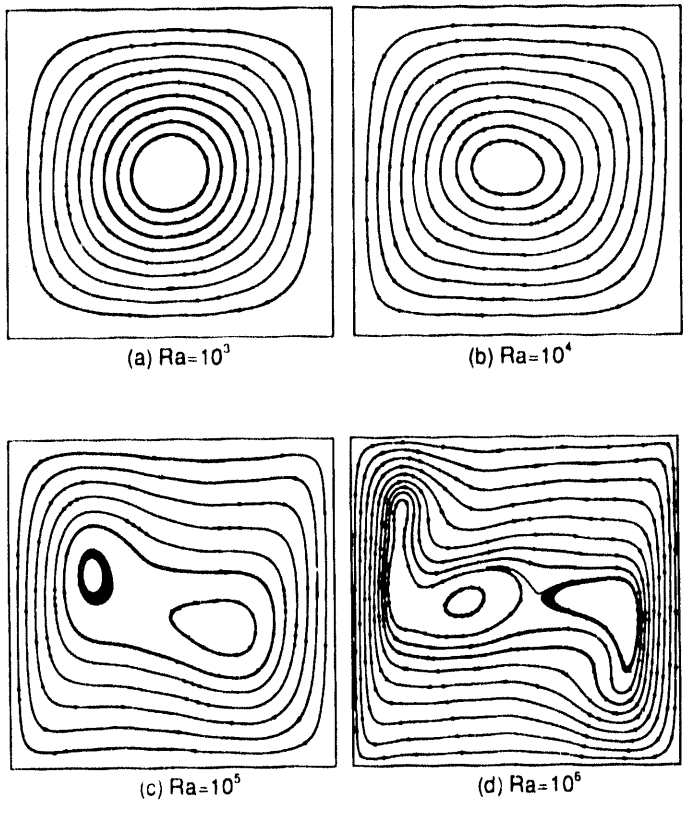

Figure 24. Streamlines computed by TECPLOT, present data.

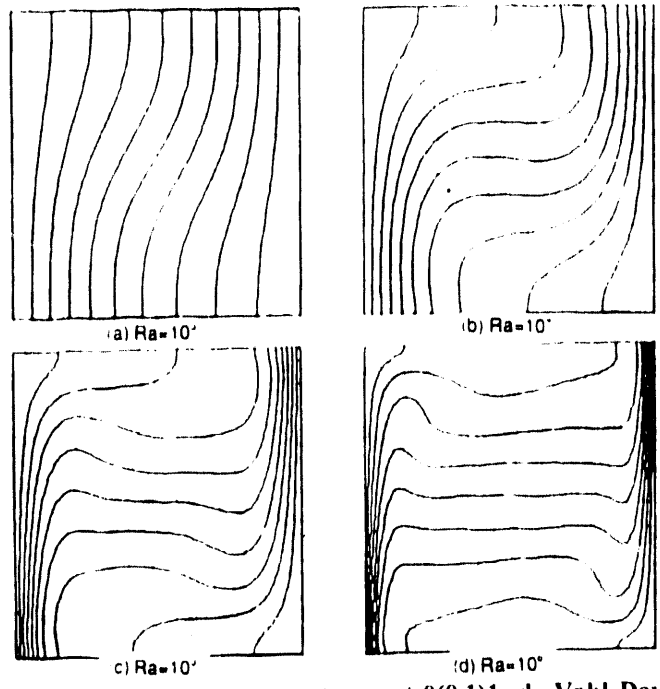

Figure 25. Temperature contours at 0(0.1)1, de Vahl Davis (1983).

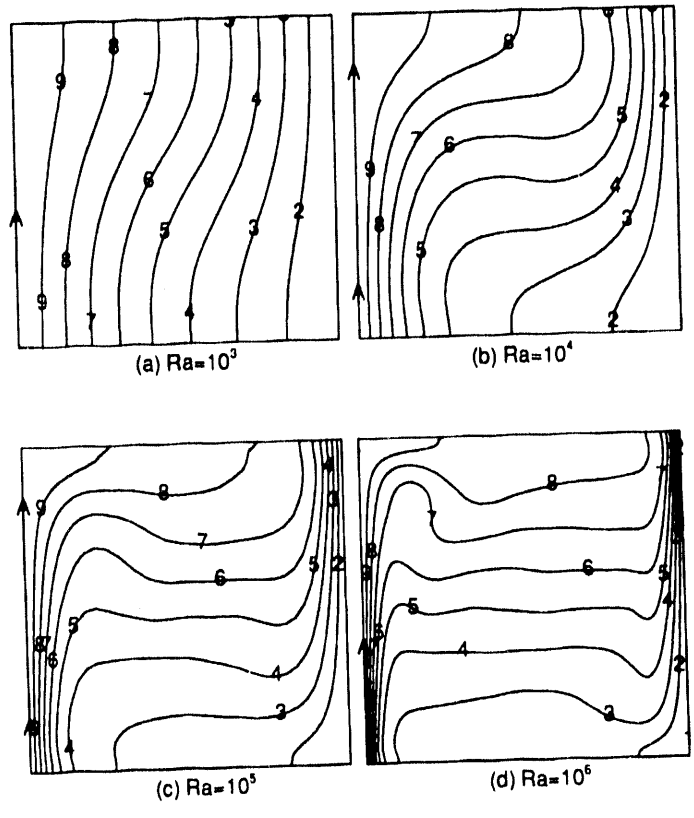

Figure 26. Temperature contours at 0(0.1)1, present data.

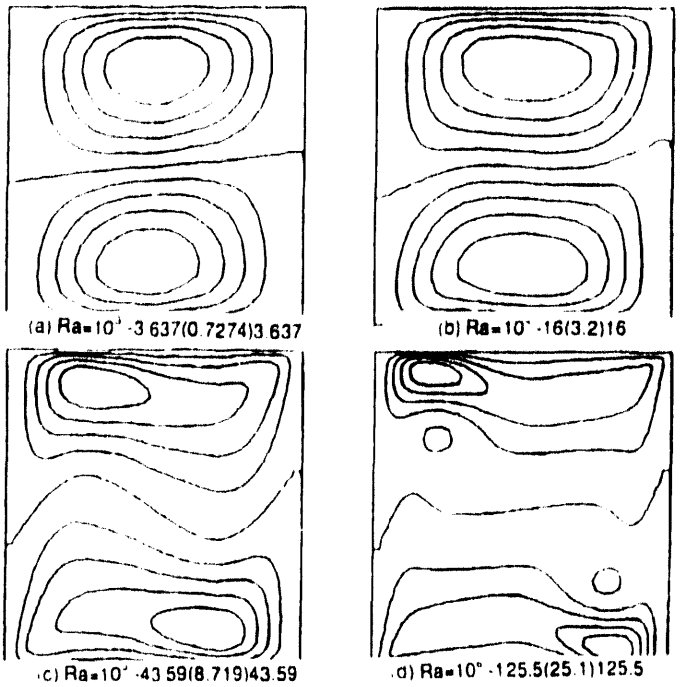

Figure 27. Contour horizontal u_i velocity component, de Vahl Davis (1983).

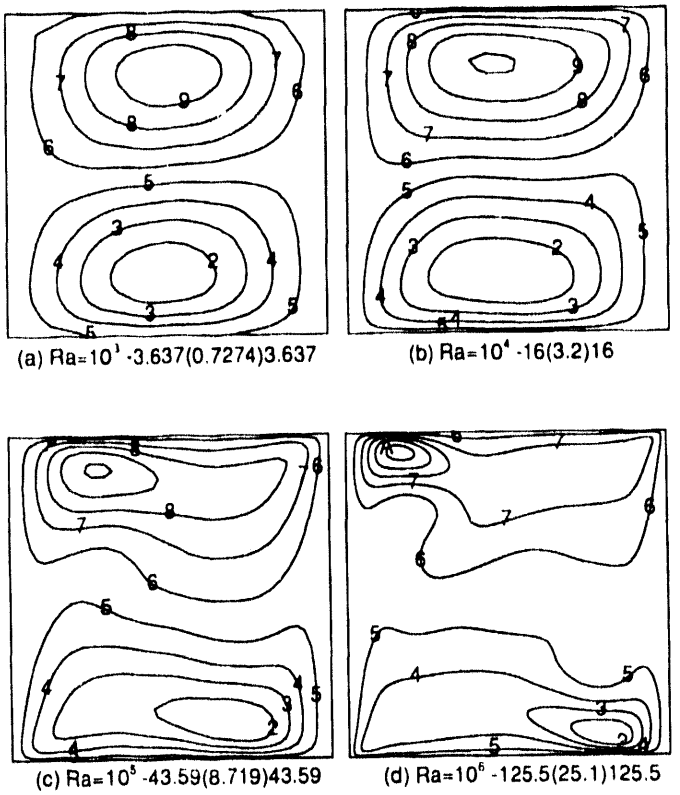

Figure 28. Contours of horizontal u_i velocity component, present data.

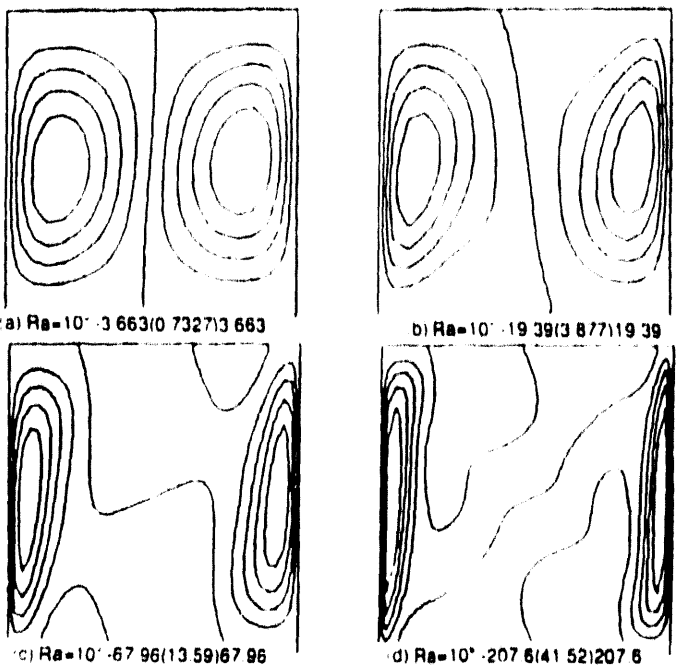

Figure 29. Contour of vertical u_2 velocity, de Vahl Davis (1983).

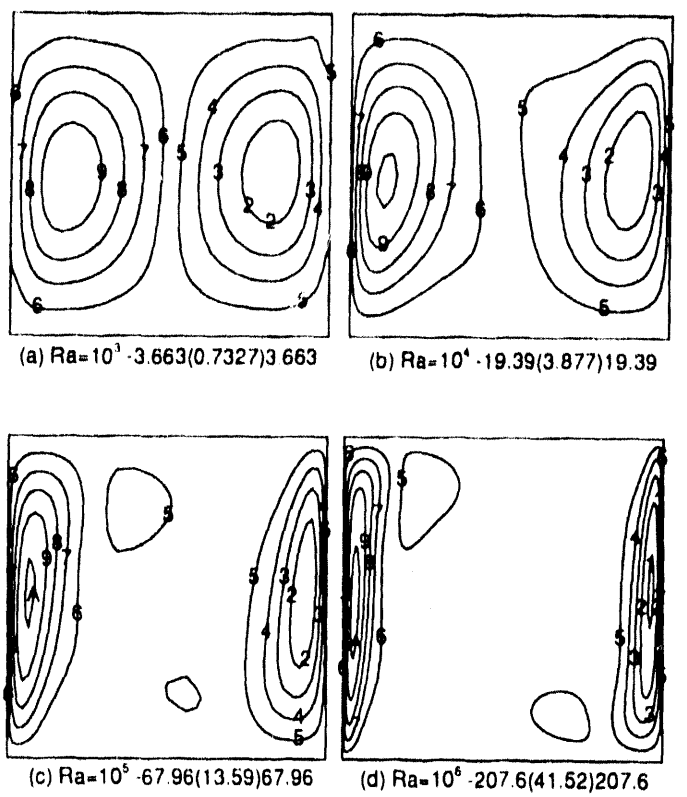

Figure 30. Contours of vertical u_2 velocity component, present data.

7.4.2 Three-Dimensional Natural Convection Cavity

The 3-dimensional extension of the "double-glazing" problem is natural convection in a rectangular box, Fig. 31, called the "window cavity" problem by Mallinson and de Vahl Davis (1977). Two opposing vertical walls are set at different temperatures, and all other walls are adiabatic. For the momentum equations, all walls have the no-slip boundary condition. Unfortunately, no verification, validation, or benchmark quality solutions have yet been published in the literature. Some limited qualitative data are available (cf. Aziz and Hellums, 1967; Reddy, 1982; Pepper and Watterberg, 1986; and Reddy et al., 1992); however, the typical intent of these papers is to demonstrate either a new CFD formulation or a new technique for flow visualization of 3-dimensional solutions. Essentially no quantitative data have been found.

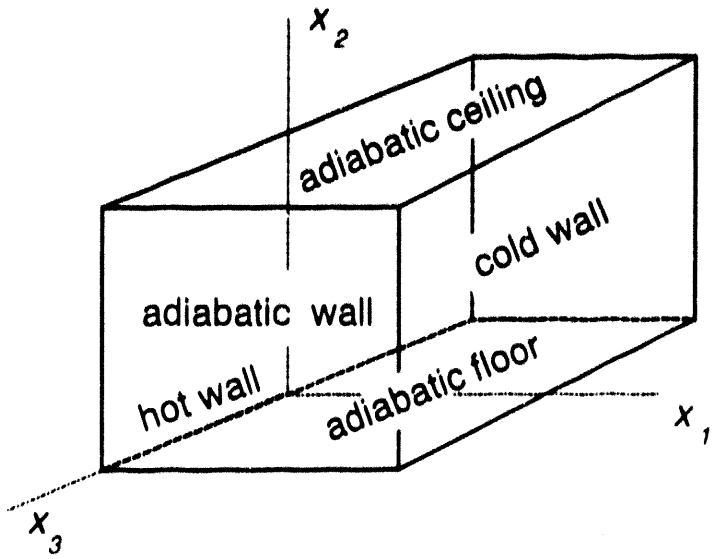

Figure 31. "Window cavity" problem.

One of the more informative studies of 3-dimensional flow structures in the "window cavity" problem is reported by Mallinson and de Vahl Davis (1977). They employed a vorticity/vector potential formulation to obtain steady-state solutions using the *method of false transient* (Mallinson and de Vahl Davis (1973)) for $0 \le Ra \le 10^6$, $0.1 \le Pr \le 100$, and box aspect ratios from 1 to 5. The majority of their solutions were obtained with a mesh of $M = 15 \times 15 \times 15$ using either a PDP-10 or an IBM 360/50 computer. This mesh was considered to represent a reasonable compromise between accuracy and computing cost, considering the limitations of computing capacity in 1977 and the exploratory nature of the study. Qualitative characterization of the essential flow structures were desired rather than establishment of benchmark quality data.

The absence of heat losses from the end-walls, floor, and ceiling of the box, combined with the no-slip boundary condition on all walls causes the three-dimensional axial flow character in the "window cavity" problem. Mallinson and de Vahl Davis (1977) describe two mechanisms associated with the end-wall that appear to cause such axial flows. The first mode, called the *inertial end effect*, is due to the kinematic interaction of the rotating fluid with the stationary end-wall. The second mode, the *thermal end effect*, results from axial temperature gradients near the ends of the box generated by variations in the flow field.

The geometry for the "window cavity" problem is shown in Fig. 32 where the end-walls, floor, and ceiling are adiabatic and the long opposing sidewalls are fixed at different temperatures. The cavity is twice as long as it is tall and wide. Due to symmetry of the geometry and boundary conditions, only half of the cavity is modeled with the $M = 30 \times 30 \times 18$ mesh depicted in Fig. 33. The global coordinate system origin is located at the lower corner of the symmetry plane, contiguous with the hot vertical sidewall. Solutions for three cases, as reported by Mallinson and de Vahl Davis (1977), were obtained using CFDL-PIII3D: (1) $Ra = 10^4$ $Pr = 0.1$, (2) $Ra = 10^4$ $Pr = 100$, and (3) $Ra = 1.5 \times 10^5$ $Pr = 0.71$.

Lagrangian particle tracks were calculated from the solutions of Cases 1 and 2 using a modified Euler integration scheme for visualization, as suggested by Mallinson and de Vahl Davis (1973). The tracks presented in Figs. 34 and 35 have origins at (0.6,0.6,0.9) and (0.6,0.6,-0.9), respectively. The tracks are reflected into the mirror quadrant for full problem characterization. The spiraling motion of the particles from the end-walls towards the central mid-plane is clearly evident. Temperature contours and velocity vectors on select horizontal and vertical cutting mid-planes are presented in Figs. 36-39 for Cases 1 and 2, respectively. The corresponding pressure contours with velocity vector plots are given in Figs. 40-43. The strong influence of the Prandtl number can be observed in these data presentations. For Case 1, at $Pr = 0.1$, the maximum computed longitudinal velocity, along the common axial center line of the horizontal and vertical mid-planes, was 3.17, after being scaled by $(Ra\ Pr/\ Ar)^{1/2}$ to reflect the reference velocity used by Mallinson and de Vahl Davis. At $Pr = 100$ in Case 2, the corresponding maximum longitudinal velocity was 0.67 in the $-x$, direction.

Particle tracks were calculated for Case 3 using the starting points specified by Mallinson and de Vahl Davis (1977), (0.5, 0.49, 0.9) for the forward flow and (0.3, 0.65, 0.2) for the reverse flow as shown in Figs. 44 and 45. Temperature and pressure contours for this case are presented in Figs. 46-49. The more complex nature of the flow at this higher Rayleigh number is apparent in these figures.

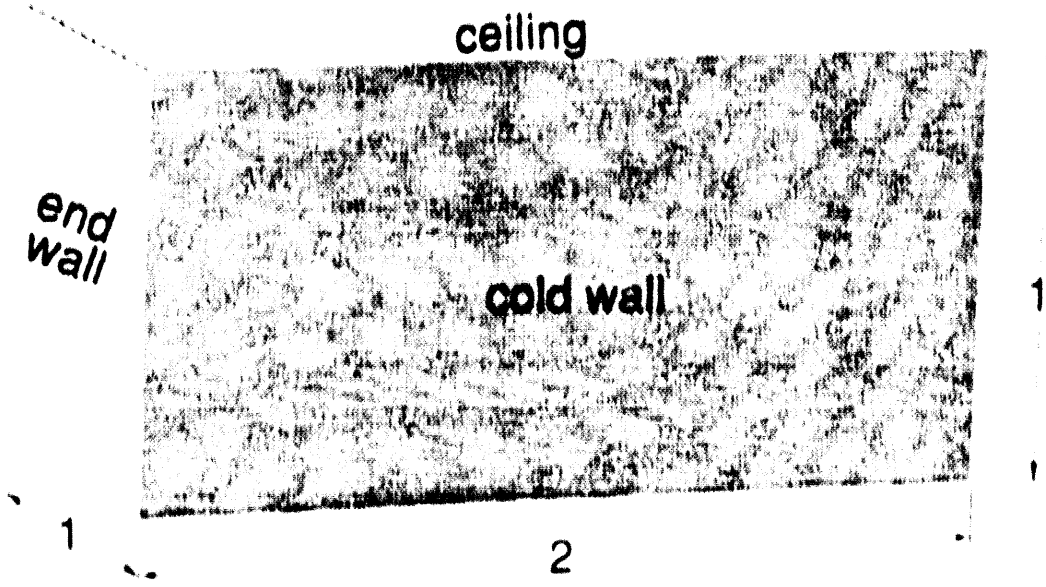

Figure 32. Geometry for the "window cavity" problem

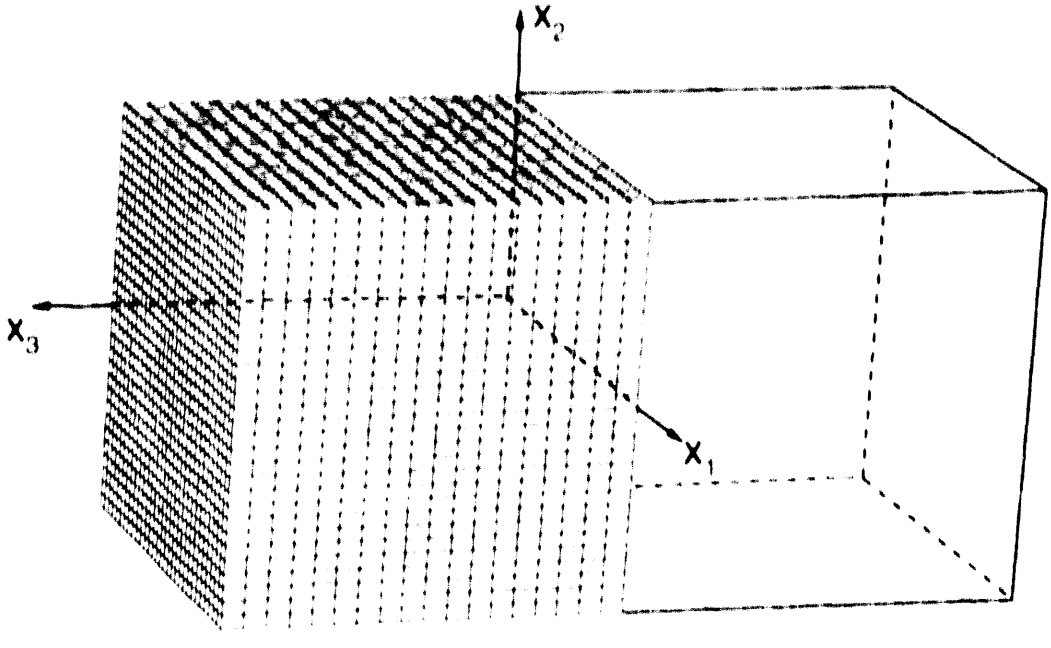

Figure 33. Mesh layout for the "window cavity" model with symmetry plane

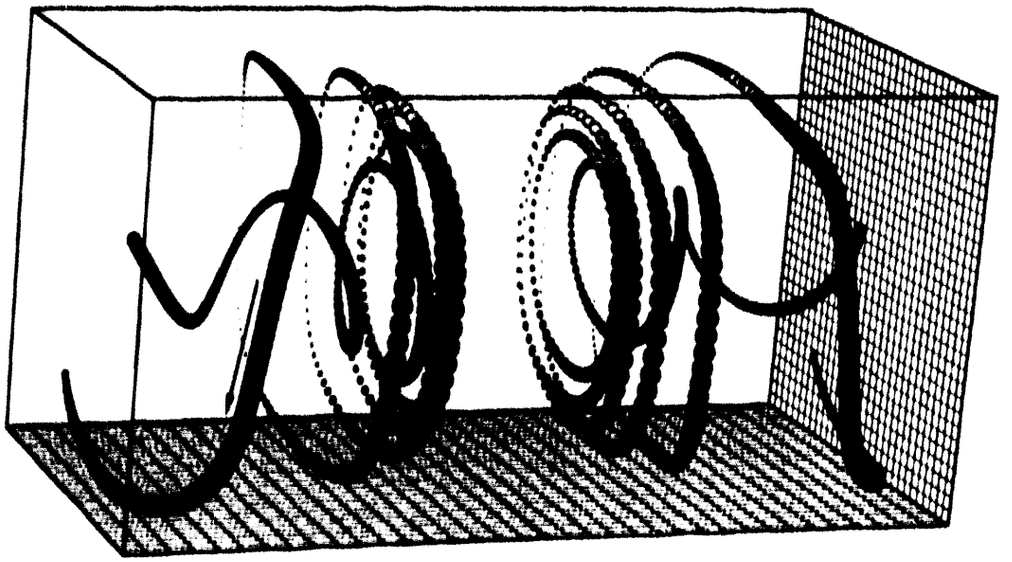

Figure 34. Particle tracks for $Ra=10^4$ $Pr=0.1$.

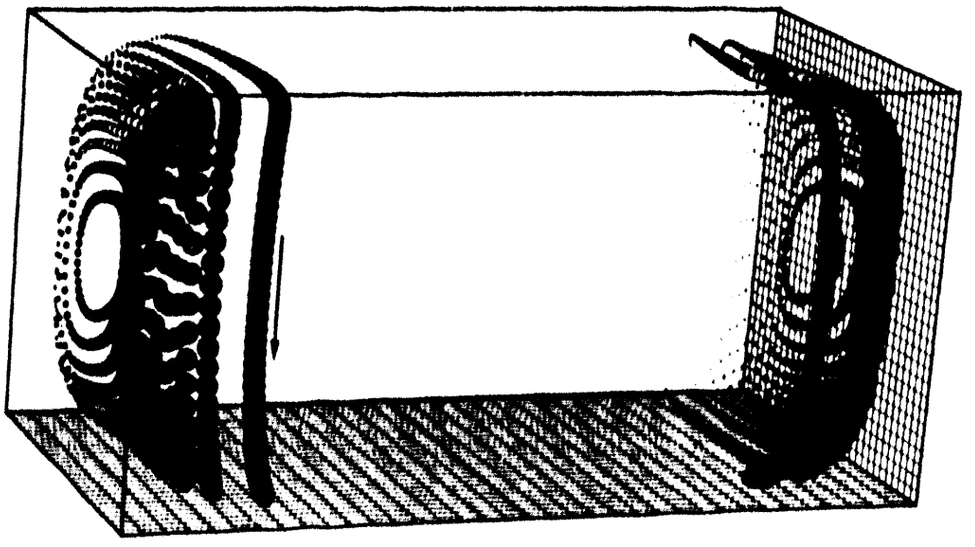

Figure 35. Particle tracks for $Ra=10^4$ $Pr=100$.

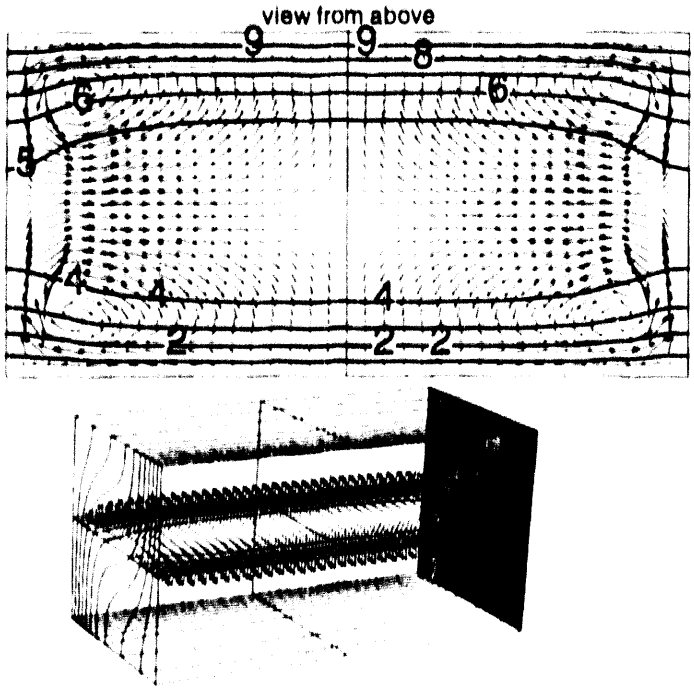

Figure 36. View of horizontal mid-plane $Ra=10^4$ Pr=0.1: temperature 0(0.1)1.

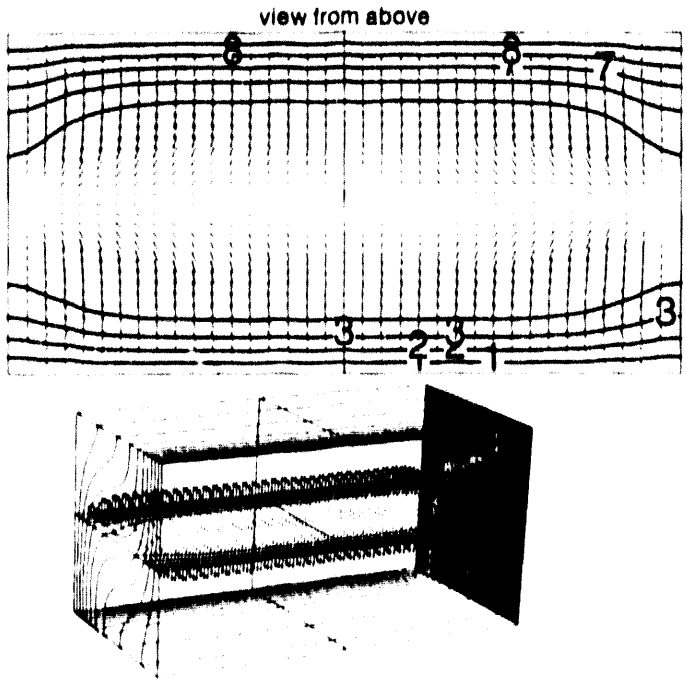

Figure 37. View of horizontal mid-plane $Ra=10^4$ Pr=100: temperature 0(0.1)1.

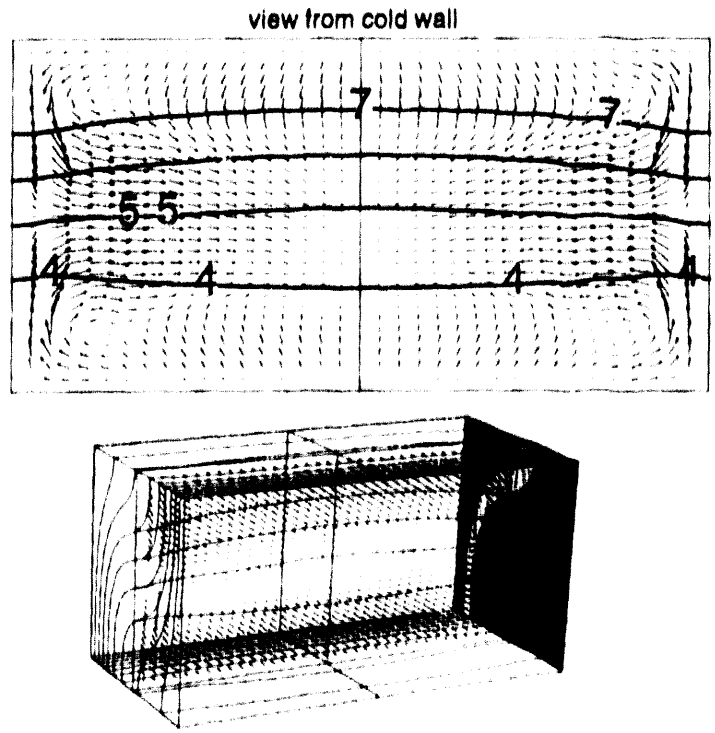

Figure 38. View of vertical mid-plane Ra=10^4 Pr=0.1: temperature 0(0.1)1.

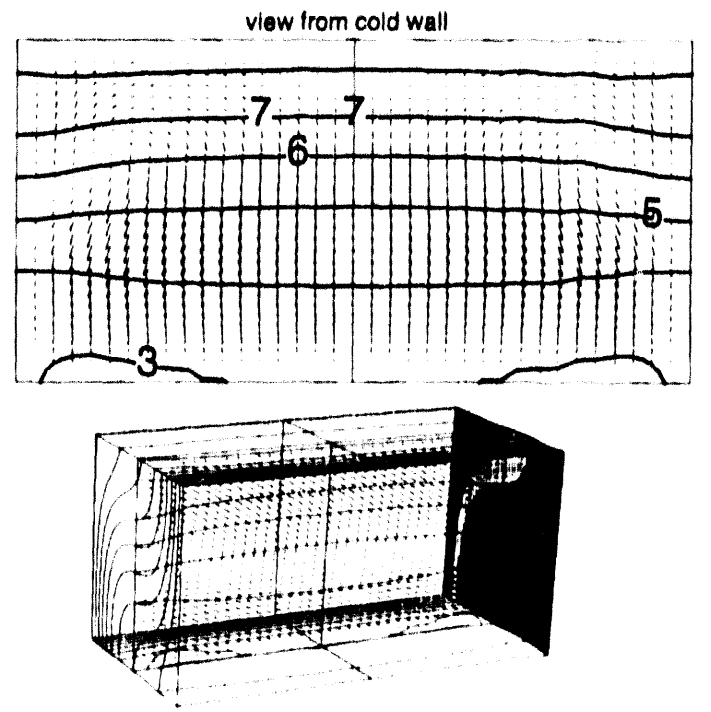

Figure 39. View of vertical mid-plane Ra=10^4 Pr=100: temperature 0(0.1)1.

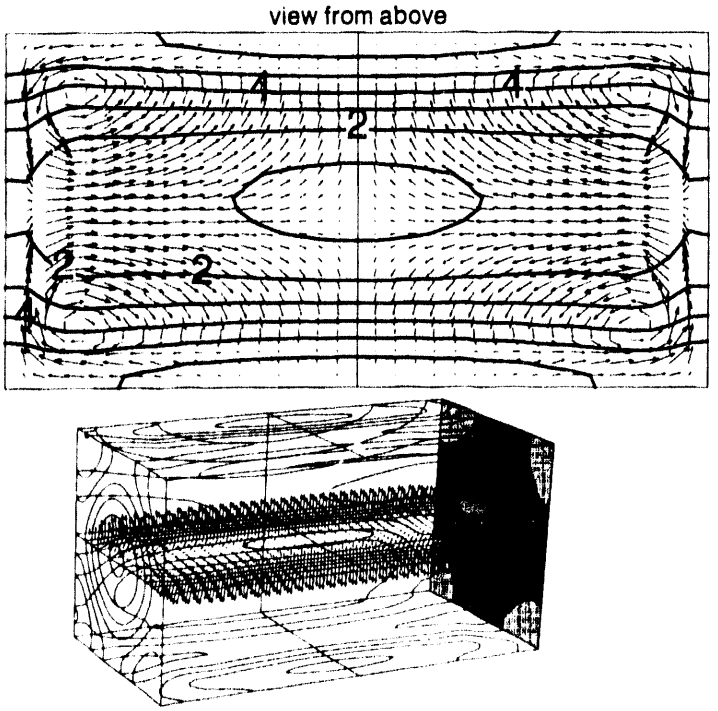

Figure 40. Horizontal mid-plane Ra=10^4 Pr=0.1: pressure $-7.1\times10^{-7}(1.42\times10^{-7})7.1\times10^{-7}$.

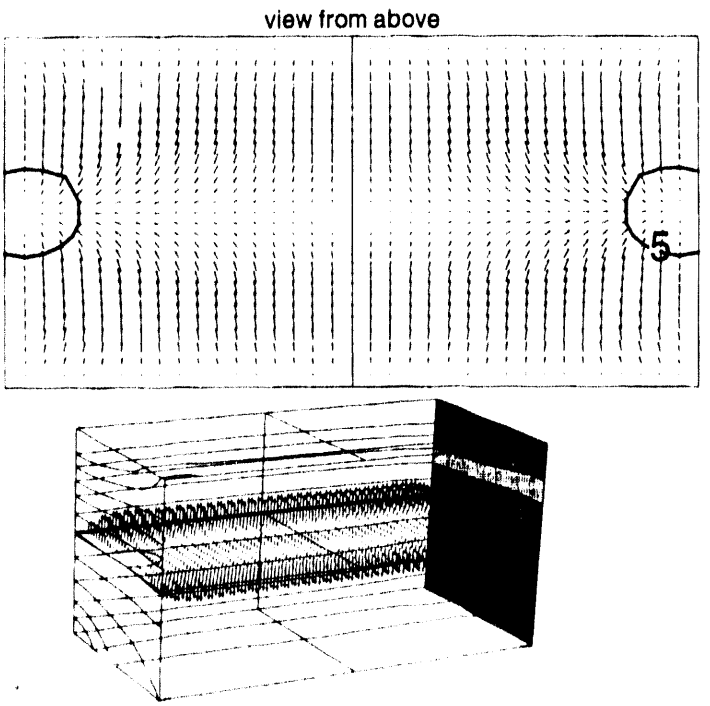

Figure 41. Horizontal mid-plane Ra=10^4 Pr=100: pressure $-2.4\times10^{-7}(4.8\times10^{-8})2.4\times10^{-7}$.

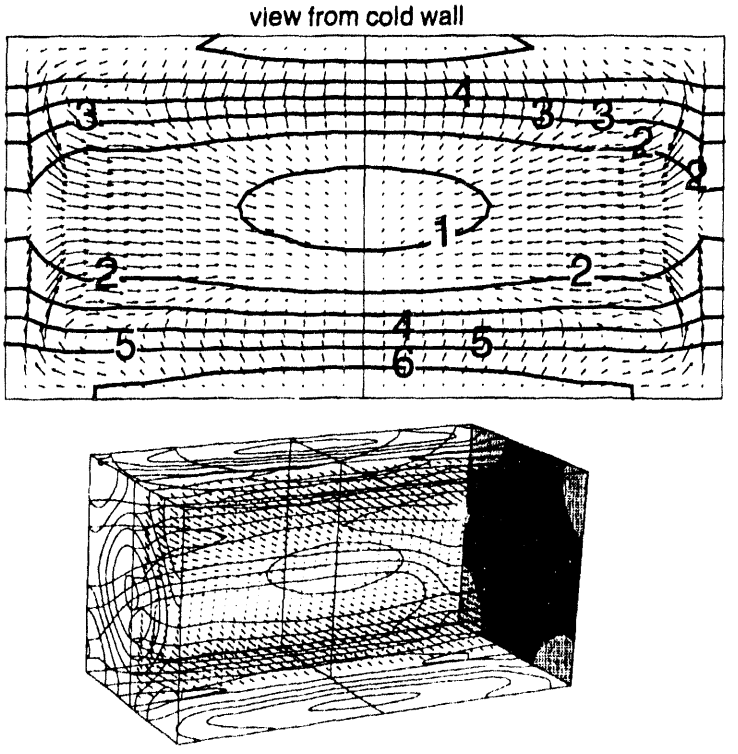

Figure 42. Vertical mid-plane Ra=10^4 Pr=0.1: pressure $-7.1\times10^{-7}(1.42\times10^{-7})7.1\times10^{-7}$.

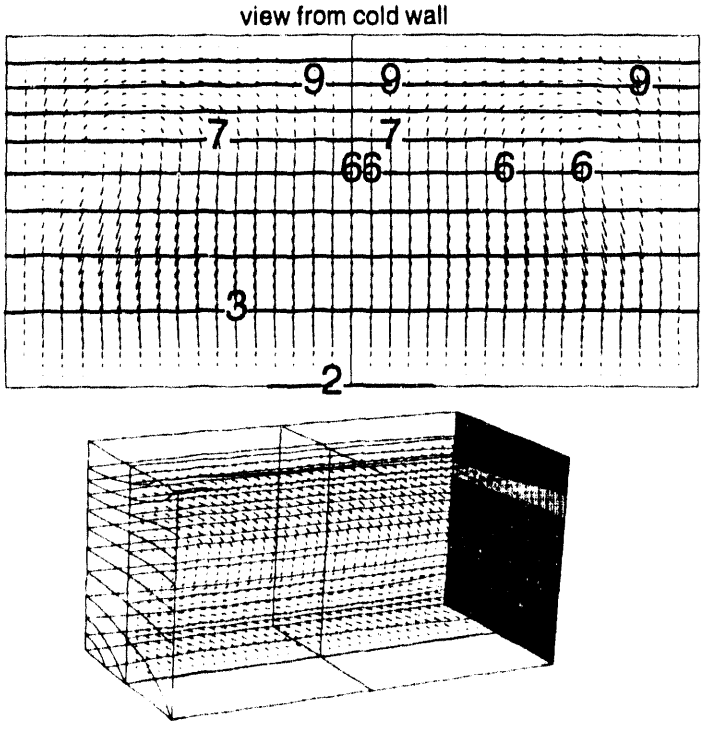

Figure 43. Vertical mid-plane Ra=10^4 Pr=100: pressure $-2.4\times10^{-7}(4.8\times10^{-8})2.4\times10^{-7}$.

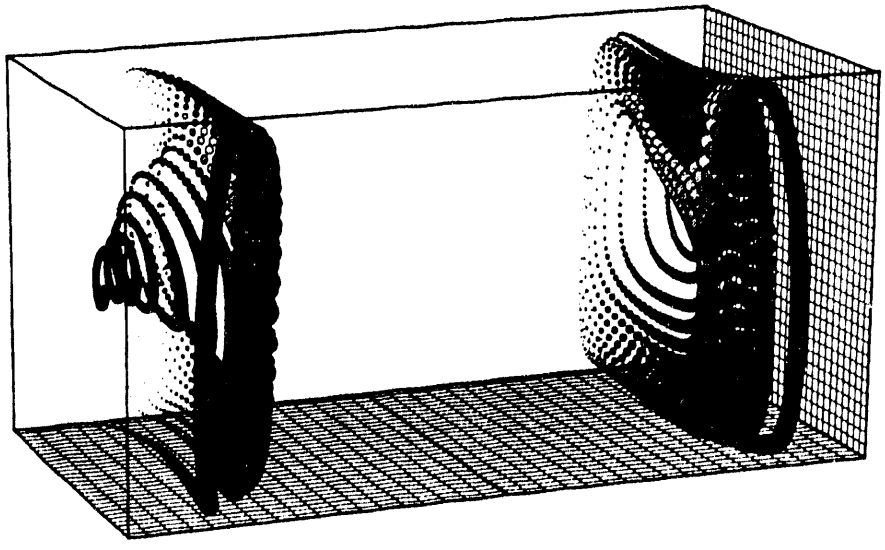

Figure 44. Particle tracks for $Ra=1.5\times10^5$ $Pr=0.71$: forward flow.

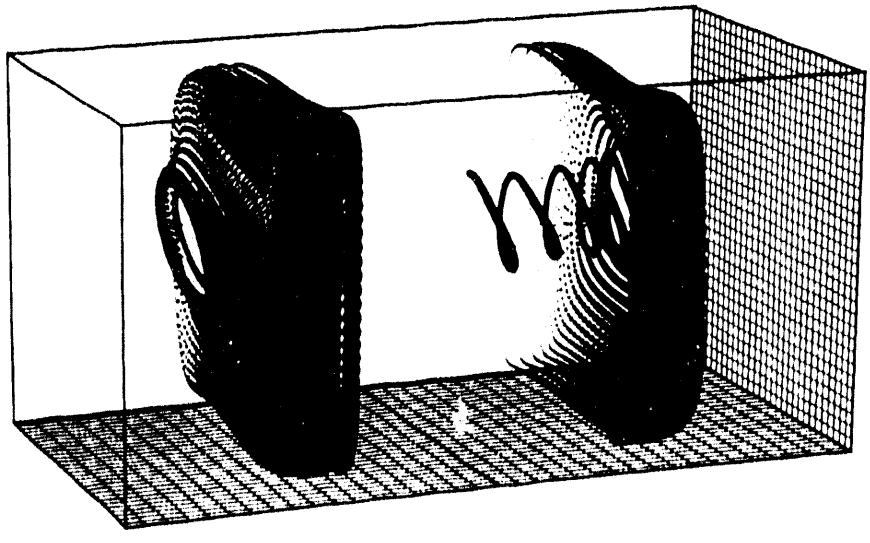

Figure 45. Particle tracks for $Ra=1.5\times10^5$ $Pr=0.71$: reverse flow.

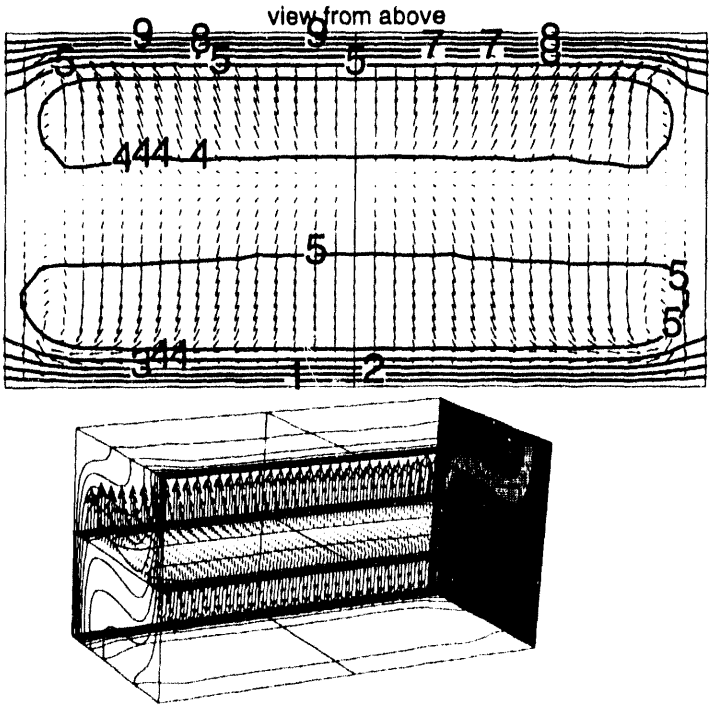

Figure 46. Horizontal mid-plane Ra=1.5×10^5 Pr=0.71: temperature 0(0.1)1.

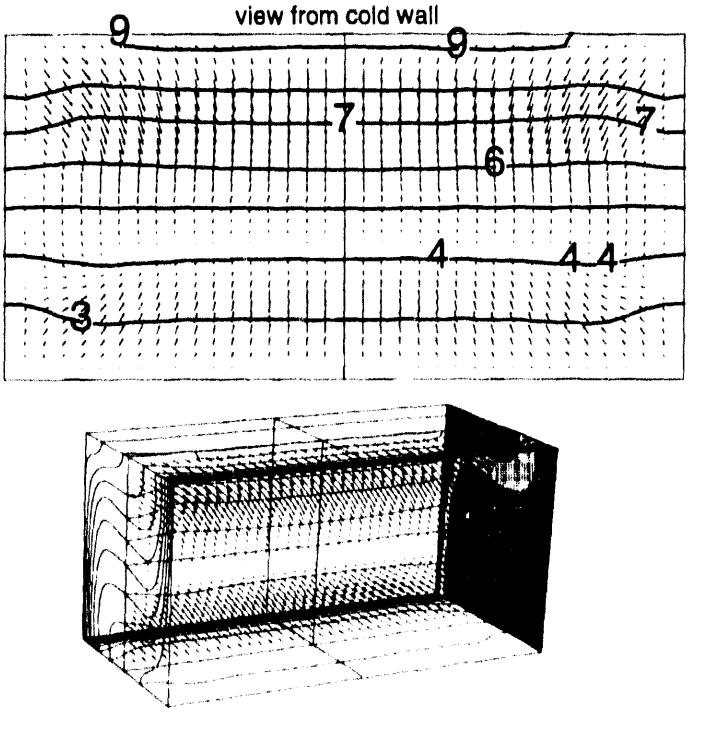

Figure 47. Vertical mid-plane Ra=1.5×10^5 Pr=0.71: temperature 0(0.1)1.

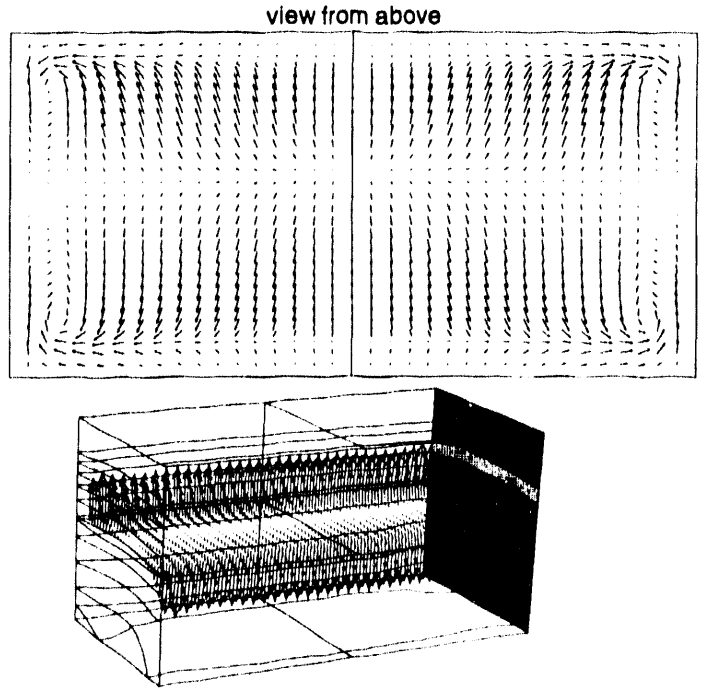

Figure 48. Horizontal mid-plane Ra=1.5×10^{5} Pr=0.71: press. $-1.72\times10^{-6}(4.52\times10^{-7})2.80\times10^{-6}$.

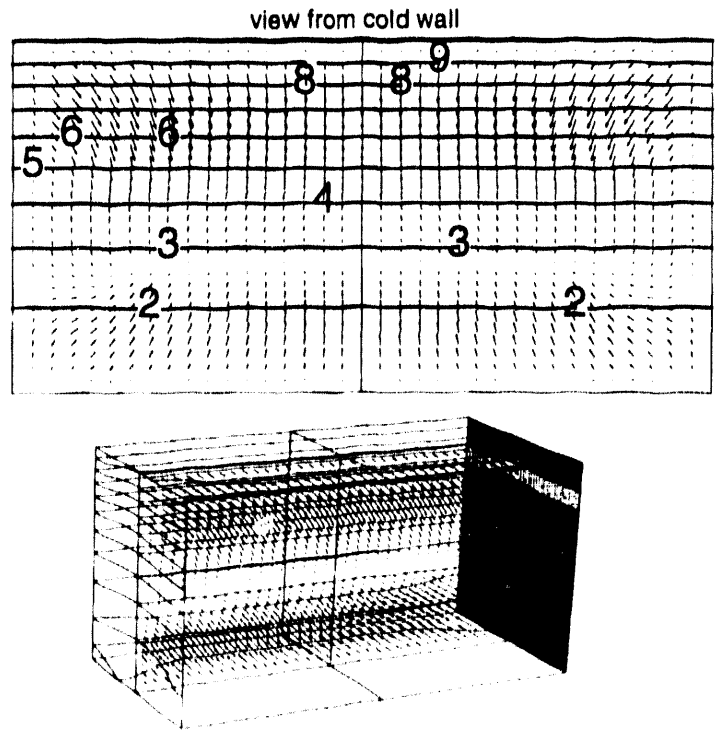

Figure 49. Vertical mid-plane Ra=1.5×10^{5} Pr=0.71: press. $-1.72\times10^{-6}(4.52\times10^{-7})2.80\times10^{-6}$.

The inertial end effect has been studied by Pao (1970) (as cited by Mallinson and de Vahl Davis, 1977) using a rotating cylinder with a stationary end-wall. For the case of a low Rayleigh number single vortex roll, the rotating cylinder approximation is fairly representative of the end effect. Based on the results of Pao's analysis, Mallinson and de Vahl Davis postulated that the intensity of the axial flow would be inversely proportional to the Prandtl number.

The thermal end effect, manifested by small axial temperature gradients near the end-walls, is due to reduced convective heat transport in the vicinity of the end walls. The reduction in convection in this region is the result of the additional viscous drag on the fluid by the proximity of the noslip boundary condition at the end-wall. Mallinson and de Vahl Davis assert that, at least for $0.2 \leq Pr \leq 100$, the thermal effect is independent of Pr. Since the axial flow due to the inertial effect decreases with increasing Pr, they argue that at Pr=100 any 3-dimensional flow structure is due to the thermal effect alone. "The total longitudinal motion at any Pr is thus the sum of a constant thermal effect and a Pr-dependent inertial effect. The magnitude of the constant thermal effect can be deduced from a high Prandtl number solution, for which the inertial effect should be negligible."

At Rayleigh numbers less than 6×10^4, the axial flow proceeds from the center of both end-walls in a spiraling motion towards the central symmetry plane, Figs. 34-35. The return path for the reverse flow is along the vertical and horizontal sidewalls. As was the case with the 2-dimensional double glazing problem, the flow structure becomes more complicated at Rayleigh numbers above 10^4 due the presence of secondary motion. For $Ra=1.5\times10^5$ and Pr=0.71, Mallinson and de Vahl Davis observed two secondary vortex rolls in the cross-sectional flow far from the end-walls. Strong axial flows occurred near the end-walls, with each secondary roll forming its own spiral center for the inward moving flow. At these higher Rayleigh numbers, the axial flows are confined to the vicinity of the end-walls, Figs. 44-49.

7.5 STEP-WALL DIFFUSER

Flow separation, a subject of fundamental importance in fluid mechanics, has been the focus of intensive study for many years. To aid in experimental and computational investigations of this phenomenon, a set of simple geometric configurations has been developed as representative test beds including (a) flow in a pipe with a sudden expansion, (b) flow in a pipe with an obstruction such as an orifice, (c) flow over an obstruction (either a step or a thin fence) in a channel, and (d) flow in a channel with a sudden expansion (step-wall diffuser or backward facing step), as depicted in Fig. 50. Within each base configuration, variations in boundary conditions and the addition of heat and/or mass transfer serve to further broaden the problem class. Among these four basic configurations, the step-wall diffuser, Fig. 50d, has become a very popular benchmarking and validation test problem for CFD codes due to its simple geometry and the availability of quality experimental data.

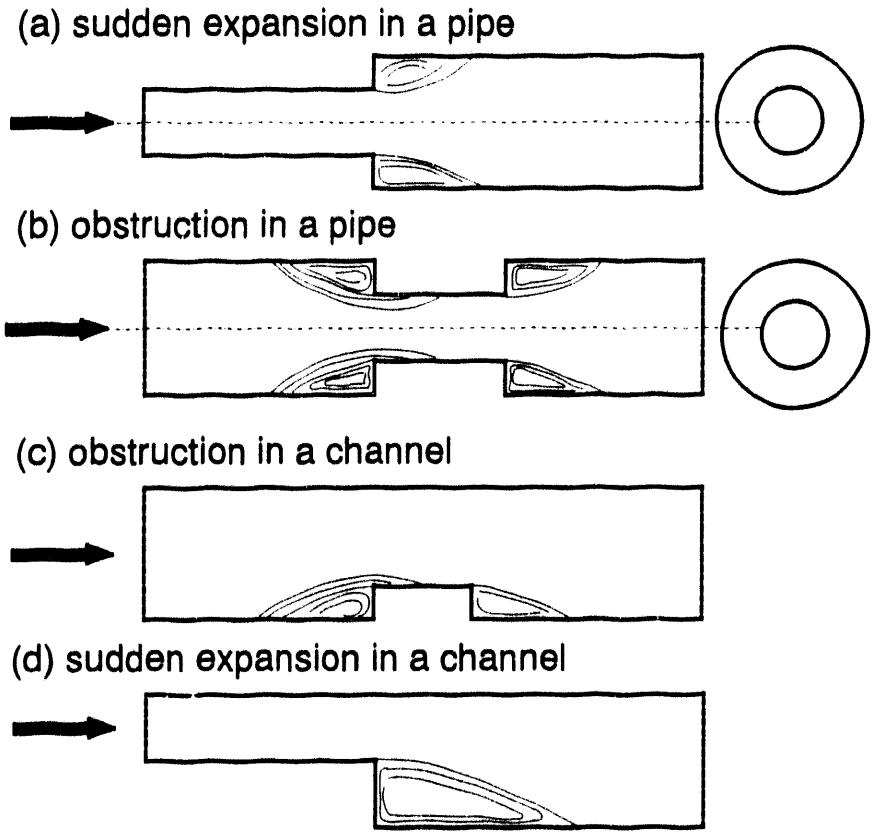

Figure 50. Test bed configurations for flow separation.

Flow separation can be defined as a region of recirculating flow adjacent to a solid boundary. The positions for detachment and reattachment of the "separation bubble" are delimited by sign changes in the vorticity of the flow field at the boundary. Within the separation bubble, the flow is characterized by recirculating vortices and flow reversals. A necessary but not sufficient condition for the onset of flow separation in both boundary layer and fully-viscous flows is the presence of an adverse pressure gradient in the flow field near the outer boundary of the separation bubble (Tritton, 1988), where "adverse" refers to an increasing pressure in the direction of the main flow stream.

Much of the early experimental data on flow separation was developed for boundary layer flows in studies of the "stall" phenomenon of external aerodynamics. A common test geometry for these studies is depicted in Figs. 50c and d in which the upper boundary is a free surface. The separation-reattachment process in boundary layer flows is a complex interaction between the separated shear-layer and the adjacent flow. Test conditions can be grouped into three distinct regimes reflecting the character of the flow at the point of detachment and reattachment: (1) laminar-laminar, (2) laminar-turbulent, and (3) turbulent-turbulent.

Abbott and Kline (1962) studied turbulent-turbulent flows over double and single backward facing steps using an open-surface water table. Three-dimensional flow structures were observed in the form of one or more vortices rotating about an axis normal to the vertical step and parallel to the floor of the test section. This 3-dimensionality is confined in space to the region immediately

downstream of the step; however, the vortices changed in size over time. Adjacent vortices were counter-rotating and varied in number depending on the step geometry and water depth. With the advent of laser-Doppler anemometry, experimental studies of turbulent boundary layer separation have continued to produce data of increasing quality (cf. Etheridge and Kemp, 1978; Kim et al., 1980; Eaton and Johnston, 1981; and Isomoto and Honami, 1989). Studies of laminar-laminar boundary layer separation (e.g., Goldstein et al., 1970) indicate that the characteristics of the separation regimes are dependent on both geometry and Reynolds number; however, for turbulent-turbulent regimes, the flow structures are dependent primarily on the step geometry and are relatively insensitive to Reynolds number.

As noted by Tritton (1988), the phenomenon of separation is not confined to boundary layer flows. When the upper boundary in Figs. 50c and d is an impermeable wall, these two configurations join Figs. 50a and b in a class of flows for which an inviscid flow regime or distinct shear layer does not exist. In this class of computational problems, the full Navier-Stokes conservation law must be simulated throughout the complete flow domain. Axisymmetric flow with a sudden enlargement, Fig. 50a, has been the subject of computational studies by Donea et al. (1982), Zienkiewicz et al. (1990), and Fang and Paraschivoiu (1991). Laminar experimental data for this configuration were obtained by Iribarne et al. (1972). Leone and Gresho (1981) and Carvalho et al. (1987) present benchmark quality solutions for channel flow over a step, Fig. 50c, and turbulent and laminar stratified channel flow with a backward-facing step has been studied computationally by Oliver (1980), Leone (1990), Gartling (1990), and Papanastasiou et al. (1992).

The present study has concentrated on isothermal 3-dimensional flows in a channel with a sudden expansion, Fig. 51, also known as a step-wall diffuser or a backward-facing step. Because of the quality of the experimental data available and the simplicity of the geometry, this configuration has become a standard test problem for validation studies of incompressible Navier-Stokes CFD algorithms. Two experimental investigations have been used extensively in the validation efforts quoted in the literature, specifically the laminar data of Denham and Patrick (1974) and the laminar and turbulent data of Armaly et al. (1983).

7.5.1 Denham and Patrick (1974) Experiments

Denham and Patrick (1974) present experimental data for 2-dimensional, laminar, recirculating flow in a channel with a backward facing step. A directionally-sensitive laser-Doppler anemometer and dye-tracer injection were used in their experiments. The test setup consisted of water flowing from a constant-head tank into a diffuser, through a settling chamber packed with flow-straightening honeycomb material, and into a 2-dimensional contraction preceding the test section. From the test section, the flow passed through a bank of flow meters and then into a lower constant-head tank. The backward-facing step was formed by inserting a block of Perspex into the main channel of the test section. The leading edge of the block was beveled to avoid separation upstream of the step. The ratio of step height to upstream channel height (S/h in Fig. 51) was 0.5 and the spanwise channel width to step height ratio (W/S) was 20. The expansion ratio for the step, defined as the ratio of the downstream to upstream channel heights (H/h), was 1.5. Laminar flow velocity profiles were measured at several stations upstream and downstream of the step, at four different Reynolds numbers (Re= 292, 500, 764, and 916, where the Reynolds number is evaluated using twice the upstream channel height as a reference length and the upstream average flow speed as a reference velocity). For the Reynolds numbers investigated, Denham and Patrick maintained that the "flow in the mainstream appeared to be truly two-dimensional over at least the central two-thirds of the width

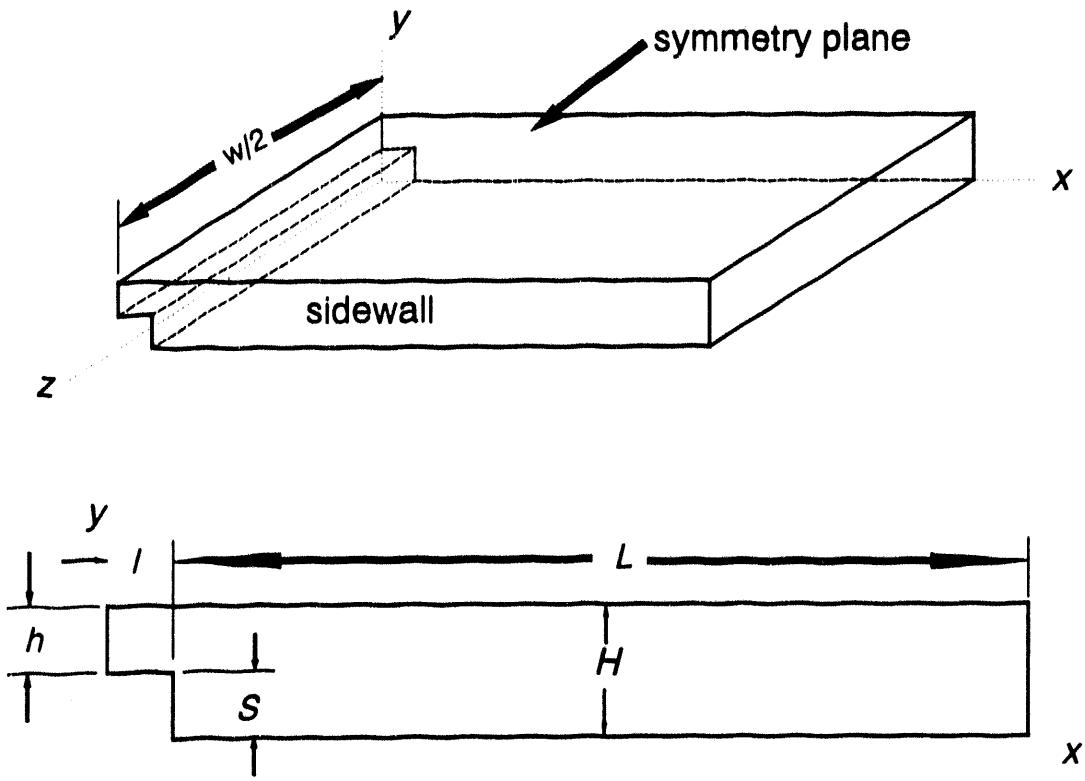

Figure 51. Step-wall diffuser geometry.

of the channel." However, 3-dimensional effects were observed in the region immediately downstream of the step. Dye-tracer observations indicated the presence of secondary 3-dimensional flow in the form of counter-rotating vortices in the recirculation region. The vortex axes were parallel to the vertical face of the step and normal to the floor. Denham and Patrick note that this secondary flow "caused the dye trace to spiral out from the centre of the duct" rather than inward as reported by Goldstein et al. (1970) in their free-surface laminar experiments. At the highest Reynolds number (Re=916), the initiation of transition to turbulence was observed as small periodic fluctuations in the velocities near the reattachment point. No secondary separation on the upper wall of the test section was observed.

Computational simulations of the step geometry used by Denham and Patrick have consistently predicted longer reattachment lengths for the primary separation bubble than were obtained experimentally (Hackman et al., 1984 and Ghia et al., 1989). This discrepancy has been attributed to the construction of the test section which included an asymmetric flared device along the lower wall of the channel upstream of the step. Ghia et al. (1989) observe that, since the resulting inlet section was relatively short, the velocity profiles obtained by Denham and Patrick just before the step indicate an asymmetric distortion from the parabolic profiles typically assumed in computational studies. The severity of this distortion increases with increasing Reynolds number.

7.5.2 Armaly et al. (1983) Experiments

An open-loop air-driven flow channel was used by Armaly et al. (1983) to measure velocity distributions and reattachment lengths downstream of a backward-facing step. Results are presented for laminar, transitional, and turbulent flow of air with a Reynolds number range of $70 < Re < 8000$. The channel height upstream of the step was 5.2 mm, and the downstream channel height was 10.1 mm, giving an expansion ratio H/h=1.9423 and a step height S of 4.9 mm. The channel width was 180 mm, and W/S=36.735. The channel floor, roof, and step face were built of aluminum, machined to close tolerances regarding wall orientation and surface roughness. The two sidewalls were made of glass, 10 mm thick, sufficiently rigid to support the test section and to facilitate laser-Doppler measurements using forward-scattered light. Air flow with 2 μm mean diameter silicone oil scattering particles was first fed from a large settling chamber through five 6 mm diameter bored tubes into the first stage of the flow channel, consisting of an expansion section packed with steel wool to smoothen the flow and to prevent input disturbances from affecting the measurements. Passing through a series of flow straighteners, the flow entered a smooth contracting nozzle whose outlet was connected to the entrance of the test section. The test section provided a 200 mm straight channel approach to the backward-facing step and a 500 mm long channel downstream of the step. Operating in a forward-scattering mode, the laser-Doppler anemometer was set up to measure only the streamwise velocity component. The optical system was fixed in space, and the test section was moved in steps using a 3-dimensional traversing table.

The reattachment lengths of the separation regions were measured by scanning the lower and upper walls in the streamwise direction at constant and known elevations. To determine the reattachment length, the position of the zero-mean-velocity line was measured. The points of detachment and reattachment were taken as the extrapolated zero-velocity line down the wall.

Measurements of the reattachment length for the primary separation bubble, x_1 in Fig. 52, just downstream of the step on the lower wall allowed the identification of the laminar ($Re < 1200$), transitional ($1200 < Re < 6600$), and turbulent ($Re > 6600$) regimes of the flow, Fig. 53 (Armaly et al., 1983). The Reynolds number is evaluated with a reference velocity equal to two-thirds of the maximum velocity measured 10 mm upstream of the step and a reference length equal to twice the upstream channel height (i.e., the hydraulic diameter of the upstream channel). For the laminar region, the separation length increases nonlinearly with the Reynolds number. The transitional flow regime is characterized by a sharp initial decrease in the reattachment length, followed by a continued gradual, but irregular, decrease to a minimum at a Reynolds number of approximately 5500. Beyond Re=5500, the reattachment length ceases to be afunction of Reynolds number. An additional separation bubble was measured along the floor of the channel downstream of the primary separation, x_2 and x_3 in Fig. 52. This secondary floor bubble disappears above a Reynolds number of 2300. A secondary separation region was also observed along the upper wall downstream of the step, x_4 and x_5 in Fig. 52. It develops in the laminar region (for $Re > 400$) and remains throughout the transition regime. The length of this upper separation bubble initially increases with increasing Reynolds number and then gradually decreases until it disappears above a Reynolds number of approximately 6600.

To determine the 2-dimensionality of the flow, spanwise velocity profiles at various constant elevations were measured at selected Reynolds numbers. At Reynolds numbers smaller than 400, the flow was predominantly 2-dimensional. Within the Reynolds number range of $400 < Re < 6600$, the

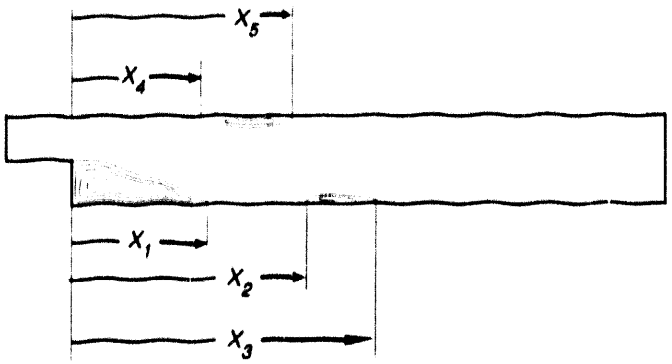

Figure 52. Separation regions identified by Armaly et al. (1983).

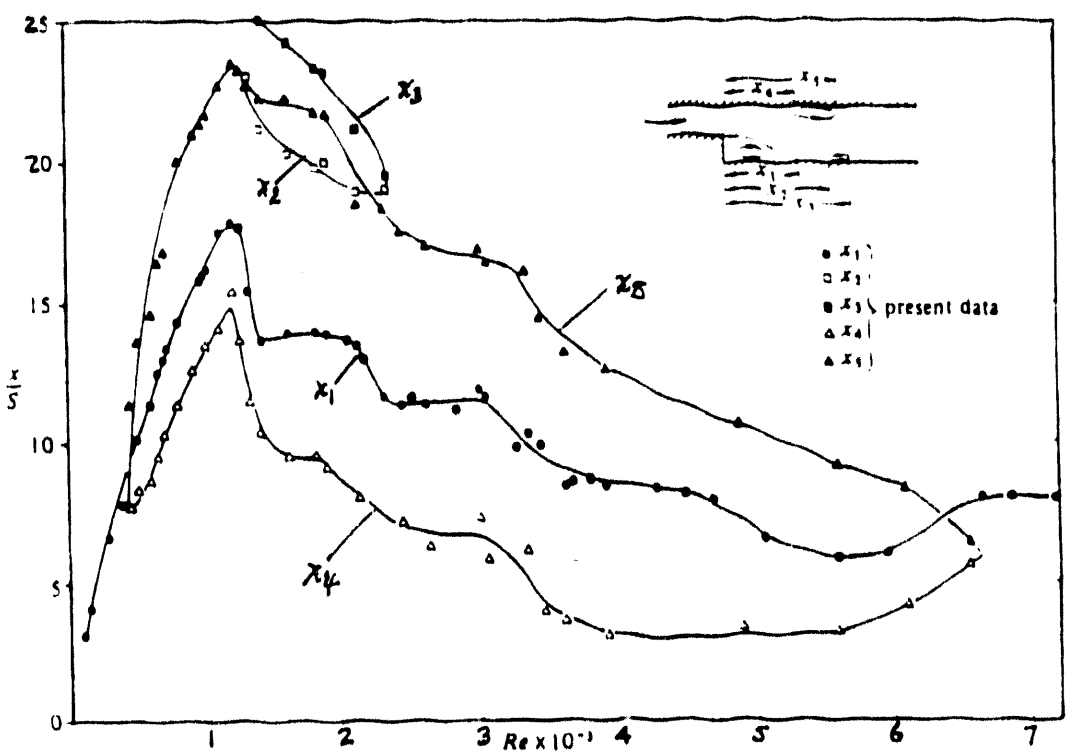

Figure 53. Location of detachment and reattachment points v. Re, Armaly et al. (1983).

flow downstream, and in the immediate vicinity of the step, was found to be 3-dimensional. The experimental data of Armaly et al. (1983) and Denham and Patrick (1974), in terms of the reattachment length of the primary separation region v. Reynolds number, are plotted in Figs. 54 and 55 for two length scale definitions, the step height S and the hydraulic diameter of the upstream channel D_h, respectively. The two data sets were obtained using test sections with different expansion ratios, H/h= 1.9423 for Armaly et al. and H/h=1.5 for Denham and Patrick. As noted by Armaly et al. (1983), the two data sets appear to correlate well with the Reynolds number evaluation in Fig. 54, incorrectly suggesting that the reattachment length is a function of Re alone. The lack of correlation between the data sets, evident in Fig. 55, demonstrates that the reattachment length may be a function of several variables including Reynolds number, step geometry, and velocity profile at the step plane. Accordingly, it is very important that validation studies correctly simulate the geometry and upstream flow conditions as well as the Reynolds number of the experiment.

7.5.3 Computational Experiments

Two- and 3-dimensional models simulating the step-wall diffuser experiments carried out by Armaly et al. (1983) were developed for CFDL.PHI3D. The 2-dimensional model, Fig. 56, used an M=4×11×1 discretization upstream of the step and M=87×20×1 downstream of the mesh, where all velocities in z-coordinate direction are set to zero. Exploiting the experimentally verified symmetry of the flow field, the 3-dimensional model, Fig. 57, employed a central vertical symmetry plane with a mesh discretization of M=4×11×24 upstream and M=87×20×24 downstream of the step plane. The upstream and downstream channels are approximately 1 and 30 step-heights long, respectively.

The final meshes for the 2- and 3- dimensional models resulted from a mesh refinement study that investigated the sensitivity of the solutions to: (a) channel lengths upstream and downstream of the step and (b) the mesh refinement and grading near all walls, the step plane, regions of separation, and the approach to the outflow plane. Seven stages of mesh refinement were investigated for the 3-dimensional model, starting with approximately 20,000 nodes and progressing to the final mesh of 47,300 nodes. Using an approach length of ten step-heights, the initial 2-dimensional results indicated that a fully-developed velocity profile was well-established within one step-height from the inlet plane, allowing the shortening of the approach channel. The 2- and 3-dimensional studies also showed that adequate mesh grading was necessary both upstream and downstream of the step-plane. Grading along the upper wall was critical in the 3-dimensional model for resolving the thin secondary separation region, and the solution became unstable if the mesh was inadequately graded near the outflow plane.

The velocity boundary conditions for both models included no-slip conditions at all impermeable walls, prescribed fully-developed laminar velocity profile at the inflow plane, and a zero traction Neumann condition as described in Chapter 4 for the outflow plane. The pressure and continuity constraint function Φ were both set to zero across the outflow plane. Except for the symmetry plane, the boundary condition for the constraint function was homogeneous Neumann. To maintain a free-slip tangency condition for the symmetry plane, a nonhomogeneous Neumann boundary condition for Φ is calculated as the solution evolves. The pressure boundary condition was homogeneous Neumann across the symmetry plane and nonhomogeneous Neumann for the inflow and no-slip boundaries. For Re=100, the initial conditions for the velocity field were a fully developed profile filling the upstream and downstream channels, where the downstream channel profile was scaled from the upstream profile by the cross-sectional area ratio (upstream to downstream) to provide

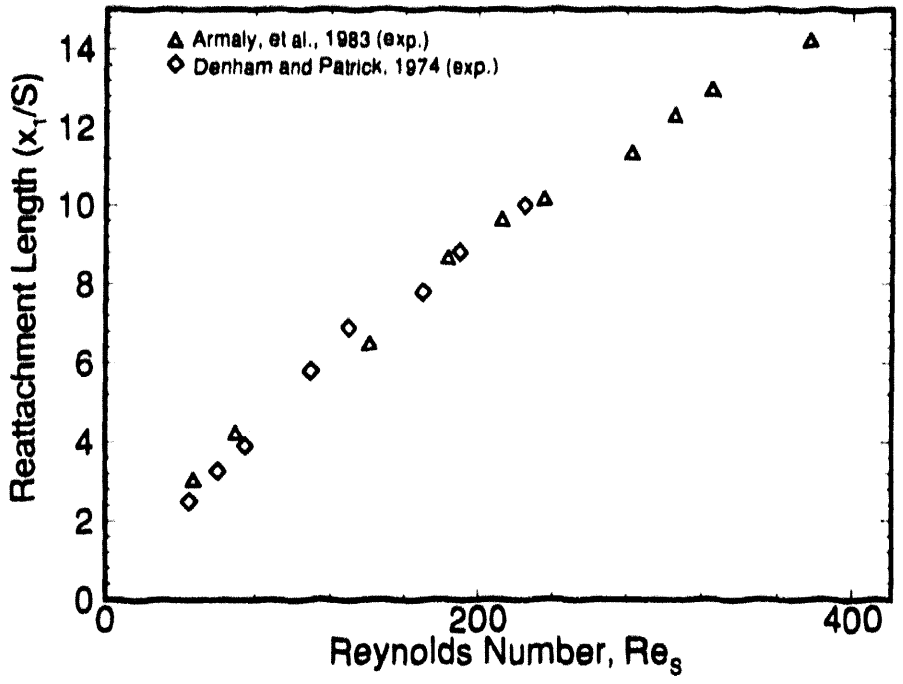

Figure 54. Experimental reattachment length data, x_r/S v. $Re_S = US/\nu$.

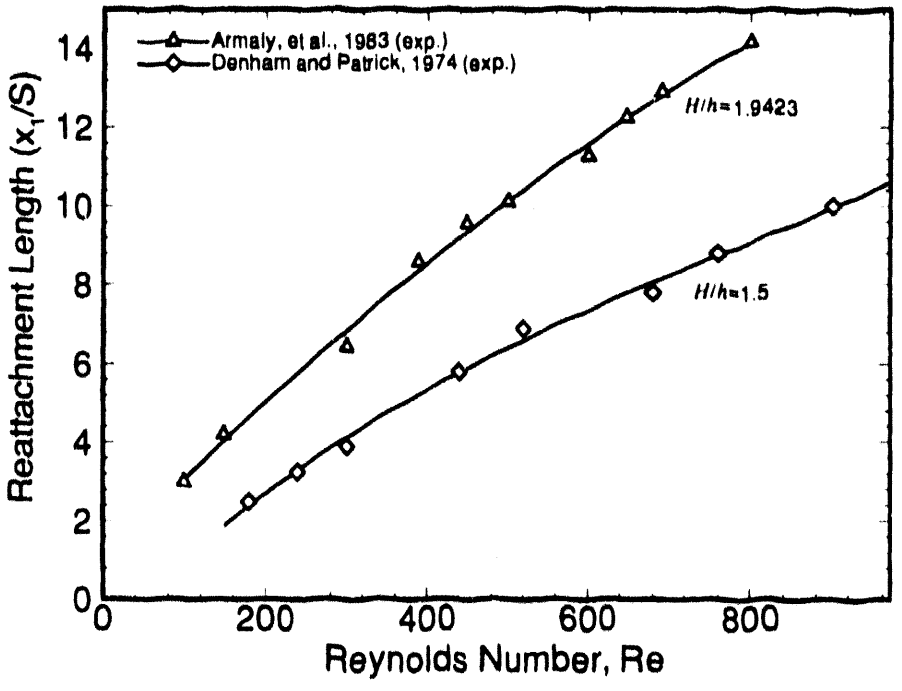

Figure 55. Experimental reattachment length data, x_r/S v. $Re = UD_h/\nu$.

a nominal conservation of mass at t=0.0. The initial pressure field was calculated by the pressure Poisson equation using the initial velocity data. For subsequent higher Re, Reynolds number continuation was used to obtain initial conditions. For both the 2- and 3-dimensional simulations, laminar steady-state solutions were obtained for $100 \leq Re \leq 800$.

Preliminary results for the 3-dimensional model indicated an instability in the computed velocity distribution at the step plane that did not respond to remeshing. It was postulated that the source of the instability was due to roundoff error, produced by the significant difference in magnitude of the three velocity components. The problem was eliminated by rotating the computational coordinate system, relative to the "laboratory" reference frame, through two successive Euler angles. The first transformation was a +45° rotation about the z-coordinate axis, producing a (x', y', z') coordinate triad, and the second transformation involved a +45° rotation about the y'-coordinate axis to produce (x'', y'', z'') where all computations were performed. In the new reference frame, all three velocity components were of the same order of magnitude as measured by their respective energy semi-norms, defined by

$$\| q \|_E^2 = \frac{1}{C} \sum_e \left(\int_{\Omega_e} \frac{\partial q}{\partial x_j} \frac{\partial q}{\partial x_j} \, d\Omega \right) \tag{373}$$

where q represents any state-variable and C is a normalizing constant.

A number of researchers have used the experimental data of Armaly et al. (1983) for computational validation studies. A representative sampling from the literature is presented in Table 10. The CFD formulations include a range of algorithms, such as the finite-difference MAC, finite-volume SIMPLE, finite-element penalty, and pseudo-spectral formulations. The Reynolds numbers cited in the far right column are calculated using a consistent reference velocity and length scale. As described by Armaly et al. the reference velocity is the average bulk velocity in the upstream channel (defined as two thirds of the maximum axial velocity measured 10 mm before the step plane), and the reference length is the hydraulic diameter of the upstream channel (defined as the twice the upstream channel height).

Present results from the 2-dimensional simulations in the region near the step are summarized in Fig. 58 for Re = 389, 648, and 800. The Re = 389 solution is close to the experimentally determined upper bound for approximate 2-dimensional velocity profiles at the central symmetry plane. Beyond Re ≈ 400, evidence of 3-dimensional flow structures are reported by Armaly et al. in the form of a variable line of reattachment for the primary separation bubble across the floor of the downstream channel. Above approximately 400, it has been postulated that the reason the 2-dimensional solutions cease to agree with the experimental reattachment data is due to the 3-dimensionality of the flow (Ghia et al., 1989). The onset of the secondary separation along the upper wall of the downstream duct also occurs near Re=400. The short vertical arrows denote the detachment and reattachment points reported by Armaly et al., and the computational locations are marked with longer vertical arrows. These computational locations were determined from the intersection of zero vorticity contours with the wall boundaries. The contours of negative streamwise velocity in Fig. 58 provide a visualization of the back-flow in the separation regions.

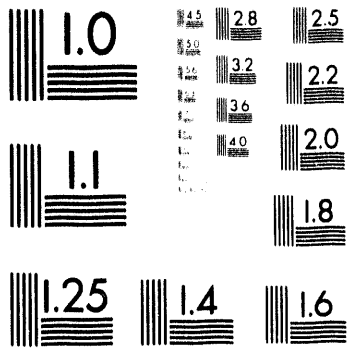
1.0
1.1
1.25
1.4
1.6
1.8
2.0
2.2
2.5
2.8
3.2
3.6
4.0
4.5
5.0

3 of 4

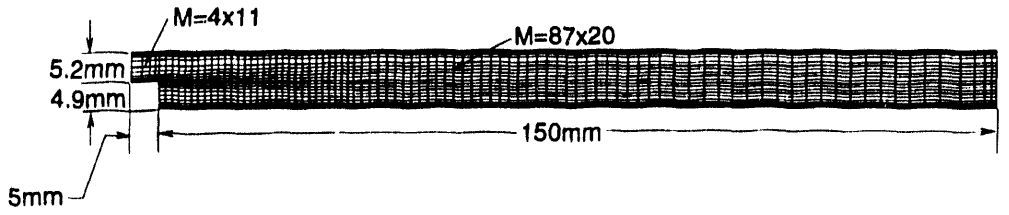

Figure 56. Mesh for 2-dimensional model, M=4×11×1 and 87×20×1.

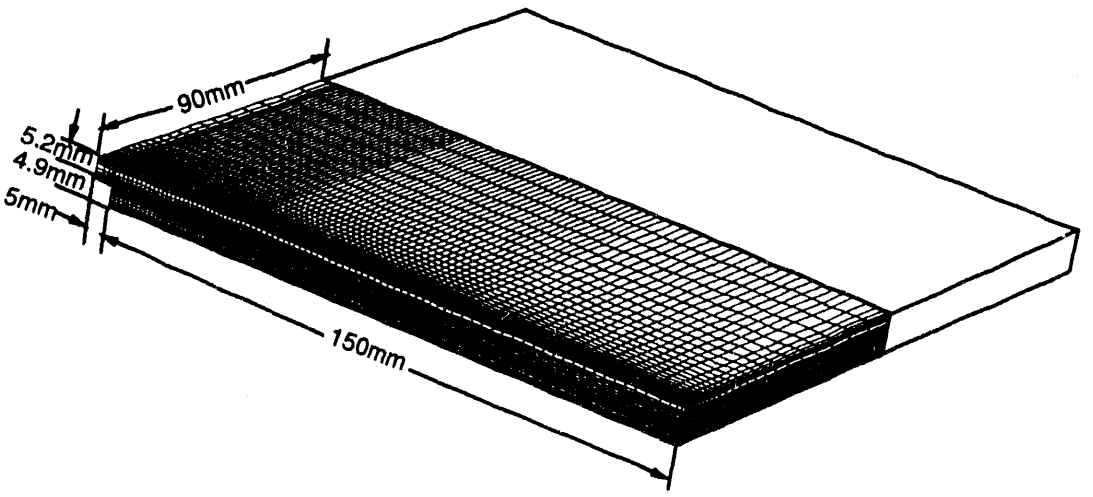

Figure 57. Mesh for 3-dimensional model, M=4×11×24 and M=87×20×24.

Primary reattachment lengths, normalized by the step height S, are plotted as a function of the Reynolds number in Fig. 59. The 2-dimensional computational data reported by various researchers show good agreement with the experimental values up to Re $\approx$ 400. Above 400, the computational results diverge, as expected, from the experiments.

Dispersion error control proved to be vitally important for maintaining solution stability above Re $\approx$ 400 in both the 2- and 3-dimensional simulations. Interestingly, the influence of dispersion error manifested itself most significantly in the pressure solution. Comparative pressure solutions are presented in Figs. 60a and 60b for Re=648. In Fig. 60a, the 2-dimensional simulation has been run 500 time steps with the steady state solution at Re=389 as the initial condition and the TWS dissipation parameter β=0. For the same initial condition but β=0.1, the pressure solution in Fig. 60b was obtained, also after 500 time steps. The presence of a dominant 2-Δx dispersive error mode can be clearly seen in Fig. 60a. A visual inspection of the corresponding velocity solutions showed no readily discernible differences; however, attempting to continue to a higher Reynolds number using the solution in Fig. 60a as the initial condition resulted in a divergence. A converged steady-state solution at Re=800 was obtained using the solution of Fig. 60b as the initial condition continuing with β=0.1. The pressure solution, therefore, represents a sensitive diagnostic measure of the presence of a very subtle, low-level, and potentially destabilizing dispersive-mode error in the velocity solution.

This sensitivity is due to the complex nature of the right-hand-side residual for the pressure Poisson solution. As discussed in Chapter 4, the residual for the pressure Poisson equation involves products of the velocity components and their spatial derivatives of the form

$$DET_e\ EIK_e\ EJM_e\ \{UJ\}^T[C30KM]\{UI\} \tag{374}$$

A number of areas were investigated to remove the dispersive error shown in Fig. 60a, including remeshing, using different iterative and direct linear algebra solvers, and modifying Eq. (374) to a simpler form

$$DET_e\ EIK_e\ EJM_e\ \overline{UJ}\ [C2KM]\{UI\} \tag{375}$$

None of these attempts were successful. Only the annihilation of the dispersive error in the velocity distribution through the TWS formulation provided the necessary smoothness in the pressure residual.

Velocity vector distributions on the symmetry plane of the 3-dimensional solution are shown in Fig. 61 for (a) Re=389, (b) Re=648, and (c) Re=800. In Fig. 62, the reattachment lengths of the primary separation region for this same symmetry plane are compared to the experimental data of Armaly et al. (1983) and the 3-dimensional computational results of Ku et al. (1989). The present 3-dimensional results show good agreement with the primary reattachment data of Armaly et al. above the Reynolds number at which the 2-dimensional solutions began to diverge. The resolution of the very thin secondary separation region on the upper wall of the channel is in general qualitatively good; however, the present mesh may not be sufficiently refined to recover the same level of detail obtained for the primary region.

Table 10. Computational Studies of Step-Wall Diffuser.

Researchers	Source	Method/Code	Mesh	Reynolds No.
Armaly et al., 1983	*J. Fluid Mech.*	SIMPLE/TEACH	45x45(2D)	≤1250
Kim and Moin, 1985	*J. Comp. Physics*	Chorin's projection method	101x101(2D)	100-800
Guj and Stella, 1988	*Int. J. Numer. Meth. Fluids*	vorticity- velocity	101x40(2D)	80-800
Sohn, 1988	*Int. J. Numer. Meth. Fluids*	penalty/FIDAP	61x33(2D)	100-800
Ku et al., 1989	*J. Comp. Physics*	pseudospectral matrix element (PSME)	297x33(2D) 42x36x48(3D)	75-450
Ghia et al., 1989	*Int. J. Numer. Meth. Fluids*	vorticity-streamfunction	195x33(2D)	300-1200
Thangam and Knight, 1990	*Comp. Fluids*	SIMPLE	120x61(2D)	33.3-600
Gartling, 1990	*Int. J. Numer. Meth. Fluids*	penalty/NACHOS II & FIDAP	800x40(2D)	800
Ikohagi and Shin, 1991	*Comp. Fluids*	SMAC	70x21(2D)	100-800
Ikohagi et al., 1992	*Comp. Fluids*	SMAC	75x35x31 (3D)	1000
Cabuk et al., 1992	*AIAA J.*	preconditioned pseudo-compressibility	121x21(2D)	100-600

(a) Re=389

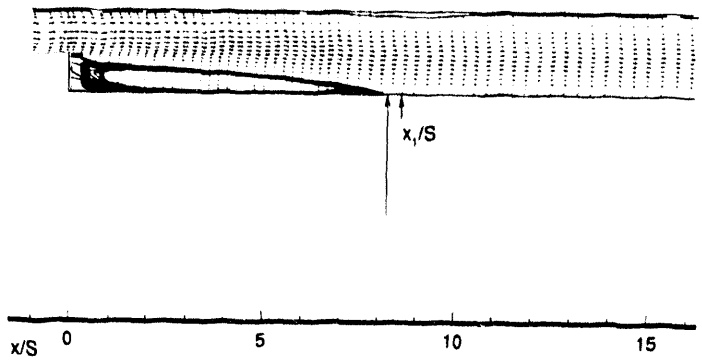

(b) Re=648

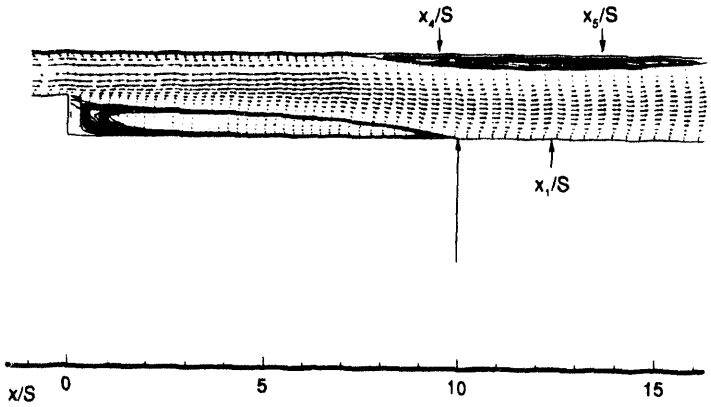

(c) Re=800

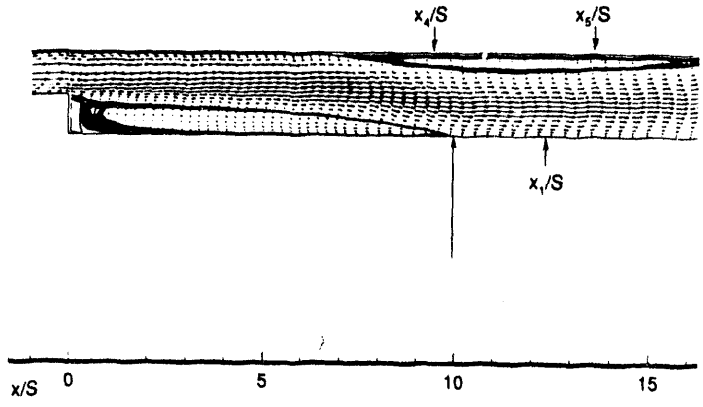

Figure 58. Present results for 2-dimensional simulations.

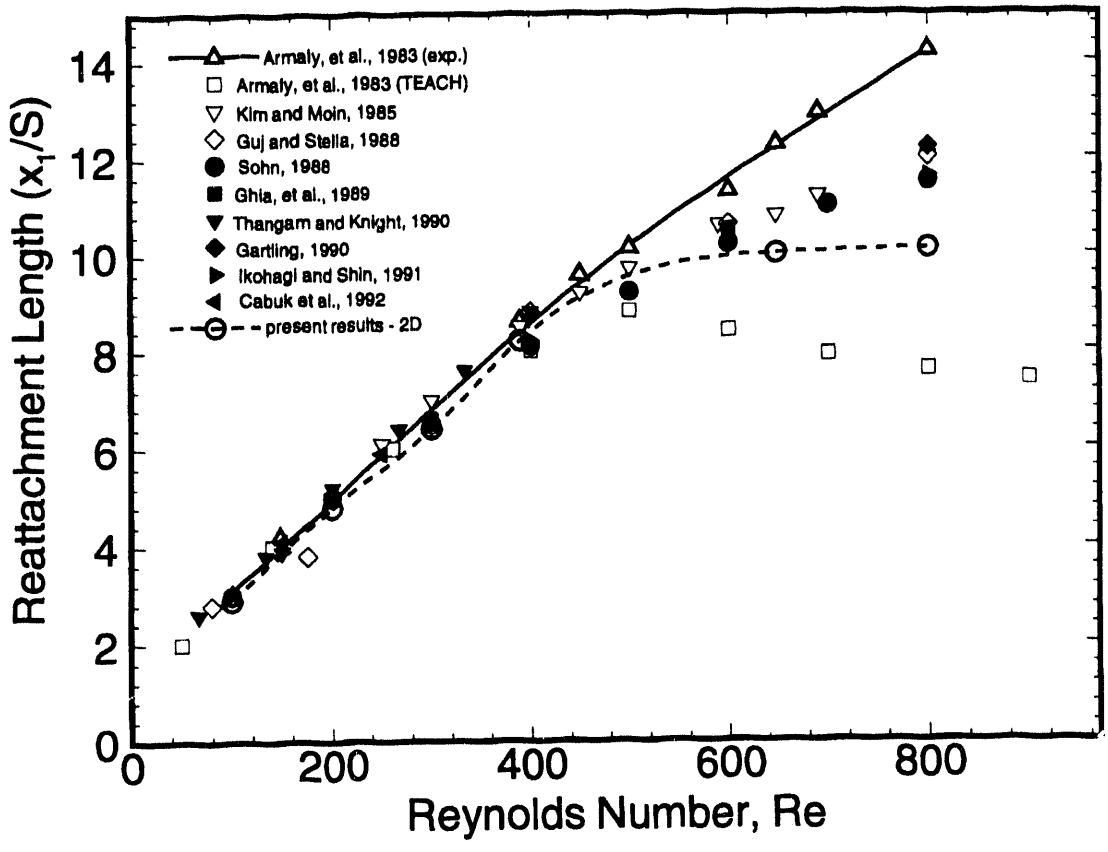

Figure 59. Primary reattachment length v. Re, 2-dimensional solutions.

(a) β=0

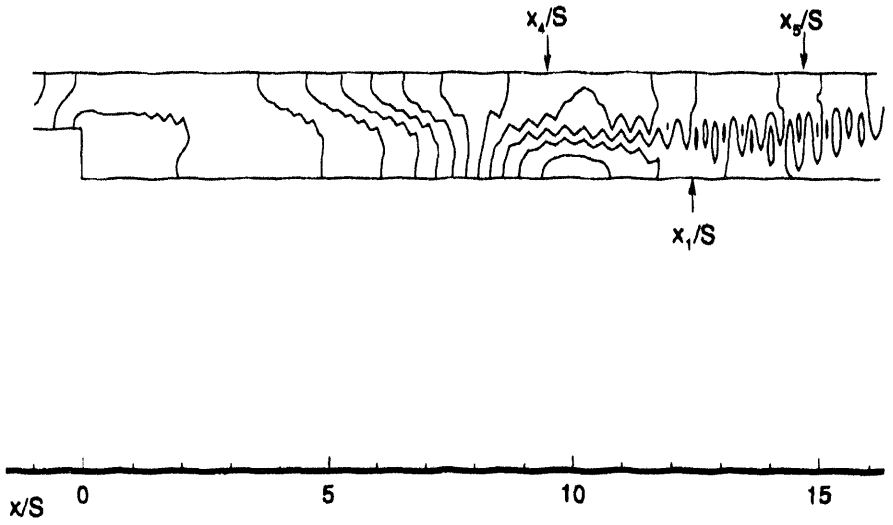

(b) β=0.1

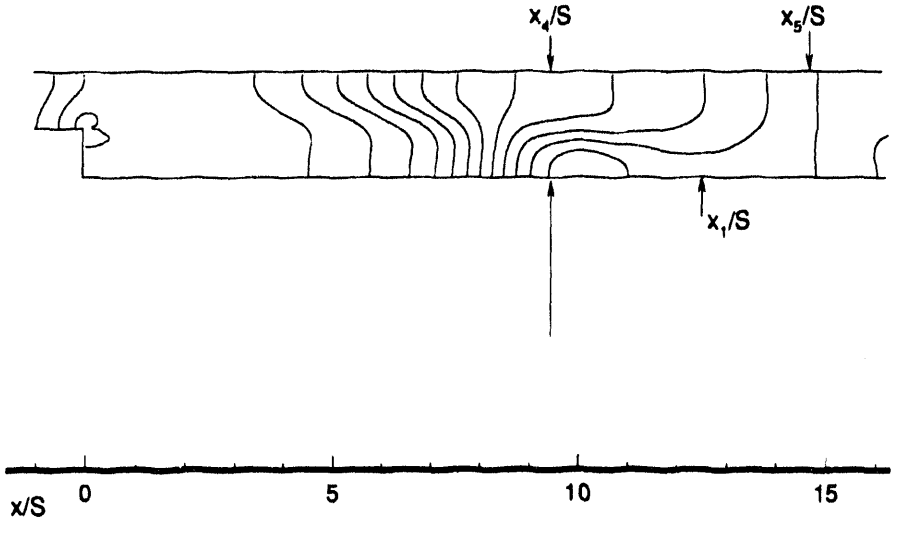

Figure 60. Two-dimensional pressure solutions at Re=648: (a) β=0, (b) β=0.1.

(a) Re=389

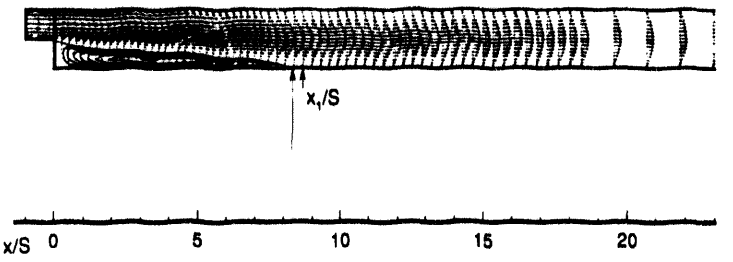

(b) Re=648

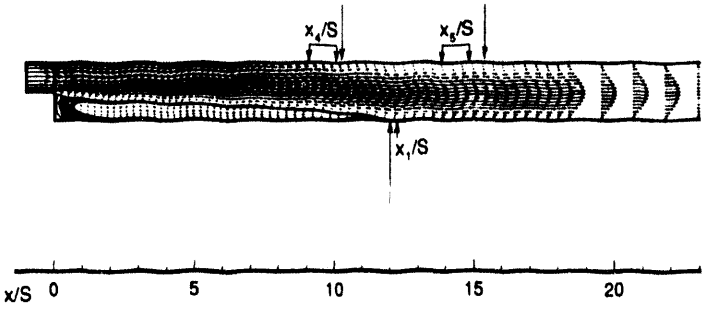

(c) Re=800

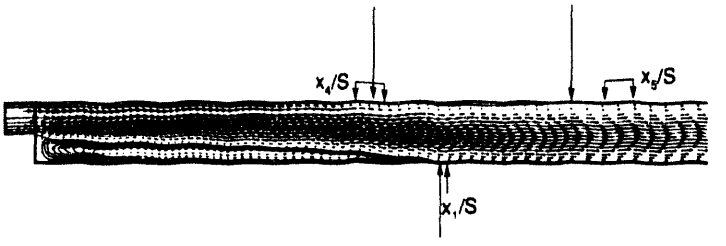

Figure 61. Present results of 3-dimensional model at symmetry plane.

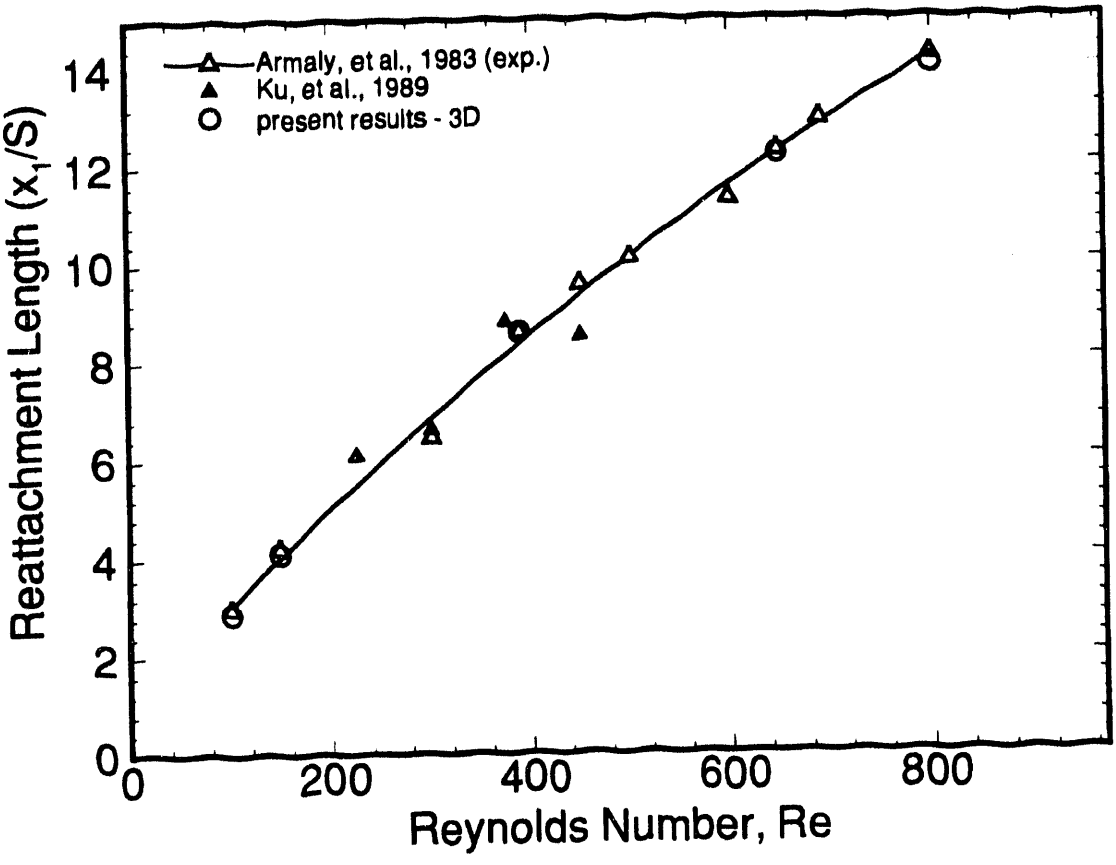

Figure 62. Primary reattachment points on the 3-dimensional symmetry plane v. Re.

As a demonstration of the 2- and 3-dimensional character of the flow below and above Re=400, respectively, Armaly et al. reported spanwise velocity profiles for Re=397 and Re=648. For Re=397, the spanwise scans were taken at an elevation 7.5 mm above the floor of the downstream channel, Fig. 63. The data from three x-stations, Figs. 64a-c, confirm that the flow is essentially 2-dimensional.

At x/S=6.22, which is upstream of the measured primary reattachment point, the 2-dimensional character of the flow field is captured by the present results; however, the magnitude of the computed axial velocity exceeds the experimental value by approximately a factor of 5. The low level of the experimental velocity is predicted to occur 2 mm above the 7.5 mm as graphed in in Fig. 64a. These experimental data
appear to be inconsistent with the magnitude of the axial velocities measured downstream of the primary reattachment point. By the conservation of mass, one would expect at least the average axial velocities at x/S=6.2 to be higher than those at x/S=14.3 and 18.9, due to the reduced axial-flow cross sectional area available where the primary recirculation region exists.

The computational results are in good agreement with the experimental axial profile at x/S=14.3, downstream of the reattachment of the primary separation. Further downstream at x/S=18.8, the experimental profile shows a significant increase in average velocity, and the computational profile indicates a slight decrease. If the flow has re-established an approximate fully-developed profile at x/S=14.3, as suggested by the agreement shown in Fig. 64b, then there appears to be a substantial error in the experimental results. The conservation of mass does not allow an increase in velocity unless additional (and undetected in both experiment and CFD simulations) separation regions were encountered in the channel. At all x-stations plotted, the 3-dimensional nature of the flow near the sidewall can be seen in the present results, which is apparently beyond the detection range of the experiment. As will be shown, the 3-dimensional structures near the sidewall are CFD-predicted to have a significant influence on the central flow field at higher Reynolds numbers.

For Re=648, experimental spanwise scans were taken at four x-stations and for two elevations, Fig. 65. The data of these scans are graphed and interpolated in Fig. 66, for y = 7.5 mm, and Fig. 67 for y = 2.35 mm. Armaly et al. report that, at this Reynolds number, the flow is 3-dimensional as confirmed by the variation in velocity across the lateral span of the flow field. In general, good agreement between CFD simulation and the experimental data at all x-stations and at both elevations is verified. However, calculated profiles present a much richer indication of the complex 3-dimensionality than is evident experimentally. The spanwise CFD mesh resolution provides a clear picture of smooth wave-like undulations in the axial velocity profile, only hinted at in the experimental data. In fact, the persistent flow reversals near the sidewall, missed in the experiments due to their limited range, are an indication of significant flow separation all along the duct sidewall.

Contours of negatively-directed axial velocity are presented in Figs. 68-71 to aid in visual interpretation of the primary and secondary separation regional extents on the lower "floor", upper "roof", and sidewall regions of the channel. The floor, roof, and sidewall data are those on the first interior plane of nodes, adjacent to the corresponding no-slip boundaries. In these figures, the roof has been rotated about the duct centroidal x-axis. At Re=389, Fig. 68, the flow is confirmed nominally 2-dimensional only over approximately the central two-thirds of the channel span. No secondary

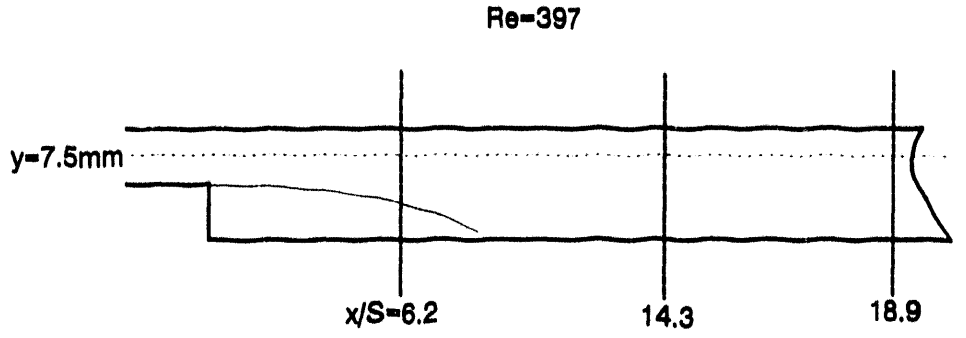

Figure 63. Locations of transverse planes for spanwise axial velocity profiles, Re=397.

(a) x/S = 6.22

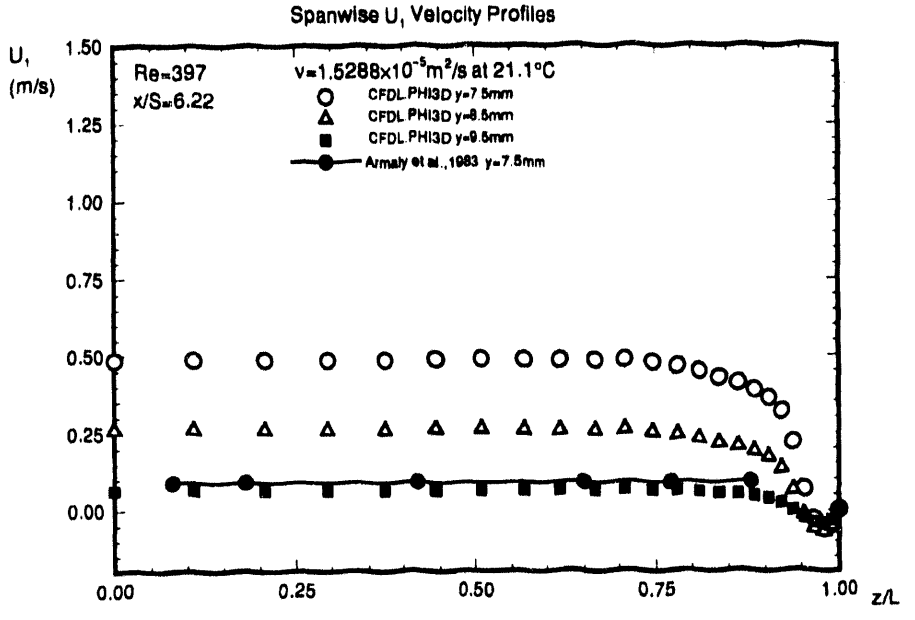

Figure 64. Comparison of spanwise velocity distributions, Re=397.

(b) x/S=14.3

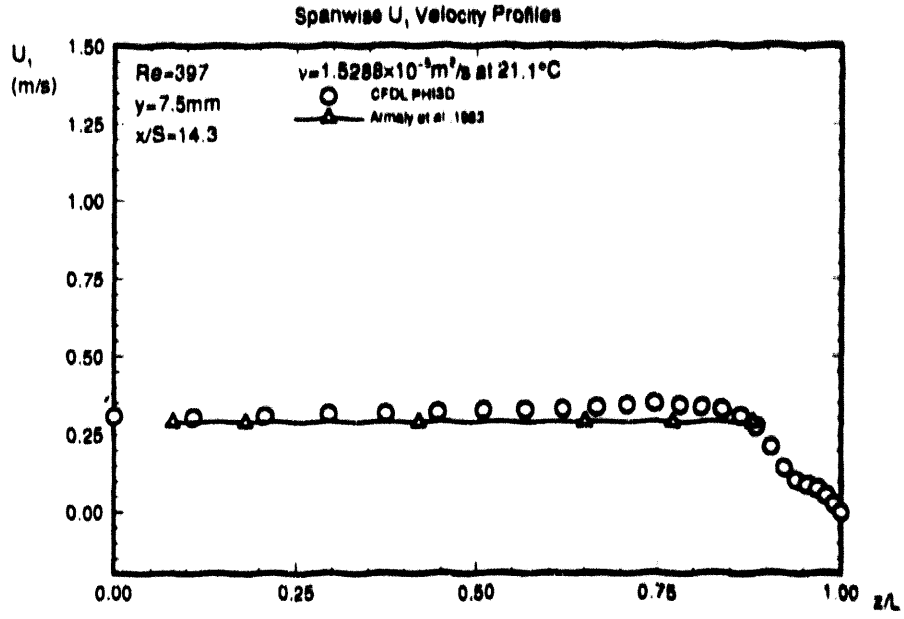

(c) x/S=18.88

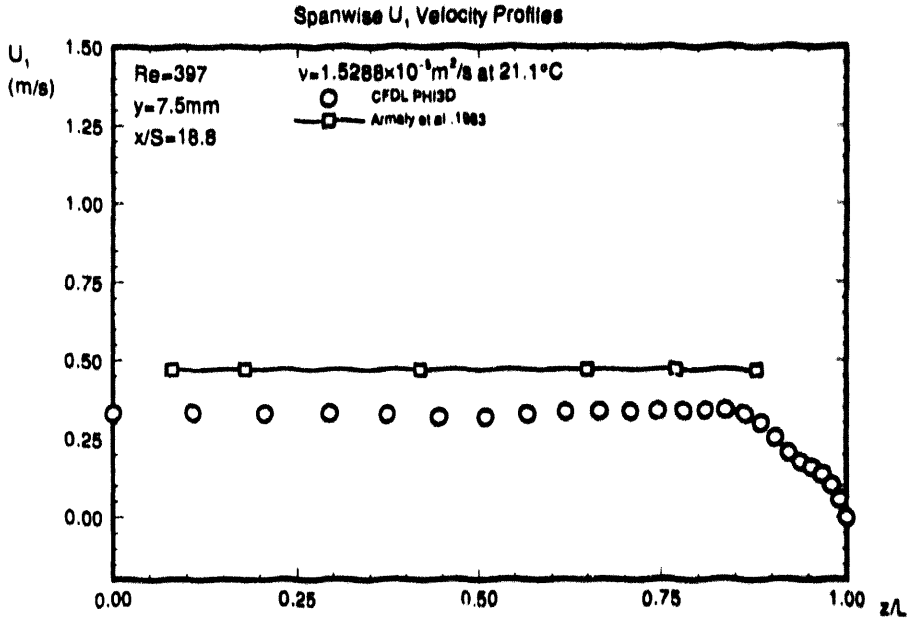

Fig 64. (continued) Comparison of spanwise axial velocity distribution, Re=397.

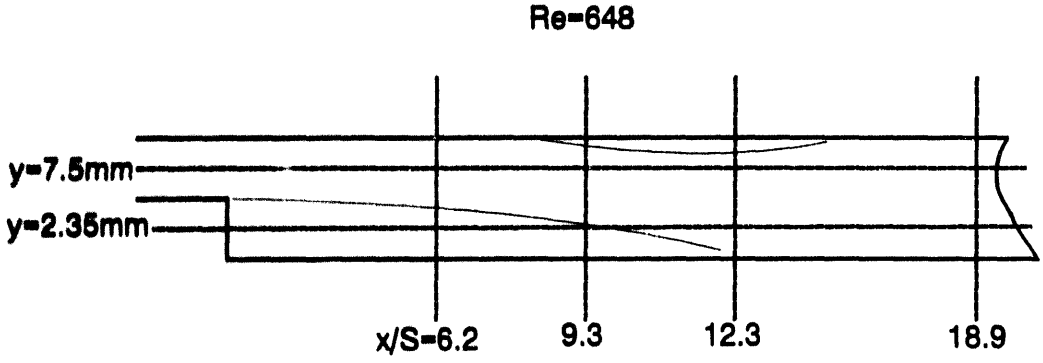

Figure 65. Locations of transverse planes for spanwise experimental velocity profile measurements, Re=648.

(a) x/S=6.22

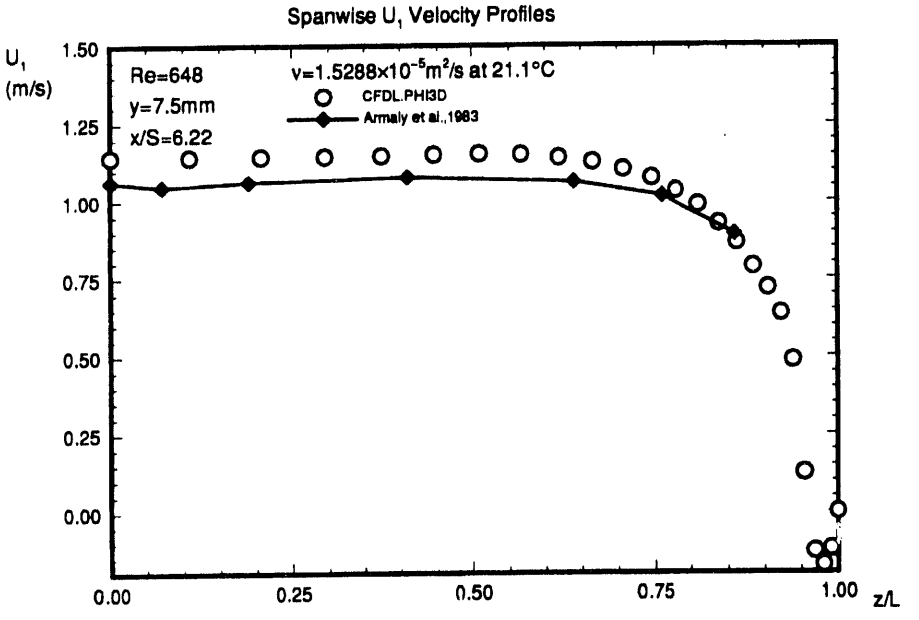

(b) x/S=9.29

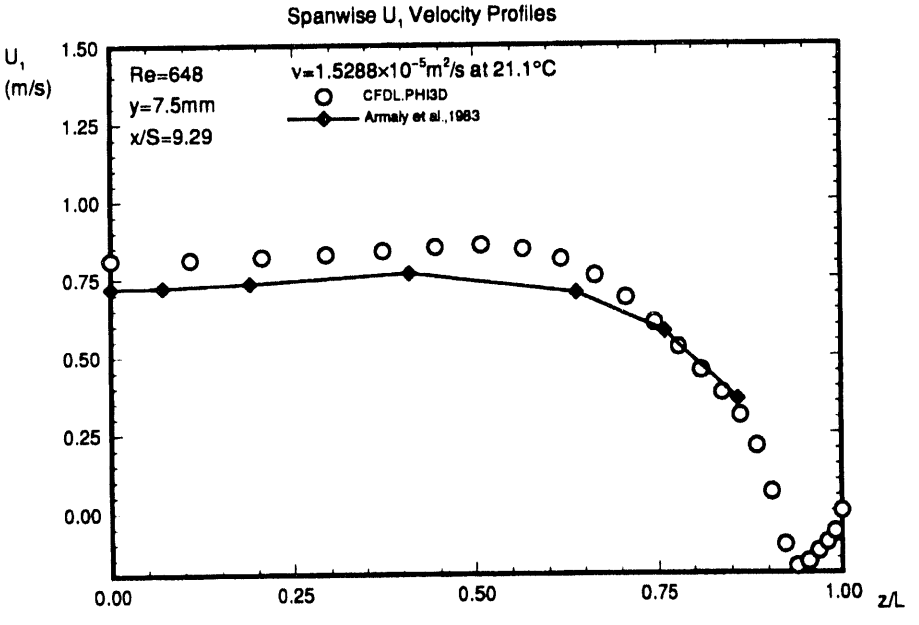

Figure 66. Comparison of CFD and experimental spanwise velocity profiles, y=7.5 mm Re=648.

(c) x/S=12.3

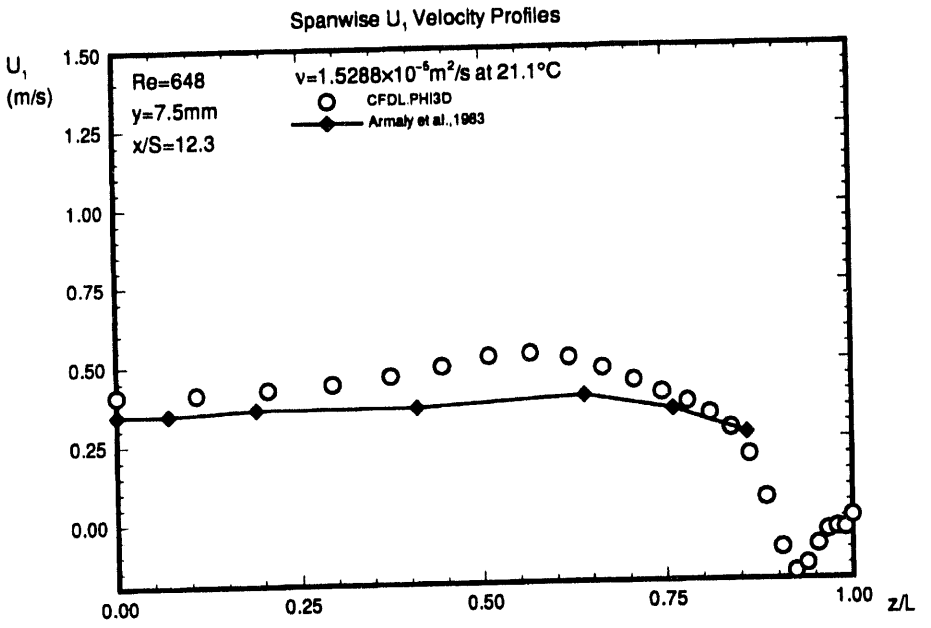

(d) x/S = 18.88

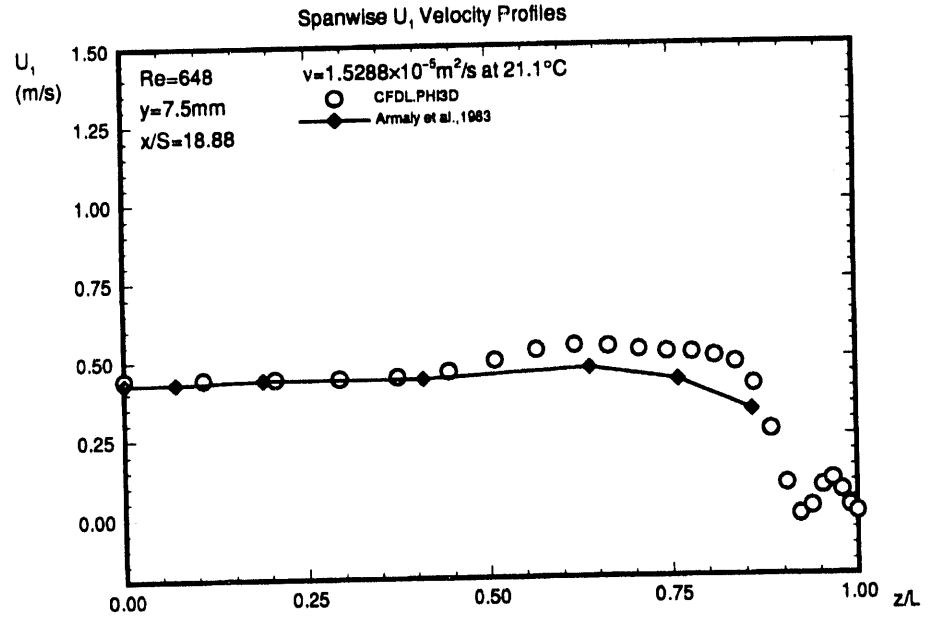

Fig. 66. (continued) Spanwise velocity profiles, Re=648 y = 7.5 mm.

(a) $x/S = 6.22$

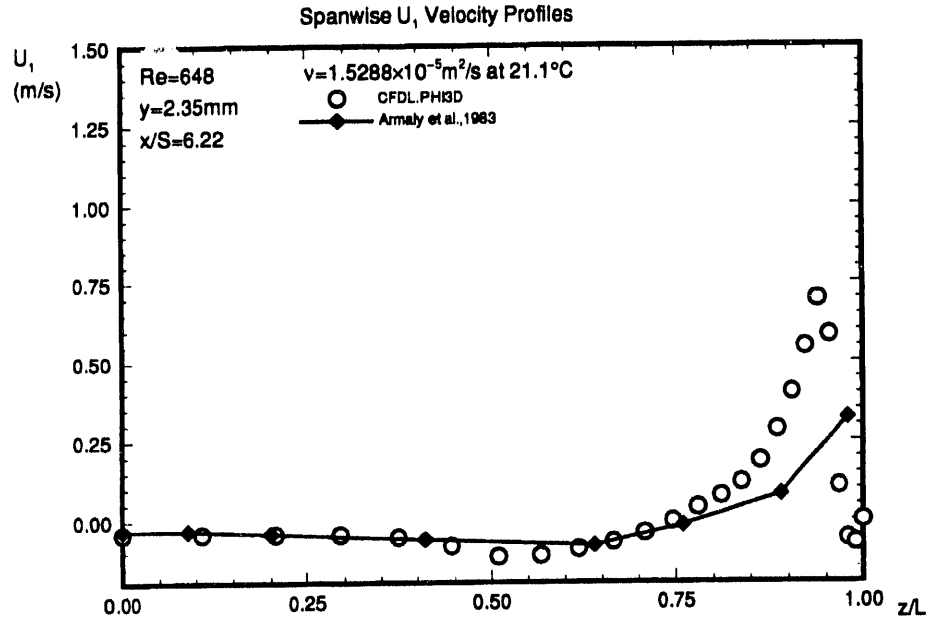

(b) $x/S = 9.29$

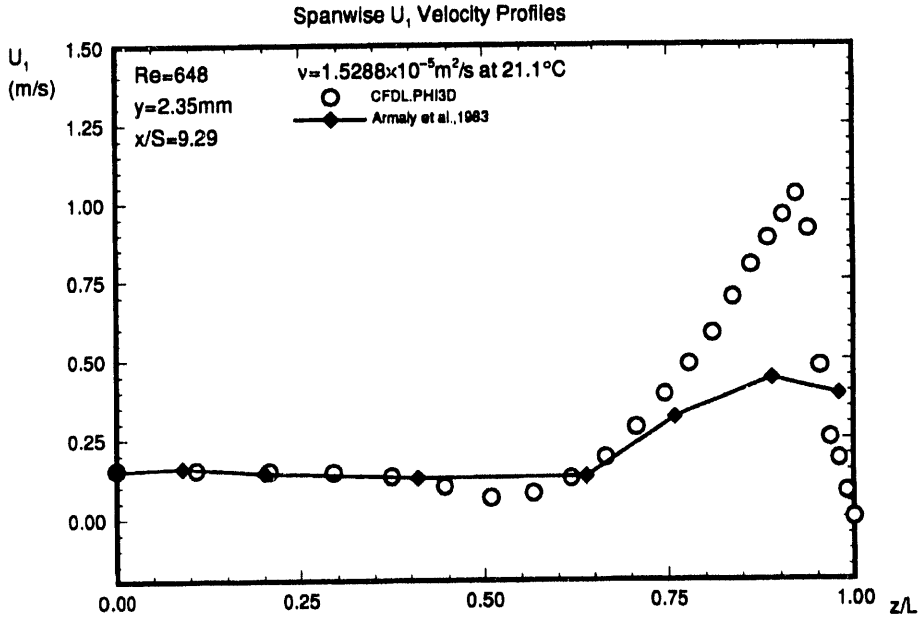

Figure 67. Comparison of CFD and experimental spanwise axial velocity profiles, y=2.35 mm Re=648.

(c) x/S = 12.3

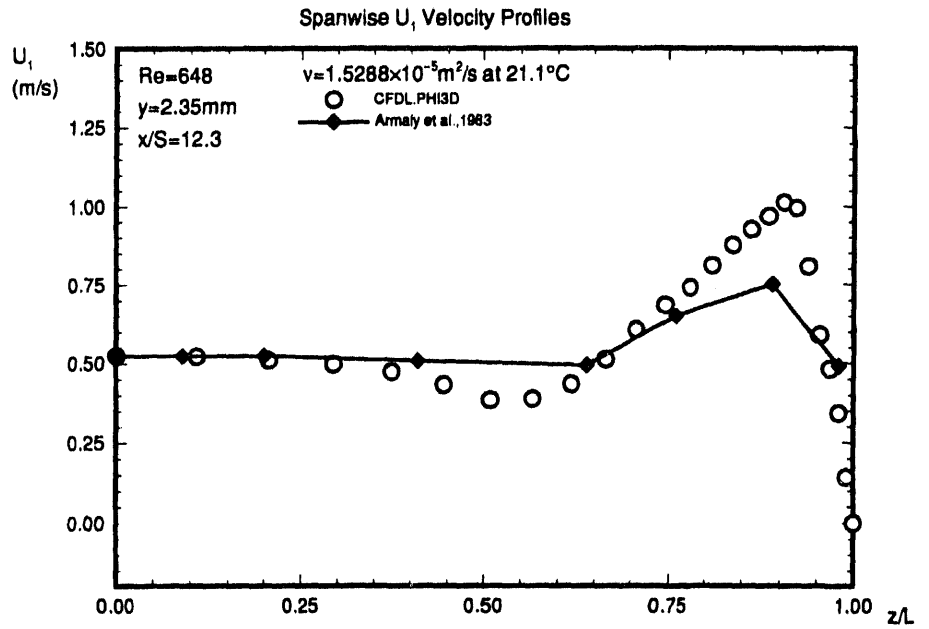

(d) x/S = 18.88

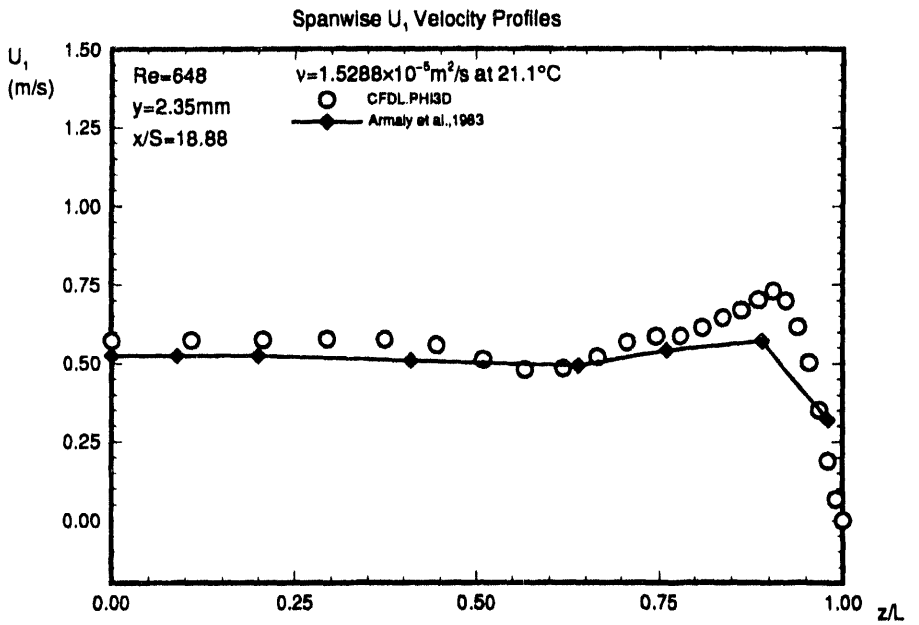

Fig. 67.(continued)Spanwise velocity profiles, Re=648 y=2.35mm.

region has yet developed on the roof near the symmetry plane; however, a significant 3-dimensional separation region exists along the sidewall axial corners, extending well downstream of the reattachment line for the primary separation region. The secondary region on the roof has appeared by Re=500, Fig. 69, but, this case was not run to a steady-state condition. During transients under Re continuation, the upper separation bubble selectively extends across the full span of the channel. However, at all steady-state solutions achieved, the upper separation region did not communicate across to the sidewall. At Re=648 and 800, Figs. 70 and 71, the primary separation bubble continues to grow, as does the penetration of the sidewall corner separation regions out into the main flow field. The separation bubble on the roof near the symmetry plane is very thin, approximately 1 mm, and does not connect with the sidewall separation region for Re $\leq$ 800.

As was the case with the 2-dimensional simulations, CFD dispersion error control was essential for obtaining stable solutions above Re$\approx$400. Two comparative pressure solutions are presented in Fig. 72 for Re=648 to illustrate this key issue. In Fig. 72a, the dissipation parameter β was set to 0, resulting in significant 2-Δx waves in the pressure solution occurring for a fully steady-state velocity prediction visually devoid of a dispersive error mode. Setting β=0.1 produced the smooth pressure distribution given, for the nominally (visually) identical velocity field, in Fig. 72b. Polluted pressure solutions from Fig. 72a are confirmed to prevent the attainment of stable steady-state solutions at Reynolds numbers above 400.

Another enhancement to improved visualization the flow field is via computation of "oil-flow" streaklines, as calculated from the projection of the velocity field onto horizontal planes near the floor and the roof. For Re=800, the solid lines with arrows, Fig. 73, are such streaklines demonstrating the significant 3-dimensional flow character around and within the primary and secondary separation regions. The solid lines without arrows are contours of negative streamwise velocity, corresponding to the contours presented in Fig. 71. The pronounced vertical-axis vortex in the flow near the roof, Fig. 73a, is very shallow (as will be examined further using a Lagrangian particle track in this region).

Flow field enlargements near the sidewall at Re=800 are projected in Fig. 74 onto transverse planes, located at x_1/S=7.72 and 18.37 step-heights from the step. These transverse projections clearly show the strong 3-dimensionality of the flow involving a wall jet at the step and complex vortex structures that extend well beyond the region of reverse flow, in the upper and lower corners of the channel, and into the central flow field. (The perspective graphs are included to enhance the location sense.)

Lagrangian particle tracks were calculated from steady-state velocity vector solutions using a modified Euler integration scheme suggested by Mallinson and de Vahl Davis (1973). For a particle release point of (5,5.1,89), the tracks for Re=389, 648, and 800 are shown in Figs. 75, 76, and 77, respectively. The diameter of the particle symbol (the"bubble") is a function of elevation above the channel floor, and the distance between each bubble represents a constant elapsed-time interval. In Fig. 78, the particle release point is near the vertical-axis vortex shown in Fig. 73b. Note that the bubble diameter is generally uniform, confirming the shallowness of the vortex structure at this location.

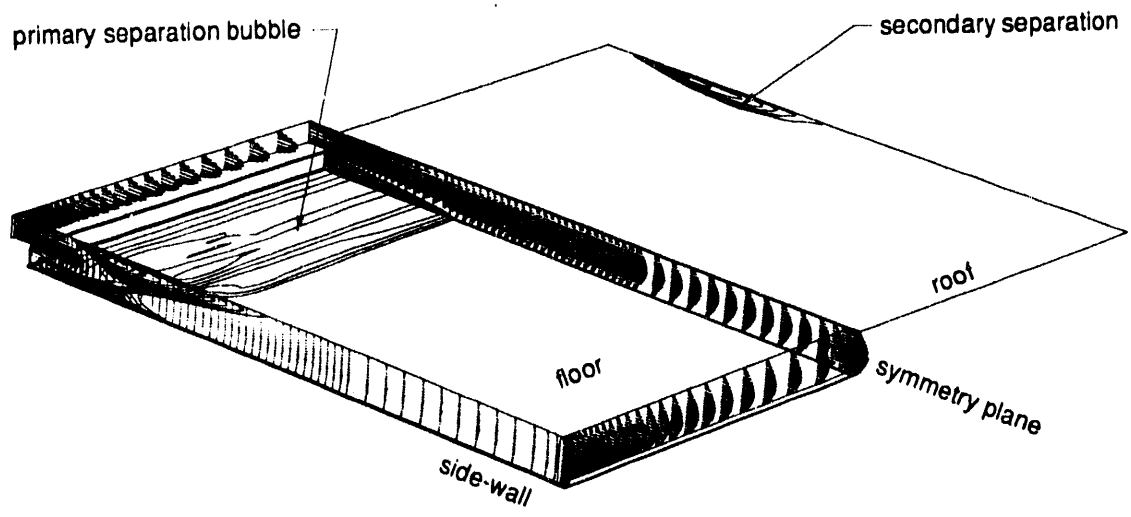

Figure 68. Separation region "footprints", Re=389.

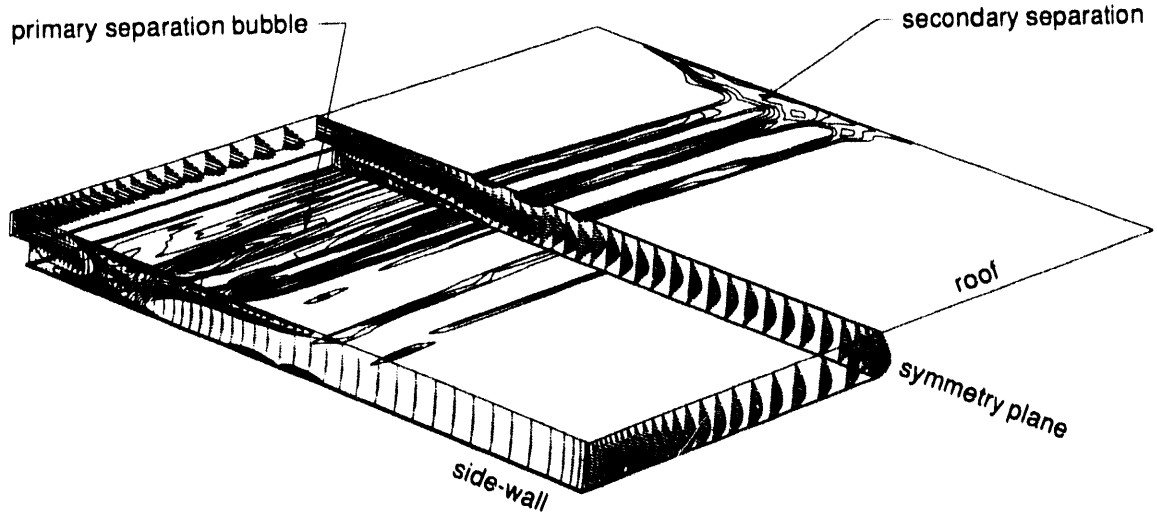

Figure 69. Separation region "footprints", Re=500.

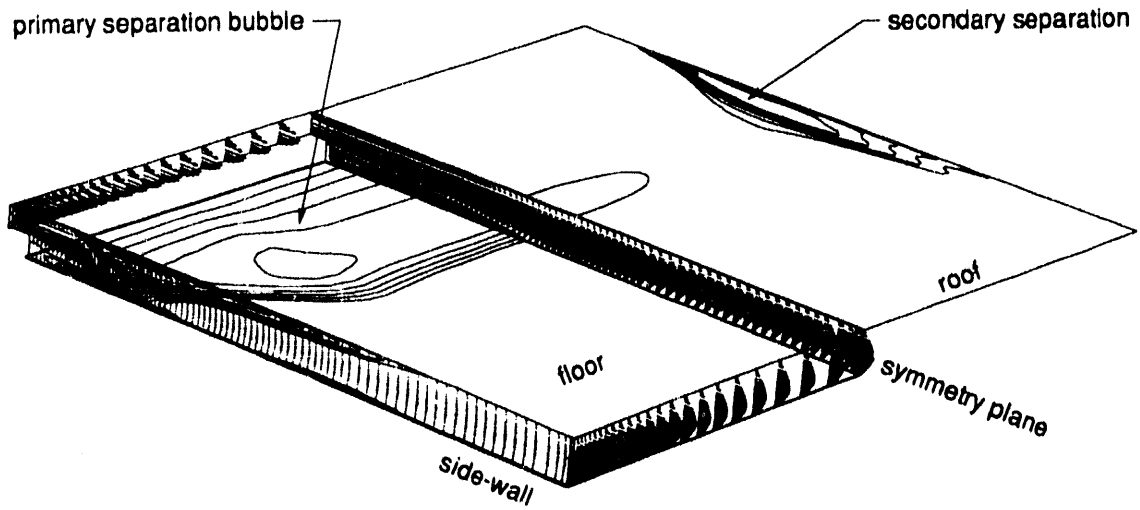

Figure 70. Separation region "footprints", Re=648.

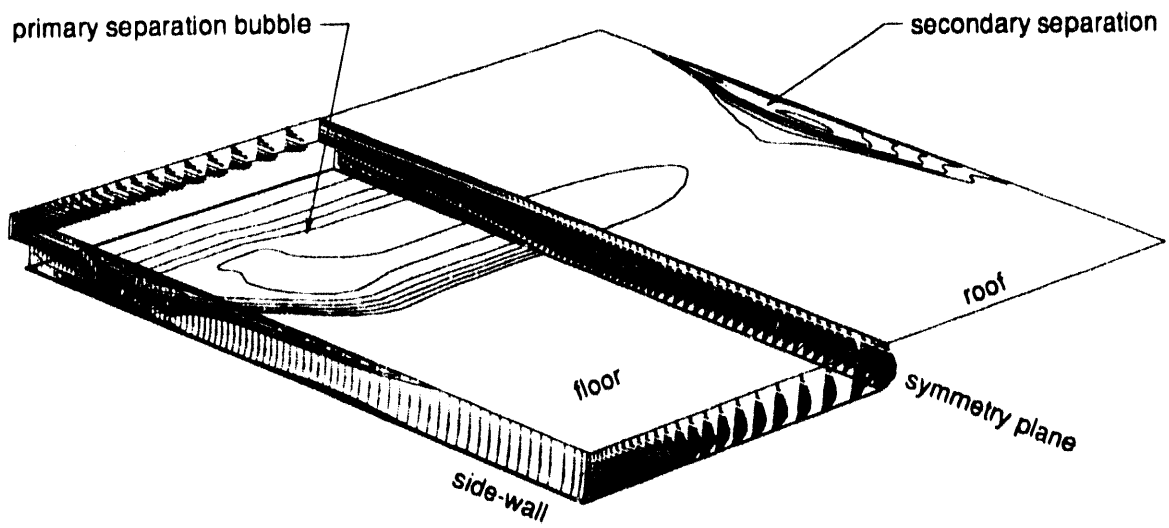

Figure 71. Separation region "footprints", Re=800.

(a) $\beta = 0$

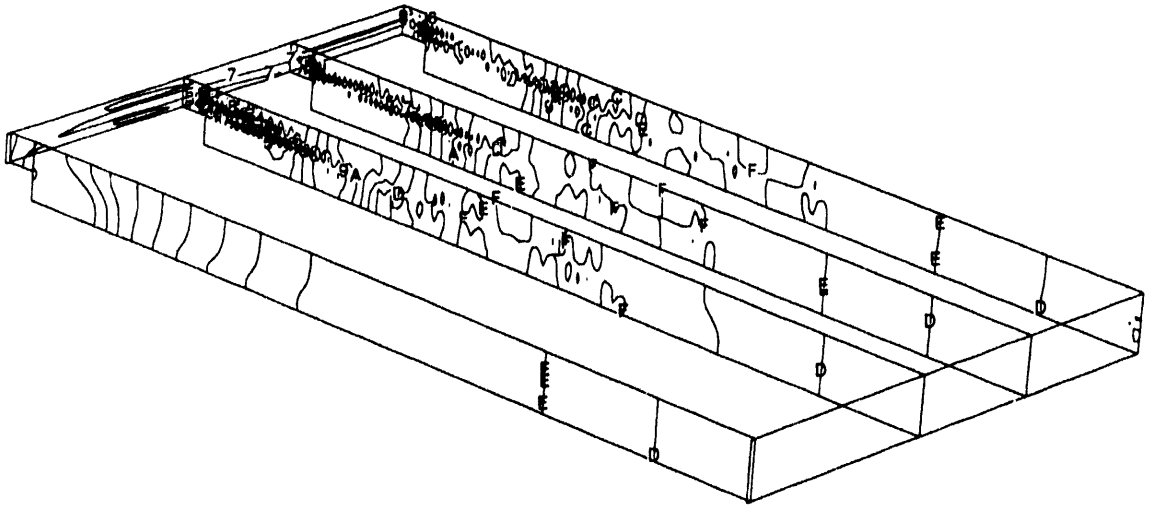

(b) $\beta = 0.1$

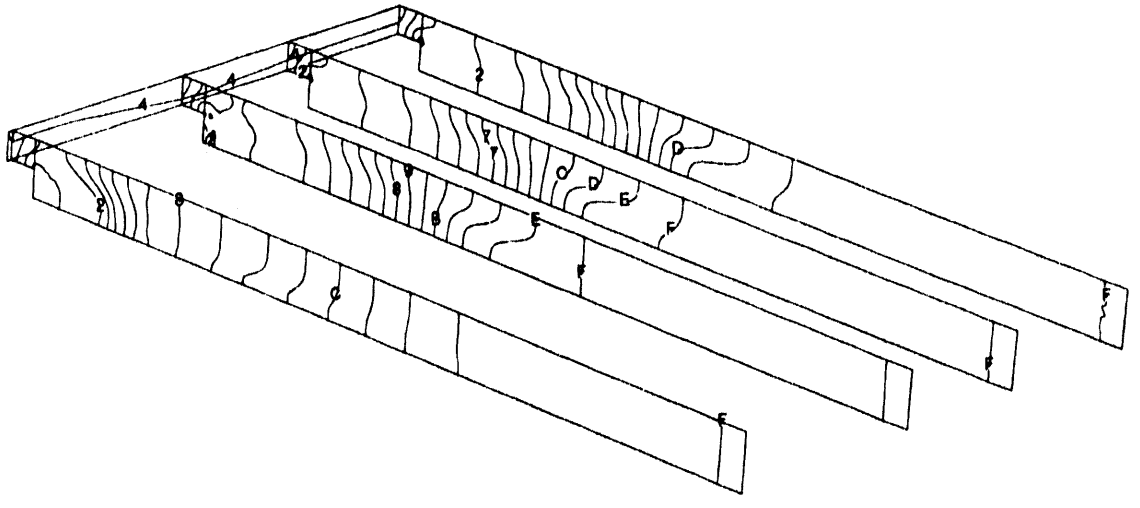

Figure 72. Pressure contours for Re=648.

(a) flow near the floor

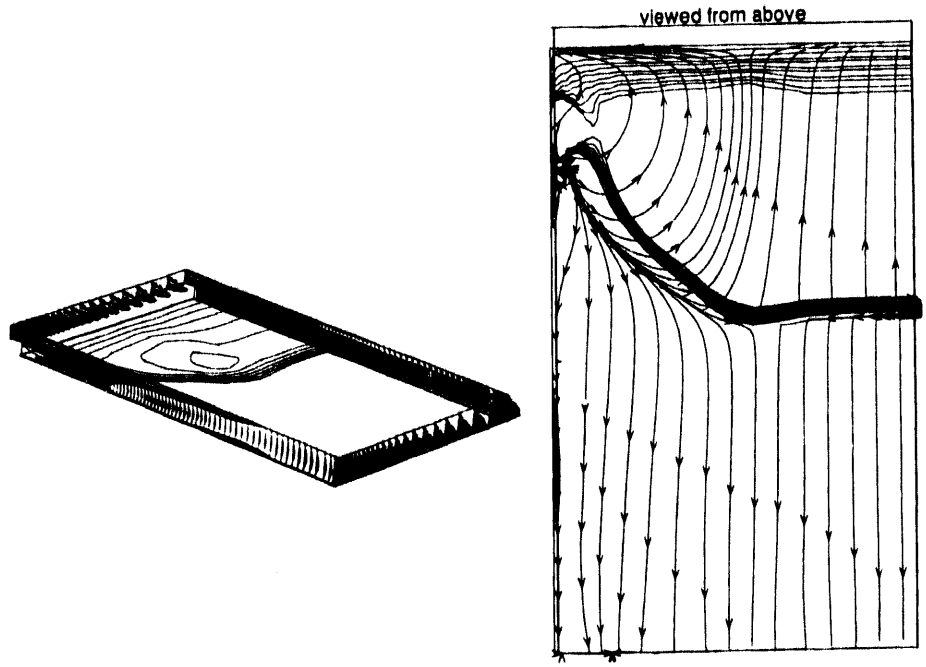

(b) flow near the roof

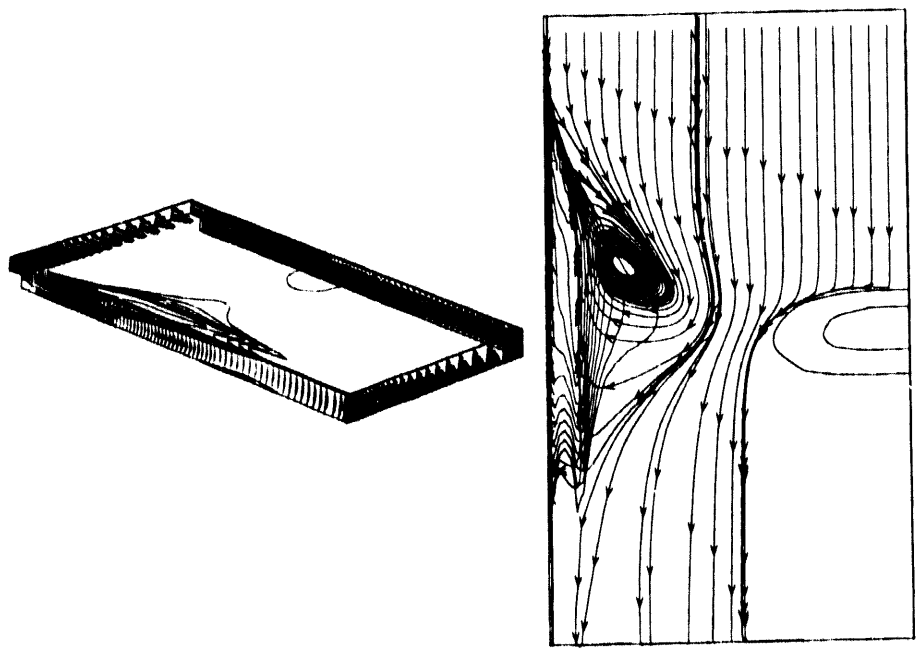

Figure 73. Oil-flow streaklines at Re=800 on horizontal planes.

(a) x/S = 7.72

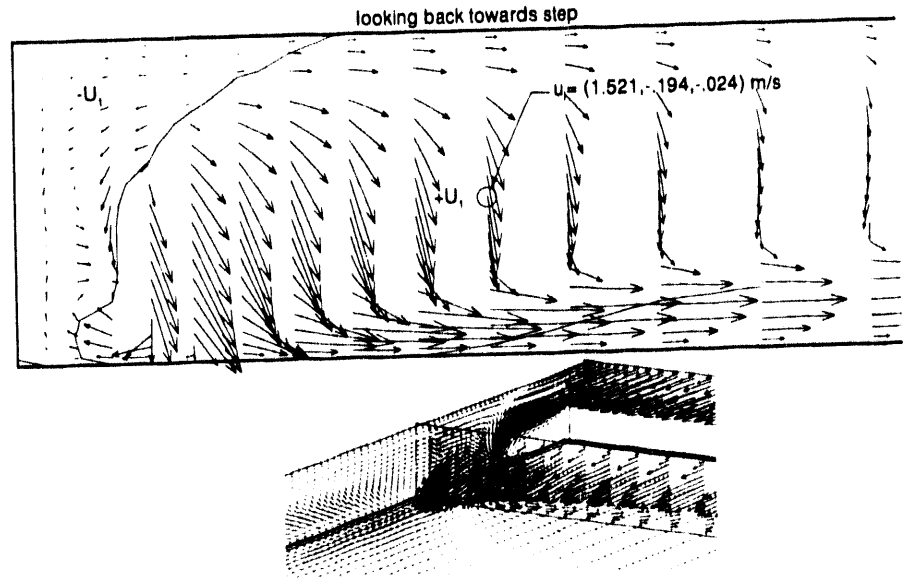

(b) x/S = 18.37

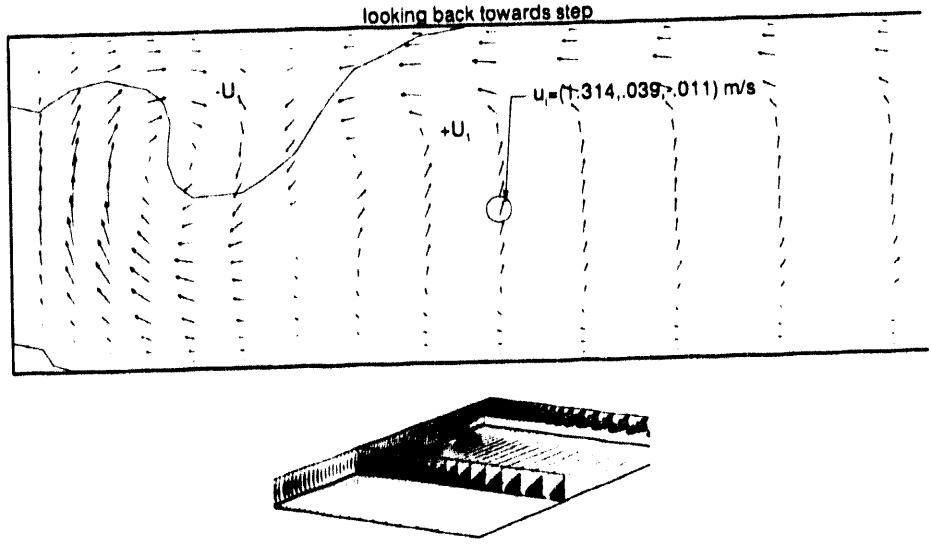

Figure 74. Flow field near the sidewall projected onto transverse planes, Re=800.

(a) view from symmetry plane

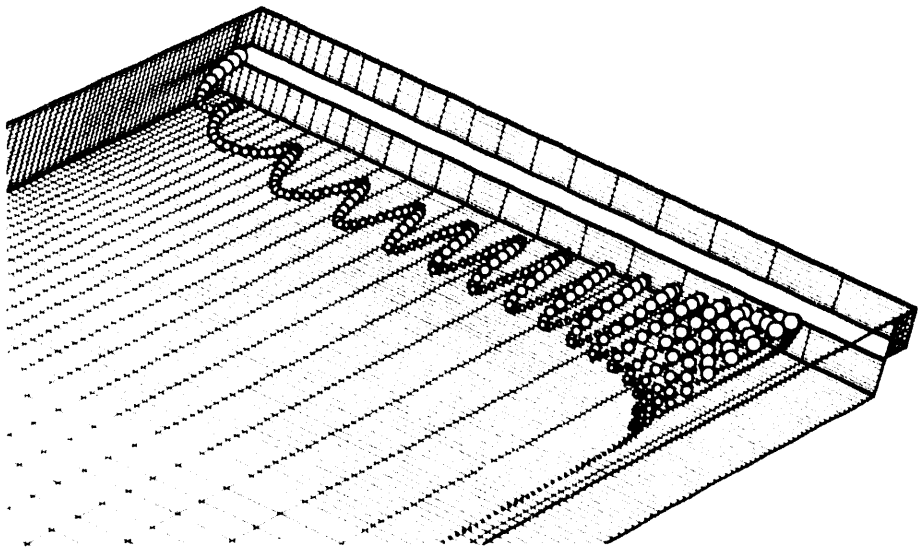

(b) view from above

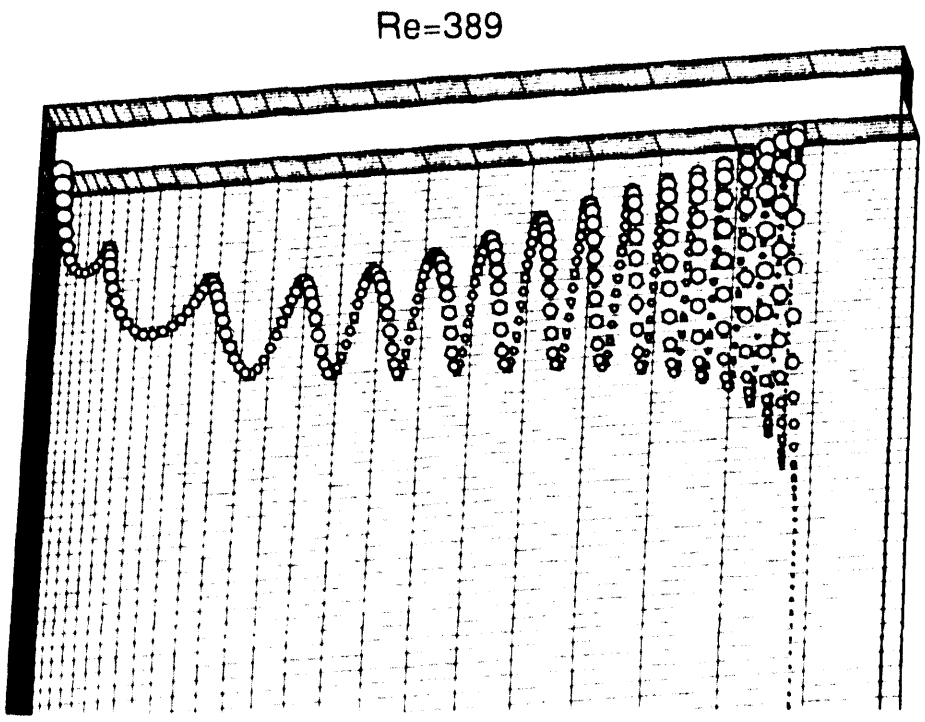

Figure 75. Lagrangian particle track for Re=389.

(a) view from symmetry plane

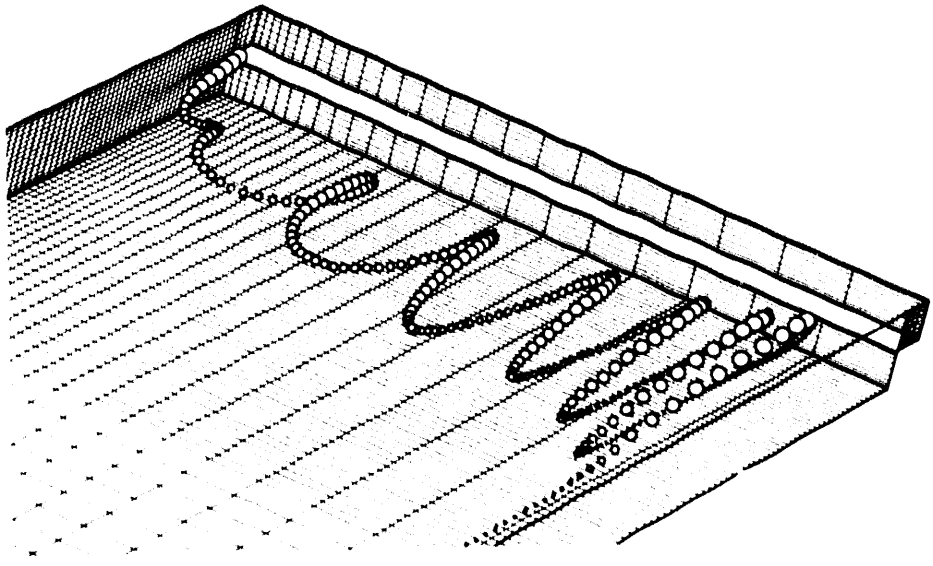

(b) view from above

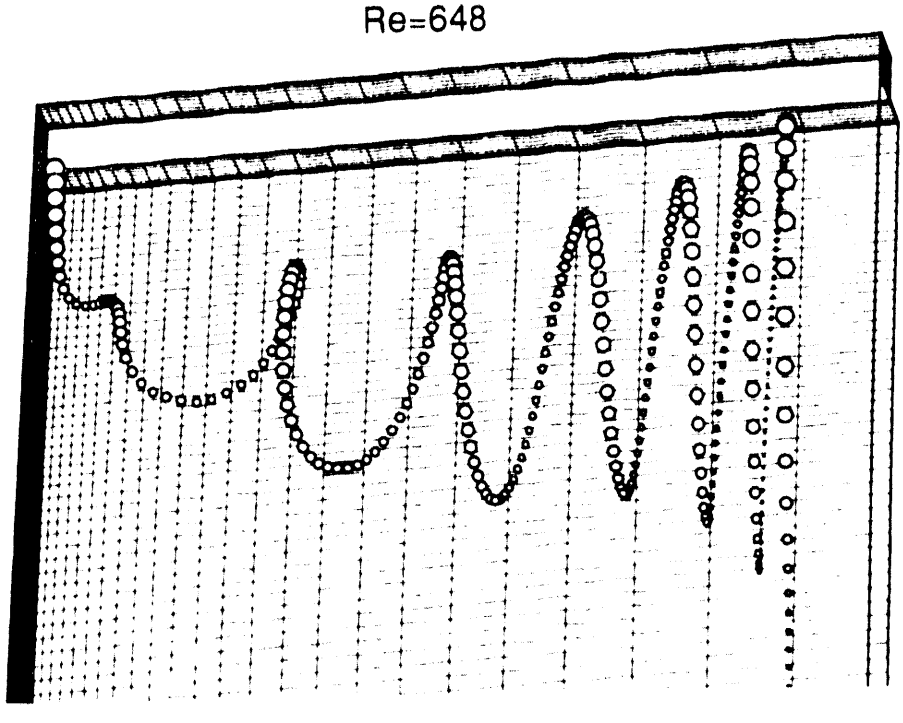

Figure 76. Lagrangian particle track for Re=648.

(a) view from symmetry plane

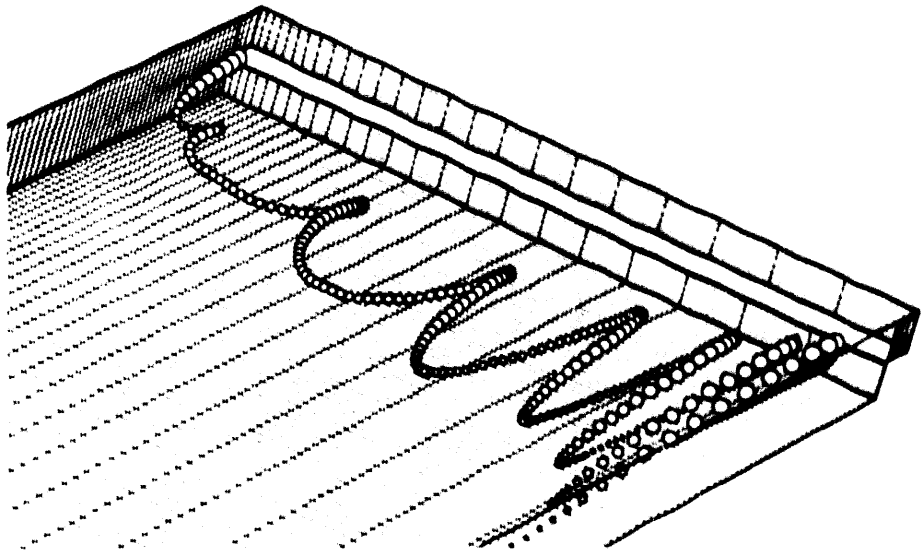

(b) view from above

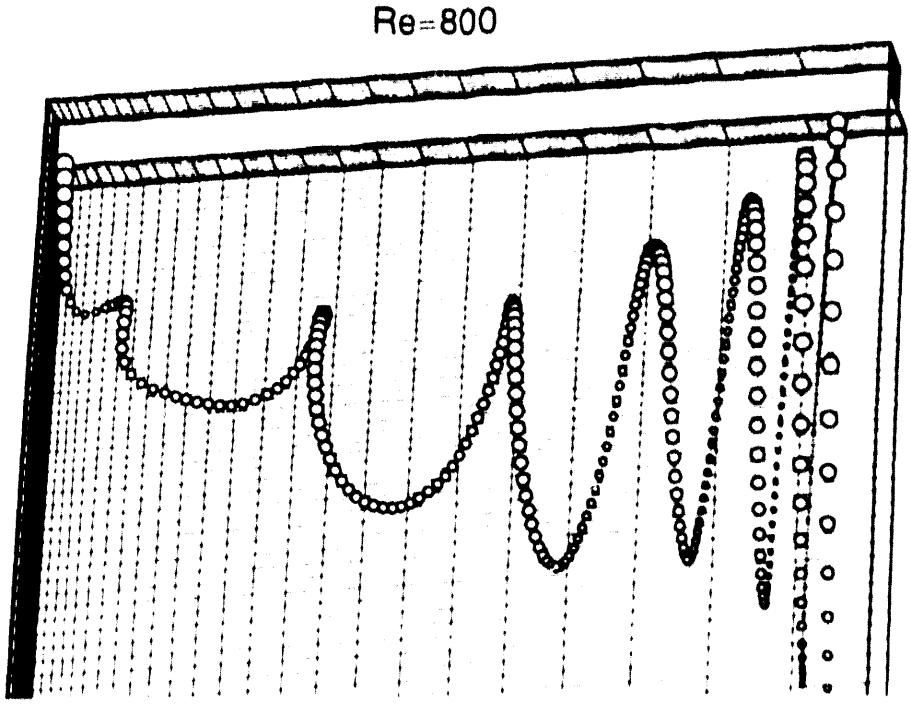

Figure 77. Lagrangian particle track for Re 800.

(a) view from symmetry plane

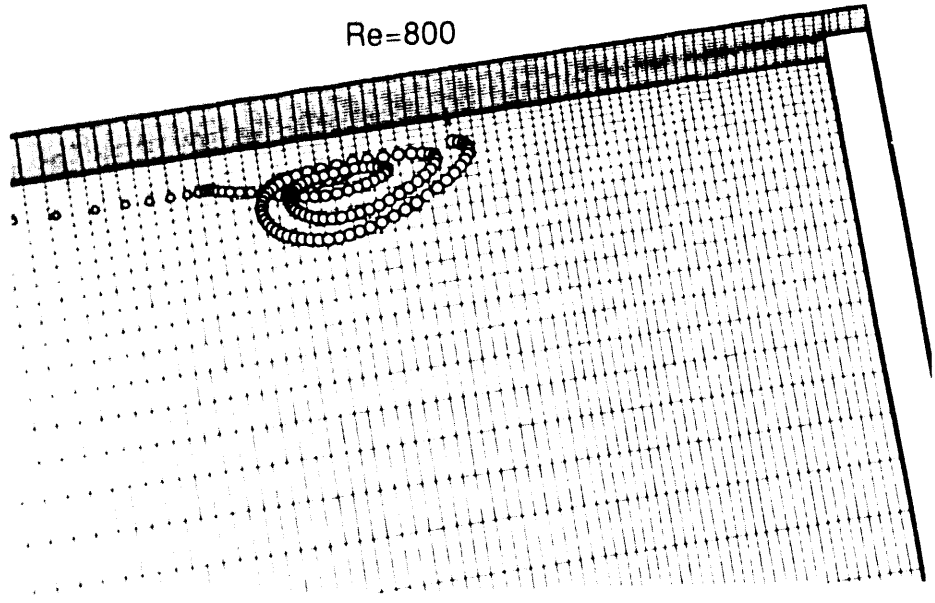

(b) view from sidewall

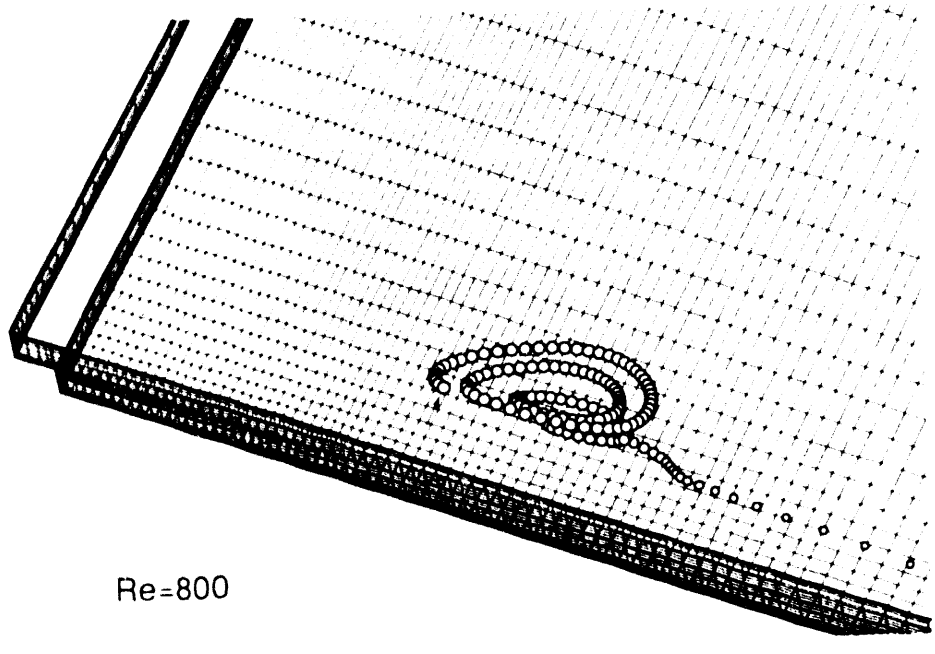

Figure 78. Lagrangian particle track, release point near vertical-axis vortex structure at roof, Re 800.

Ghia et al. (1989) have suggested two possible mechanisms for what they termed an "abrupt change" in flow structure from 2- to 3-dimensional flow when the secondary separation bubble first appears on the upper wall at Re≈400. They note that 2-dimensional boundary layer flows, subject to a locally destabilizing concave curvature of the boundary, are susceptible to a Taylor-Görtler vortex instability. Spanwise-periodic counter-rotating pairs of vortices with axes aligned with the main flow direction are formed as a result of this instability. It has been suggested that such a vortex instability could be a common phenomenon near 2-dimensional separation points. Ghia et al. postulate that the appearance of the secondary separation bubble on the upper wall provides the necessary conditions for the formation of Taylor-Görtler vortices, and they propose "that the additional mixing which would accompany a developing Taylor-Görtler instability would tend to delay the upper wall separation; thus causing the secondary separation point, x_s, to occur farther downstream than would be predicted on the basis of a strictly two-dimensional analysis." The delay of the detachment of the secondary separation decreases its blocking effect and allows the development of a longer reattachment length for the primary separation bubble than would be predicted in the absence of this 3-dimensional disturbance.

The alternative mechanism suggested by Ghia et al. involves the growth and interaction of the boundary layers on the sidewalls of the test section. They rejected this mechanism based upon their assumption that the effect would tend to decrease with increasing Reynolds number due to a thinning of the sidewall boundary layers.

The present results support the contention that the formation and structure of the upper separation region is a critical element in explaining the divergence of 2-dimensional simulations from the experimentally observed primary reattachment lengths. Comparison of the 2- and 3-dimensional results in Figs. 58 and 61, respectively, shows that a much thicker separation bubble is formed in the 2-dimensional simulation which, once established, produces a relatively stationary blockage of the channel. This blocking effect serves to prevent the growth of the primary reattachment length with increasing Reynolds number.

Armaly et al. present the spanwise velocity profiles shown in Figs. 64, 66, and 67 as evidence for their contention that the flow is 2-dimensional for Re < 400 and 3-dimensional for Re > 400. There is generally good agreement between the present results and their experiments for Re = 397 and excellent agreement for Re = 648. The present computational results, however, reveal details of the flow structure, unavailable to Armaly et al., which suggest a third mechanism for the development of strongly 3-dimensional flow with increasing Reynolds number.

A wall jet, attached to the sidewall as shown in Fig. 74, forms at the step plane and grows in strength with increasing Reynolds number. Observed at the lowest Reynolds number simulated (Re=100), this wall jet, interacting with separation regions along the upper and lower corners of the sidewall, is the source of 3-dimensional vortices in the vicinity of the sidewall which penetrate the central flow stream within the primary separation region. The particle tracks in Figs. 75-77 reveal a fascinating picture of very complex 3-dimensional flow structures. Even at Re = 389, the tracking particle, released at the source of the wall jet in Fig. 78, shows a spiralling 3-dimensional path from the sidewall to the central symmetry plane. Nearing the symmetry plane, the particle joins the essentially 2-dimensional primary separation region. As the Reynolds number increases, the wall jet strengthens, and the point at which the tracking particle is caught up by the central separation region moves closer to the symmetry plane, Figs. 76 and 77. Rather than thinning, the separation region along the sidewall continues to develop with increasing Reynolds number. Complex 3-dimensional

vortices can be observed along the sidewall, Fig. 73, and roof, Fig. 78. In summary, the present results show that the transition from 2- to 3-dimensional flow is not an "abrupt change" but rather a continuous penetration of 3-dimensional flow, fed by a wall jet, from the sidewall to the central symmetry plane.

7.6 FULL-SCALE ROOM AIR EXPERIMENT

In the Ph.D. dissertation of Spitler (1990), see also Spitler et al. (1991) and Cantillo (1990), flow field and temperature data were taken for several settings of the University of Illinois Dept. of Mechanical Engineering full-scale room ventilation test facility. Figure 79 illustrates the basic supply/exhaust configuration for the test facility which is 15 ft long, 9 ft high, and 9 ft wide. The walls have individually controllable heating panels, and the ceiling and floor of the room are insulated. Two supply discharge locations are available, in the east side-wall, flush with the north wall, and in the center of the ceiling. In the selected experiment, only the east side-wall supply and west side-wall exhaust are active.

A ventilation system is available to supply cool air to the room through one of the supply discharges at flow rates ranging between 2 and 100 air changes per hour (ACH). Additional details on the room experimental facility and the available control systems can be found in the cited references.

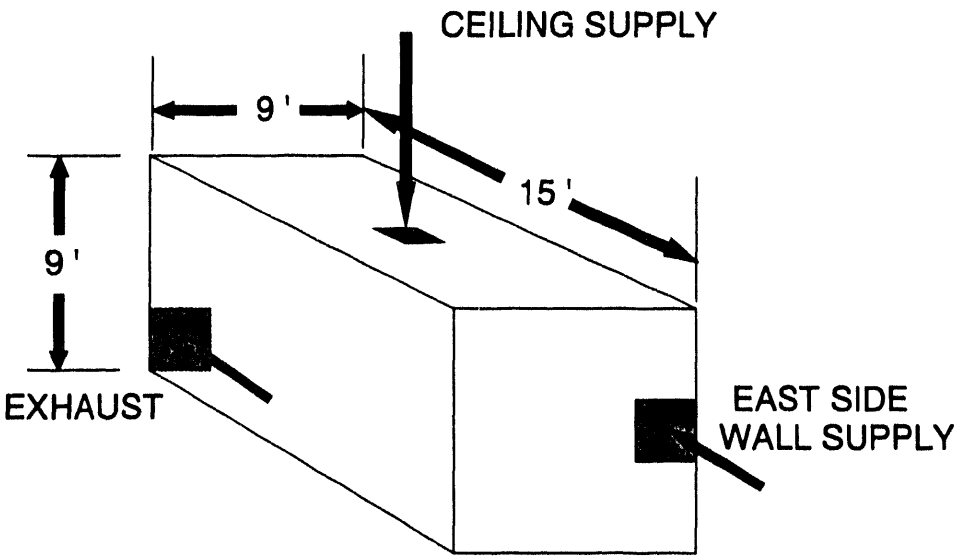

Figure 79. Schematic of U. Illinois room ventilation test facility.

Two data sets were selected from Spitler (1990) for comparison to the developed CFD simulation. These are: (a) buoyancy-dominated flow rate of 15 ACH and Archimedes number (Ar) =4.3 and (b) a flow rate of 30 ACH and Ar=0.82. Other data at selectively larger ACH are also reported, but these specifications are well beyond nominal HVAC comfort performance specifications. The data presentations are mainly grey-scale graphs of measured room air speed on select planes, Fig. 80, and as room-averaged thermal stratification maps at select locations, Fig. 81. Somewhat more detailed velocity (speed) and temperature data are presented in Cantillo (1990), Fig. 82 and Fig. 83, but the air flow rate of 50 ACH well exceeds the nominal comfort range for HVAC systems. Cantillo (1990) did not report Archimedes numbers.

For the test conditions studied, the supply outlet was an unobstructed opening (no vanes). The mass-average inflow speed for 15 ACH was ~80 fpm at 69°F, while, for the 30 ACH test, the supply flow average speed was ~160 fpm, also at 69°F. The experiment Reynolds numbers, based on the molecular viscosity of air and the supply duct hydraulic diameter and bulk velocity, are Re_{15}=15,000 and Re_{30}=30,000, respectively, where the subscript denotes ACH. The reported Archimedes numbers (Spitler, 1990) are Ar_{15}=4.3 and Ar_{30}=0.82, based on bulk velocity in the supply duct, as the velocity scale, and the longest possible "throw" of the supply jet (15 ft) as a reference length scale. Finally, the ΔT_{ref} used in the Ar definition is the difference between the supply and exhaust air temperatures.

The selection of an appropriate and consistent set of U_{ref}, L_{ref}, and ΔT_{ref} to compute the Ar and Re is somewhat arbitrary. Spitler (1990) discusses various combinations used by different researchers to correlate room ventilation experimental data. The primary application for the Archimedes number is in the development of empirical correlations for predicting the trajectory of the supply jet. Such correlations are typically independent of viscous effects, i.e., they do not include the Reynolds number. To the experimentalist, it is, therefore, not necessary that both the Ar and the Re be defined in terms of the same characteristic length and velocity scales.

For CFD applications, however, the Ar and Re both appear as scaling parameters in the momentum equations, so they must be defined consistently. For these CFD experiments, the length scale was taken to be the height of the room, 9 ft, and the velocity scale was the bulk velocity in the supply duct. The ΔT_{ref} is defined as the difference between the prescribed wall boundary temperature and the supply temperature, ~13°F for 15 ACH and ~10°F for 30 ACH. This definition for ΔT_{ref} was selected since both temperatures are known *a priori* the CFD experiment, while the exhaust air temperature is to be computed.

7.6.1 CFD Experiments

A series of CFD experiments have been conducted to simulate two test conditions for the University of Illinois ME full scale experimental facility. The *INGRID* mesh generator (Stillman and Hallquist, 1985) was used to build the computational mesh depicted in Fig. 84. This non-uniform 3-dimensional distribution contains 19,926 nodes for 17,712 trilinear hexahedra (8-node) finite elements. One-foot-long extensions into the supply and exhaust ducts were necessary to facilitate boundary condition specifications that did not compromise local flow field accuracy. (Note: The typical CFD experimental procedure reported in the ASHRAE literature does not explore such extensions, such that local first-order accurate (upwind) discretizations are necessary for stability.)

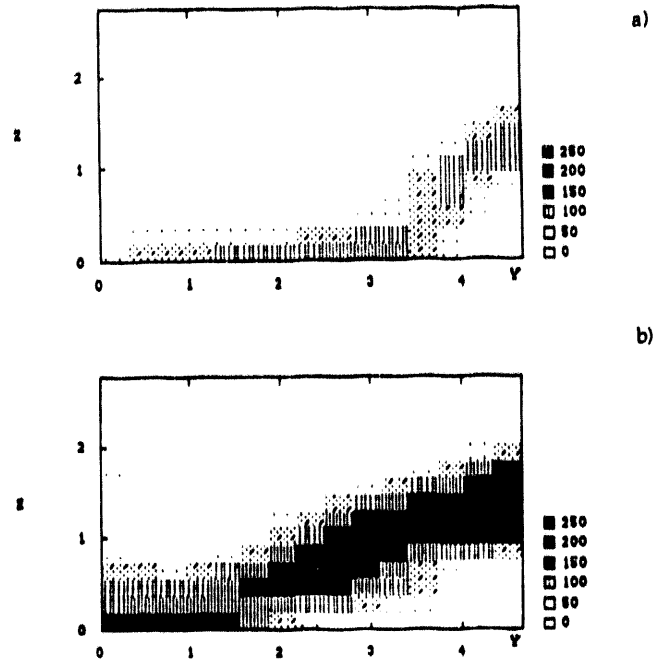

Figure 80. Measured distributions of room air speed in supply centerplane, (a) 15ACH, Ar=4.3, (b) 30 ACH, Ar=0.82, range $0 \leq U \leq 250$ fpm, from Spitler (1990).

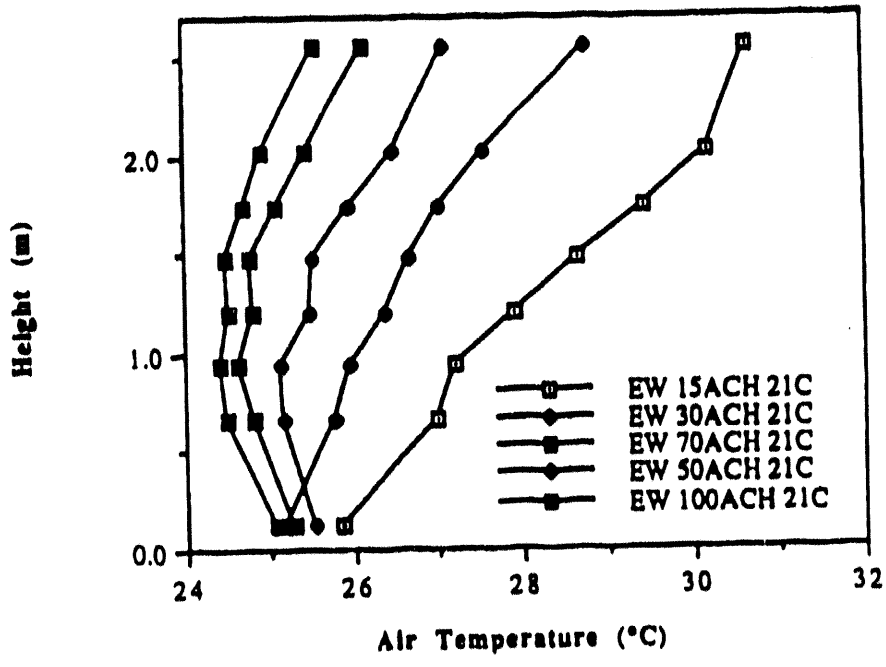

Figure 81. Vertical temperature distribution, room supply centerplane, averaged over the horizontal plane, from Spitler (1990).

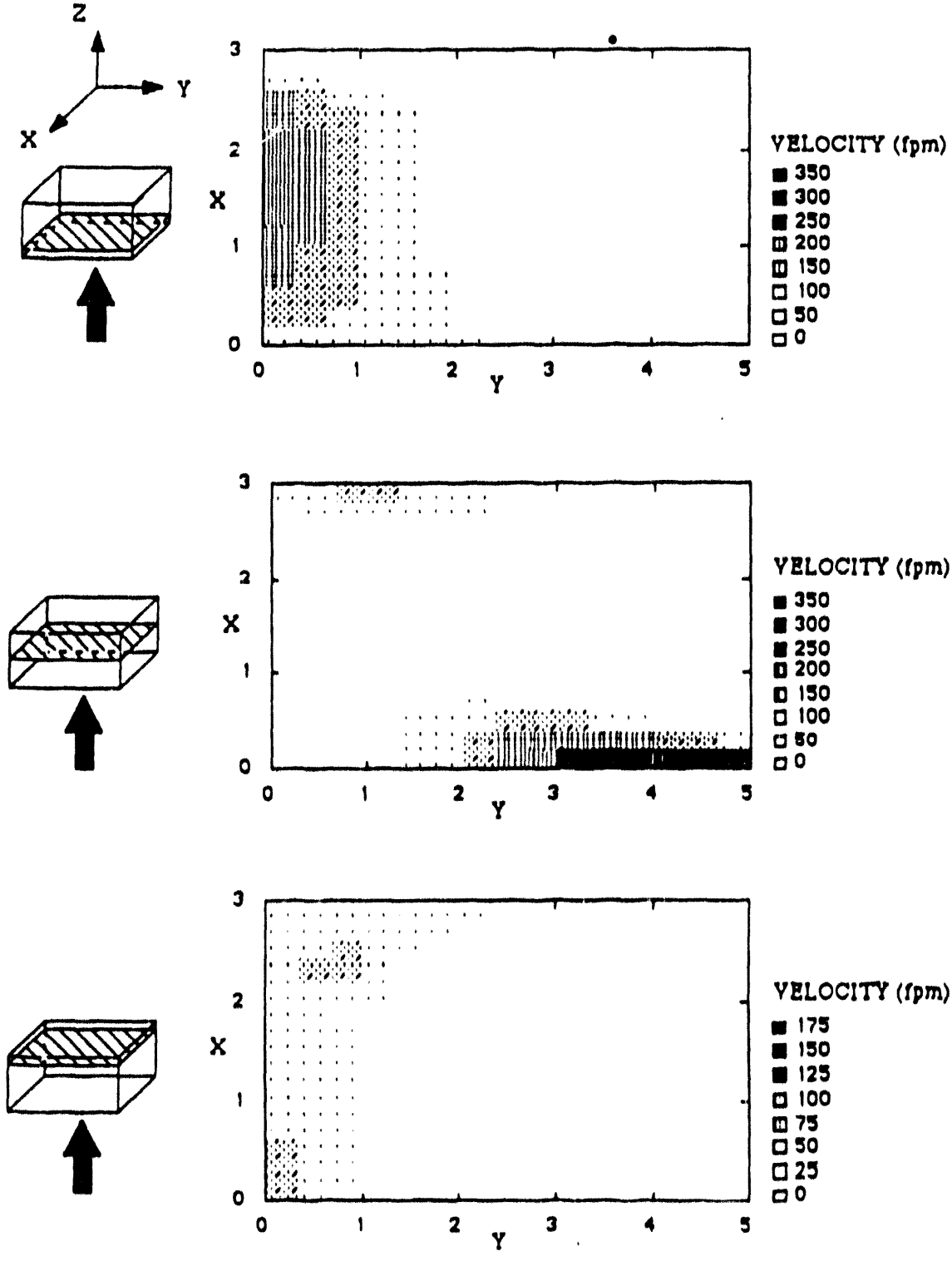

Figure 82. Measured room flow speed distributions in horizontal planes, 50 ACH, range $0 \leq l \leq 350$ fpm, from Cantillo (1990).

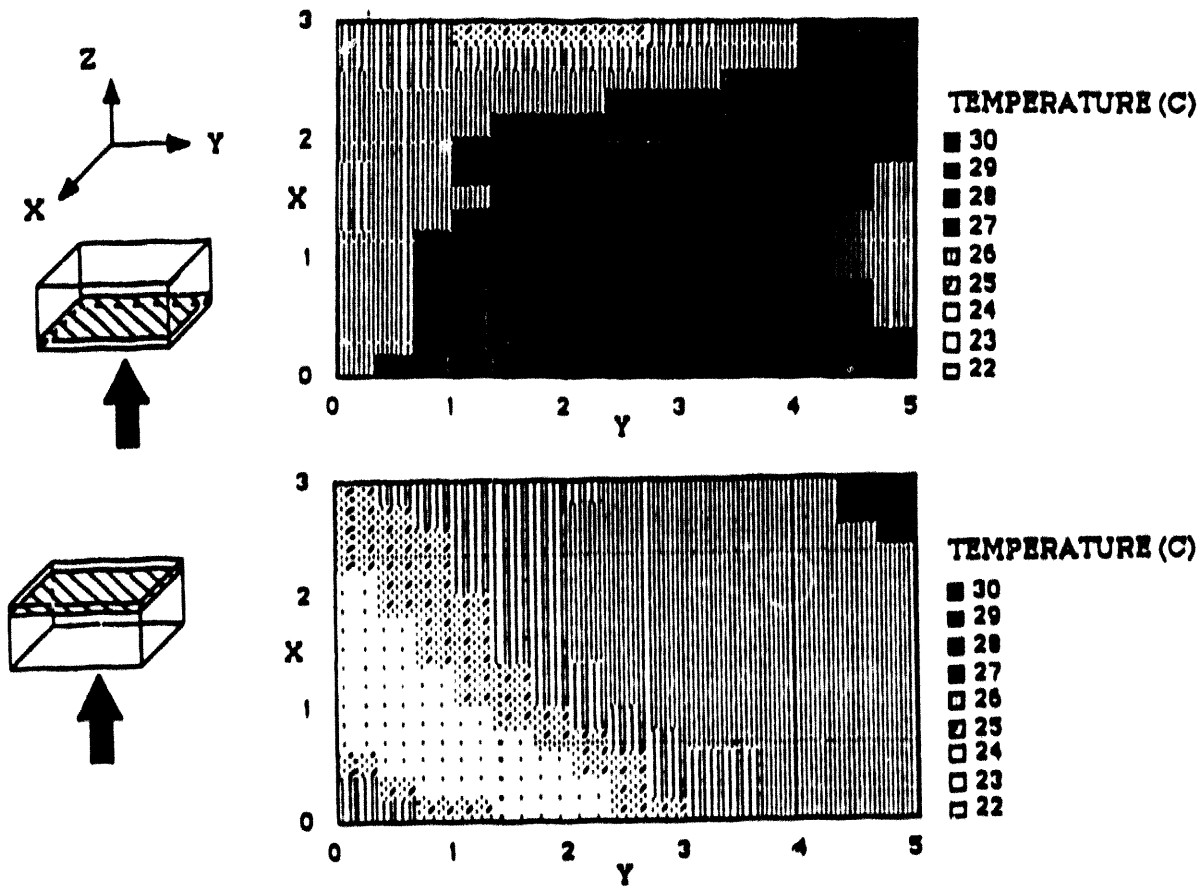

Figure 83. Measured room temperature distributions in horizontal planes, 50 ACH,Cantillo(1990).

(a) wireframe view

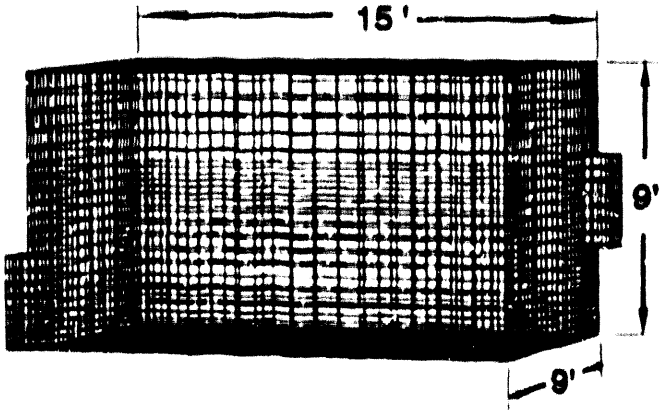

(b) hidden line view

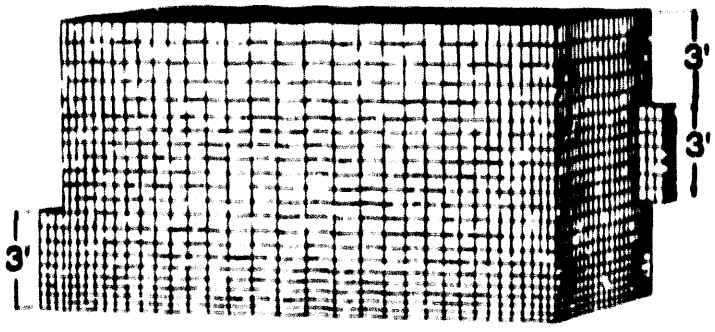

(c) cut-away view

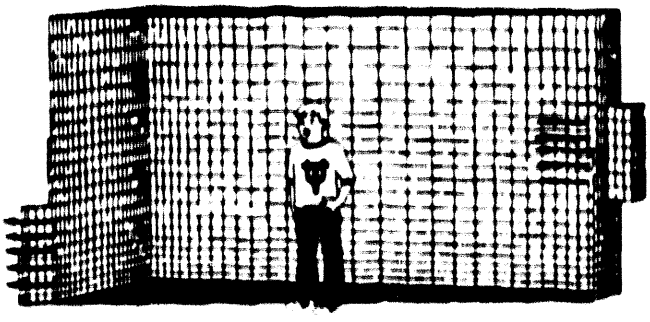

Figure 84. Three views of the mesh for ventilation room problem.

Both the supply and exhaust ducts are 3 ft tall by 1.3 ft wide, and one side wall of each duct is flush with its corresponding room wall. The full scale room enclosure is 9 ft tall, 9 ft wide, and 15 ft long. The "young graduate student" in Fig. 84c gives an approximate sense of scale.

The supply duct velocity condition is assumed a slug flow profile at uniform temperature. A continuative Neumann boundary condition is specified at the outflow duct exhaust plane for velocity and temperature. Along all room surfaces, a drag boundary condition is used to simulate a turbulent boundary layer coupled with flow tangency. The assumed functional form for shear stress, τ_{slip} , at the slip plane near the wall is

$$\tau_{slip} = a + bU^{\dagger} + c\left(U^{\dagger} - U^{\dagger}_{slip}\right)^{d} \tag{376}$$

where $a,b,c,$ and d are dimensional constants, $U^{\dagger}$ is the CFD-computed tangential velocity, and $U^{\dagger}_{slip}$ is a prescribed wall tangential velocity. The mesh is assumed to be offset some small distance Λ (on the order of an inch) from the solid wall; therefore, to calculate a shear stress at $y^{*}=\Lambda$ one differentiates $U^{\dagger}$ with respect to y^{*} , evaluating the derivative at $y^{*}=\Lambda$,

$$\tau_{slip} = \frac{\mu}{g_c}\left[\frac{\partial U^{\dagger}}{\partial y^{*}}\right]_{y^{*}=\Lambda} \tag{377}$$

Following Murakami et al. (1988), the 1/ 7th power-law profile for turbulent flow over a flat plate was selected, hence

$$\frac{U^{\dagger}}{U_{ref}} = \left[\frac{y^{*}}{\delta}\right]^{m} \tag{378}$$

where y^{*} is a normal distance from the wall, and δ is a length scale representative of a typical turbulent boundary layer thickness. Carrying out the differentiation of Eq. (378), one obtains

$$\tau_{slip} = \frac{\mu}{g_c}\left[\frac{\partial U^{\dagger}}{\partial y^{*}}\right]_{y^{*}=\Lambda}$$

$$\frac{\mu}{g_c}\frac{\partial}{\partial y^{*}}\left[U_{ref}\left[\frac{y^{*}}{\delta}\right]^{m}\right]_{y^{*}=\Lambda} = \frac{\mu}{g_c}\frac{U_{ref}}{\delta}m\left[\frac{y^{*}}{\delta}\right]^{m-1}_{y^{*}=\Lambda} = \left[\frac{\mu}{g_c}\frac{m}{\delta}\frac{\delta}{\Lambda}\right]U^{\dagger} \tag{379}$$

In Eq. (379), μ is the dynamic viscosity, and g_c is a conversion constant to insure that τ_{slip} has the dimensions of force per unit length squared. From Eq. (379), applying the 1/7th power law amounts to setting $a=c=0$, $m=1/7$, and

$$b = \frac{\mu}{g_c}\frac{m}{\Lambda} \tag{380}$$

As stated, throughflow boundary conditions for the energy equation are a uniform temperature at the supply duct and vanishing normal derivative at the exhaust plane. Both the ceiling and floor are assumed adiabatic. A heat flux is prescribed using Newton's law of cooling for all vertical walls. This general flux boundary condition has the functional form

$$q'' = a + bT + c(T - T_{wall})^d \tag{381}$$

where a,b,c, and d are dimensional constants, and T_{wall} is a wall fixed temperature. Newton's law of cooling is the specification

$$q'' = h(T - T_{wall}) \tag{382}$$

with h the heat transfer coefficient for forced convection. Based upon Spitler's (1990) heat transfer data, the average value h=5 Btu/h-ft^2-°F was selected for the CFD simulations. Comparing Eqs. (381) and (382), c=0, b=h, a= $-hT_{wall}$, and d =1 yields the desired enforcement.

For the continuity constraint Poisson equation, the boundary condition Φ=0 is required on the exhaust plane. All other boundaries require a homogeneous Neumann constraint. The pressure Poisson equation boundary conditions include a prescribed uniform pressure on the exhaust plane, and non-homogeneous turbulent Reynolds number dependent Neumann boundary conditions on all walls and the supply plane.

The supply flow is modestly turbulent, and the room flow would be low turbulent. A significant unknown in these CFD experiments is the turbulence intensity of the supply air. Hence, as an approximation, the turbulent Reynolds number Re^t was set uniformly at 14 and 29, respectively, for the initial tests at Re_{15}=15,000 and Re_{30}=30,000. The sensitivity of this decision was tested by running a parametric study varying Re^t .

Two test cases were selected from Spitler (1990), both using the east-side, mid-wall supply configuration. These cases differed primarily in their air flow rate and side-wall temperature.

7.6.1.1 Problem 1: 15 ACH and T_{wall}= 83°F

For Problem 1, the total air flow to the room is 15 air changes per hour (ACH) with an inflow air temperature of 69.8°F. The term "air changes per hour" are the units of volumetric flow rate, where, for the experimental room, a complete air change involves a volume of 9×9×15ft or 1215 ft^3. Through the room's heater control system, the side walls are maintained at 83°F. The bulk velocity of the air in the inlet duct (1.3 ft/s) was selected as the reference velocity, U_{ref} . The Ar number reported by Spitler (1990) for this case is 4.3. The local Re in the inlet duct can be computed using the hydraulic diameter of a 1.3 ft × 3 ft rectangular cross section as the reference length. This Re is approximately 15,000. The level of turbulence in the air flow entering the room can be estimated by prescribing a value for Re^t, defined as the ratio of the eddy viscosity ν^t to the molecular kinematic viscosity ν. The base case for this problem assumed an Re^t of 14, producing an effective diffusion coefficient Re^t of 1000, where Re^t=Re/(1+Re^t). To explore the sensitivity of the steady-state solution to this critical assumption, two additional cases were run with Re^t values of 29 (Re^t=500) and 149 (Re^t=100).

Figures 85–92 present different views of the steady-state solutions for Problem 1 at the three values for Re^t. The east-side wall supply diffuser abuts the north wall. In Fig. 85, the velocity vectors plotted are for the first plane of nodes off the north wall, the east and west walls, and the floor and ceiling. Notice in Fig. 85a that the low level of turbulence (hence low turbulent mixing) coupled with the large buoyancy forces cause the significant jet of cold air towards the

(a) $Re^t = 14$

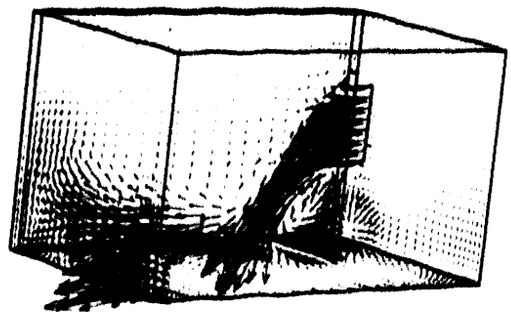

1 ft/s

(b) $Re^t = 29$

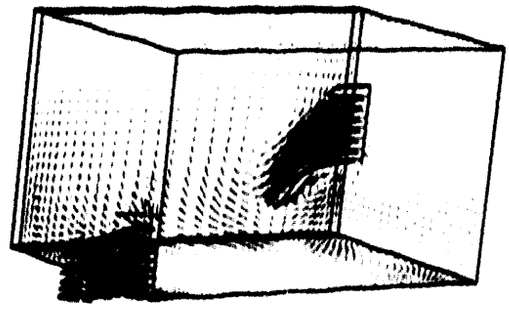

(c) $Re^t = 149$

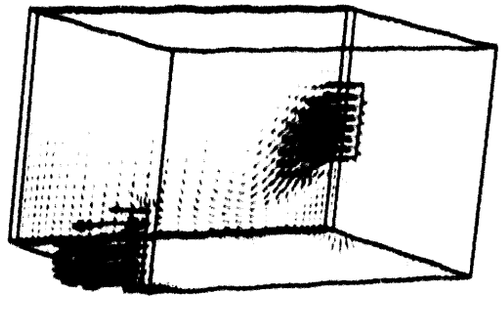

Figure 85. Velocity solutions for 15 ACH.

(a) $Re^t = 14$

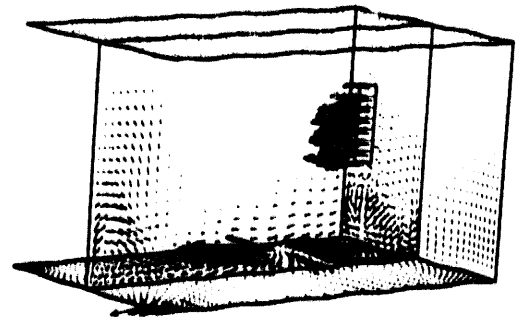

1 ft/s

(b) $Re^t = 29$

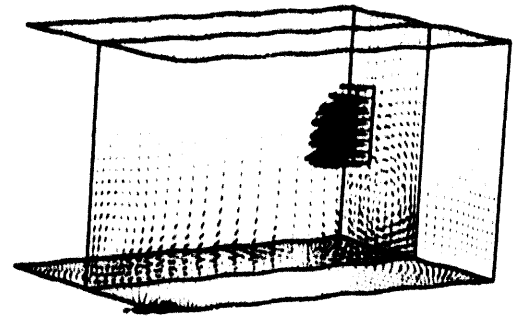

(c) $Re^t = 149$

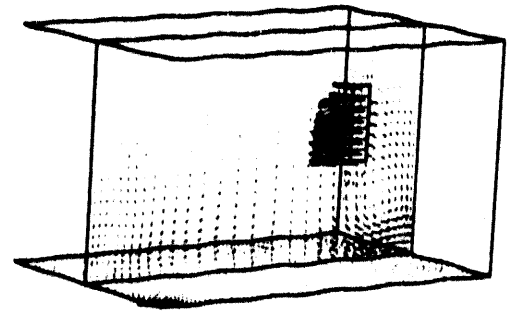

Figure 86. Longitudinal plane for 15 ACH.

(a) $Re^t = 14$

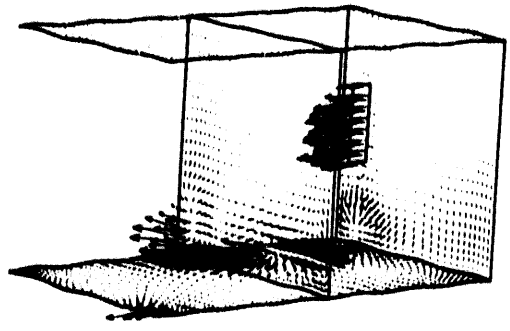

1 ft/s

(b) $Re^t = 29$

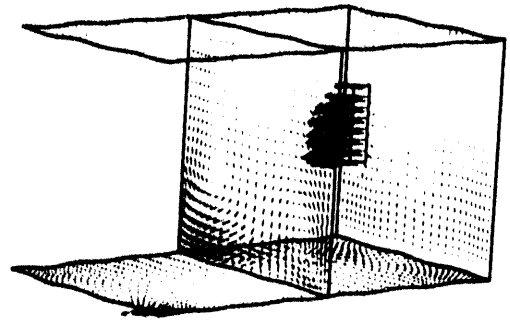

(c) $Re^t = 149$

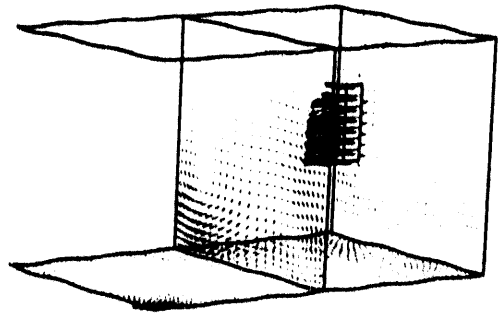

Figure 87. Transverse plane for 15 ACH.

floor. This region where the cold air jet hits the floor is appropriately termed a "splat". Increasing the level of turbulent transport and mixing by increasing $Re^{\prime}$, the intensity of this "splat" decreases.

Figures 85–87 also demonstrate that the velocity distributions within this simple room geometry are a quite complex 3-dimensional flow field. The cold air sweeping along the floor feeds buoyancy-induced 3-dimensional vortex rolls along each of the walls, including the supply plane wall for smallest $Re^{\prime}$. In Fig. 92, isotherms are plotted for the three values of $Re^{\prime}$. In Fig. 92a, at the lowest level of turbulent mixing, large temperature stratification near the floor can be observed as well as the temperature gradients associated with the falling inflow jet and floor "splat". As the $Re^{\prime}$ is increased in Figs. 92b and 92c, the higher turbulent mixing progressively smoothens out the temperature gradients. Figures 88 and 89 show contours for the static and total pressure, respectively. In the stagnation region associated with the "splat" on the floor, a high static pressure region is produced, lessening as the effect of the "splat" as $Re^{\prime}$ increases. Contours of constant speed (isovels) in the units of ft/s are shown in Fig. 90. The distribution of the divergence error in the solution as measured by the energy norm of the continuity constraint function Φ can be depicted by plotting contours of constant $\|\Phi\|_{\prime}$. Nodal values for $\|\Phi\|_{\prime}$ are calculated by taking the average of the associated element-based $\|\Phi\|_{\prime}$ normalized by the element volume and projecting each element contribution onto the node. The resulting distribution is a measure of the kinetic energy per unit volume of the divergence error in the velocity solution.

The variation in the distribution and magnitude of the divergence error for the three $Re^{\prime}$ levels, depicted by the $\|\Phi\|_{\prime}$ contour plots in Figs. 91a-c, gives an excellent quantitative description of the influence of dispersion error (in the absence of any dispersion error control, $\beta=0$) on solution quality. At the lowest $Re^{\prime}$ (=14, Fig. 91a), numerical dissipation is minimal, and the divergence error is significant ($\|\Phi\|_{\prime}\approx 10^{-2}$) and broadly distributed. Increasing $Re^{\prime}$, implying more turbulent mixing, increases physical diffusion, and the divergence error is significantly lowered ($\|\Phi\|_{\prime}\approx 10^{-6}$), becoming localized near geometric singularities such as the sharp corners of the supply and exhaust ducts.

7.6.1.2 Problem 2: 30 ACH and T_{wall}= 80°F

In the second problem, the flow rate is increased to 30 ACH, and the set point for the wall temperature is decreased to 80 °F. This produces a reference velocity of 2.6 ft/s and a ΔT_{wall} of 10 °F. The local Re in the supply duct is approximately 30,000, and the reported Ar for the room is 0.83. For this Archimedes number, the convective forces are relatively more dominant than buoyancy forces, the reverse of the condition in problem 1. Figures 93–95 present views of steady-state velocity solutions for three values of $Re^{\prime}$. As evidenced by Fig. 93, the supply jet follows a much straighter path (due to the reduced importance of the buoyancy body force) into the room. However, the flow is still strongly 3-dimensional as in problem 1. The isotherms shown in Fig. 96 present the variation in temperature stratification as influenced by the differing levels of turbulent mixing, yielding $Re^{\prime}$ = 1000, 500, and 100 for $Re^{\prime}$ = 29, 59, and 299, respectively. Contours of constant static and total pressure are given in Figs. 97 and 98, and contours of constant speed and $\|\Phi\|_{\prime}$ in Figs. 99 and 100. Compared to problem 1, good control of the divergence error, as shown in Fig. 100, did not vary significantly over the range of $Re^{\prime}$ tested.

In problem 1, the 3-dimensional character of the flow is dominated by the descending supply jet and the "sweep" of cold air along the floor. The resulting buoyancy-driven vortex rolls are thereby evident along each of the room walls. Conversely, in problem 2, the center of the room

(a) $Re^t = 14$

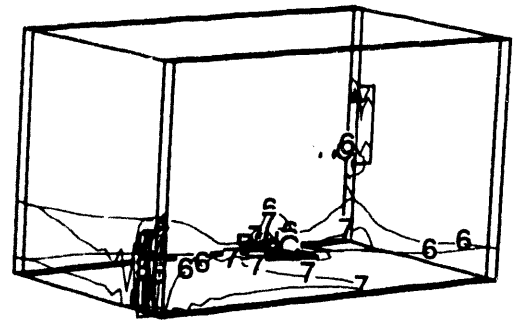

(b) $Re^t = 29$

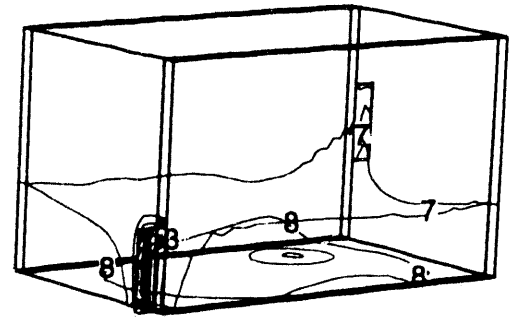

(c) $Re^t = 149$

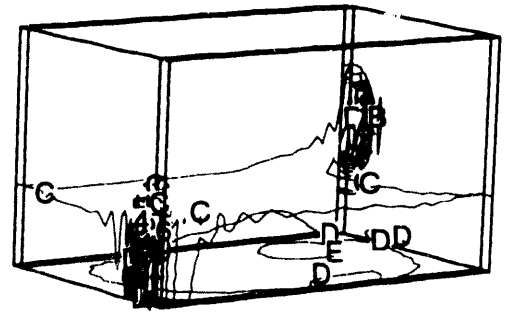

Figure 88. Isobars for 15 ACH.

(a) $Re^t = 14$

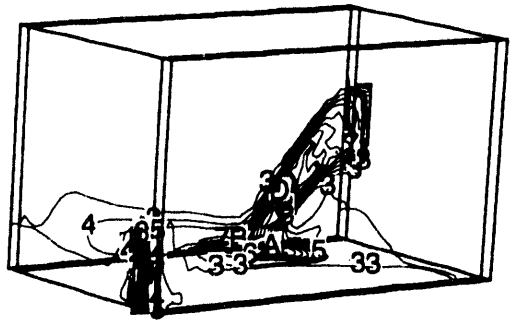

(b) $Re^t = 29$

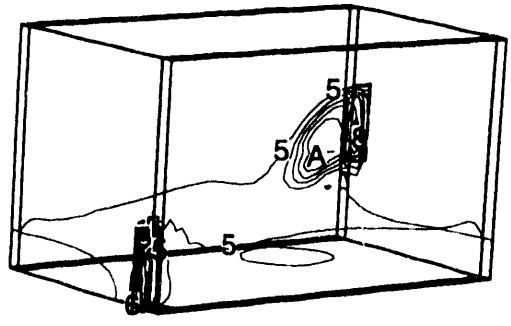

(c) $Re^t = 149$

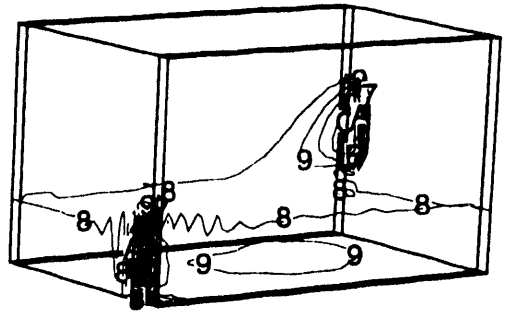

Figure 89. Total pressure for 15 ACH.

(a) $Re^t = 14$

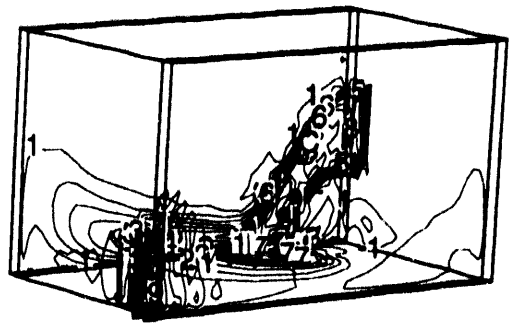

(b) $Re^t = 29$

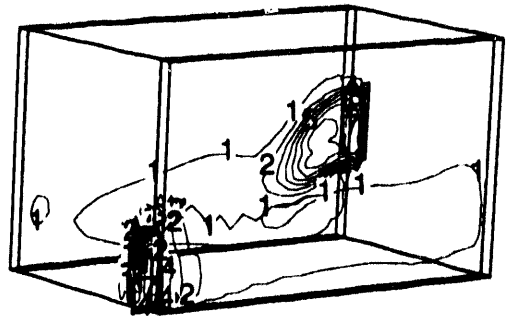

(c) $Re^t = 149$

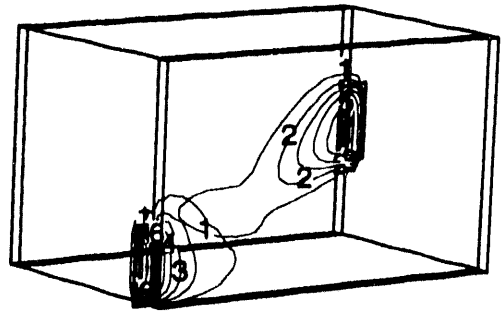

Figure 90. Isovels for 15 ACH.

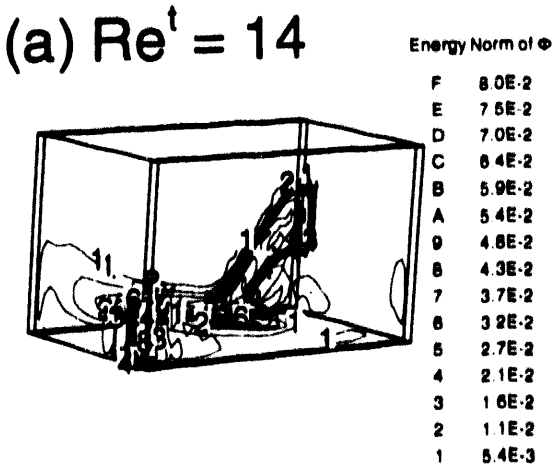

Figure 91. Energy norm of Φ for 15 ACH.

(a) $Re^t = 14$

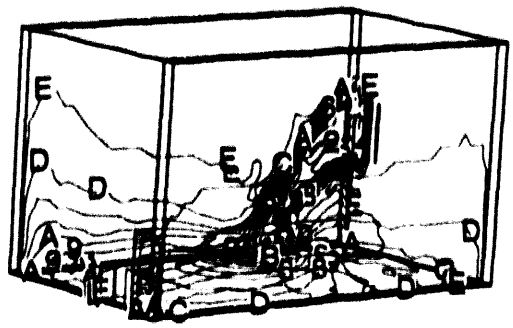

(b) $Re^t = 29$

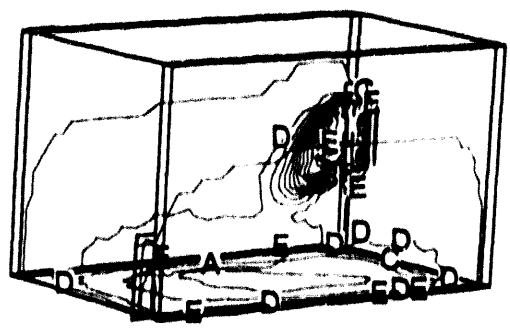

(c) $Re^t = 149$

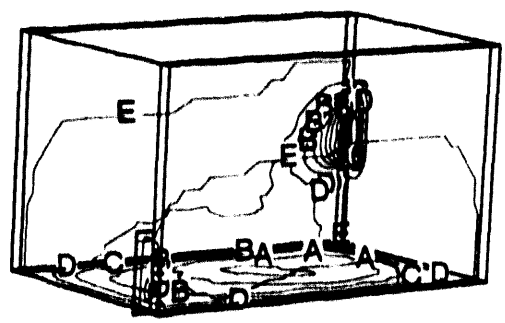

Figure 92. Isotherms for 15 ACH.

contains the most interesting fully 3-dimensional flow characteristics. Viewing Figs. 94 and 95, the assumption for Re' is again confirmed to be critical in determining the robustness of the 3-dimensional character of the flow. Specifically, the distinctive *S* shape produced by the isovel contours in Fig. 99(a) is lost as the simulation turbulence level, Re', increases, Fig. 99(c).

7.6.2 Comparison Between CFD and Physical Experiments

In his dissertation, Spitler (1990) reports measured room air speed distributions on the vertical plane, parallel to the room north wall and offset therefrom by 0.127m, which coincides with the centerplane of the air supply duct. For the two selected room flowrates, 15 and 30 air changes per hour (ACH), these data were collected using 16 TSI 8470 omnidirectional air velocity transducers mounted on a trolley, which could be moved throughout the room. This instrumentation measured flow speed only (not components of the velocity vector), and the reported measurement accuracy was +12/-23% (+10/-14 fpm). In addition, temperature measurements were made in horizontal planes using 16 type T thermocouples mounted on the same trolley. Each temperature data point, as reproduced in Fig. 81, "represents the average of 112 temperature measurements in a horizontal plane," which presumably extended throughout the entire room.

Figures 80a and 101 present (on approximately the same scale) the experimental and CFD computed distributions of room air speed for the 15 ACH, Ar=4.3 case, with the latter for the three selected turbulent Reynolds number (Re') settings. A very good qualitative comparison occurs for the smallest Re' level, for which the supply jet is predicted to literally "crash" downwards, due to buoyancy effects, yielding a pronounced floor jet. This CFD prediction yields an extremum speed (143 fpm) that agrees very well with the (apparent) 150 fpm measured maximum. The more diffusive (Re'=29 and Re'=149) CFD solutions do not predict the significant measured floor jet, and the associated predicted extremum speed is reduced to the order 100 fpm or lower. Clearly, then, the Spitler data appears to correspond to a low turbulence level room air experiment, for which the smallest Re' CFD experimental speed prediction is qualitatively and quantitatively in good agreement.

In distinction, this comparison between the CFD experiments and data, for the 30 ACH, Ar=0.82 case, indicates neither qualitative nor quantitative agreement, Figs. 80b and 102. Spitler measured large regions with air speeds of the order 200-250 fpm, while the CFD predicted extremum is 165 fpm. The CFD simulation predicts these planar flow field speed distributions as rather insensitive to Re', as are the underlying velocity distributions, Fig. 93. (Recall however, that the CFD *velocity* distributions are very sensitive to Re' elsewhere in the room, Fig. 94.) Based on the good comparison achieved for the 15 ACH test, one might conclude that a significant scaling error may exist in the 30 ACH test specification, as reported.

Consistent with experimental procedure, reported by Spitler (1990) for planar-averaged temperature stratification, the CFD data summary shown for Figs. 103 and 104 averages the calculated temperatures over every horizontal plane in the computational mesh. For the 15 ACH case, Fig. 103 confirms a much stronger room-averaged temperature stratification exists in the experimental data than for the CFD results. The exception lies in the first 0.5m above the floor, for the lowest turbulence level (Re'=14) test, which shows quite good level and slope agreement with the experiment. This flow region is dominated by the cold floor jet, which apparently has been quite accurately predicted (in these norms). At all higher elevations in the room, the CFD results predict a much more isothermal state than was measured experimentally on the average.

(a) $Re^{t} = 29$

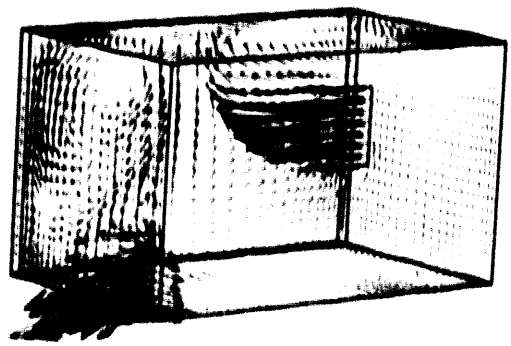

- 1 ft/s

(b) $Re^{t} = 59$

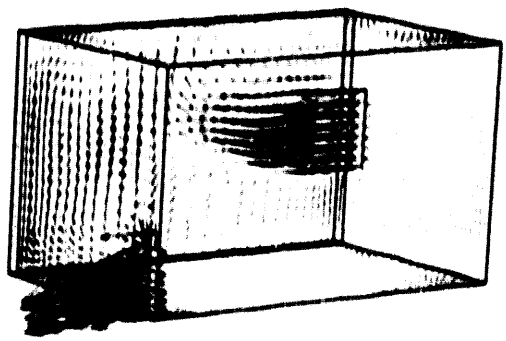

(c) $Re^{t} = 299$

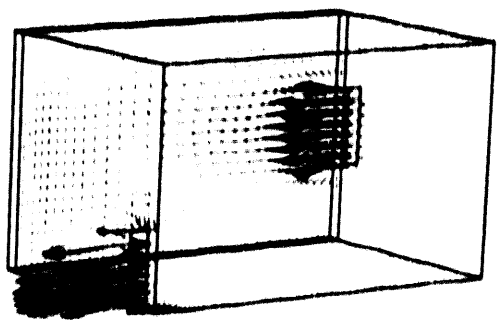

Figure 93. Velocity solutions for 30 ACH.

(a) $Re^t = 29$

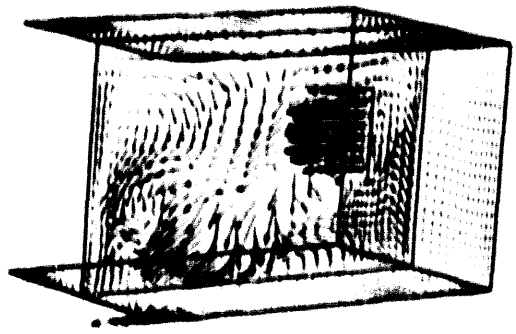

1 ft/s

(b) $Re^t = 59$

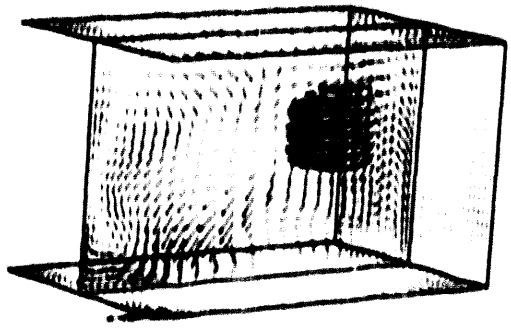

(c) $Re^t = 299$

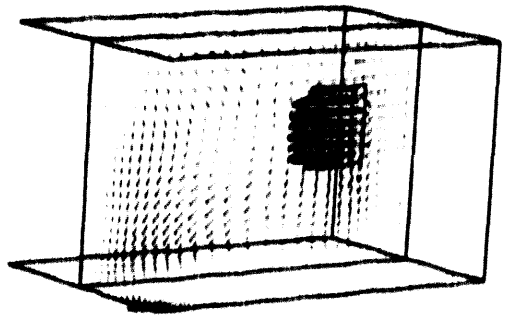

Figure 94. Longitudinal plane for 30 ACH.

(a) $Re^{t} = 29$

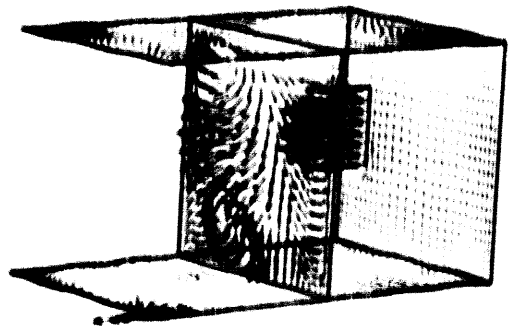

1 ft/s

(b) $Re^{t} = 59$

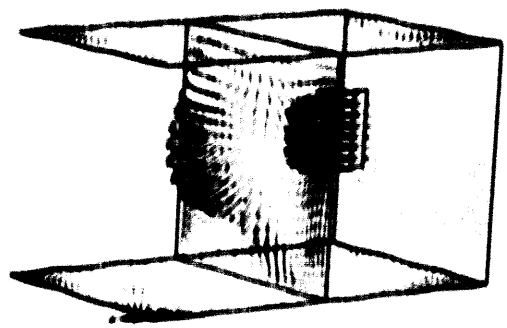

(c) $Re^{t} = 299$

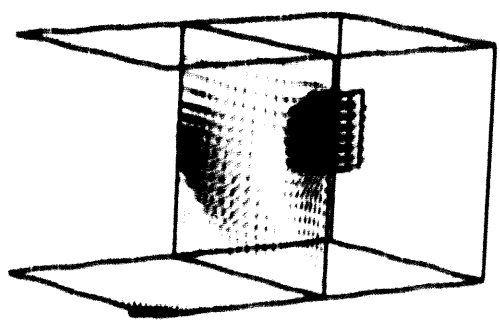

Figure 95. Transverse plane for 30 ACH.

(a) $Re^{1} = 29$

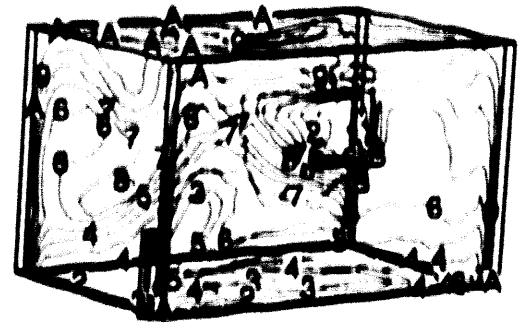

(b) $Re^{1} = 59$

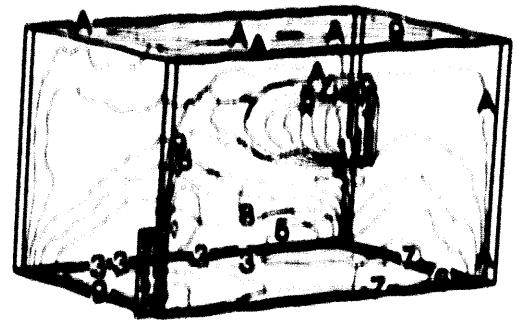

(c) $Re^{1} = 299$

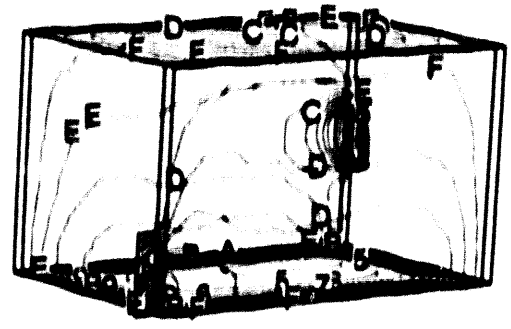

Figure 96. Isotherms for 30 ACH.

(a) $Re^{1} = 29$

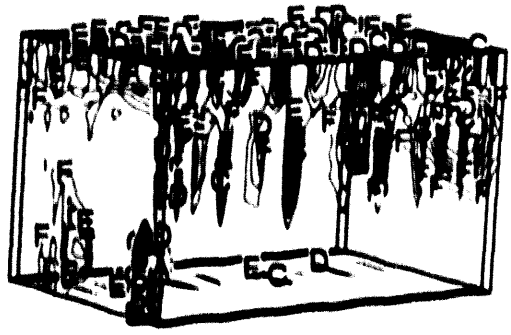

(b) $Re^{1} = 59$

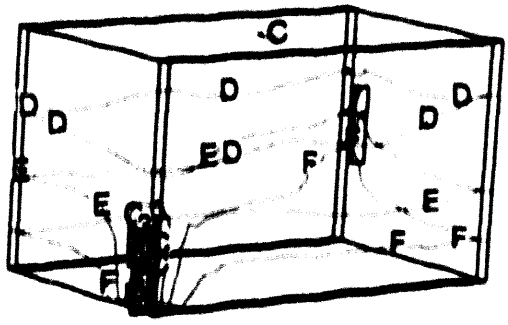

(c) $Re^{1} = 299$

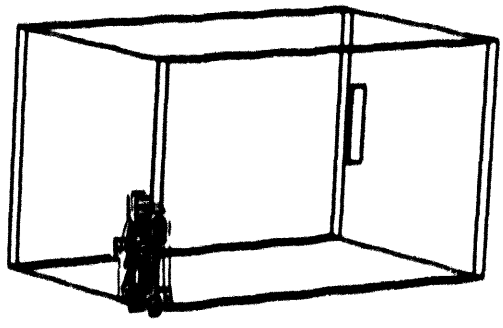

Figure 97. Isobars for 30 ACH.

(a) $Re^t = 29$

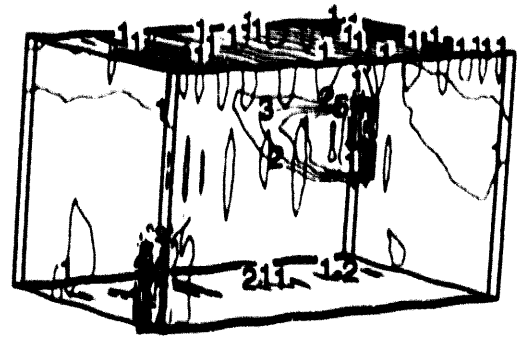

(b) $Re^t = 59$

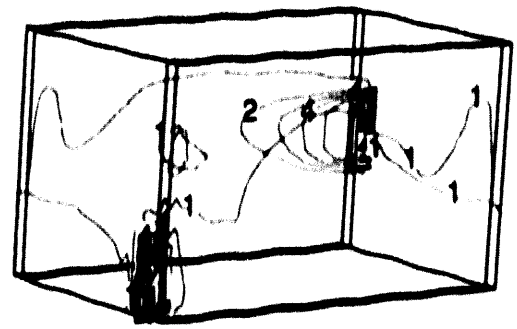

(c) $Re^t = 299$

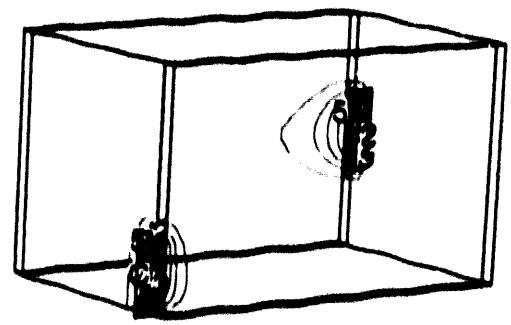

Figure 98. Total pressure for 30 ACH.

(a) $Re^t = 29$

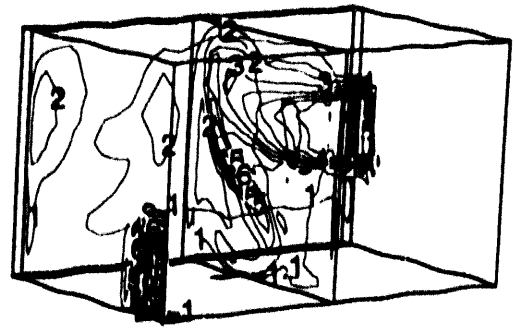

(b) $Re^t = 59$

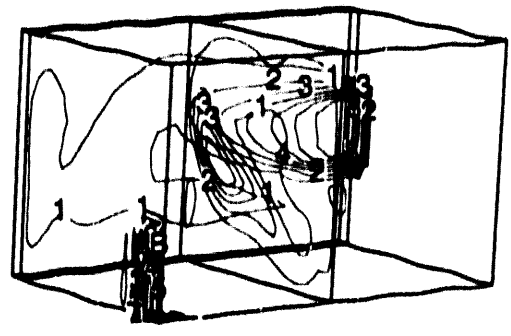

(c) $Re^t = 299$

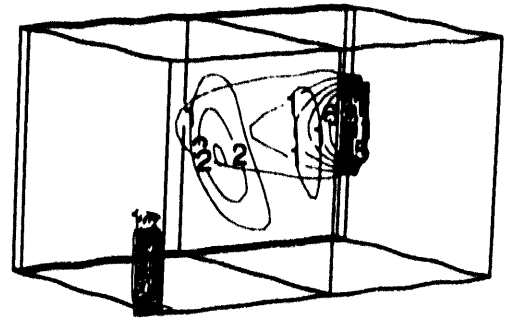

Figure 99. Isovels for 30 ACH.

(a) $Re^t = 29$

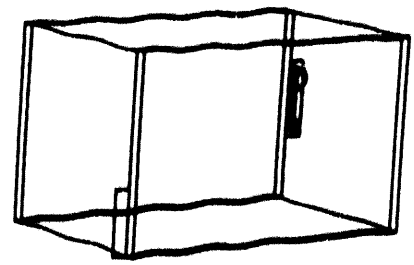

Energy Norm of Φ

F	4.6E-5
E	4.3E-5
D	4.0E-5
C	3.7E-5
B	3.4E-5
A	3.1E-5
9	2.8E-5
8	2.5E-5
7	2.2E-5
6	1.9E-5
5	1.6E-5
4	1.2E-5
3	9.3E-6
2	6.2E-6
1	3.1E-6

(b) $Re^t = 59$

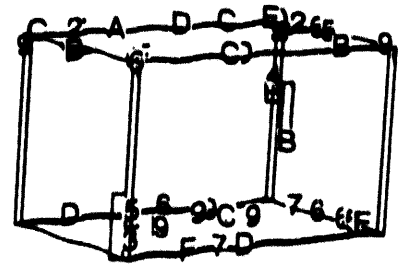

Energy Norm of Φ

F	1.0E-4
E	9.4E-5
D	8.7E-5
C	8.1E-5
B	7.5E-5
A	6.8E-5
9	6.2E-5
8	5.6E-5
7	4.9E-5
6	4.3E-5
5	3.6E-5
4	3.0E-5
3	2.4E-5
2	1.7E-5
1	1.1E-5

(c) $Re^t = 299$

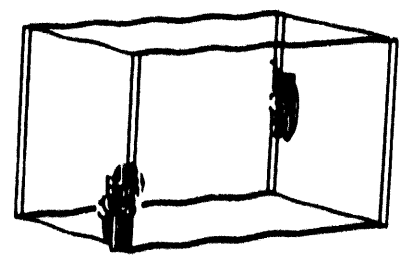

Energy Norm of Φ

F	1.0E-4
E	9.4E-5
D	8.7E-5
C	8.1E-5
B	7.5E-5
A	6.8E-5
9	6.2E-5
8	5.6E-5
7	4.9E-5
6	4.3E-5
5	3.6E-5
4	3.0E-5
3	2.4E-5
2	1.7E-5
1	1.1E-5

Figure 100. Energy norm of Φ for 30 ACH.

(a) $Re^t = 14$

Level	vel
F	143
E	134
D	124
C	115
B	105
A	96
9	86
8	76
7	67
6	57
5	48
4	38
3	29
2	19
1	10

(b) $Re^t = 29$

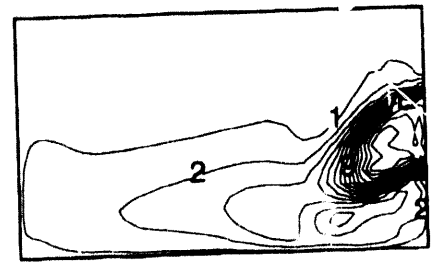

Level	vel
F	100
E	93
D	87
C	80
B	73
A	67
9	60
8	53
7	47
6	40
5	33
4	27
3	20
2	13
1	7

(c) $Re^t = 149$

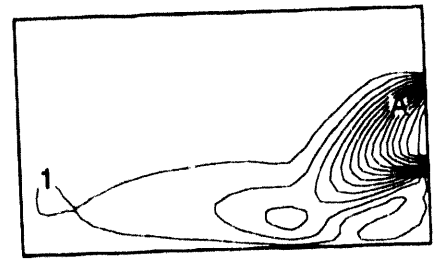

Level	vel
F	85
E	79
D	74
C	68
B	62
A	57
9	51
8	45
7	40
6	34
5	28
4	23
3	17
2	11
1	6

Figure 101. Air speed contours for 15 ACH, Ar=4.3.

(a) $Re^t = 29$

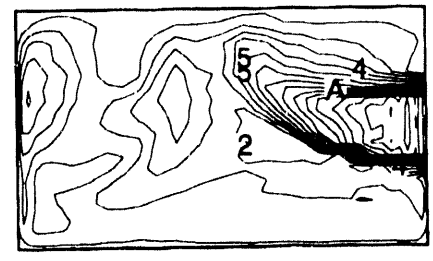

Level	vel
F	177
E	165
D	153
C	141
B	130
A	118
9	106
8	94
7	83
6	71
5	59
4	47
3	35
2	24
1	12

(b) $Re^t = 59$

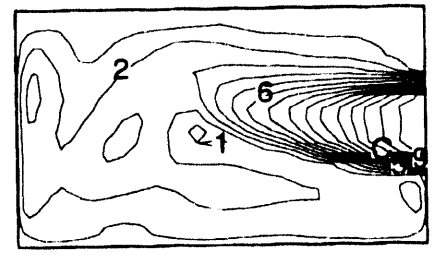

Level	vel
F	168
E	157
D	146
C	135
B	123
A	112
9	101
8	90
7	78
6	67
5	56
4	45
3	34
2	22
1	11

(c) $Re^t = 299$

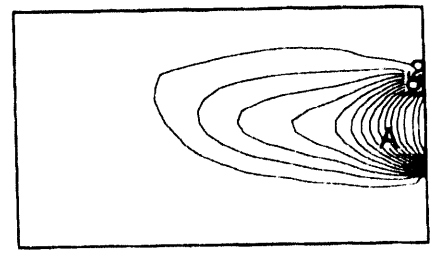

Level	vel
F	165
E	154
D	143
C	132
B	121
A	110
9	99
8	88
7	77
6	66
5	55
4	44
3	33
2	22
1	11

Figure 102. Air speed contours for 30 ACH, Ar=0.82.

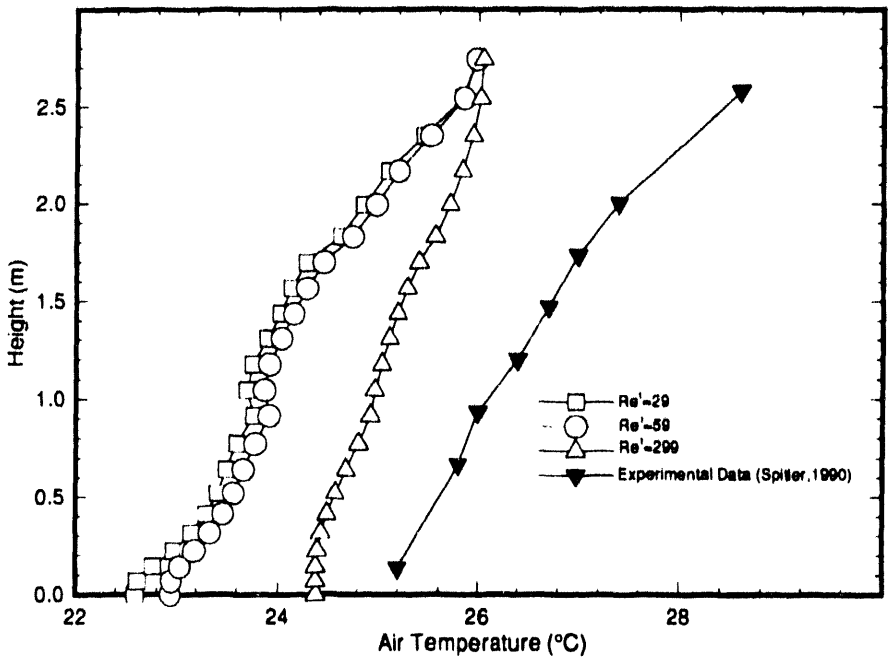

Figure 104. Temperature stratification for 30ACH, Ar=0.82.

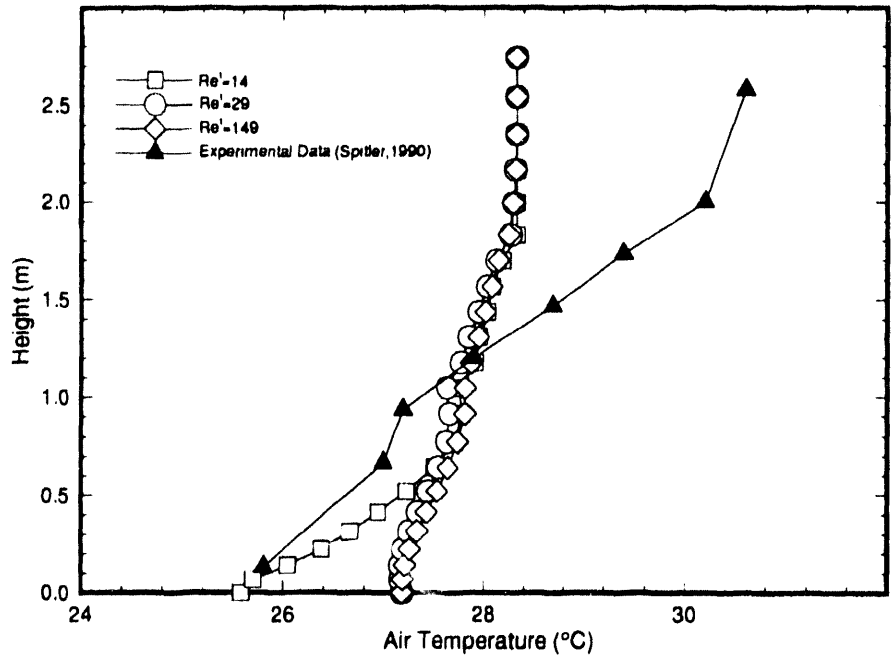

Figure 103. Temperature stratification for 15ACH, Ar=4.3.

At the 30 ACH flowrate, the temperature stratification for the lowest two turbulence level simulations, as measured by vertical gradient, shows quite good agreement with the experimental data, Fig. 104. The fact that the CFD data produce a much colder overall room air temperature level confirms the expressed suspicion regarding a scaling error in this experiment definition.

7.7 NATURAL CONVECTION IN A TWO-CELL ENCLOSURE WITH A "DOOR"

Engineering interest in natural convection in complex enclosures with restricted communication has been stimulated by applications involving energy-efficient passive-solar buildings, cryogenic storage equipment, natural convection cooling of electronic equipment, solar energy collectors, and room heating and ventilation. A basic configuration for the study of room ventilation involves the "association of two enclosures which communicate laterally through an opening in the same manner as two rooms connected through a doorway, window, corridor, or over an incomplete dividing wall" (Lin and Bejan, 1983). The experimental program carried out by researchers at Colorado State University (cf. Neymark, 1988; Neymark et al., 1989; and Boardman et al., 1989) has provided heat transfer and flow visualization data, obtained from partially-divided air- and water-filled enclosures, Fig. 105, that can be used for CFD validation studies.

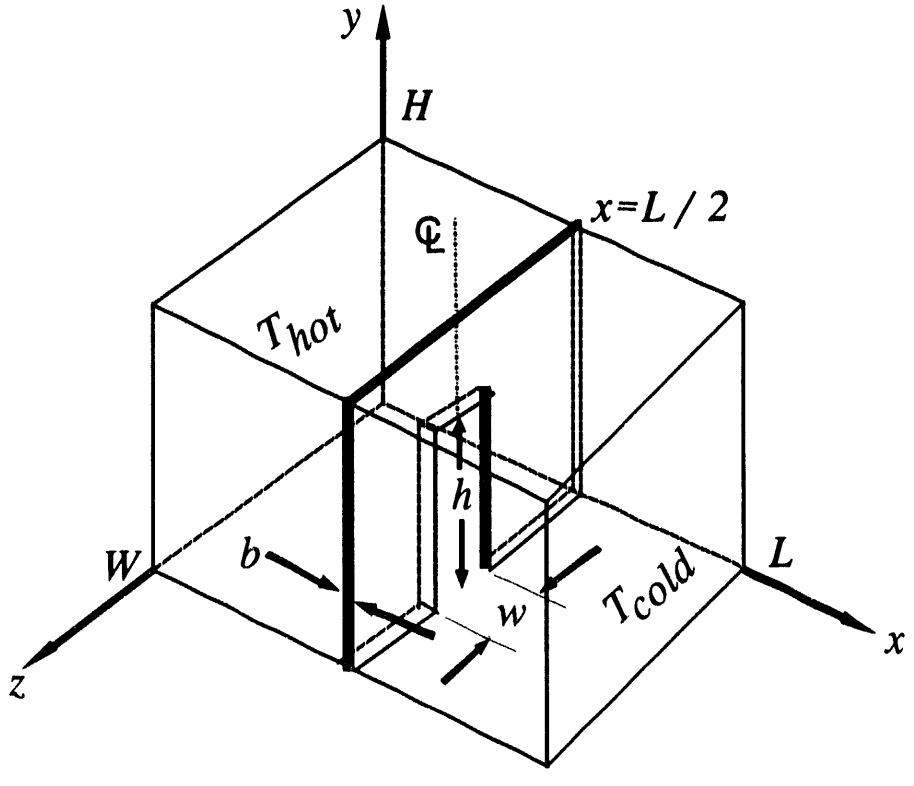

Fig. 105. Geometry for a partially-divided enclosure.

Early work on natural convection in partitioned enclosures by Brown and Solvason (1962) examined convective heat transfer through an aperture resulting from a zone-to-zone bulk density difference across the aperture. Nansteel and Greif (1981) investigated the effect of 2-dimensional conducting and nonconducting centrally-located partitions of various lengths extending vertically downward from the ceiling of a water-filled rectangular enclosure. Flow visualization and vertical temperature profiles were reported along with correlations for the overall cross-cavity heat transfer. Bajorek and Lloyd (1982) described a series of experiments with air and CO_2 in a square enclosure with two partial dividers, one attached to the top wall and the other to the bottom, amounting to two chambers communicating through a mid-height window. Comparing heat transfer data taken in the partitioned enclosure with the corresponding measurements in the unpartitioned single enclosure, they found that the partitions reduce the heat transfer rate appreciably.

Other investigators (cf. Lin and Bejan, 1983; and Nansteel and Greif, 1984) have used small-scale water-filled enclosures to correlate cross-cavity heat transfer with the enclosure wall temperatures. Nusselt-Rayleigh number data for a water-filled partially-divided enclosure were correlated by Lin and Bejan (1983) for Rayleigh numbers between 10^9 and 10^{10}, where the Rayleigh number was evaluated using the enclosure height as the reference length and the hot-to-cold wall temperature difference. High Rayleigh number natural convection heat transfer measurements were reported by Nansteel and Greif (1984) for water-filled enclosures with both 2- and 3-dimensional vertical partitions and $10^9 < \mathrm{Ra} < 10^{11}$. In both of these studies, the flow field was found to be laminar along the heated and cooled walls.

Numerical investigations of partially- and fully-partitioned enclosures have almost exclusively been 2-dimensional (cf. Kelkhar and Patankar, 1986; Winters, 1988; Nishimura et al., 1988; Fu et al., 1989; Ciofalo and Karayiannis, 1991; Ghosh et al., 1992; and Karayiannis et al., 1992). Using the SIMPLER algorithm with an M=26×52 mesh, Kelkar and Patankar (1986) reported results for laminar flow in a square enclosure for two partition geometries, a single partition located vertically at the center of the enclosure and two identical partitions located at the top and bottom walls. Calculations were made for a range of Rayleigh numbers, partition heights, and partition conductivities. Nishimura et al. (1988) performed both an experimental and numerical investigation with water-filled enclosures having multiple vertical partitions for $10^6 < \mathrm{Ra} < 10^9$. The problem of transient heating in an enclosure with an off-centered partition was studied numerically by Fu et al. (1989). Ciafalo and Karayiannis (1991) and Karayiannis et al. (1992) applied the SIMPLEC algorithm to study fully- and partially-partitioned 2-dimensional enclosures. They found that the characterization of the thermal boundary conditions at the upper and lower end walls can have significant effects on local and mean heat transfer rates across the enclosure. Adiabatic and linear temperature profiles (LTP) were investigated, and the LTP boundary condition provided a better comparison with experimental data. Ghosh et al. (1992) studied the effect of shifting the position of a full partition on flow structure and heat transfer.

The author has found only one 3-dimensional computational study of natural convection in a partially-partitioned enclosure. Fusegi et al. (1992) present the results of a 3-dimensional simulation of air in a cubical enclosure with a solid partition, as shown in Fig. 105 with $H = L = W$. The centrally located rectangular opening in the partition is of height h and width w, and the thickness of the partition wall is much smaller than the size of the enclosure ($b/L = 0.03$). Two partition geometries were examined; Case A used $w/W = 0.4$ with $\mathrm{Ra} = 10^7$, and Case B used $w/W = 1.0$ with $\mathrm{Ra} = 5\times10^9$. The area aspect ratio A_p, defined as $A_p \equiv (h\times w)/(H\times W)$, for the partition was 0.2 for Case A and 0.5 for Case B.

In Case A, the SIMPLE algorithm with the QUICK scheme for dispersion error control was used to calculate laminar flow field and temperature distributions on an M=82×62×62 nonuniform mesh. A *free-fall* reference velocity resulted in an Archimedes number of 1.0. Boundary conditions included fixed hot and cold wall temperatures, and all side, floor, and ceiling walls were assumed adiabatic. Conduction heat transfer was allowed through the solid partition (soffit), and all solid boundaries were treated as no-slip for the momentum equations. Perspective views of isotherm and isovorticity surfaces revealed prominent 3-dimensional flow structures.

Near the hot sidewall as the heated fluid moves upward, the flow is blocked by the partition in the upper portion of the hot chamber, resulting in a near-stagnant region in the upper-level compartment between the partition and the heated sidewall. Away from the boundary layers, developing near the sidewalls and partition, the vertical temperature stratification can be characterized by a two-zone structure. The strongly buoyant flow generated near the heated vertical sidewall descends the hot-zone side of the internal partition and is discharged into the cold zone by turning sharply under the top of the doorway. At this point near and including the vertical symmetry plane passing the through the center of the doorway, the flow behaves like a free jet directed toward the upper corner of the cold zone.

For Case B with Ra=5×10^9 and an M=112×102×62 mesh, the flow exhibited steady periodic oscillations which were assumed to be indicative of a transition to turbulent flow. The entire flow field is thermally stratified, and very thin thermal and hydrodynamic boundary layers were seen to develop near the heated and cooled walls. The boundary layer on the heated sidewall penetrates up to only the mid-height of the enclosure, above which the flow was in a stratified and stagnant state. At this level, the boundary layer separates from the heated surface and moves horizontally toward the door. Reaching the doorway, the flow turns under the top of the door and moves up the cold-zone side of the partition. The flow path follows the inner vertical and horizontal walls. No jet-like flow was observed in the cold zone.

7.7.1 Colorado State Water-Filled Enclosure Experiments

Researchers at Colorado State University have investigated natural convection in partially-divided enclosures using a full-scale air test cell, built at Colorado State, and a small-scale water cell at the Solar Energy Research Institute (SERI). The objectives of the research were to determine under what conditions an enclosure will develop large zone-to-zone temperature differences (and the resulting effect on cross-cavity Nusselt numbers) and to compare the behavior of small-scale water models with full-scale air enclosures (Neymark et al., 1989). The small-scale water model has been selected for CFD simulation because the flow was experimentally determined to be laminar within the boundary layers along the walls.

The water test cell, Fig. 106, was equipped with a constant heat flux hot wall, a constant temperature cold wall, and an insulating partition with an aperture (doorway) of constant height (h = H/2) and varying width w. The details relating to the original construction of the water cell are reported by Scott et al. (1988), and the modifications made for the Colorado State experiments are given by Neymark (1988). Flow visualization experiments using dye injection were performed for two aperture widths, w/W=0.01 and w/W=0.2, at a flux Rayleigh number of 2×10^{12}. The flux Rayleigh number is defined as

$$Ra^* = \frac{g\beta H^4 q}{(k\nu\alpha)} \tag{383}$$

where q is the uniform heat flux at the hot wall, g is the acceleration of gravity, and β, k, ν, and α are the coefficient of volume expansion, thermal conductivity, kinematic viscosity, and thermal diffusivity of water, respectively. The thermal properties of water were evaluated at the average of the cold wall temperature T_c and the midpoint temperature of the hot wall T_H.

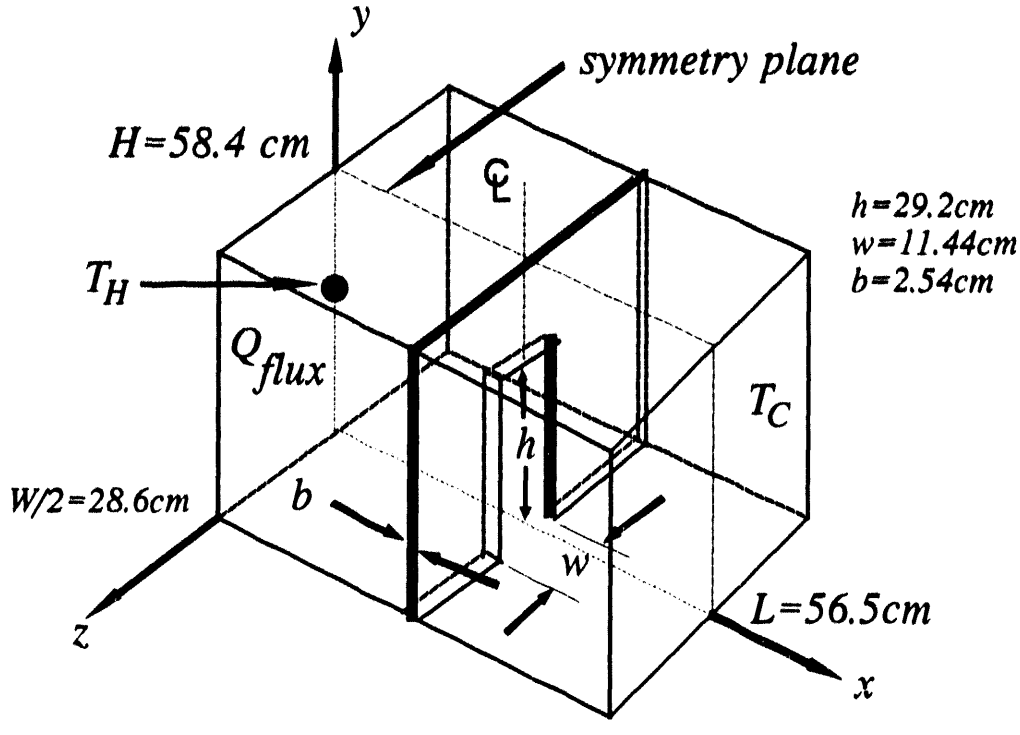

Figure 106. Geometry of small-scale water model.

The primary flow loop at the symmetry plane of the test cell for w/W=0.01 is shown in Fig. 107. The laminar upward boundary-layer flow along the hot wall separated from the wall at $H/4 < y < H/2$. The detached flow moved horizontally toward the top of the door, accelerating as it passes through the doorway, and exiting into the cold zone as a turbulent jet directed toward the cold wall at approximately a 45° angle. The turbulent fluctuations of the jet were visible without the assistance of the injected dye and were measured by a thermocouple traverse. Along the cold wall, the downward flow was wavy laminar with small vortices along the edge of the boundary layer.

For w/W=0.2, the flow up the hot wall was characterized by a wavy laminar boundary layer, Fig. 108. Separation occurred at $(3/8)H < y < (5/8)H$ with a resulting horizontal flow moving toward the top of the door. Entering the cold chamber, the flow rose as a laminar plume upward

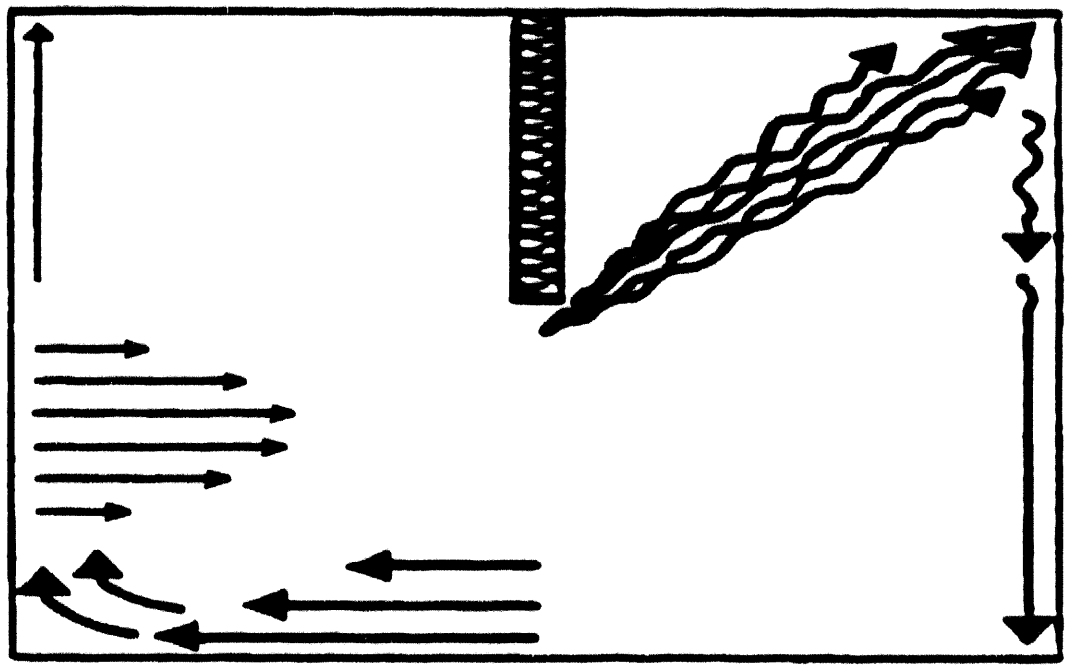

Figure 107. Flow visualization in the water cell, w/W=0.01 (Neymark, 1988).

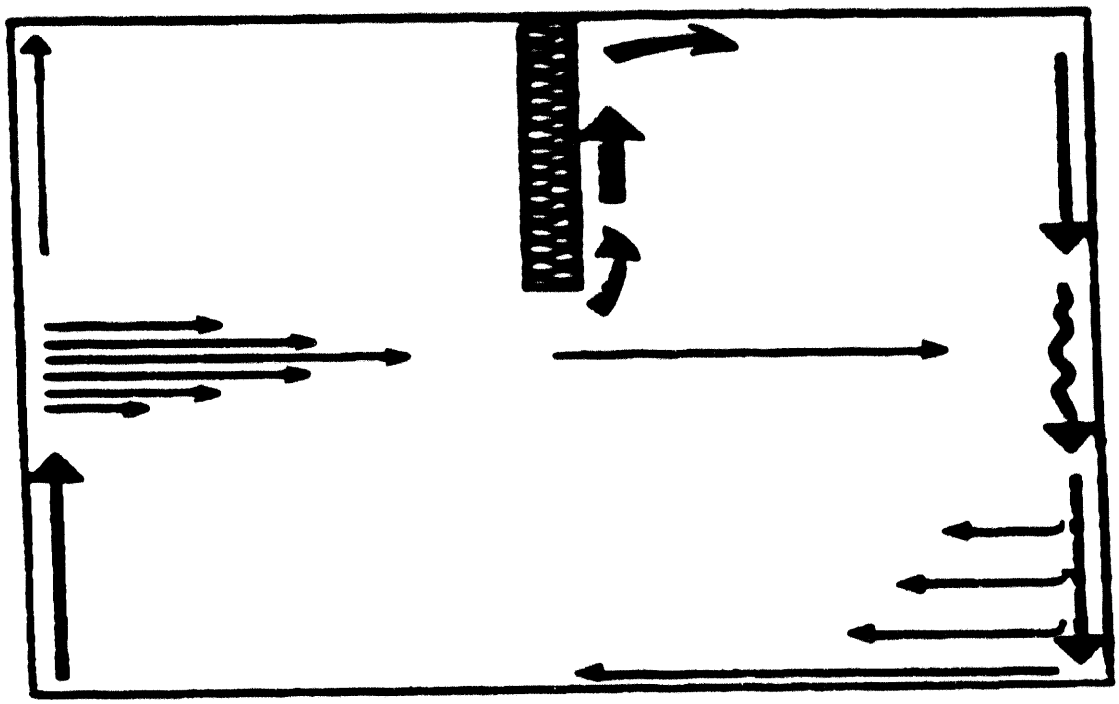

Figure 108. Flow visualization in the water cell, w/W=0.2 (Neymark, 1988).

along the partition with a small component of entrained fluid moving horizontally toward the cold wall. The plume rose to the top of the cold chamber where it turned and thickened as it approached the constant temperature cold wall. Descending the cold wall, the boundary layer started out as wavy laminar near $y = H$ and grew more turbulent as it approached $y = H/2$. Below $H/2$, the cold wall boundary layer turbulence subsided into wavy laminar flow.

7.7.1.1 CFD Experiments

The small-scale water experiment with $w/W = 0.2$ ($A_r = 0.1$) was selected for simulation by CFDL..PHI3D. Since the experimental flow visualization data showed the flow was symmetric about a vertical longitudinal plane passing through the middle of the door, a half-model was constructed with an $M=52\times42\times26$ mesh, Fig. 109, containing 57,000 nodes. The mesh shown in Fig. 109 is the final result of a meshing study which began with a relatively uniform 24,000 node discretization. Mesh refinement and adaptation, based upon visual inspection of solutions at $Ra\approx10^6$, proceeded through a sequence of discretizations that focused mainly on attainment of solution stability in the region of the doorway and the hot zone with its dominant vertical buoyant plume. Previous benchmark experience verified the requirement for active dispersion error control, $\beta > 0$, hence $\beta\approx0.1$-0.2 was used in this meshing study.

Boundary conditions for the momentum equations were no-slip on all surfaces of the dividing partition and doorway and a tangency condition with an applied drag on all other boundaries except for the symmetry plane. The decision to apply a no-slip boundary condition on surfaces near the doorway and internal partition was based upon computational experience and the expectation that solution stability, hence accuracy, would be critically dependent upon the resolution of the momentum and thermal boundary layers in this critical region. Drag and tangency boundary conditions can certainly be applied on surfaces farther away from the door, resulting in a significant savings in computational costs. The far wall drag boundary condition was calculated by integrating Blasius's solution for a developing boundary layer over a flat plate of length H (White, 1974), yielding

$$\tau_w = \left(\frac{1.328}{\sqrt{Re_H}} \right) \frac{\rho U^2}{2 g_c} = \left(\frac{1.328}{2 g_c} \rho \sqrt{\frac{\nu}{H}} \right) U^{3/2} \qquad (384)$$

$$\tau_w = 0.008487\, U^{3/2} \quad [\text{dynes/cm}^2]$$

The final integrated shear stress at the wall, τ_w in Eq. (384), was evaluated in cgs units using the water property data in Table 11. Boundary conditions for the energy equation included a fixed uniform temperature, T_c, for the cold wall and a constant heat flux, q, applied uniformly across the hot wall. All other surfaces, including the floor, ceiling, symmetry plane, and internal partition, were adiabatic. The experiment was run at a flux Rayleigh number (Ra^*) of 2×10^{12}, corresponding to a uniform heat flux across the hot wall of 0.0641 W/cm^2. Correlating the water-filled heat transfer data for this geometry, Neymark (1988) presents the Nusselt number (Nu) as a function of Ra^*, as,

$$Nu = 0.297\ (Ra^*)^{0.189} \qquad (385)$$

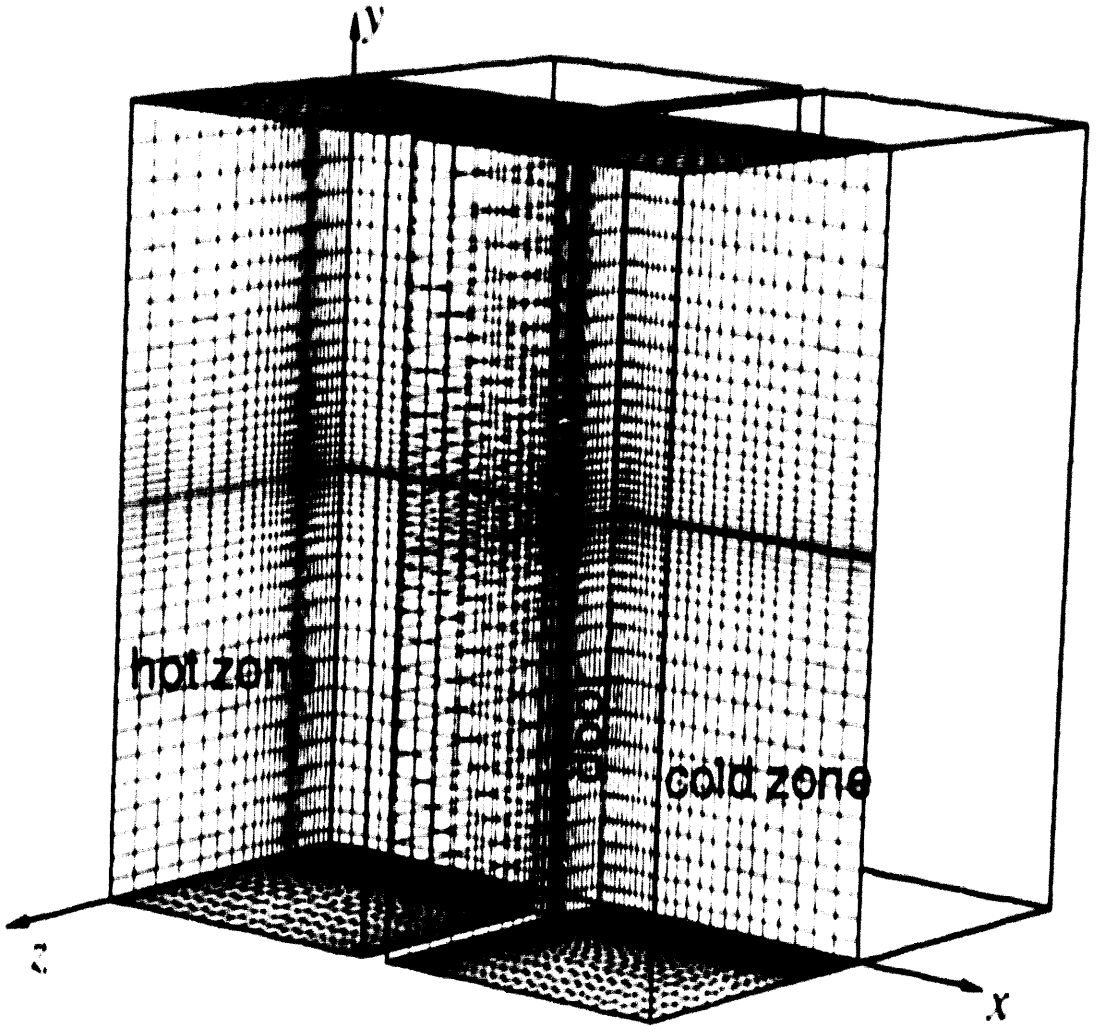

Figure 109. Mesh layout for the water test cell, $M = 52 \times 42 \times 26$.

where

$$\mathrm{Nu} = \frac{q\,H}{k\,(T_H - T_C)} \tag{386}$$

and T_C is the cold wall temperature, T_H is the hot wall mid-point temperature, k is the thermal conductivity of water evaluated at $T_{m(f)} = (T_C + T_H)/2$, and H is the height of the enclosure. For $\mathrm{Ra}^* = 2 \cdot 10^{12}$, Nu = 62.7, $T_{m(f)} = 22^\circ\mathrm{C}$, $(T_H - T_C) = 10^\circ\mathrm{C}$, $T_H = 27^\circ\mathrm{C}$, and $T_C = 17^\circ\mathrm{C}$. The corresponding wall-to-wall Rayleigh and Grashof numbers for these conditions are

$$Ra = \frac{\beta g (T_h - T_c) H^3}{\nu \alpha} = 3.2 \times 10^{10} \quad ; \quad Gr = \frac{Ra}{Pr} = 4.8 \times 10^9$$

For Ar = 10,000, the reference velocity is 0.09 cm/s, and the Reynolds and Peclet numbers are

$$Re = \left[\frac{Gr}{Ar} \right]^{1/2} = 692.8 \quad ; \quad Pe = Re\,Pr = 4,642$$

Table 11. Water Properties at 22°C , Neymark (1988).

density, ρ	1.0 g/cm^3
kinematic viscosity, ν	0.00954 cm^2/s
thermal diffusivity, α	0.00143 cm^2/s
coeff. of volume expansion, β	0.000224 K^{-1}
thermal conductivity, k	0.006 W/cm-K
Prandtl number, Pr	6.7

Rayleigh number continuation was used to work up to the target test conditions beginning at Ra = 10^4. The initial velocity distribution was assumed zero, and an initial horizontal temperature distribution was interpolated linearly between the hot and cold walls. The approximate steady-state solution at each intermediate Rayleigh number was used as the initial condition for the next higher Rayleigh number, incrementing Ra by an order of magnitude for each step.

The solution at Ra = 10^6 represents a geometrically-important case for future benchmarking considerations. The thermal boundary conditions were simplified by using a constant uniform temperature for the hot wall rather than a uniform heat flux. The user-selected velocity scale directly impacts solution stability through the scaling of the body-force (Ar), diffusion (Re and Pe), and advection terms in the momentum and energy equations. This flexibility, resulting from the scaling rules chosen for nondimensionalization, is especially critical for natural convection in water, where Pr≈6. Since Pe=Re Pr, a velocity scale, selected to produce a stable value for Re, may still result in an adversely high Peclet number, thus exposing the energy solution to a potentially destabilizing dispersion error mode. For Ra = 10^6, Ar = 100, and Pr = 6, the Reynolds number was 41.2 and Pe = 242.9. These low Reynolds and Peclet numbers provided sufficient natural diffusion in the problem to easily establish a benchmark-candidate case for further Rayleigh number continuation.

The computed velocity and temperature distributions on the symmetry plane at Ra = 10^6 are given in Fig. 110. The temperature boundary conditions are a uniform cold wall temperature of 17°C and a uniform hot wall temperature of 27°C. At this low Rayleigh number, the buoyant plume rising up the cold zone partition above the door is well established. However, the boundary layer separation in the hot zone, observed in the dye injection experiments at Ra=3.2×10^{10}, does not form. Lateral and spanwise temperature distributions on cutting planes in the middle of the cold and hot zone quadrants, Fig. 111, indicate the extent of thermal boundary layers along the heated and cooled walls.

(a) velocity distribution projected onto the symmetry plane

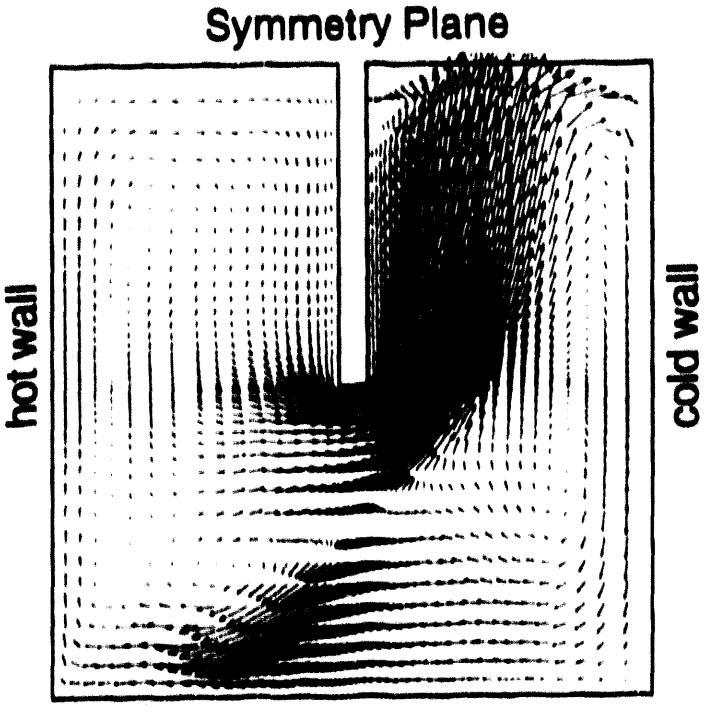

(b) temperature distribution on symmetry plane

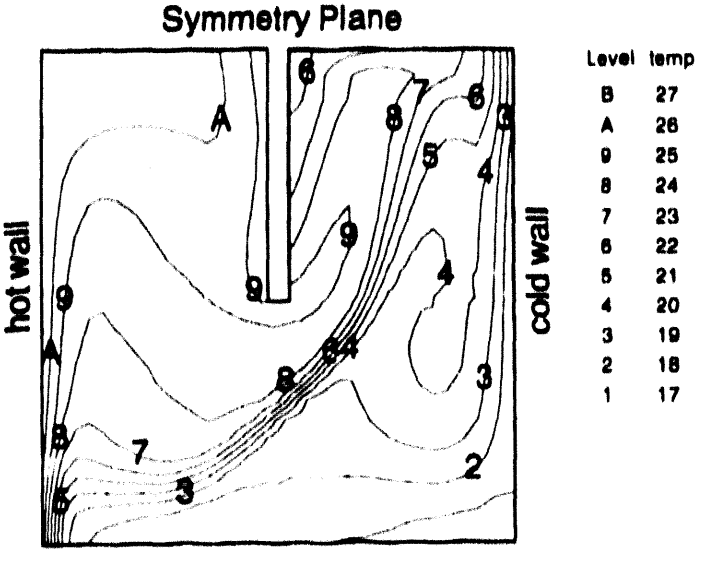

Figure 110. Symmetry plane velocity and temperature distributions at Ra = 10^6.

(a) temperature distribution on lateral cutting planes

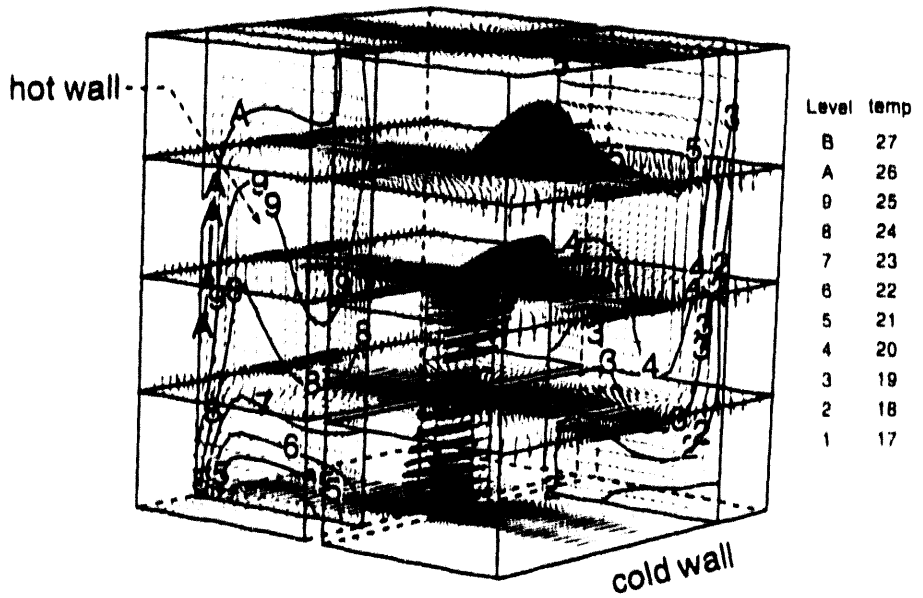

(b) temperature distributions on spanwise cutting planes

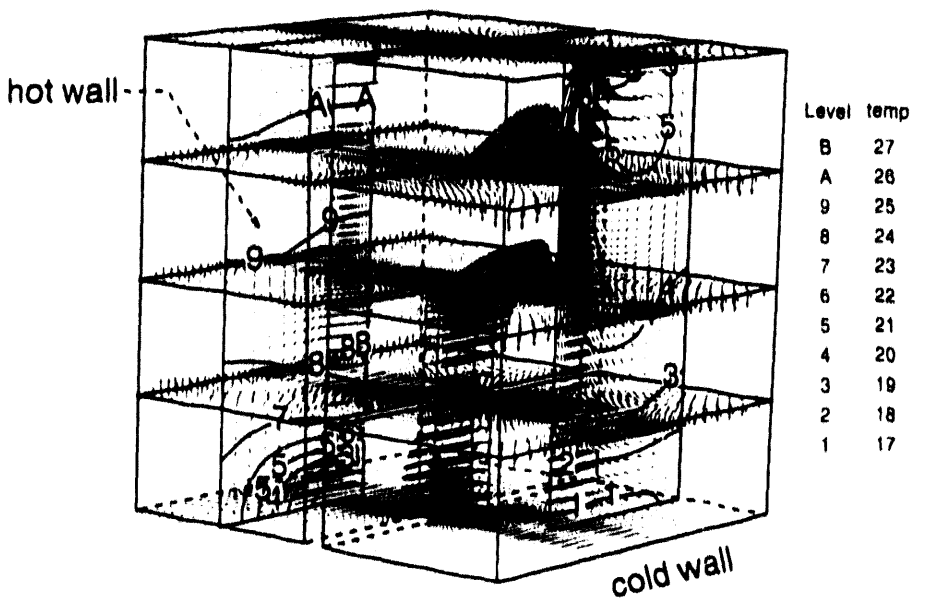

Figure 111. Temperature distributions on lateral and spanwise cutting planes, Ra=10^6.

Lagrangian particle tracks for three release points in the doorway are shown in Figs. 112-114, presented from view points in the hot and cold rooms, respectively. The release point (28.25,28,0.5) for the first particle, Fig. 112, is near the top of the door jam and offset 0.5 cm from the symmetry plane. Caught in the buoyant plume, the particle rises to the ceiling of the cold zone and then descends to the floor through a winding path. Once entrained by the main flow along the floor and near the symmetry plane, the particle rapidly moves into the hot zone where it closely follows the boundary layers along the walls. The direction of motion is indicated along the track, and the time interval between particle symbols ("bubbles") is again a uniform constant. Therefore, local relative particle speed is discernible by bubble separation distances.

The second particle, Fig. 113, is released slightly below the mid-height of the doorway, halfway between the symmetry plane and the door jam, at (28.25,10,2.5). Initially moving into the hot zone, the particle is engaged by the complex 3-dimensional flow within the central core of the hot zone. It eventually proceeds horizontally toward the top of the door, reenters the cold zone, and is entrained by the dominant buoyant plume. Descending to its release point, the particle enters the hot zone a second time.

Released 2 cm above the floor near the door jam, the third particle, Fig. 114, follows an initial path that is somewhat similar to the second particle, briefly entering the hot zone and then moving horizontally toward the door and the cold zone. The buoyant plume again captures the particle where it follows a path in the cold zone eventually passing back into the hot zone near its original release point. Note that particles 2 and 3 manifest a horizontal flow across the midplane of the hot zone that is not, however, associated with a boundary layer separation as described in the experiments.

The steady-state solution obtained for $Ra=10^6$ was used as the initial condition for the water-cell experiment case of $Ra=3.2\times10^{10}$ ($Ra^*=2\times10^{12}$). To better simulate the experiment, the hot wall boundary condition was changed from a constant uniform temperature to a constant uniform heat flux of 0.0641 W/cm^2. Figures 115-124 present the results of the solution after 3000 time-steps (~ 9000 outer iterations), where the time-step was ~ 0.016 sec., giving an elapsed time of ~ 48.0 sec. This solution is not at a steady-state condition; however, it has progressed far enough from the $Ra=10^6$ solution to observe distinct differences. Figures 115 and 116 indicate the development of strong boundary layer flows, and the buoyant plume just above doorway along the interior wall continues to dominate the flow field. The horizontal streamlines shown in Fig. 117 demonstrate the definite 3-dimensionality of the flow. An oblique shear layer, intersecting the doorway at mid-height, is a distinctive feature of the flow through the aperture. The structure of the thermal boundary layers can be seen in Figs. 118-120.

Lagrangian particle tracks for various release points are presented in Figs. 121-124. The elapsed time for each track in these figures is 600 sec. In Fig. 121, the release point is near the top of the doorway where the particle immediately follows the buoyant plume up to the top of the cold zone. Moving slowly back to the partition, it descends briefly until caught by a rising current and transferred over to the cold wall boundary layer. Rapidly descending the cold wall, the particle rises towards the doorway where it is captured by the lower stream of the shear layer and swept into the hot zone. Released at approximately the mid-height of the door, the particle in Fig. 122 is also captured by the lower stream of the shear layer and, thereby, drawn into the hot zone. Moving along the floor of the hot zone, it follows two loops that are a part of a large vortex roll driven by the boundary layer flow along the hot wall. Eventually the particle is caught up by the upper stream of the doorway shear layer, where it proceeds through the door and enters the buoyant plume. The third particle, shown in

(a) view of cold zone

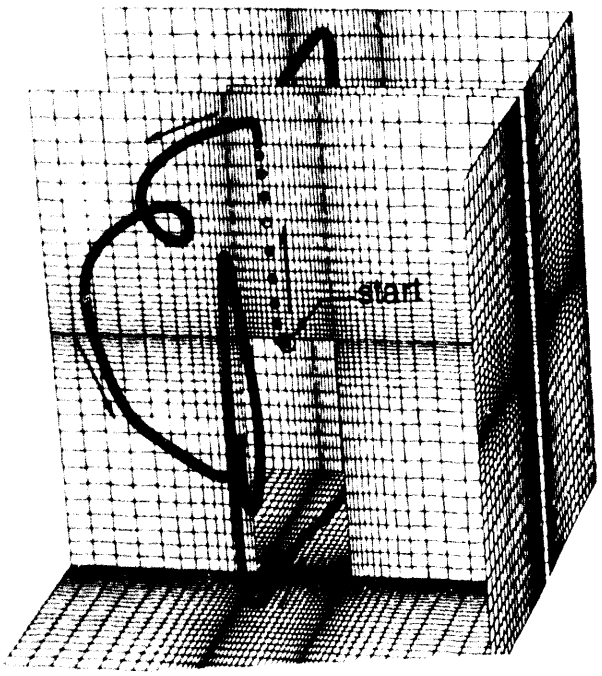

(b) side view of hot and cold zones

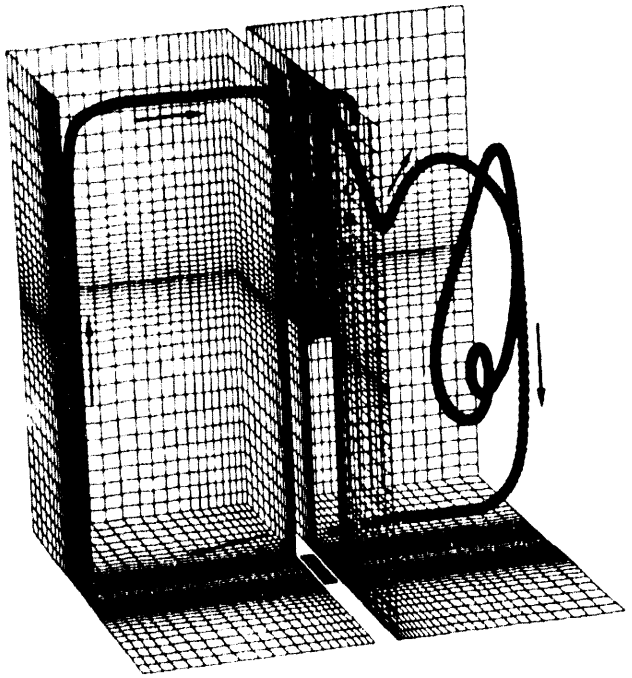

Figure 112. Lagrangian particle track, Ra=10^6, release point=(28.25,28,0.5).

(a) view of cold zone

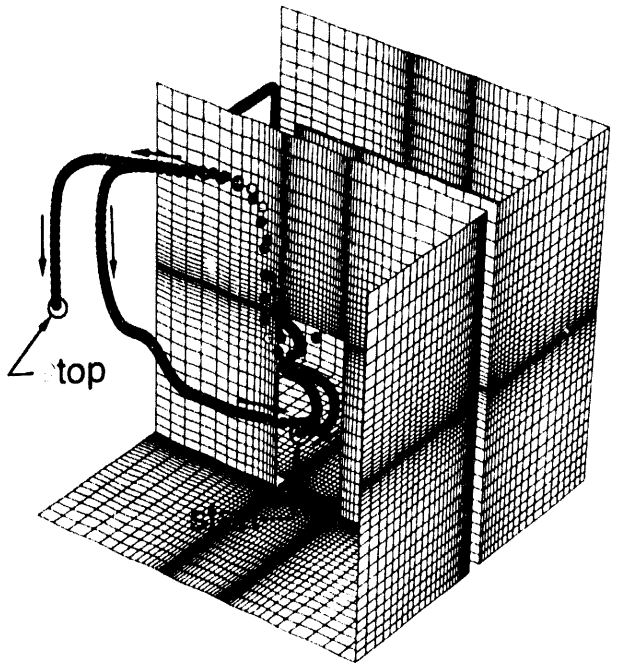

(b) side view of hot and cold zones

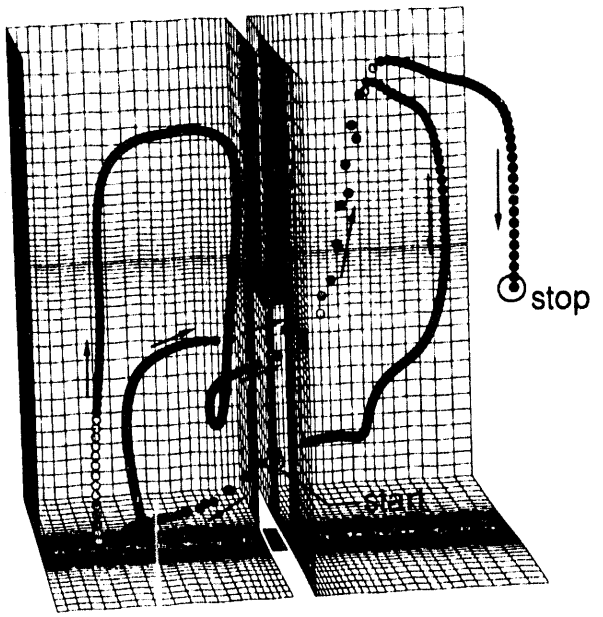

Figure 113. Lagrangian particle track, Ra=10^6, release point=(28.25,10,2.5).

(a) side view of hot and cold zone

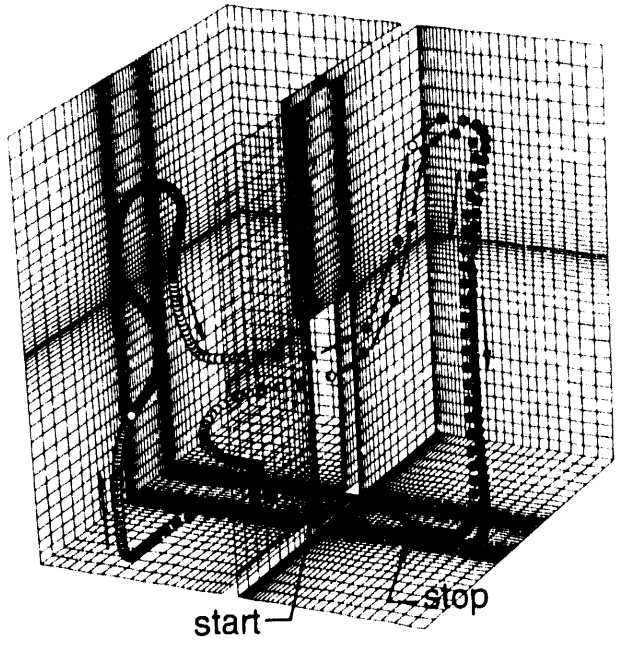

(b) view of hot zone

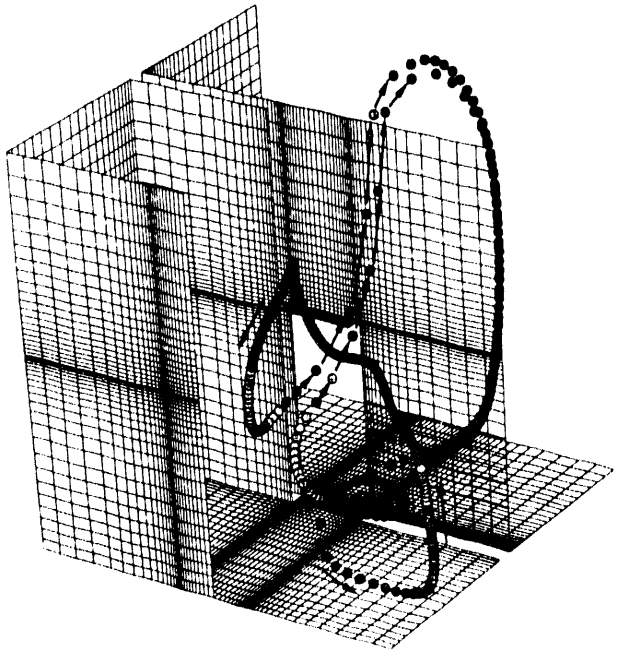

Figure 114. Lagrangian particle track, Ra=10^6, release point=(28.25,2,5).

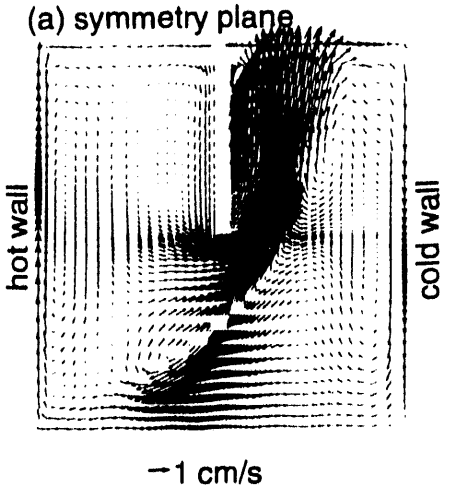

Figure 115. Velocity distribution at selected vertical planes, Ra=3.2×10^{10}.

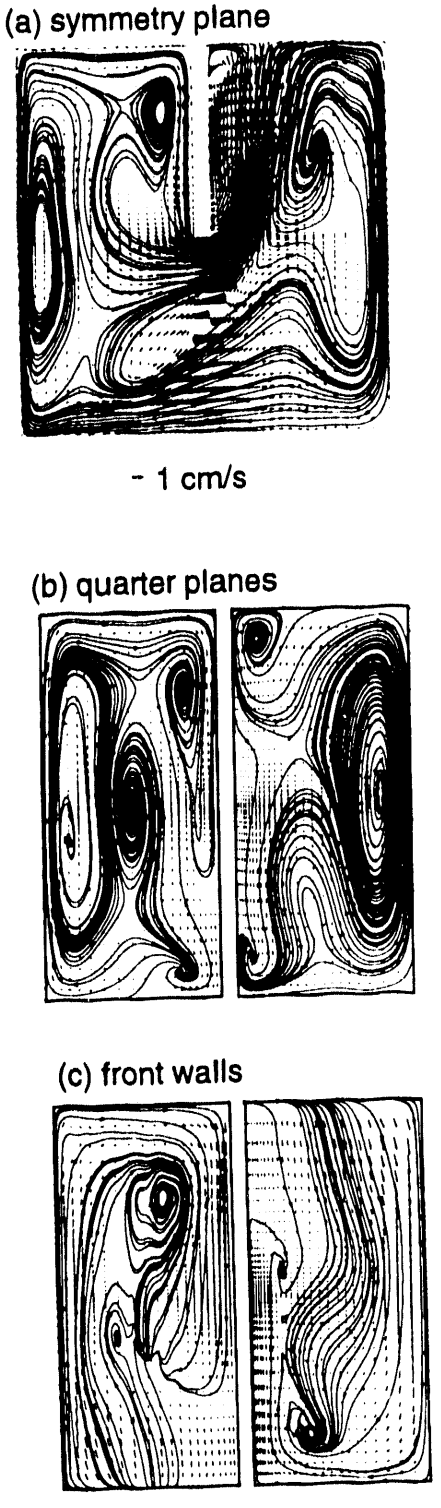

Figure 116. Streamlines projected onto vertical planes - Ra=3.2×10^{10}.

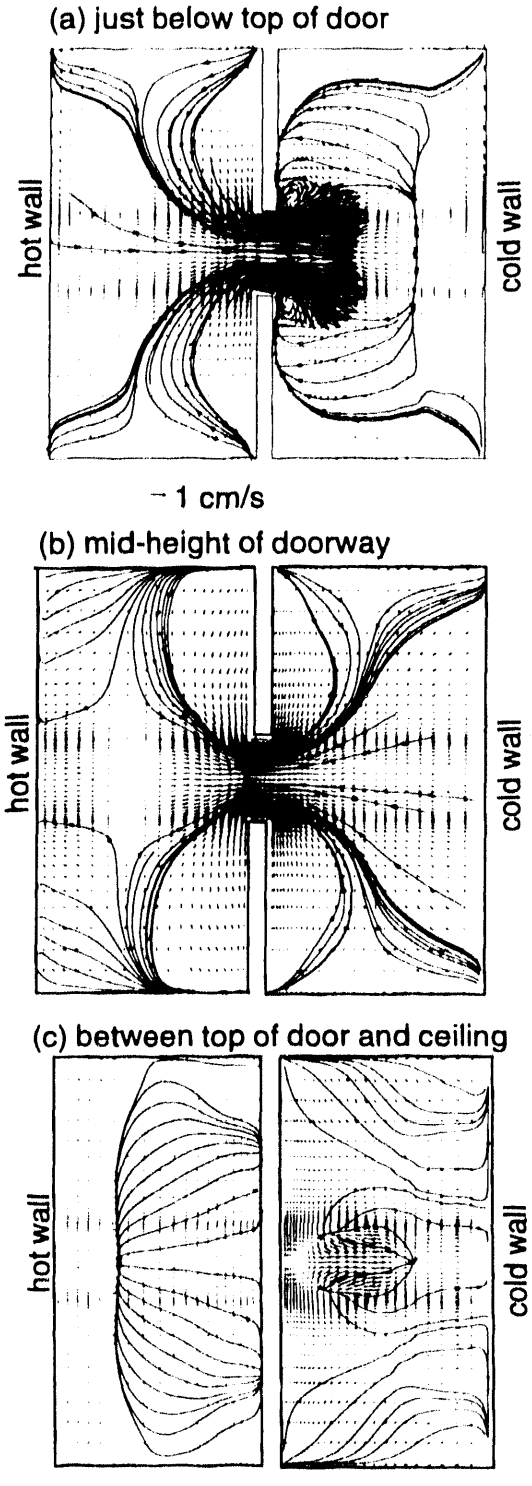

Figure 117. Streamlines projected onto horizontal planes - Ra=3.2×10^{10}.

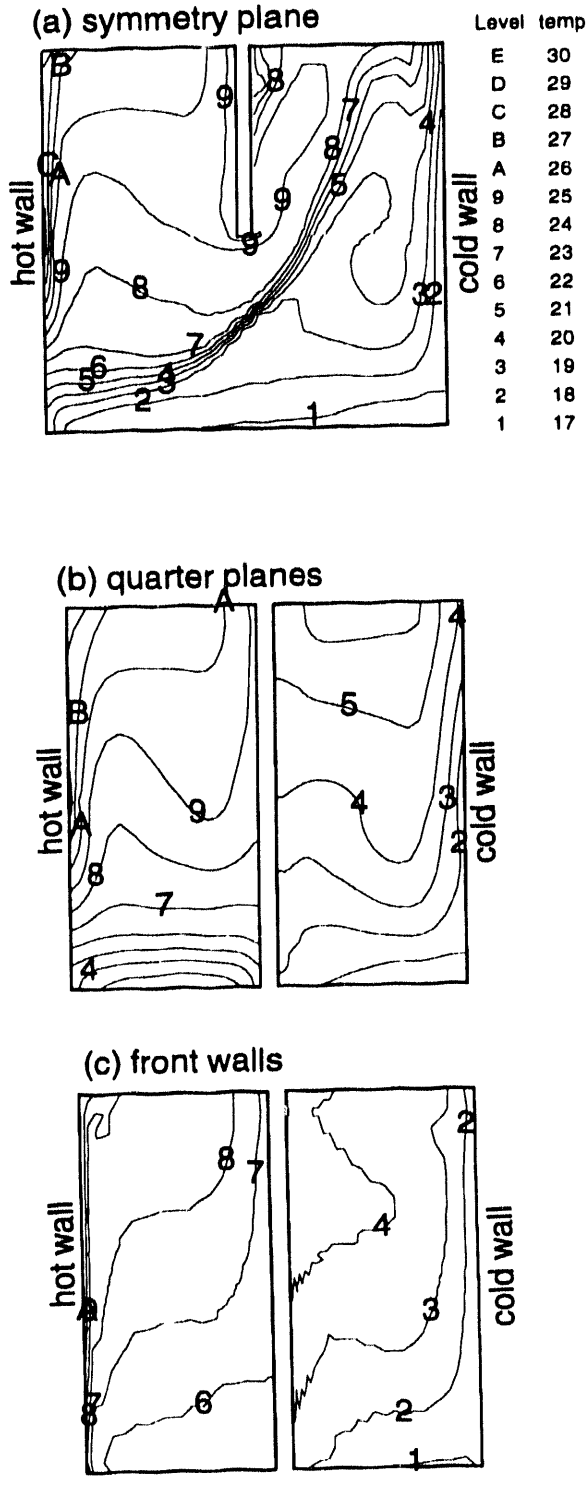

Figure 118. Isotherms on selected vertical planes - Ra=3.2×10^{10}.

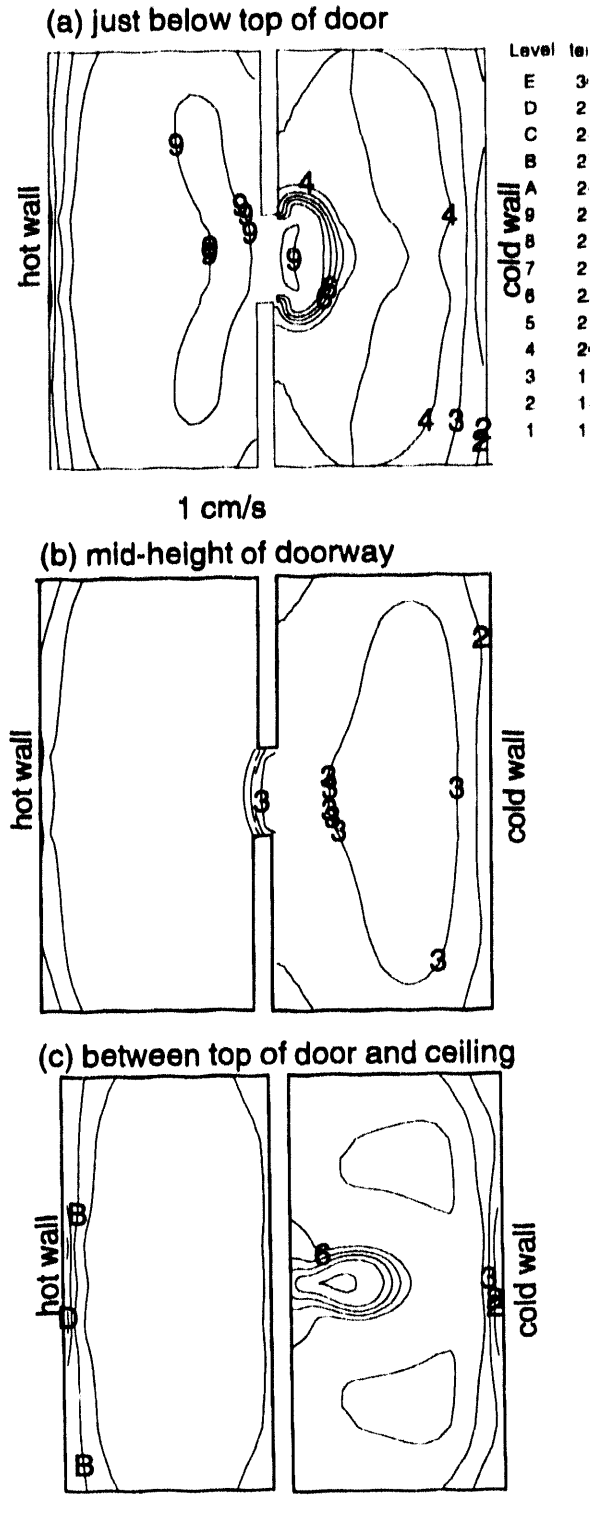

Figure 119. Isotherms on selected horizontal planes - Ra=3.2×10^{10}.

(a) temperature distribution on lateral cutting planes

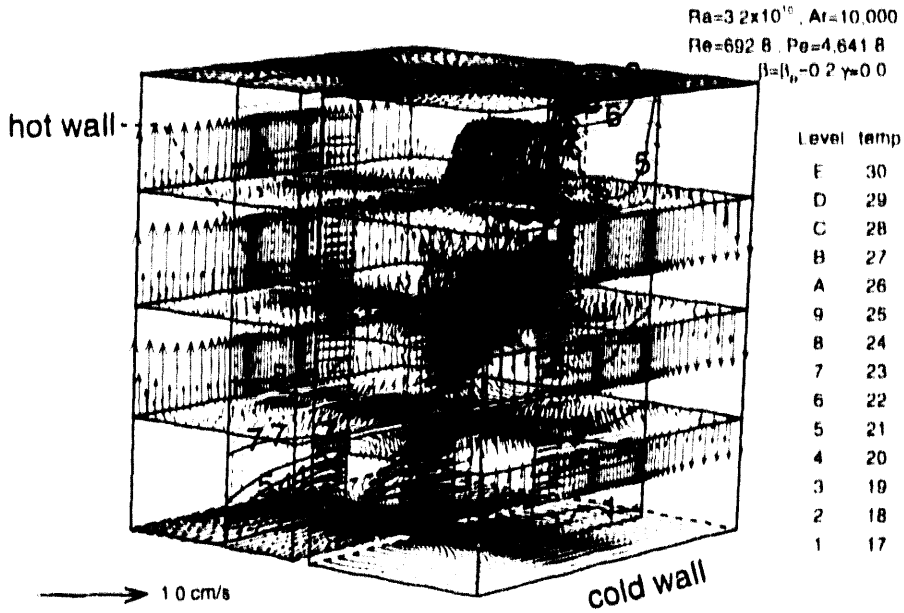

(b) temperature distributions on spanwise cutting planes

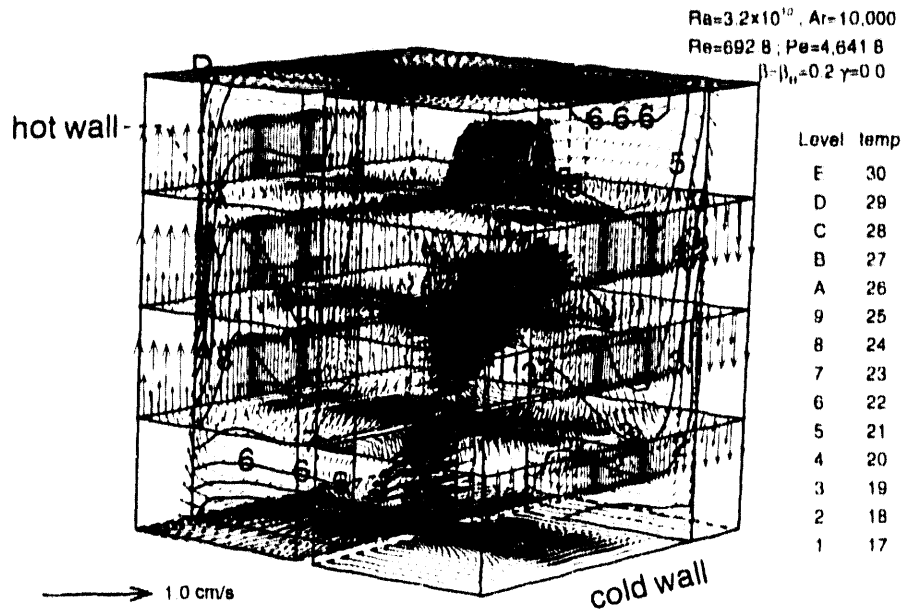

Figure 120. Isotherms on lateral and spanwise cutting planes, Ra=3.2 × 10^{10}.

(a) view of cold zone

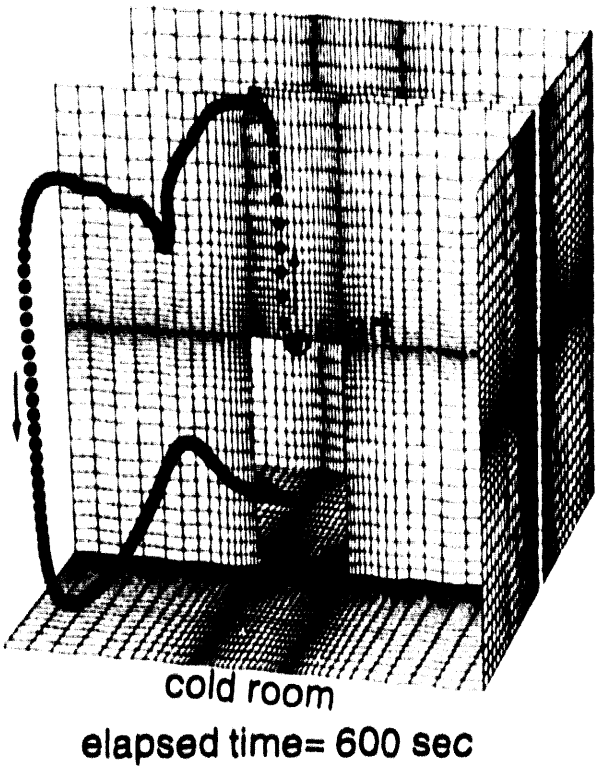

(b) side view of hot and cold zones

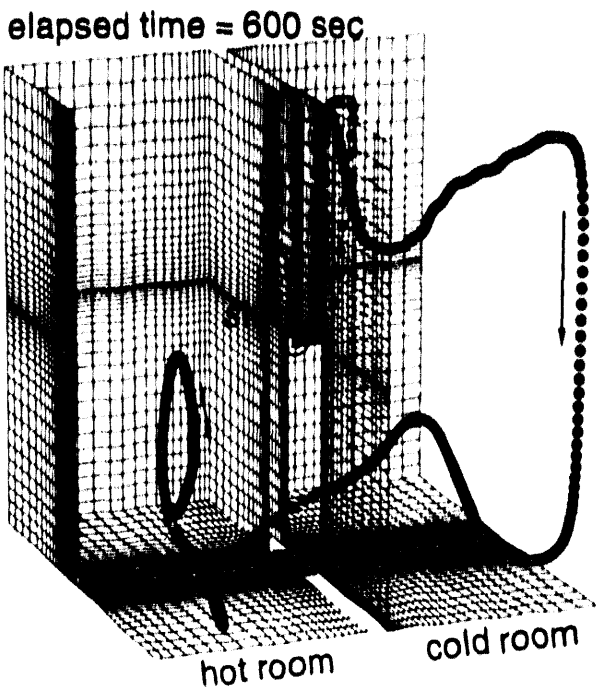

Figure 121. Lagrangian particle track, Ra=3.2×10^{10}, release point=(28.25,28,0.5).

(a) view of cold zone

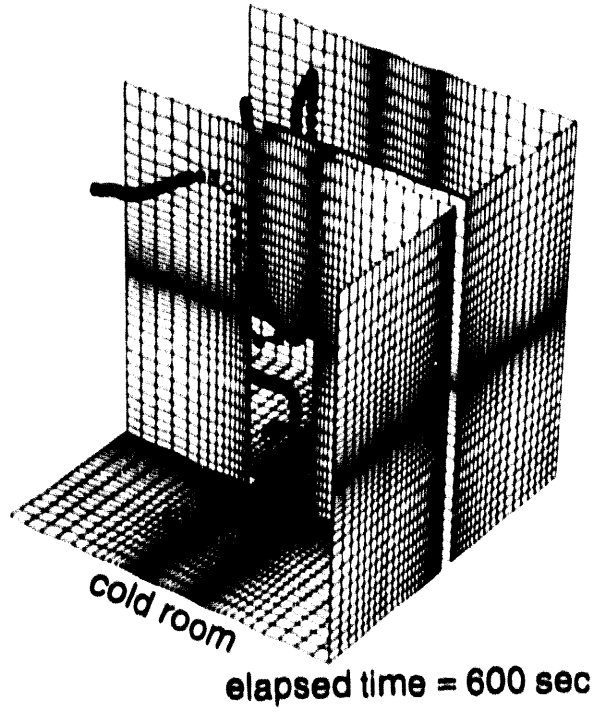

(b) side view of hot and cold zones

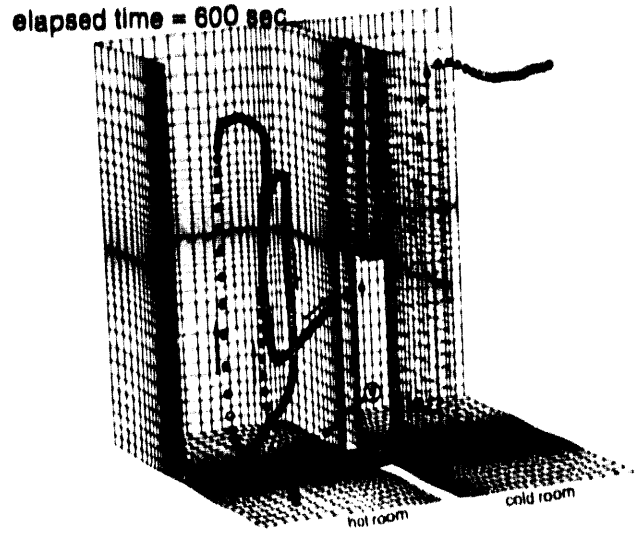

Figure 122. Lagrangian particle track, Ra=3.2×10^{10}, release point=(28.25,10,2.5).

(a) view of cold zone

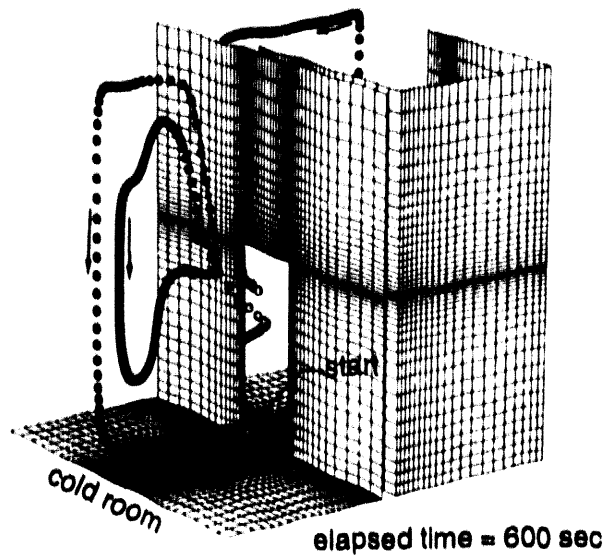

(b) side view of hot and cold zones

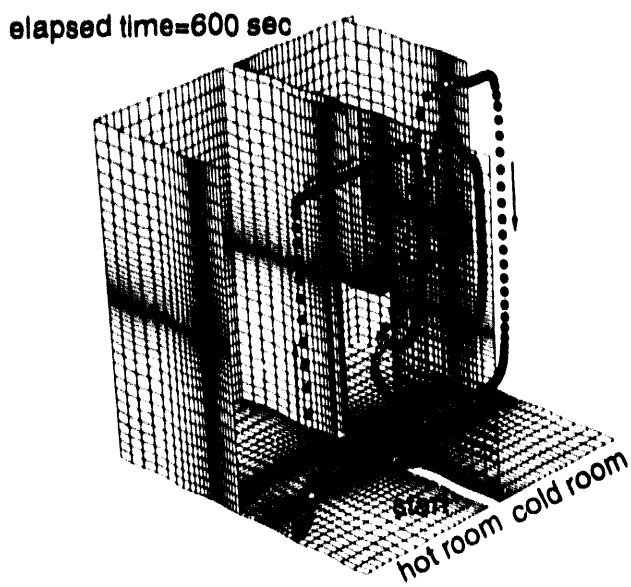

Figure 123. Lagrangian particle track, $Ra=3.2\times10^{10}$, release point=(28.25,2,5).

(a) release point=(3.2,22.8,20)

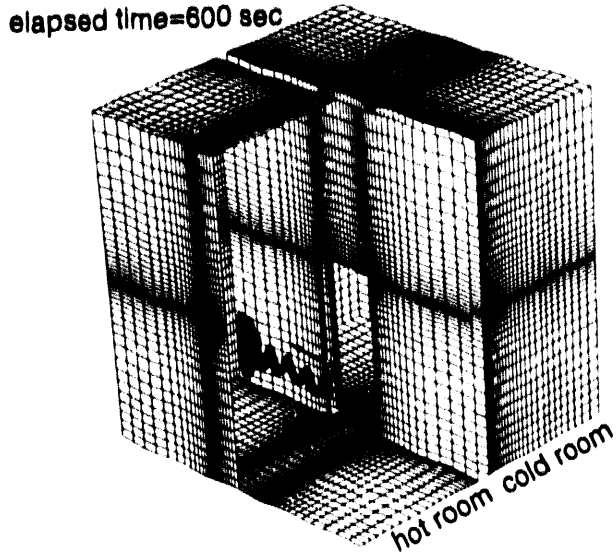

(b) release point=(22.2,49,20)

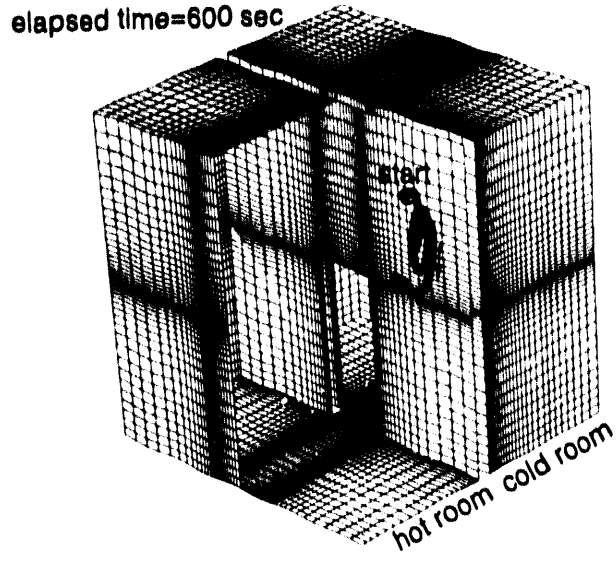

Figure 124. Lagrangian particle tracks in hot zone, Ra=3.2×10^{10}.

Fig. 123, is released near the corner of the door, just abovethe floor. Moving briefly into the hot zone, the particle follows the upper stream of the shear layer into the coldzone where it tracks one loop of a large, slow vortex roll in the middle of the zone before being captured by the buoyant plume and driven to the ceiling. Following the boundary layer flow along the cold wall, the particle moves back into the hot zone. Two release points, located in the interior of the hot zone, are shown in Fig. 124. These particle tracks demonstrate some of the structure of the slowly moving vortex rolls that dominate the flow field outside of the strong boundary layer flows along the walls. The solution has not progressed far enough toward its steady-state condition to show the experimentally observed separation of the hot wall boundary layer; however, even after 48 sec. into the transient, there is significant horizontal flow near the top of the door in the hot zone. When separation occurs, the stagnant region in the upper portion of the hot zone should increase in temperature. The boundary layer flows are well-established and should continue to strengthen. Future work will develop the solution onto a steady-state condition where a direct comparison can be made with the experimental data.

8. CONCLUSIONS AND RECOMMENDATIONS

A new primitive-variable finite-element CFD algorithm, the Continuity Constraint Method (CCM), has been developed to produce approximate time-accurate and/or steady-state solutions for the unsteady, incompressible Navier-Stokes conservation law system in three dimensions. Recognition of the dual role of pressure, as a consequence of the constraint of continuity and as a force in the mechanical balance law for conservation of momentum, has been the fundamental principle guiding the CCM development.

An implicit time integration scheme, with quasi-Newton iterative cycling within the time step, allows the two roles for pressure to be completely separated computationally. Specifically, a mass-conserving potential function is used to enforce the continuity constraint, and the resulting dominant "2 Δ-x" dispersive error mode is prevented from polluting the velocity vector distribution by replacing the accumulated "pseudo-pressure" with the genuine pressure computation at the end of the time step, as required. Induced by a solenoidal velocity vector field, the genuine pressure is calculated with well-posed boundary conditions by the pressure Poisson equation. This separation of tasks produces a theoretically appealing and computationally clear view of the individual and totally distinct boundary conditions required for the continuity constraint function and the genuine pressure.

As implemented in the computer program CFDL.PHI3D, the CCM employs a θ-implicit time-integration scheme, a consistent mass matrix, an optional (as required) Taylor Weak Statement (TWS) formulation for dispersion error control, and equal-order interpolation of all state-variables. Isoparametric 8-node hexahedra with trilinear basis functions are used to support the semi-discrete approximation on the computational domain. The CFDL.PHI3D code was developed for a UNIX platform, taking advantage of the recent expansion of computing capacity with the emergence of engineering workstations as the primary compute engines for modern computational analysis.

As original contributions to the field of incompressible CFD, this dissertation has presented:

(a) a derivation of an accurate expression for the unsteady evolution of the divergence error, thus providing a firm and exact theoretical foundation for the CCM,

(b) an investigation of the separate roles of the non-smooth continuity-constraint function ϕ^h, dominated by a "2 Δx" dispersion error, and the smooth physically-motivated genuine pressure P^h,

(c) an investigation of the Galerkin weak statement for the Reynolds-averaged pressure Poisson equation, thus minimizing the required order of the Sobolev functional space required for a turbulent flow simulation,

(d) an investigation and resolution of physically and numerically well-posed boundary conditions for all state-variables including the mass-conserving potential function,

(e) an implementation of the CCM using a finite element semi-discretization of a Galerkin weak statement with an optional Taylor Weak Statement extension for Ω in $\mathbb{R}^3$,

(f) an efficient solution strategy for work-station-based computing,

(g) an investigation of sparse iterative solvers and sparse data structures for solving the terminal matrix linear algebra statements required by the CCM, and

(h) a verification, benchmarking, and validation study of the CCM for isothermal and nonisothermal flows in challenging 3-dimensional flow geometries.

It has become clear, during the present research, that a paucity of quality detailed 3-dimensional test cases exist in the literature for support of verification, benchmarking, and validation of incompressible CFD algorithms. The cases presented in this dissertation provide a starting point for future development of benchmark-quality solutions and validation-quality experimental data for 3-dimensional flows. The present investigation of the step-wall diffuser is the first published study to quantitatively explore the rich detail of 3-dimensional flow structures produced by this basic geometry. Additionally, buoyancy-driven flows in nonpartitioned and partitioned enclosures provide suitable 3-dimensional test configurations, incorporating a range of simple geometries and easily applied boundary conditions. The development of 3-dimensional turbulent test cases is another area for future research.

Additional research into the CCM should include a study of adaptive time-step control, an extended examination of the Taylor Weak Statement incorporating the influence of all of the terms identified by Baker and Kim (1987), a continued investigation into advanced numerical linear algebra techniques, the implementation of suitable turbulence models to explore the implications of the pressure Poisson equation for Reynolds-averaged state variables derived in the present study, and an exploration of parallel implementations for this (and other) segregated forms of the CCM.

Finally, the long-term viability of 3-dimensional CFD is in part dependent upon the development of effective methods of presenting the large amounts of data produced by simulations of steady and transient flows. The present study has investigated a number of available methods for solution display and flow visualization, including 2- and 3-dimensional contour plots of relevant state-variables, vector and contour plots on selected cutting planes, and Lagrangian particle tracking displayed on 3-dimensional perspective views of the flow domain. Methods of visualization of 3-dimensional data represent a new and productive field of research for all areas of computational mechanics.

ACKNOWLEDGMENTS

This report was originally published as a dissertation in partial fulfillment of the requirements for the Doctor of Philosophy degree in Engineering Science at the University of Tennessee. The author's first exposure to computational fluid dynamics (CFD) and the finite element method came at a short course given by Profs. A. J. Baker and J. T. Oden in the summer of 1984. Two years later, the author enrolled in the graduate school of the University of Tennessee to study CFD with Prof. Baker as his major professor. The ensuing years have proven to be extremely rewarding, educationally, professionally, and personally, thanks to the guidance, tutelage, and encouragement of Dr. Baker. Modern scientific research is a collaborative effort, and the discussions, in and out of the class room, between the author and his fellow graduate students, Drs. Jim Freels, Joe Iannelli, and Wilbert Noronha and Messrs. David Chaffin, Jhang Jing, Subrata Roy, Ed Schaub, and Kwai Wong, provided a valuable resource. The author also benefitted from many stimulating discussions with his colleagues at Oak Ridge National Laboratory, including Drs. John Drake, John Kirkpatrick, and Jim Park, and Messrs. Ken Childs, Gary Giles, Michael Taylor, and Mark Wendel. This graduate study was made financially possible by the support of the Educational Assistance Program of the author's employer, Martin Marietta Energy Systems. The author acknowledges the contributions of his graduate committee: Profs. R. V. Arimilli, A. J. Baker, R. D. Krieg, and J. E. Stoneking. Manuscript preparation and technical editing for this report were provided by A. I. Rose and C. H. Shappert, respectively. The author's wife, Pamela S. Williams, translated from the French Témam's classic paper on the fractional step method. She also spent many long hours painstakingly proofreading this rather lengthy dissertation. Her immeasurable patience, support, and encouragement over the seven years of study are most gratefully acknowledged.

REFERENCES

Abbott, D. E., and S. J. Kline. 1962. "Experimental Investigations of Subsonic Turbulent Flow over Single and Double Backward-Facing Steps." *Trans. ASME D: Journal of Basic Engineering* **84**: 317.

Abdallah, S. 1987. "Numerical Solutions for the Incompressible Navier-Stokes Equations in Primitive Variables Using a Non-Staggered Grid, II." *Journal of Computational Physics* **70**: 193-202.

Aksoy, H., and C. J. Chen. 1992. "Numerical Solution of Navier-Stokes Equations with Nonstaggered Grids Using Finite Analytic Method." *Numerical Heat Transfer, Part B* **21:** 287-306.

Amsden, A. A. and F. H. Harlow. 1970. *The SMAC Method: A Numerical Technique for Calculating Incompressible Fluid Flows*. Los Alamos, New Mexico: Los Alamos Scientific Laboratory. University of California. LA-4370.

Anderson, D. A., J. C. Tannehill, and R. H. Pletcher. 1984. *Computational Fluid Mechanics and Heat Transfer*. New York: Hemisphere Publishing Corp.

Arakawa, A. 1966. "Computational Design for Long-Term Numerical Integration of the Equations of Fluid Motion: Two-Dimensional Incompressible Flow. Part I." *Journal of Computational Physics* **1**: 119-143.

Aregbesola, Y. A. S., and D. M. Burley. 1977. "The Vector and Scalar Potential Method for the Numerical Solution of Two- and Three-Dimensional Navier-Stokes Equations." *Journal of Computational Physics* **24**: 398-415.

Aris, R. 1962. *Vectors, Tensors, and the Basic Equations of Fluid Mechanics*. Englewood Cliffs, N.J.: Prentice-Hall, Inc.

Armaly, B. F., F. Durst, J. C. F. Pereira, and B. Schönung. 1983. "Experimental and Theoretical Investigation of Backward-Facing Step Flow." *Journal of Fluid Mechanics* **127**: 473-496.

Aziz, K., and J. D. Hellums. 1967. "Numerical Solution of the Three-Dimensional Equations of Motion for Laminar Natural Convection." *The Physics of Fluids* **10** no. 2: 314-324.

Babuska, I. 1973. "The Finite Element Method with Lagrange Multipliers." *Numer. Math.* **20**: 179-192.

Babuska, I., and A. Aziz. 1972. "Survey Lectures on the Mathematical Foundations of the Finite Element Method." *The Mathematical Foundations of the Finite Element Method with Application to Partial Differential Equations*. ed. by A. Aziz. New York: Academic Press.

Bajorek, S. M., and J. R. Lloyd. 1982. "Experimental Investigation of Natural Convection in Partitioned Enclosures." *Journal of Heat Transfer* **104**: 527-531.

Baker, A. J. 1973. "Finite Element Solution Algorithm for Viscous Incompressible Fluid Dynamics." *International Journal for Numerical Methods in Fluids* **6**: 89-101.

Baker, A. J. 1982. "On Current Aspects of Finite Element Computational Fluid Mechanics for Turbulent Flow." *Computer Methods in Applied Mechanics and Engineering* **32**: 261-282.

Baker, A. J. 1983. *Finite Element Computational Fluid Mechanics*. New York: Hemisphere Publishing Corporation.

Baker, A. J., and J. W. Kim. 1987. "A Taylor Weak-Statement Algorithm for Hyperbolic Conservation Laws." *International Journal for Numerical Methods in Fluids* **7**: 489-520.

Baker, A. J., and D. W. Pepper. 1991. *Finite Elements 1-2-3*. New York: McGraw-Hill Book Company.

Baker, A. J., P. T. Williams, and R. M. Kelso. 1992a. "Development and Validation of a Finite Element CFD Algorithm for Prediction of Room Air Motion." paper presented at *ROOMVENT'92: Air Distribution in Rooms, Third International Conference* Aalborg, Denmark.

Baker, A. J., P. T. Williams, and R. M. Kelso. 1992b. "Numerical Calculation of Room Air Motion, I. Math, Physics, and CFD Modeling." under review for publication in *ASHRAE TRANSACTIONS*.

Baker, A. J., P. T. Williams, and R. M. Kelso. 1992c. "A Computational Fluid Dynamics (CFD) Procedure for 3D Room Air Motion Prediction." ASHRAE Contract Technical Report ESM91-2.1-CFDL. University of Tennessee: Knoxville, Tennessee.

Batchelor, G. K. 1967. *An Introduction to Fluid Dynamics*. Cambridge: Cambridge University Press.

Benim, A. C., and W. Zinser. 1986. "A Segregated Formulation of Navier-Stokes Equations with Finite Elements." *Computer Methods in Applied Mechanics Engineering* **57**: 223-237.

Boland, J., and R. Nicolaides. 1983. "Stability of Finite Elements Under Divergence Constraints." *SIAM Journal of Numerical Analysis* **20**: 722-731.

Boussinesq, J. 1877. "Essai Sur La Théorie Des Eaux Courantes." ["Essay on the Theory of Water Currents."] *Mem. Présentés Acad. Sci.* **23**: 46.

Boussinesq, J. 1903. *Theorie Analytique de la Chaleur, vol. 2.* [*Analytic Theory of Heat.*] Paris: Gauthier-Villars.

Braaten, M. E., and W. Shyy. 1987. "Study of Pressure Correction Methods with Multigrid for Viscous Flow Calculations in Nonorthogonal Curvilinear Coordinates." *Numerical Heat Transfer* **11**: 417-442.

Bradshaw, P. 1971. *An Introduction to Turbulence and its Measurement*. Oxford: Pergamon Press.

Brezzi, F. 1974. "On the Existence, Uniqueness, and Approximation of Saddle-Point Problems Arising from Lagrange Multipliers." *RAIRO Anal. Numer.* **8**: 129-151.

Briley, W. R. 1974. "Numerical Method for Predicting 3D Steady Viscous Flow in Ducts." *Journal of Computational Physics* **14**: 8.

Brooks, A. N. and T. J. R. Hughes. 1982. "Streamline Upwind/Petrov-Galerkin Formulations for Convection Dominated Flows with Particular Emphasis on the Incompressible Navier-Stokes Equations." *Computer Methods in Applied Mechanics and Engineering* **32**: 199-259.

Brown, W. G., and K. R. Solvason. 1962. "Natural Convection through Rectangular Openings in Partitions – 1." *International Journal of Heat and Mass Transfer* **5**: 859–868.

Cabuk, H., C. H. Sung, and V. Modi. 1992. "Explicit Runge-Kutta Method for Three-Dimensional Internal Incompressible Flows." *AIAA Journal* **30** no. 8: 2024-2031.

Cahouet, J., and Chabard, J. P. 1988. "Some Fast 3D Solvers for the Generalized Stokes Problem." *International Journal for Numerical Methods in Fluids* **8**: 269-295.

Campion-Renson, A., and M. J. Crochet. 1978. "On the Stream Function-Vorticity Finite Element Solutions of Navier-Stokes Equations." *International Journal for Numerical Methods in Engineering* **12** no. 12: 1809-1818.

Cantillo, J. 1990. "Air Velocity and Temperature Measurements in a Full Ventilative Cooling Research Facility." M.Sc. thesis. Urbana, IL: University of Illinois.

Carvalho, M. G., F. Durst, and J. C. F. Pereira. 1987. "Predictions and Measurements of Laminar Flow over Two-Dimensional Obstacles." *Appl. Math. Modeling* **11**: 23-34.

Cebici, T., and A. M. O. Smith. 1974. *Analysis of Turbulent Boundary Layers*. Applied Mathematics and Mechanics. ed. by F. N. Frenkiel and G. Temple. **15** New York: Academic Press.

Chandra, R., S.C. Eisenstat, and M. H. Schultz. 1977. *The Modified Conjugate Residual Method for Partial Differential Equations*. New Haven, CT: Yale University Department of Computer Science. Research Report 107.

Cheesewright, R., K. J. King, and S. Ziai. 1986. "Experimental Data for the Validation of Computer Codes for the Prediction of Two-Dimensional Buoyant Cavity Flows." In *Natural Convection in Enclosures: Significant Questions in Buoyancy Affected Enclosures or Cavity Flows in Anaheim, CA , December 7-12, 1986*, edited by R. S. Figliola and I. Catton, 75-81. New York: American Society of Mechanical Engineers.

Cheesewright, R., and S. Ziai. 1986. "Distribution of Temperature and Local Heat-Transfer Rate in Turbulent Natural Convection in a Large Rectangular Cavity." *In Proceedings of 8th International Heat Transfer Conference in San Francisco, 1986*, edited by C. L. Tien, V. P. Carey, and J. K. Ferrell, 1465-1470.

Chen, C.-J. 1988. "Finite Analytic Method." in *Handbook of Numerical Heat Transfer*, edited by W. J. Minkowycz et al., 723-746. New York: John Wiley and Sons, Inc.

Chen, K. H., and R. H. Pletcher. 1991. "Primitive Variable, Strongly Implicit Calculation Procedure for Viscous Flows at All Speeds." *AIAA Journal* **29** no. 8: 1241-1249.

Chorin, A. J. 1967. "A Numerical Method for Solving Incompressible Viscous Flow Problems." *Journal of Computational Physics* **2**: 12-26.

Chorin, A. J. 1968. " Numerical Solution of the Navier-Stokes Equations." *Mathematics of Computation* **22**: 745-762.

Chorin, A. J. 1969. "On the Convergence of Discrete Approximations to the Navier-Stokes Equations." *Mathematics of Computation* **23**: 341-353.

Christie, I., D. F. Griffiths, A. R. Mitchell, and O. C. Zienkiewicz. 1976. "Finite Element Methods for Second Order Differential Equations with Significant First Derivatives." *International Journal for Numerical Methods in Engineering* **10**: 1389-1396.

Ciofalo, M., and T. G. Karayiannis. 1991. "Natural Convection Heat Transfer in a Partially- or Completely-Partitioned Vertical Rectangular Enclosure." *International Journal of Heat and Mass Transfer* **34**: 167-179.

Coleman, T. F., and C. Van Loan. 1988. *Handbook for Matrix Computations*. Philadelphia: Society for Industrial and Applied Mathematics.

Connell, S. D., and P. Stow. 1986. "The Pressure Correction Method." *Computers and Fluids* **14** no. 1: 1-10.

Daly, B. J., and F. H. Harlow. 1970. "Transport Equations in Turbulence." *The Physics of Fluids* **13** no. 11: 2634-2649.

Denham, M. K., and M. A. Patrick. 1974. "Laminar Flow over a Downstream Facing Step in a Two-Dimensional Flow Channel." *Transactions of the Institution of Chemical Engineering* **52**: 361-367.

Dennis, S. C. R., D. B. Ingham, and R. N. Cook. 1979. "Finite-Difference Methods for Calculating Steady Incompressible Flows." *Journal of Computational Physics* **33**: 325-339.

de Vahl Davis, G., and G. D. Mallinson. 1976. "An Evaluation of Upwind and Central Difference Approximations by a Study of Recirculating Flow." *Computers and Fluids* **4**: 29-43.

de Vahl Davis, G. 1983. "Natural Convection of Air in a Square Cavity: A Bench Mark Numerical Solution." *International Journal for Numerical Methods in Fluids* **3**: 249-264.

Dodge, P. R. 1977. "Numerical Method for 2D and 3D Viscous Flows." *AIAA Journal* **15**: 961-965.

Donea, J. 1984. "A Taylor-Galerkin Method for Convective Transport Problems." *International Journal for Numerical Methods in Engineering* **20**: 101-119.

Donea, J., S. Giuliani, and H. Laval. 1982. "Finite Element Solution of the Unsteady Navier-Stokes Equations by a Fractional Step Method." *Computer Methods in Applied Mechanics and Engineering* **30**: 53-73.

Dongarra, J. J., I. S. Duff, D. C. Sorensen, and H. A. van der Vorst. 1991. *Solving Linear Systems on Vector and Shared Memory Computers*. Philadelphia: Society for Industrial and Applied Mechanics.

Duff, I. S., A. M. Erisman, C. W. Gear, and J. K. Reid. 1986. *Direct Methods for Sparse Matrices*. London: Oxford University Press.

Duff, I. S. 1980. *MA28 – A Set of Fortran Subroutines for Sparse Unsymmetric Linear Equations*. A.E.R.E. Harwell, Oxon., England: Report No. AERE-R.8730.

Dukowicz, J. K., and J. D. Ramshaw. 1979. "Tensor Viscosity Method for Convection in Numerical Fluid Dynamics." *Journal of Computational Physics* **32**: 71-79.

Eaton, J. K., and J. P. Johnston. 1981. "A Review for Research on Subsonic Turbulent Reattachment." *AIAA Journal* **19**: 1092-1100.

Eisenstat, S. C., M. H. Schultz, and A. H. Sherman. 1977a. *Minimal Storage Band Elimination*. New Haven, CT: Yale University Department of Computer Science. Research Report 105.

Eisenstat, S. C., M. C. Gursky, M. H. Schultz, and A. H. Sherman. 1977b. *Yale Sparse Matrix Package: II. The Nonsymmetric Case*. New Haven, CT: Yale University Department of Computer Science. Research Report 114.

Elder, J. W. 1965. "Laminar Free Convection in Vertical Slot." *Journal of Fluid Mechanics* **23**: 77-98.

Etheridge, D. W., and P. H. Kemp. 1978. "Measurements of Turbulent Flow Downstream of a Rearward-Facing Step." *Journal of Fluid Mechanics* **86**: 545-566.

Everestine, G. C. 1979. "A Comparison of Three Resequencing Algorithms for the Reduction of Matrix Profile and Wavefront." *International Journal for Numerical Methods in Fluids* **14**: 837-853.

Fang, Z., and I. Paraschivoiu. 1991. "Numerical Solutions of the Incompressible Navier-Stokes Equations with Boundary Condition Switching." *AIAA Journal* **29** no. 5: 851-853.

Farouk, B., and T. Fusegi. 1985. "A Coupled Solution of the Vorticity-Velocity Formulation of the Incompressible Navier-Stokes Equations." *International Journal for Numerical Methods in Fluids* **5**: 1017-1034.

Fasel, H. 1976. "Investigation of the Stability of Boundary Layers by a Finite-Difference Model of the Navier-Stokes Equations." *Journal of Fluid Mechanics* **78**: 355-383.

Ferziger, J. H. 1987. "Simulation of Incompressible Turbulent Flows." *Journal of Computational Physics* **69**: 1-48.

Fletcher, R. 1976. *Conjugate Gradient Methods for Indefinite Systems, Lecture Notes in Mathematics*. **506**. Berlin: Springer-Verlag.

Fortin, M., and A. Fortin. 1985. "A Generalization of Uzawa's Algorithm for the Solution of the Navier-Stokes Equations." *Communications in Applied Numerical Mathematics* **1**: 205-208.

Freels, J. D. 1992. "A Taylor Weak Statement Finite Element Algorithm for Real-Gas Compressible Navier-Stokes Simulation." Ph.D. diss., University of Tennessee.

Freitas, C. J., H. S. Rhee, and R. L. Street. 1986. "Momentum Buoyancy Interactions in a Three-Dimensional Cavity Flow." In *Natural Convection in Enclosures: Significant Questions in Buoyancy Affected Enclosures or Cavity Flows in Anaheim, CA , December 7-12, 1986*, edited by R. S. Figliola and I. Catton, 53-58. New York: American Society of Mechanical Engineers.

Fromm, J. E. 1963. "A Method for Computing Nonsteady, Incompressible, Viscous Fluid Flows." Los Alamos Scientific Laboratory Report No. 2910. Los Alamos, New Mexico.

Fromm, J. E. 1964. "The Time Dependent Flow of an Incompressible Viscous Fluid." *Methods in Computational Physics* **3**:345-382.

Fu, W.-S., J. C. Perng, and W.-J. Shieh. 1989. "Transient Laminar Natural Convection in an Enclosure Partitioned by an Adiabatic Baffle." *Numerical Heat Transfer* **16**: 325-350.

Fusegi, T., J. M. Hyun, and K. Kuwahara. 1992. "Numerical Simulations of Natural Convection in a Differentially Heated Cubical Enclosure with a Partition." *International Journal of Heat and Fluid Flow* **13** no. 2: 176-183.

Galpin, P. F., and G. D. Raithby. 1986. "Numerical Solution of Problems in Incompressible Fluid Flow: Treatment of the Temperature-Velocity Coupling." *Numerical Heat Transfer* **10**: 105-129.

Gartling, D. K. 1990. "A Test Problem for Outflow Boundary Conditions - Flow Over a Backward-Facing Step." *International Journal for Numerical Methods in Fluids* **11**: 953-967.

Gatski, T.B., C.E. Grosch, and M. E. Rose. 1989. "The Numerical Solution of the Navier-Stokes Equations for 3-Dimensional, Unsteady, Incompressible Flows by Compact Schemes." *Journal of Computational Physics* **82**: 298-329.

Gebhart, B. 1973. "Natural Convection Flows and Stability." *Advances in Heat Transfer* **9**: 273-348.

Gebhart, B., Y. Jaluria, R. L. Mahajan, B. Sammakia. 1988. *Buoyancy-Induced Flows and Transport*. New York: Hemisphere Publishing Corp.

Gentry, R. A., R. E. Martin, and B. J. Daly. 1966. "An Eulerian Differencing Method for Unsteady Compressible Flow Problems." *Journal of Computational Physics* **1**: 87-118.

Ghia, K. N., W. L. Hankey, Jr., and J. K. Hodge. 1979. "Use of Primitive Variables in the Solution of Incompressible Navier-Stokes Equations." *AIAA Journal* **17** no. 3: 298-301.

Ghia, K. N., G. A. Osswald, and U. Ghia. 1989. "Analysis of Incompressible Massively Separated Viscous Flows Using Unsteady Navier-Stokes Equations." *International Journal for Numerical Methods in Fluids* **9**: 1025-1050.

Ghosh, P. K., A. Sarkar, and V. M. K. Sastri. 1992. "Natural Convection Heat Transfer in an Enclosure with a Partition – A Finite-Element Analysis." *Numerical Heat Transfer* Part A **21**: 231-248.

Gill, A. E. 1966. "The Boundary-Layer Regime for Convection in a Rectangular Cavity." *Journal of Fluid Mechanics* **26**: 515-536.

Girault, V. 1988. "Incompressible Finite Element Methods for Navier-Stokes Equations with Nonstandard Boundary Conditions in R3." *Mathematics of Computation* **51** no. 183: 55-74.

Glowinski, R., and O. Pironneau. 1992. "Finite Element Methods for Navier-Stokes Equations." *Annual Review of Fluid Mechanics* **24**: 167-204.

Goda, K. 1979. "A Multistep Technique with Implicit Difference Schemes for Calculating Two- or Three-Dimensional Cavity Flows." *Journal of Computational Physics* **30**: 76-95.

Goldstein, R. J., and D. K. Kreid. 1967. "Measurement of Laminar Flow Development in a Square Duct Using a Laser-Doppler Flowmeter." *Journal of Applied Mechanics* **34**: 813-818.

Goldstein, R. J., V. L. Eriksen, R. M. Olson, and E. R. G. Eckert. 1970. "Laminar Separation, Reattachment, and Transition of Flow over a Downstream-Facing Step." *Journal of Basic Engineering* **92**: 732-741.

Golub, G. H., and C. F. Van Loan. 1989. *Matrix Computations*. 2d ed. Baltimore: Johns Hopkins University Press.

Gray, D. D., and A. Giorgini. 1976. "The Validity of the Boussinesq Approximation for Liquids and Gases." *International Journal for Heat and Mass Transfer* **19**: 545-551.

Grear, J. F. 1990. *Matrix Stretching for Linear Equations*. Livermore,CA: Sandia National Laboratories. SAND90-8723.

Gresho, P. M. 1990. "On the Theory of Semi-Implicit Projection Methods for Viscous Incompressible Flow and Its Implementation via a Finite Element Method That Also Introduces a Nearly Consistent Mass Matrix. Part 1: Theory." *International Journal for Numerical Methods in Fluids* **11**: 587-620.

Gresho, P.M. 1991. "Incompressible Fluid Mechanics: Some Fundamental Formulation Issues." *Annual Review of Fluid Mechanics* **23**: 413-453.

Gresho, P. M., S. T. Chan, R. L. Lee, and C. D. Upson. 1984. "A Modified Finite Element Method for Solving the Time-Dependent, Incompressible Navier-Stokes Equations. Part 1: Theory." *International Journal for Numerical Methods in Fluids* **4**: 557-598.

Gresho, P. M., and Chan, S. T. 1990. "On the Theory of Semi-Implicit Projection Methods for Viscous Incompressible Flow and Its Implementation via a Finite Element Method That Also Introduces a Nearly Consistent Mass Matrix. Part 2: Implementation." *International Journal for Numerical Methods in Fluids* **11**: 621-659.

Gresho, P. M., and R. L. Sani. 1987. "On Pressure Boundary Conditions for the Incompressible Navier-Stokes Equations." *International Journal for Numerical Methods in Fluids* **7**: 1111-1145.

Groff, J. R., and P. N. Weinberg. 1988. *Understanding UNIX: A Conceptual Guide*, 2 ed. Carmel, Indiana: Que™ Corporation.

Guevremont, G., W. G. Habashi, P. L. Kotiuga, and M. M. Hafez. 1990. "Finite Element Solution of the 3D Compressible Navier-Stokes Equations by a Velocity-Vorticity Method." *Presented at the 28th Aerospace Sciences Meeting held at Reno, NV, January 8-11, 1990.* AIAA Paper No. AIAA-90-0404

Guj, G., and F. Stella. 1988. "Numerical Solutions of High-Re Recirculating Flows in Vorticity-Velocity Form." *International Journal for Numerical Methods in Fluids* **8**: 405-416.

Gunzburger, M. D. 1989a. *Finite Element Methods for Viscous Incompressible Flows*. New York: Academic Press, Inc.

Gunzburger, M. D. 1989b. "Iterated Penalty Methods for the Stokes and Navier-Stokes Equations." in *Finite Element Analysis in Fluids, Proceedings of the 7th International Conference on Finite Element Methods in Flow Problems*. University of Alabama Press: 1040-1045.

Gupta, M. M., and R. P. Manohar. 1979. "Boundary Approximations and Accuracy in Viscous Flow Computations." *Journal of Computational Physics* **31**: 265-288.

Gupta, M. M., T. H. Kwon, and Y. Jaluria. 1992. "Multivariant Finite Elements for Three-Dimensional Simulation of Viscous Incompressible Flows." *International Journal for Numerical Methods in Fluids* **14**: 557-585.

Hackman, L. P., G. D. Raithby, and A. B. Strong. 1984. "Numerical Predictions of Flows over Backward Facing Steps." *International Journal for Numerical Methods in Fluids* **4**: 711-724.

Hadid, A. H., D. C. Chan, R. I. Issa, and M. M. Sindir. 1988. "Convergence and Accuracy of Pressure-Based Finite Difference Schemes for Incompressible Viscous Flow Calculations in a Nonorthogonal Coordinate System." *Presented at the First National Fluid Dynamics Congress, Cincinnati, OH*: AIAA Paper No. AIAA-88-3529.

Haghighat, F., Z. Jiang, J. C. Y. Wang, and F. Allard. 1992. "Air Movement in Buildings Using Computational Fluid Dynamics." *Journal of Solar Energy Engineering* **114**: 84-92.

Hageman, L. A., and D. M. Young. 1981. *Applied Iterative Methods*. New York: Academic Press, Inc.

Hagstrom, T. 1990. "Conditions at the Downstream Boundary for Simulations of Viscous Incompressible Flow." Cleveland,OH: Institute for Computational Mechanics in Propulsion, NASA Lewis Research Center. NASA Technical Memorandum 102510.

Halpern, L., and M. Schatzman. 1989. "Artificial Boundary Conditions for Incompressible Viscous Flows." *SIAM J. MATH. ANAL.* **20** no. 2: 308-353.

Hamming, R. W. 1973. *Numerical Methods for Scientists and Engineers* 2d ed. New York: McGraw-Hill, Inc.

Han, L. S. 1960. "Hydrodynamic Entrance Lengths for Incompressible Laminar Flow in Rectangular Ducts." *Journal of Applied Mechanics* **27**: 403-409.

Harlow, F.H., and A. A. Amsden. 1968. "Numerical Calculation of Almost Incompressible Flow." *Journal of Computational Physics* **3**: 80-93.

Harlow, F. H., and A. A. Amsden. 1971. "A Numerical Fluid Dynamics Calculation Method for All Flow Speeds." *Journal of Computational Physics* **8**: 197-213.

Harlow, F. H., and P. I. Nakayama. 1967. "Turbulence Transport Equations." *The Physics of Fluids* **10** no. 11: 2323-2332.

Harlow, F. H., and P. I. Nakayama. 1968. "Transport of Turbulence Energy Decay Rate." Los Alamos, New Mexico: Los Alamos Scientific Laboratory Report No. LA-3854.

Harlow, F. H., and J. E. Welch. 1965. "Numerical Calculation of Time-Dependent Viscous Incompressible Flow of Fluid with Free Surface." *The Physics of Fluids* **8** no. 12: 2182-2189.

Harlow, F. H., and J.E. Welch. 1966. "Numerical Study of Large-Amplitude Free-Surface Motions." *The Physics of Fluids* **9** no. 5: 842-851.

Haroutunian, V. 1988. *Turbulent Flows with FIDAP: Seminar Notes*. Evanston, Illinois: Fluid Dynamics International, Inc.

Hassager, O., P. Henriksen, P. Townsend, M.F. Webster, and D. Ding. 1991. "The Quarterbend, A Three-Dimensional Benchmark Problem." *Computers and Fluids* accepted for publication.

Heath, M. T. 1974. "The Numerical Solution of Ill-Conditioned Systems of Linear Equations." Oak Ridge, TN: Oak Ridge National Laboratory. ORNL-4957.

Hestenes, M. R., and E. L. Stiefel. 1952. "Methods of Conjugate Gradients for Solving Linear Systems." *J. Res. Nat. Bur. Standards* **49:** 409-436.

Hétu, J., and D. H. Pelletier. 1992. "Adaptative [sic] Remeshing for Viscous Incompressible Flows." *AIAA Journal* **30** no. 8: 1986-1992.

Hinze, J. O. 1975. *Turbulence*, 2d ed. New York: McGraw-Hill Book Co.

Hirasaki, G. J., and J. D. Hellums. 1970. "Boundary Conditions on the Vector and Scalar Potentials in Viscous Three-Dimensional Hydrodynamics." *Quart. Appl. Math.* **28**: 293-296.

Hirt, C. W., and F. H. Harlow. 1967. "A General Corrective Procedure for the Numerical Solution of Initial-Value Problems." *Journal of Computational Physics* **2**: 114-119.

Hoffman, K. A. 1989. *Computational Fluid Mechanics for Engineers*. Austin, TX: Engineering Education System™.

Horn, R. A., and C. R. Johnson. 1985. *Matrix Analysis*. Cambridge: Cambridge University Press.

Howard, D., W. M. Connolley, and J. S. Rollett. 1990. "Unsymmetric Conjugate Gradient Methods and Sparse Direct Methods in Finite Element Flow Simulation." *International Journal for Numerical Methods in Fluids* **10**: 925-945.

Hsu, C. H., Y. M. Chen, and C. H. Liu. 1992. "Preconditioned Upwind Methods to Solve Incompressible Navier-Stokes Equations." *AIAA Journal* **30** no. 2: 550-552.

Hughes, T. J. R. 1978. "A Simple Scheme for Developing 'Upwind' Finite Elements." *International Journal for Numerical Methods in Engineering* **12**: 1359-1365.

Hughes, T. J. R., W. K. Liu, and A. Brooks. 1979. "Finite Element Analysis of Incompressible Viscous Flows by the Penalty Method." *Journal of Computational Physics* **30**: 1-60.

Hughes, T. J. R., M. Mallet, and A. Mizukami. 1986a. "A New Finite Element Formulation for Computational Fluid Dynamics: II. Beyond SUPG." *Computer Methods in Applied Mechanics and Engineering* **54**: 341-355.

Hughes, T. J. R., and M. Mallet. 1986b. "A New Finite Element Formulation for Computational Fluid Dynamics: III. The Generalized Streamline Operator for Multidimensional Advective-Diffusive Systems." *Computer Methods in Applied Mechanics and Engineering* **58**: 305-328.

Hughes, T. J. R., L. P. Franca, and M. Balestra. 1986c. "A New Finite Element Formulation for Computational Fluid Dynamics: V. Circumventing the Babuska-Brezzi Condition: A Stable Petrov-Galerkin Formulation of the Stokes Problem Accommodating Equal-Order Interpolations." *Computer Methods in Applied Mechanics and Engineering* **59**: 85-99.

Hunt, J. C. R. 1991. "Industrial and Environmental Fluid Mechanics." *Annual Review of Fluid Mechanics* **23**: 1-41.

Ikohagi, T., and B. R. Shin. 1991. "Finite-Difference Schemes for Steady Incompressible Navier-Stokes Equations in General Curvilinear Coordinates." *Computers and Fluids* **19** no. 3/4: 479-488.

Ikohagi, T., B. R. Shin, and H. Daiguji. 1992. "Application of an Implicit Time-Marching Scheme to a Three-Dimensional Incompressible Flow Problem in Curvilinear Coordinate Systems." *Computers and Fluids* **21** no. 2: 163-175.

Iribarne, A., F. Frantisak, R. L. Hummel, and J. W. Smith. 1972. *AIChE Journal* **18:** 689.

Issa, R. I. 1985. "Solution of the Implicitly Discretised Fluid Flow Equations by Operator-Splitting." *Journal of Computational Physics* **62**: 40-65.

Issa, R. I., A. D. Gossman, and A. P. Watkins. 1986. "The Computation of Compressible and Incompressible Recirculating Flows by a Non-Iterative Implicit Scheme." *Journal of Computational Physics* **62**: 66-82.

Jaluria, Y. 1980. *Natural Convection Heat and Mass Transfer*. Oxford, UK: Pergamon Press.

Jang, D. S., R. Jetli, and S. Acharya. 1986. "Comparison of the PISO, SIMPLER, and SIMPLEC Algorithms for the Treatment of the Pressure-Velocity Coupling in Steady Flow Problems" *Numerical Heat Transfer* **10**: 209-228.

Jones, W. P., and B. E. Launder. 1972. "The Prediction of Laminarization with a Two-Equation Model of Turbulence." *International Journal of Heat and Mass Transfer* **15**: 301-314.

Karayiannis, T. G., M. Ciofalo, and G. Barbaro. 1992. "On Natural Convection in a Single and Two Zone Rectangular Enclosure." *International Journal of Heat and Mass Transfer* **35** no. 7: 1645-1657.

Karki, K. C., and S. V. Patankar. 1987. "Pressure Based Calculation Procedure for Viscous Flows at All Speeds in Arbitrary Configurations." *AIAA Journal* **27** no. 89: 1167-1174.

Kawahara, M., and K. Ohmiya. 1985. "Finite Element Analysis of Density Flow Using the Velocity Correction Method." *International Journal for Numerical Methods in Fluids* **5**: 981-993.

Kelkar, K. M., and S. V. Patankar. 1986. "Numerical Prediction of Natural Convection in Partitioned Enclosures." In *Natural Convection in Enclosures: Significant Questions in Buoyancy Affected Enclosures or Cavity Flows in Anaheim, CA, December 7-12, 1986*, edited by R. S. Figliola and I. Catton, 63-71. New York: American Society of Mechanical Engineers.

Kim, J., S. J. Kline, and J. P. Johnston. 1980. "Investigation of a Reattaching Turbulent Shear Layer: Flow Over a Backward Facing Step." *Journal of Fluids Engineering - ASME Trans.* **102**: 302-308.

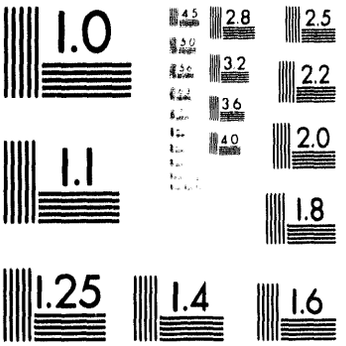
1.0
1.1
1.25
1.4
1.6
1.8
2.0
2.2
2.5
2.8
3.2
3.6
4.0
4.5

4 of 4

Kim, J., and P. Moin. 1985. "Application of a Fractional-Step Method to Incompressible Navier-Stokes Equations." *Journal of Computational Physics* **59**: 308-323.

Kernighan, B. W., and D. M. Ritchie. 1988. *The C Programming Language*. Englewood Cliffs, New Jersey: Prentice Hall.

Ku, H. C., R. S. Hirsh, T. D. Taylor, and A. P. Rosenburg. 1989. "A Pseudospectral Matrix Element Method for Solution of Three-Dimensional Incompressible Flows and Its Parallel Implementation." *Journal of Computational Physics* **83**: 260-291.

Ladyzhenskaya, O. 1969. *The Mathematical Theory of Viscous Incompressible Flow*. New York: Gordon and Breach.

Lam, C. K. G., and K. Bremhorst. 1981. "A Modified Form of the k-ε Model for Predicting Wall Turbulence." *Journal of Fluids Engineering* **103**: 456-460.

Lamb, H. 1932. *Hydrodynamics*. 6th ed. Cambridge: Cambridge University Press.

Launder, B. E., and D. B. Spalding. 1974. "The Numerical Computation of Turbulent Flows." *Computer Methods in Applied Mechanics and Engineering* **3**: 269-289.

Launder, B. E., G. J. Reece, and W. Rodi. 1975. "Progress in the Development of a Reynolds Stress Turbulence Closure." *Journal of Fluid Mechanics*. **68**: 537-586.

Lee, K. D., J. M. Loellbach, and M. S. Kim. 1990. "Adaptation of Structured Grids for Improved Navier-Stokes Solutions." *Presented at the 28th Aerospace Sciences Meeting held in Reno, NV, Jan 8-11, 1990.* AIAA Paper No. AIAA-90-0125.

Lee, R. L. 1992. "A Finite Element/Finite Difference Approach for Modelling Three-Dimensional Flow and Pollutant Dispersion Around Structures." Livermore, CA. Lawrence Livermore National Laboratory. UCRL-JC-107758 R 1.

Lee, R. L., P. M. Gresho, and R. L. Sani. 1979. "Smoothing Techniques for Certain Primitive Variable Solutions of the Navier-Stokes Equations." *International Journal for Numerical Methods in Engineering* **14**: 1785-1804.

Leonard, B. P. 1979. "A Stable and Accurate Convective Modelling Procedure Based on Quadratic Upstream Interpolation." *Computer Methods in Applied Mechanics and Engineering* **19**: 59-98.

Leonardi, E., and J. A. Reizes. 1981. "Convective Flows in Closed Cavities with Variable Fluid Properties." *Numerical Methods in Heat Transfer*: 387-412.

Leone, Jr., J. M., and P. M. Gresho. 1981. "Finite Element Simulations of Steady, Two-Dimensional, Viscous Incompressible Flow Over a Step." *Journal of Computational Physics* **41**: 167-191.

Leone,Jr., J. M. 1990. "Open Boundary Condition Symposium Benchmark Solution: Stratified Flow Over A Backward Facing Step." Livermore, CA: Lawrence Livermore National Laboratory. UCRL-JC-103414 Rev. 1 .

Lin, N. N., and A. Bejan. 1983. "Natural Convection in a Partially Divided Enclosure." *International Journal of Heat and Mass Transfer* **26**: 1867-1878.

Lohner, R. 1990. "A Fast Finite Element Solver for Incompressible Flows." *Presented at the 28th AIAA Aerospace Sciences Meeting Jan. 8-11, 1990, Reno, NV*: AIAA Paper No. AIAA-90-0398.

Mallinson, G. D., and G. de Vahl Davis. 1973. "The Method of the False Transient for the Solution of Coupled Elliptic Equations." *Journal of Computational Physics* **12**: 435-461.

Mallinson, G. D., and G. de Vahl Davis. 1977. "Three-Dimensional Natural Convection in a Box: A Numerical Study." *Journal of Fluid Mechanics* **83**, part 1: 1-31.

Malvern, L. E. 1969. *Introduction to the Mechanics of a Continuous Medium*. Englewood Cliffs, New Jersey: Prentice-Hall, Inc.

Markatos, N. C., M. R. Malin, and G. Cox. 1982. "Mathematical Modelling of Buoyancy-Induced Smoke Flow in Enclosures." *International Journal of Heat and Mass Transfer* **25** no. 1: 63-75.

Markatos, N. C., and K. A. Pericleous. 1984. "Laminar and Turbulent Natural Convection in an Enclosed Cavity." *International Journal of Heat and Mass Transfer* **27** no. 5: 755-772.

Mazher, A. K., and D. P. Giddens. 1991. "New Pressure Correction Equation for Incompressible Internal Flows." *AIAA Journal* **29** no. 3: 418-424.

Miller, T. F., and F. W. Schmidt. 1988. "Use of A Pressure-Weighted Interpolation Method for the Solution of the Incompressible Navier-Stokes Equations on a Nonstaggered Grid System." *Numerical Heat Transfer* **14**: 213-233.

Mizukami, A., and M. Tsuchiya. 1984. "A Finite Element Method for the Three-Dimensional Non-Steady Navier-Stokes Equations." *International Journal for Numerical Methods in Fluids* **4**: 349-357.

Moin, P. 1992. "The Computation of Turbulence." *Aerospace America* (January): 42-46.

Morino, L. 1986. "Helmholtz Decomposition Revisited: Vorticity Generation and Trailing Edge Condition." *Computational Mechanics* **1**: 65-90.

Morrison, G. L., and V. Q. Tran. 1978. "Laminar Flow Structure in Vertical Free Convective Cavities." *International Journal of Heat and Mass Transfer* **21**: 203-213.

Mull, W., and H. Reiher. 1930. "Der Wärmeshutz von Luftschichten." ["The Thermal Resistance of Air Layers."] *Beih. Gesundh-Ing* Reihe **1 28**.

Murakami, S., S. Kato, and Y. Suyama. 1988. "Numerical and Experimental Study on Turbulent Diffusion Fields in Conventional Flow Type Clean Rooms." *ASHRAE Trans.* **94**: 469-493.

Nallasamy, M. 1985. "A Critical Evaluation of Various Turbulence Models as Applied to Internal Fluid Flows." NASA Technical Paper 2474. Marshall Space Flight Center. Alabama.

Nansteel, M. W., and R. Greif. 1981. "Natural Convection in Undivided and Partially Divided Rectangular Enclosures." *Journal of Heat Transfer* **103**: 623-629.

Nansteel, M. W., and R. Greif. 1984. "An Investigation of Natural Convection in Enclosures with Two and Three Dimensional Partitions." *International Journal of Heat and Mass Transfer* **27**: 561-571.

Napolitano, M., and G. Pascazio. 1991. "A Numerical Method for the Vorticity-Velocity Navier-Stokes Equations in Two and Three Dimensions." *Computers and Fluids* **19** no. 3/4: 489-495.

Navier, L. 1822. "Mémoire sur les Lois du Mouvement des Fluides." ["Treatise on the Laws of the Movement of Fluids."] *Mén. de l' Acad. des Sciences* **vi**: 389.

Newell, M. E., and F. W. Schmidt. 1970. "Heat Transfer by Laminar Natural Convection within Rectangular Enclosures." *Journal of Heat Transfer* **92**: 159-168.

Neymark, J. 1988. *Aperture and Prandtl Number Effect on Interzonal Natural Convection*. Masters thesis, Colorado State University, Department of Mech. Engr.

Neymark, J., C. R. Boardman, and A. Kirkpatrick. 1989. "High Rayleigh Number Natural Convection in Partially Divided Air and Water Filled Enclosures." *International Journal of Heat and Mass Transfer* **32** no. 9: 1671-1679.

Nicolaides, R. A. 1991. "Analysis and Convergence of the MAC Scheme." Hampton, VA: Institute for Computer Applications in Science and Engineering, NASA Langley Research Center. NASA CR-187536 ICASE Report No. 91-28.

Nishimura, T., M. Shiraishi, F. Nagasawa, and Y. Kawamura. 1988. "Natural Convection Heat Transfer in Enclosures with Multiple Vertical Partitions." *International Journal of Heat and Mass Transfer* **31**: 1679-1686.

Noronha, W. P. 1989. "Accuracy, Convergence and Stability of Finite Element Algorithms for Incompressible Fluid Flow." Ph.D. diss., University of Tennessee.

Noronha, W. P., P. T. Williams, and A. J. Baker. 1990. "A Time-Accurate, Unsteady, Incompressible Navier-Stokes CFD Algorithm." *Presented at the 28th Aerospace Sciences Conference in Reno, NV, January 8-11, 1990.* AIAA Paper No. AIAA-90-0238.

Noronha, W. P., and A. J. Baker. 1989. "A Taylor Weak Statement for Finite Element CFD Algorithm for 2D Incompressible Navier-Stokes Equations." *Presented at the 27th Aerospace Sciences Meeting in Reno, NV, Jan 9-12, 1989.* AIAA Paper No. AIAA-89-0659.

Oberbeck, A. 1879. "Über die Wärmeleitung der Flüssigkeiten bei Berücksichtigung der Strömungen infolge von Temperatur Differenzen." ["On Heat Transfer in Liquids with Consideration of the Case of Flow Induced by Temperature Differences."] *Ann. Phys. Chem.* **7**: 271-292.

Oden, J. T., and L. Demkowicz. 1991. "*h-p* Adaptive Finite Element Methods in Computational Fluid Dynamics." *Computer Methods in Applied Mechanics and Engineering* **89**: 11-40.

Oppe, T. C., W. D. Joubert, and D. R. Kincaid. 1988. *NSPCG User's Guide, Version 1.0 – A Package for Solving Large Sparse Linear Systems by Various Iterative Methods.* Center for Numerical Analysis. Austin, Texas: University of Texas.

Orszag, S. A., and M. Israeli. 1974. "Numerical Simulation of Viscous Incompressible Flows." *Annual Review of Fluid Mechanics* **6**: 281-318.

Orszag, S. A., M. Israeli, and M. O. Deville. 1986. "Boundary Conditions for Incompressible Flows." *Journal of Scientific Computing* **1** no. 1: 75-111.

Ortega, J. M. 1972. *Numerical Analysis – A Second Course.* New York: Academic Press, Inc.

Ortega, J. M. 1987. *Introduction to Parallel and Vector Solution of Linear Systems.* manuscript to be published by Plenum Press.

Ortega, J. M., and W. G. Poole, Jr. 1981. *An Introduction to Numerical Methods for Differential Equations.* London: Pitman Publishing Ltd.

Ostrach, S. 1982. "Natural Convection Heat Transfer in Cavities and Cells." in *Proceedings of the Seventh International Heat Transfer Conference* **1**: 365-379.

Papanastasiou, T. C., N. Malamataris, and K. Ellwood. 1992. "A New Outflow Boundary Condition." *International Journal for Numerical Methods in Fluids* **14**: 587-608.

Patankar, S. V. 1980. *Numerical Heat Transfer and Fluid Flow.* New York: Hemisphere Publishing Co.

Patankar, S. V., and D. B. Spalding. 1972. "A Calculation Procedure for Heat, Mass, and Momentum Transfer in Three-Dimensional Parabolic Flows." *International Journal of Heat and Mass Transfer* **15:** 1787-1793.

Patel, V. C., W. Rodi, and G. Scheuerer. 1985. "Turbulence Models for Near-Wall and Low Reynolds Number Flows: A Review." *AIAA Journal* **23** no. 9: 1308-1319.

Pelletier, D., A. Fortin, and R. Camarero. 1989. "Are FEM Solutions of Incompressible Flows Really Incompressible? (or How Simple Flows Can Cause Headaches!)." *International Journal for Numerical Methods in Fluids* **9**:99-112.

Pepper, D. W., C. D. Kern, and P. E. Long. 1979. "Modeling the Dispersion of Atmospheric Pollution Using Cubic Splines and Chapeau Functions." *Atmos. Environ.* **13**: 223-237.

Pepper, D. W., and P. A. Watterberg. 1986. "Calculating and Visualizing Three-Dimensional Convective Flow." *Significant Questions in Buoyancy Affected Enclosure or Cavity Flows* presented at the winter annual meeting of the American Society of Mechanical Engineers, Anaheim, CA HTD **60**: 1-9.

Peshkin, A., and R. Cooper. 1990. "A Direct Role for the Continuity Equation in the Numerical Solution of the Incompressible Navier-Stokes Equations." *Presented at the 28th Aerospace Sciences Meeting in Reno, NV, January 8-11,1990*: AIAA Paper No. AIAA-90-0240.

Peyret, R., and T. D. Taylor. 1983. *Computational Methods for Fluid Flow*. New York: Springer Verlag New York, Inc.

Prandtl, L. 1925. "Über die Ausgebildete Turbulenz."["On Fully-Developed Turbulence."] *ZAMM* **5**: 136-139.

Quartapelle, L., and M. Napolitano. 1984. "A Method for Solving the Factorized Vorticity-Stream Function Equations by Finite Elements." *International Journal for Numerical Methods in Fluids* **4**: 109-125.

Raymond, W. H., and A. Garder. 1976. "Selective Damping in a Galerkin Method for Solving Wave Problems with Variable Grids." *Mon. Weather Review* **104**: 1570-1583.

Ramshaw, J. D., and G. L. Mesina. 1991. "A Hybrid Penalty-Pseudocompressibility Method for Transient Incompressible Fluid Flow." *Computers and Fluids* **20** no. 2: 165-175.

Ramshaw, J.D., and V. A. Mousseau. 1991. "Damped Artificial Compressibility Method for Steady-State Low-Speed Flow Calculations." *Computers and Fluids* **20** no. 2: 177-186.

Ramaswamy, B., T. C. Jue, and J. E. Akin. 1992. "Finite-Element Analysis of Unsteady Two-Dimensional Navier-Stokes Equations" *Numerical Heat Transfer, Part B* **21**: 147-182.

Reddy, J. N. 1982. "Penalty Finite Element Analysis of 3-D Navier-Stokes Equations." *Computer Methods in Applied Mechanics and Engineering* **35**: 87-106.

Reddy, J. N. 1986. *Applied Functional Analysis and Variational Methods in Engineering*. New York: McGraw-Hill Book Company.

Reddy, M. P., J. N. Reddy, and H. U. Akay. 1992. "Penalty Finite Element Analysis of Incompressible Flows Using Element by Element Solution Algorithms." *Computer Methods in Applied Mechanics and Engineering* **100:** 169-205.

Rhie, C.M. 1989. "Pressure-Based Navier-Stokes Solver Using the Multigrid Method." *AIAA Journal* **27** no. 8: 1017-1018.

Rhie, C. M., and W. L. Chow. 1983. "Numerical Study of the Turbulent Flow Past an Airfoil with Trailing Edge Separation." *AIAA Journal* **21** no. 11: 1325-1332.

Rice, J.G., and R. J. Schnipke. 1985. "A Monotone Streamline Upwind Finite Element Method for Convection-Dominated Flows." *Computer Methods in Applied Mechanics and Engineering* **48**: 313-327.

Rice, J. G., and R. J. Schnipke. 1986. "An Equal-Order Velocity-Pressure Formulation that Does Not Exhibit Spurious Pressure Modes." *Computer Methods in Applied Mechanics and Engineering* **58**: 135-149.

Richardson, S. M., and A. R. H. Cornish. 1977. "Solution of Three-Dimensional Incompressible Flow Problems." *Journal of Fluid Mechanics* **82** part 2: 309-319.

Roache, P. J. 1972. *Computational Fluid Dynamics*. Albuquerque, NM: Hermosa Publishers.

Rodi, W. 1980. *Turbulence Models and Their Application in Hydraulics*. The Netherlands: International Association for Hydraulics Research.

Rogers, S. E., and D. Kwak. 1991. "Steady and Unsteady Solutions of the Incompressible Navier-Stokes Equations." *AIAA Journal* **29** no. 4: 603-610.

Roscoe, D. F. 1976. "The Solution of the Three-Dimensional Navier-Stokes Equations Using a Finite Difference Approach." *International Journal for Numerical Methods in Engineering* **10**: 1299-1308.

Rosenhead, L. ed. 1963. *Laminar Boundary Layers*. Oxford: The Clarendon Press.

Rösler, M., and B. Hanel. 1992. "Numerical Computation of Flow and Heat Transfer in Air-Conditioned Rooms by a Special Velocity-Pressure Iteration and a Multigrid Method." paper presented at *ROOMVENT'92 : Air Distribution in Rooms Third International Conference* Aalborg, Denmark.

Saad, Y., and M. H. Schultz. 1986. "GMRES: A Generalized Minimal Residual Algorithm for Solving Nonsymmetric Linear Systems." *SIAM Journal of Science and Statistical Computing* **7** no. 3: 856-869.

Sani, R. L., P. M. Gresho, R. L. Lee, and D. F. Griffiths. 1981. "The Cause and Cure (?) of the Spurious Pressures Generated by Certain FEM Solutions of the Incompressible Navier-Stokes Equations." *International Journal for Numerical Methods in Fluids* **1**: 17-43.

Schlichting, H. 1979. *Boundary Layer Theory*. 7th ed. New York: McGraw-Hill Book Co.

Schneider, G. E., G. D. Raithby, and M. M. Yovanovich. 1978. "Finite Element Solution Procedures for Solving the Incompressible Navier-Stokes Equations Using Equal Order Variable Interpolation." *Numerical Heat Transfer* **1**: 433-451.

Schneider, G. E., and G. D. Raithby. 1980. "Finite Element Analysis of Incompressible Fluid Flow Incorporating Equal Order Pressure and Velocity Interpolation." in *Computer Methods in Fluids*. edited by K. Morgan. New York: Pentech Press, Inc.: 49-83.

Schnipke, R. J., and J. G. Rice. 1987. "A Finite Element Method for Free and Forced Convection Heat Transfer." *International Journal for Numerical Methods in Engineering* **24**: 117-128.

Schwarz, H. R. 1988. *Finite Element Methods*. London: Academic Press, Ltd.

Scott, D., R. Anderson, and R. Figliola. 1988. "Blockage of Natural Convection Boundary Layer Flow in a Multizone Enclosure." *International Journal for Heat and Fluid Flow* **9**: 208-214.

Shames, I. H. 1962. *The Mechanics of Fluids*. New York: McGraw-Hill Book Company.

Shaw, C. T. 1991. "Using a Segregated Finite Element Scheme to Solve the Incompressible Navier-Stokes Equations." *International Journal for Numerical Methods in Fluids* **12**: 81-92.

Shen, J., and R. Temam. 1989. "A New Fractional Scheme for the Approximation of Incompressible Flows." *Mat. Applic. Comp.* **8** no. 1: 3-22.

Shih, T.-M. 1984. *Numerical Heat Transfer*. New York: Hemisphere Publishing Corporation.

Shimura, M., and M. Kawahara. 1988. "Two Dimensional Finite Element Flow Analysis Using the Velocity Correction Method." *Structural Eng./Earthquake Eng.* **5** no. 2: 255-263.

Skalický, T., G. Morgenstern, A. Auge, B. Hanel, and M. Rösler. 1992. "Comparative Studies of Selected Discretization Methods for the Numerical Solution of Room Air Flow Problems." paper presented at *ROOMVENT'92 : Air Distribution in Rooms Third International Conference* Aalborg, Denmark.

Spencer, A. J. M. 1980. *Continuum Mechanics*. London: Longman Group Ltd.

Speziale, C. G. 1991. "Analytical Methods for the Development of Reynolds-Stress Closures in Turbulence." *Annual Review of Fluid Mechanics* **23**: 107-157.

Spitler, J. D. 1990. "An Experimental Investigation of Air Flow and Convective Heat Transfer in Enclosures Having Large Ventilation Flow Rates," Ph.D. diss. Urbana, IL: University of Illinois.

Spitler, J. D., C. O. Pederson, D. E. Fisher, P. F. Menne, and J. Cantillo. 1991. "An Experimental Facility for Investigation of Interior Convective Heat Transfer." *ASHRAE Trans.* **97** Pt. 1.

Stenberg, R. 1984. "Analysis of Mixed Finite Element Methods for the Stokes Problem: A Unified Approach." *Mathematics of Computation* **42** no. 165: 9-23.

Stenberg, R. 1987. "On Some Three-Dimensional Finite Elements for Incompressible Media." *Computer Methods in Applied Mechanics and Engineering* **63**: 261-269.

Stillman, D. W., and J. O. Hallquist. 1985. *INGRID: A Three-Dimensional Mesh Generator for Modeling Nonlinear Systems*. Livermore, Ca: Lawrence Livermore National Laboratory.

Stephen, A. B., J. B. Bell, J. M. Solomon, and L. B. Hackerman. 1984. "A Finite Difference Galerkin Formulation for the Incompressible Navier-Stokes Equations." *Journal of Computational Physics* **53**: 152-172.

Stokes, G. G. 1845. "On the Theories of the Internal Friction of Fluids in Motion, etc." *Camb. Trans.* **viii**: 287.

Tecplot™ Version 5 User's Manual. 1992. Bellevue, WA: Amtec Engineering, Inc.

Temam, R. 1968. "Une Méthode d'Approximation de la Solution des Équations de Navier-Stokes." ["A Method of Approximation of the Solution for Navier-Stokes Equations."] *Bull. Soc. Math. France* **96**: 115-152.

Temam, R. 1969. "Sur l'Approximation de la Solution des Équations de Navier-Stokes par la Méthode des Pas Fractionnaires (I)." ["On the Approximation of the Solution of the Navier-Stokes Equations by the Fractional Step Method."] *Arch. Rational Mech. Anal.* **32**:135-153.

Temam, R. 1983. *Navier-Stokes Equations and Nonlinear Functional Analysis*. Philadelphia: Society for Industrial and Applied Mechanics.

Tennekes, H., and J. L. Lumley. 1972. *A First Course in Turbulence*. Cambridge: The MIT Press.

Tezduyar, T. E., J. Liou, D. K. Ganjoo, M. Behr, and R. Glowinski. 1990. "Unsteady Incompressible Flow Computations with Finite Element Method." Minneapolis, MN: University of Minnesota Supercomputer Institute: Research Report UMSI 90/36.

Tezduyar, T. E., M. Behr, S. K. A. Abadi, S. Mittal, and S. E. Ray. 1991. "A Mixed CEBE/CC Preconditioning for Finite Element Computations." Minneapolis, MN: University of Minnesota Supercomputer Institute. Research Report.

Tezduyar, T. E., S. Mittal, S. E. Ray, and R. Shih. 1992. "Incompressible Flow Computations with Stabilized Bilinear and Linear Equal-Order-Interpolation Velocity-Pressure Elements." *Computer Methods in Applied Mechanics and Engineering* **95**: 221-242.

Thangam, S., and D. D. Knight. 1990. "A Computational Scheme in Generalized Coordinates for Viscous Incompressible Flows." *Computers and Fluids* **18** no. 4: 317-327.

Thompson, C. P., N. S. Wilkes, and I. P. Jones. 1987. "Numerical Studies of Buoyancy-Driven Turbulent Flow in a Rectangular Cavity." *International Journal for Numerical Methods in Engineering* **24**: 89-99.

Tritton, D. J. 1988. *Physical Fluid Dynamics*. 2d ed. Oxford: The Clarendon Press.

Tuann, S-Y, and M. D. Olson. 1978. "Review of Computing Methods for Recirculating Flows." *Journal of Computational Physics* **29**: 1-19.

Turkel, E. 1987. "Preconditioned Methods for Solving the Incompressible and Low Speed Compressible Equations." *Journal of Computational Physics* **72** no. 2: 277-298.

Upson, C. D., P. M. Gresho, and R. L. Lee. 1980. *Finite Element Simulations of Thermally Induced Convection in an Enclosed Cavity*. Livermore, CA: Lawrence Livermore National Laboratory. UCID-18602.

Van Doormaal, J. P., and G. D. Raithby. 1984. "Enhancements of the SIMPLE Method for Predicting Incompressible Fluid Flows." *Numerical Heat Transfer* **7**: 147-163.

Wachspress, E. L. 1966. *Iterative Solution of Elliptic Systems and Applications to the Neutron Diffusion Equations of Reactor Physics*. Englewood Cliffs, New Jersey: Prentice-Hall, Inc.

Welch, J. E., F. H. Harlow, J. P. Shannon, and B. J. Daly. 1966. *The MAC Method: A Computing Technique for Solving Viscous, Incompressible, Transient Fluid-Flow Problems Involving Free Surfaces*. Los Alamos, New Mexico: Los Alamos Scientific Laboratory. LA-3425.

White, F. M. 1974. *Viscous Fluid Flow*. New York: McGraw-Hill Book Company.

Winters, K. H. 1988. "Laminar Natural Convection in a Partially Divided Rectangular Cavity at High Rayleigh Number." *International Journal for Numerical Methods in Fluids* **8**: 247-281.

Williams, G. P. 1969. "Numerical Integration of the Three-Dimensional Navier-Stokes Equations." *Journal of Fluid Mechanics* **37** part 4: 727-750.

Williams, M. 1992. "A Helmholtz Pressure Equation Method for the Calculation of Unsteady Incompressible Viscous Flows." *International Journal for Numerical Methods in Fluids* **14**: 1-12.

Williams, P. T., R. F. Graham, G. N. Lagerberg, and T. C. Chung. 1989. *Assessment of Thermal Analysis Software for the DOE Office of Civilian Radioactive Waste Management*. Oak Ridge, TN: Oak Ridge National Laboratory. ORNL/TM-10940.

Williams, P. T., A. J. Baker, and R. M. Kelso. 1992. "Numerical Calculation of Room Air Motion, II: The Continuity Constraint FE Method for 3D Incompressible Thermal Flows." *ASHRAE Transactions*. ASHRAE Paper No. H-0749 (under review).

Yang, H., and R. Camarero. 1991. "Internal Three-Dimensional Viscous Flow Solutions Using the Vorticity-Potential Method." *International Journal for Numerical Methods in Fluids* **12**: 1-15.

Yih, C. 1969. *Fluid Mechanics: A Concise Introduction to the Theory*. New York: McGraw-Hill Book Company.

Young, D. M., and R. T. Gregory. 1972. *A Survey of Numerical Mathematics Vol. II*. Reading, Mass.: Addison-Wesley Publishing.

Young, D. M., and T. Mai. 1987. "Iterative Algorithms and Software for Solving Large Sparse Linear Systems." Austin, Texas: Center for Numerical Analysis, The University of Texas. Report No. CNA-215.

Zienkiewicz, O. C., J. Szmelter, and J. Peraire. 1990. "Compressible and Incompressible Flow: An Algorithm for All Seasons." *Computer Methods in Applied Mechanics and Engineering* **78**: 105-121.

Zienkiewicz, O. C. 1977. *The Finite Element Method.* 3d ed. New York: McGraw-Hill Book Co.

APPENDIX A

COMPACT NOTATION

A form of *compact notation* is used throughout this dissertation to describe matrix-vector operations that form element-based contributions to the global linear algebra matrix statement. This notation was first presented by Baker (1983) (cf. Baker and Pepper, 1991) and has proved to be a very effective and accurate tool for the translation of general statements of algorithmic theory into a computer programming language such as Fortran. The following discussion describes the notation with the aid of detailed examples taken from the text.

A.1 BASIS FUNCTIONS AND METRIC DATA

The inertial term in the residual for the momentum equations requires the following element-level integral and subsequent matrix-vector inner product to be evaluated.

$$\int_{\Omega_e} \{N\}\{N\}^T \det[J]\, d\Omega \quad (\{U\}^{n+1} - \{U\}^n)_e \tag{A1}$$

where the column-vectors $\{U\}_e$ contain the discrete approximations for the u_i velocity components at the eight nodes of the element; discrete time stations are denoted by the superscripts "n" and "$n+1$"; superscript "T" denotes the transpose operator; and $\{N\}$ is a column-vector holding the trilinear basis functions that span the 8-node hexahedron, defined by

$$\{N(\eta_i)\} = \frac{1}{8}\begin{Bmatrix} (1-\eta_1)(1-\eta_2)(1-\eta_3) \\ (1+\eta_1)(1-\eta_2)(1-\eta_3) \\ (1+\eta_1)(1+\eta_2)(1-\eta_3) \\ (1-\eta_1)(1+\eta_2)(1-\eta_3) \\ (1-\eta_1)(1-\eta_2)(1+\eta_3) \\ (1+\eta_1)(1-\eta_2)(1+\eta_3) \\ (1+\eta_1)(1+\eta_2)(1+\eta_3) \\ (1-\eta_1)(1+\eta_2)(1+\eta_3) \end{Bmatrix} \tag{A2}$$

As shown in Fig. 5 in Chapter 4, the η_i are generalized coordinates in transform space ($-1 \le \eta_i \le +1$ for $i = 1,2,3$). The outer product $\{N\}\{N\}^T$ produces an 8×8 matrix of polynomial functions of η_i.

The Jacobian J of the coordinate transformation or mapping from transform space (η_i) to Euclidean space (x_i) is defined by

$$J = [J_{ij}]_{(3\times3)} = \left[\frac{\partial x_j}{\partial \eta_i}\right]_{(3\times3)} = \begin{Bmatrix} \frac{\partial}{\partial \eta_1} \\ \frac{\partial}{\partial \eta_2} \\ \frac{\partial}{\partial \eta_3} \end{Bmatrix} \{x_1, x_2, x_3\} = \begin{bmatrix} J_{11} & J_{12} & J_{13} \\ J_{21} & J_{22} & J_{23} \\ J_{31} & J_{32} & J_{33} \end{bmatrix} \tag{A3}$$

The term "det [J]" is the determinant of the transformation Jacobian with the closed-form solution

$$\begin{aligned} \det[J] &= J_{11}(J_{22}J_{33} - J_{32}J_{23}) - J_{12}(J_{21}J_{33} - J_{31}J_{23}) + J_{13}(J_{21}J_{32} - J_{31}J_{22}) \\ &= \frac{\partial x_1}{\partial \eta_1}\left(\frac{\partial x_2}{\partial \eta_2}\frac{\partial x_3}{\partial \eta_3} - \frac{\partial x_2}{\partial \eta_3}\frac{\partial x_3}{\partial \eta_2}\right) - \frac{\partial x_2}{\partial \eta_1}\left(\frac{\partial x_1}{\partial \eta_2}\frac{\partial x_3}{\partial \eta_3} - \frac{\partial x_1}{\partial \eta_3}\frac{\partial x_3}{\partial \eta_2}\right) + \\ &\quad \frac{\partial x_3}{\partial \eta_1}\left(\frac{\partial x_1}{\partial \eta_2}\frac{\partial x_2}{\partial \eta_3} - \frac{\partial x_1}{\partial \eta_3}\frac{\partial x_2}{\partial \eta_2}\right) \end{aligned} \tag{A4}$$

For general hexahedra, det [J] depends on its position within the element.

The actual evaluation of Eq. (A1) in CFDL.PHI3D involves a simplifying approximation that produces an element-independent *master matrix*, so that

$$\begin{aligned} &\int_{\Omega_e} \{N\}\{N\}^T \det[J]\, d\Omega \quad (\{UI\}^{n+1} - \{UI\}^n) \approx \\ &DET_e \left(\int_{\Omega_e} \{N\}\{N\}^T d\Omega\right) \quad (\{UI\}^{n+1} - \{UI\}^n)_e \end{aligned} \tag{A5}$$

where the notation DET_e signifies that det [J] has been approximated by its value at the centroid of the element, $\eta_i = (0,0,0)$, thus allowing the only element-dependent term in the integrand to be brought outside the integral.

Spatial derivatives occur in terms like the expression for the viscous flux vector,

$$\Delta t \int_{\Omega_e} \left(\frac{1 + \mathrm{Re}^t}{\mathrm{Re}}\right) \frac{\partial \eta_k}{\partial x_j} \frac{\partial \{N\}}{\partial \eta_k} \frac{\partial \eta_m}{\partial x_j} \frac{\partial \{N\}^T}{\partial \eta_m} \det[J] \; d\Omega \; \{UI\} \tag{A6}$$

where repeated latin indices imply summation over the dimension of the domain Ω_e. The metric data "$\frac{\partial \eta_j}{\partial x_i}$" are elements of the inverse of the transformation Jacobian $[J_{ij}]^{-1}$,

$$[J_{ij}]^{-1} = \left[\frac{\partial \eta_j}{\partial x_i}\right] = \frac{1}{\det[J]} \begin{bmatrix} (J_{22}J_{33} - J_{32}J_{23}), & (J_{13}J_{32} - J_{12}J_{33}), & (J_{12}J_{23} - J_{13}J_{22}) \\ (J_{31}J_{23} - J_{21}J_{33}), & (J_{11}J_{33} - J_{13}J_{31}), & (J_{21}J_{13} - J_{23}J_{11}) \\ (J_{21}J_{32} - J_{31}J_{22}), & (J_{12}J_{31} - J_{32}J_{11}), & (J_{11}J_{22} - J_{12}J_{21}) \end{bmatrix} \quad \text{(A7)}$$

and, as with det [*J*], the metric data are functions of position within the element. As a simplifying approximation, the metric data can be evaluated at the centroid of the element, designated by

$$EJK_e \equiv \left.\frac{\partial \eta_k}{\partial x_j}\right|_{\eta_i = (0,0,0)} \quad \text{(A8)}$$

The contribution of the viscous flux vector term to the residual for u_i can, therefore, be approximated by

$$\Delta t \int_{\Omega_e} \left(\frac{1 + \mathrm{Re}^t}{\mathrm{Re}}\right) \frac{\partial \eta_k}{\partial x_j} \frac{\partial \{N\}}{\partial \eta_k} \frac{\partial \eta_m}{\partial x_j} \frac{\partial \{N\}^T}{\partial \eta_m} \det[J] \, d\Omega \, \{UI\} \approx \frac{1}{\mathrm{Re}^E} \Delta t \, DET_e \, EJK \, EJM \left(\int_{\Omega_e} \frac{\partial \{N\}}{\partial \eta_k} \frac{\partial \{N\}^T}{\partial \eta_m} d\Omega\right) \{UI\} \quad \text{(A9)}$$

where the "effective Reynolds number", Re^E, is

$$\frac{1}{\mathrm{Re}^E} \equiv \left.\frac{1 + \mathrm{Re}^t}{\mathrm{Re}}\right|_{\eta_i = (0,0,0)} \quad \text{(A10)}$$

A.2 MASTER MATRICES

In the above examples, the simplifying approximations have resulted in an element-independent integral that can be evaluated *once and for all*, producing a *master matrix* that is dependent only upon the choice of basis functions. A special notation is used to describe these master matrices with the general form [*Mabcd*], where

M: prefix denoting the dimensionality of the element master matrix, *M* = *A* for 1D, *B* for 2D, and *C* for 3D

a: an integer indicating how many bases occur in the integral

b,c,d: integers 1,2, or 3, denoting the η_i-direction of the derivatives in the matrix, or 0 for no derivative

In the first example, the element master matrix is

$$[C200] \equiv \int_{\Omega_e} \{N\}\{N\}^T \, d\Omega = \int_{-1}^{+1}\int_{-1}^{+1}\int_{-1}^{+1} \{N\}\{N\}^T \, d\eta_1 d\eta_2 d\eta_3 \qquad \text{(A11)}$$

where C signifies that 3-dimensional basis functions are being used, and two bases occur in the integrand with no derivative operations. The master matrix associated with the viscous flux vector is

$$[C2KM] \equiv \int_{\Omega_e} \frac{\partial\{N\}}{\partial\eta_k}\frac{\partial\{N\}^T}{\partial\eta_m} \, d\Omega = \int_{-1}^{+1}\int_{-1}^{+1}\int_{-1}^{+1} \frac{\partial\{N\}}{\partial\eta_k}\frac{\partial\{N\}^T}{\partial\eta_m} \, d\eta_1 d\eta_2 d\eta_3 \qquad \text{(A12)}$$

In Eq. (A12), the 3-dimensional master matrix has two bases and each is differentiated. When combined with the metric data, the summation convention is applied to give the expanded expression

$$\begin{aligned} EJK\ EJM \left(\int_{\Omega_e} \frac{\partial\{N\}}{\partial\eta_k}\frac{\partial\{N\}^T}{\partial\eta_m} \, d\Omega \right) = EJK\ EJM\ [C2KM] = \\ [C211](E11\,E11 + E21\,E21 + E31\,E31) + \\ [C222](E12\,E12 + E22\,E22 + E32\,E32) + \\ [C233](E13\,E13 + E23\,E23 + E33\,E33) + \\ [C212](E11\,E12 + E21\,E22 + E31\,E32) + \\ [C221](E11\,E12 + E21\,E22 + E31\,E32) + \\ [C213](E11\,E13 + E21\,E23 + E31\,E33) + \\ [C231](E11\,E13 + E21\,E23 + E31\,E33) + \\ [C223](E12\,E13 + E22\,E23 + E32\,E33) + \\ [C232](E12\,E13 + E22\,E23 + E32\,E33) \end{aligned} \qquad \text{(A13)}$$

All of the required master matrices can be calculated and stored as a pre-processing step. The following examples were computed using a 5th-order gaussian quadrature rule.

$$[C200] = \frac{1}{27}\begin{bmatrix} 8 & 4 & 2 & 4 & 4 & 2 & 1 & 2 \\ 4 & 8 & 4 & 2 & 2 & 4 & 2 & 1 \\ 2 & 4 & 8 & 4 & 1 & 2 & 4 & 2 \\ 4 & 2 & 4 & 8 & 2 & 1 & 2 & 4 \\ 4 & 2 & 1 & 2 & 8 & 4 & 2 & 4 \\ 2 & 4 & 2 & 1 & 4 & 8 & 4 & 2 \\ 1 & 2 & 4 & 2 & 2 & 4 & 8 & 4 \\ 2 & 1 & 2 & 4 & 4 & 2 & 4 & 8 \end{bmatrix} \quad ; \quad [C201] = \frac{1}{18}\begin{bmatrix} -4 & 4 & 2 & -2 & -2 & 2 & 1 & -1 \\ -4 & 4 & 2 & -2 & -2 & 2 & 1 & -1 \\ -2 & 2 & 4 & -4 & -1 & 1 & 2 & -2 \\ -2 & 2 & 4 & -4 & -1 & 1 & 2 & -2 \\ -2 & 2 & 1 & -1 & -4 & 4 & 2 & -2 \\ -2 & 2 & 1 & -1 & -4 & 4 & 2 & -2 \\ -1 & 1 & 2 & -2 & -2 & 2 & 4 & -4 \\ -1 & 1 & 2 & -2 & -2 & 2 & 4 & -4 \end{bmatrix} \tag{A14}$$

$$[C202] = \frac{1}{18}\begin{bmatrix} -4 & -2 & 2 & 4 & -2 & -1 & 1 & 2 \\ -2 & -4 & 4 & 2 & -1 & -2 & 2 & 1 \\ -2 & -4 & 4 & 2 & -1 & -2 & 2 & 1 \\ -4 & -2 & 2 & 4 & -2 & -1 & 1 & 2 \\ -2 & -1 & 1 & 2 & -4 & -2 & 2 & 4 \\ -1 & -2 & 2 & 1 & -2 & -4 & 4 & 2 \\ -1 & -2 & 2 & 1 & -2 & -4 & 4 & 2 \\ -2 & -1 & 1 & 2 & -4 & -2 & 2 & 4 \end{bmatrix} \quad ; \quad [C203] = \frac{1}{18}\begin{bmatrix} -4 & -2 & -1 & -2 & 4 & 2 & 1 & 2 \\ -2 & -4 & -2 & -1 & 2 & 4 & 2 & 1 \\ -1 & -2 & -4 & -2 & 1 & 2 & 4 & 2 \\ -2 & -1 & -2 & -4 & 2 & 1 & 2 & 4 \\ -4 & -2 & -1 & -2 & 4 & 2 & 1 & 2 \\ -2 & -4 & -2 & -1 & 2 & 4 & 2 & 1 \\ -1 & -2 & -4 & -2 & 1 & 2 & 4 & 2 \\ -2 & -1 & -2 & -4 & 2 & 1 & 2 & 4 \end{bmatrix} \tag{A15}$$

$$[C211] = \frac{1}{18}\begin{bmatrix} 4 & -4 & -2 & 2 & 2 & -2 & -1 & 1 \\ -4 & 4 & 2 & -2 & -2 & 2 & 1 & -1 \\ -2 & 2 & 4 & -4 & -1 & 1 & 2 & -2 \\ 2 & -2 & -4 & 4 & 1 & -1 & -2 & 2 \\ 2 & -2 & -1 & 1 & 4 & -4 & -2 & 2 \\ -2 & 2 & 1 & -1 & -4 & 4 & 2 & -2 \\ -1 & 1 & 2 & -2 & -2 & 2 & 4 & -4 \\ 1 & -1 & -2 & 2 & 2 & -2 & -4 & 4 \end{bmatrix} \quad ; \quad [C212] = \frac{1}{12}\begin{bmatrix} 2 & 2 & -2 & -2 & 1 & 1 & -1 & -1 \\ -2 & -2 & 2 & 2 & -1 & -1 & 1 & 1 \\ -2 & -2 & 2 & 2 & -1 & -1 & 1 & 1 \\ 2 & 2 & -2 & -2 & 1 & 1 & -1 & -1 \\ 1 & 1 & -1 & -1 & 2 & 2 & -2 & -2 \\ -1 & -1 & 1 & 1 & -2 & -2 & 2 & 2 \\ -1 & -1 & 1 & 1 & -2 & -2 & 2 & 2 \\ 1 & 1 & -1 & -1 & 2 & 2 & -2 & -2 \end{bmatrix} \tag{A16}$$

$$[C213] = \frac{1}{12}\begin{bmatrix} 2 & 2 & 1 & 1 & -2 & -2 & -1 & -1 \\ -2 & -2 & -1 & -1 & 2 & 2 & 1 & 1 \\ -1 & -1 & -2 & -2 & 1 & 1 & 2 & 2 \\ 1 & 1 & 2 & 2 & -1 & -1 & -2 & -2 \\ 2 & 2 & 1 & 1 & -2 & -2 & -1 & -1 \\ -2 & -2 & -1 & -1 & 2 & 2 & 1 & 1 \\ -1 & -1 & -2 & -2 & 1 & 1 & 2 & 2 \\ 1 & 1 & 2 & 2 & -1 & -1 & -2 & -2 \end{bmatrix} \quad ; \quad [C223] = \frac{1}{12}\begin{bmatrix} 2 & 1 & 1 & 2 & -2 & -1 & -1 & -2 \\ 1 & 2 & 2 & 1 & -1 & -2 & -2 & -1 \\ -1 & -2 & -2 & -1 & 1 & 2 & 2 & 1 \\ -2 & -1 & -1 & -2 & 2 & 1 & 1 & 2 \\ 2 & 1 & 1 & 2 & -2 & -1 & -1 & -2 \\ 1 & 2 & 2 & 1 & -1 & -2 & -2 & -1 \\ -1 & -2 & -2 & -1 & 1 & 2 & 2 & 1 \\ -2 & -1 & -1 & -2 & 2 & 1 & 1 & 2 \end{bmatrix} \tag{A17}$$

Expressions involving the interpolation of two state-variables, such as the kinematic flux vector term, produce a special master matrix called a *hypermatrix*, e.g.,

$$
\begin{aligned}
&-\Delta t\ \{UJ\}^T \int_{\Omega_e} \{N\} \frac{\partial \eta_k}{\partial x_j} \frac{\partial \{N\}}{\partial \eta_k} \{N\}^T \det[J]\ d\Omega\ \{UI\} \approx \\
&-\Delta t\ DET_e\ EJK_e\ \{UJ\}_e^T \left(\int_{\Omega_e} \{N\} \frac{\partial \{N\}}{\partial \eta_k} \{N\}^T\ d\Omega \right) \{UI\}_e = \\
&-\Delta t\ DET_e\ EJK_e\ \{UJ\}_e^T [C30K0]\ \{UI\}_e
\end{aligned}
\tag{A18}
$$

where the elements of the three [*C*30K0] hypermatrices are 8×1 column vectors, e.g.,

$$
[C3010] = \frac{1}{216}
\begin{bmatrix}
\begin{pmatrix}-18\\-9\\-3\\-6\\-6\\-3\\-1\\-2\end{pmatrix} & \begin{pmatrix}-9\\-18\\-6\\-3\\-3\\-6\\-2\\-1\end{pmatrix} & \begin{pmatrix}-3\\-6\\-6\\-3\\-1\\-2\\-2\\-1\end{pmatrix} & \begin{pmatrix}-6\\-3\\-3\\-6\\-2\\-1\\-1\\-2\end{pmatrix} & \begin{pmatrix}-6\\-3\\-1\\-2\\-6\\-3\\-1\\-2\end{pmatrix} & \begin{pmatrix}-3\\-6\\-2\\-1\\-3\\-6\\-2\\-1\end{pmatrix} & \begin{pmatrix}-1\\-2\\-2\\-1\\-1\\-2\\-2\\-1\end{pmatrix} & \begin{pmatrix}-2\\-1\\-1\\-2\\-2\\-1\\-1\\-2\end{pmatrix} \\
\begin{pmatrix}18\\9\\3\\6\\6\\3\\1\\2\end{pmatrix} & \begin{pmatrix}9\\18\\6\\3\\3\\6\\2\\1\end{pmatrix} & \begin{pmatrix}3\\6\\6\\3\\1\\2\\2\\1\end{pmatrix} & \begin{pmatrix}6\\3\\3\\6\\2\\1\\1\\2\end{pmatrix} & \begin{pmatrix}6\\3\\1\\2\\6\\3\\1\\2\end{pmatrix} & \begin{pmatrix}3\\6\\2\\1\\3\\6\\2\\1\end{pmatrix} & \begin{pmatrix}1\\2\\2\\1\\1\\2\\2\\1\end{pmatrix} & \begin{pmatrix}2\\1\\1\\2\\2\\1\\1\\2\end{pmatrix} \\
\vdots & \vdots & \vdots & \vdots & \vdots & \vdots & \vdots & \vdots \\
\vdots & \vdots & \vdots & \vdots & \vdots & \vdots & \vdots & \vdots \\
\vdots & \vdots & \vdots & \vdots & \vdots & \vdots & \vdots & \vdots \\
\vdots & \vdots & \vdots & \vdots & \vdots & \vdots & \vdots & \vdots \\
\vdots & \vdots & \vdots & \vdots & \vdots & \vdots & \vdots & \vdots \\
\begin{pmatrix}-2\\-1\\-1\\-2\\-2\\-1\\-1\\-2\end{pmatrix} & \begin{pmatrix}-1\\-2\\-2\\-1\\-1\\-2\\-2\\-1\end{pmatrix} & \begin{pmatrix}-1\\-2\\-6\\-3\\-1\\-2\\-6\\-3\end{pmatrix} & \begin{pmatrix}-2\\-1\\-3\\-6\\-2\\-1\\-3\\-6\end{pmatrix} & \begin{pmatrix}-2\\-1\\-1\\-2\\-6\\-3\\-3\\-6\end{pmatrix} & \begin{pmatrix}-1\\-2\\-2\\-1\\-3\\-6\\-6\\-3\end{pmatrix} & \begin{pmatrix}-1\\-2\\-6\\-3\\-6\\-18\\-9\end{pmatrix} & \begin{pmatrix}-2\\-1\\-3\\-6\\-6\\-3\\-9\\-18\end{pmatrix}
\end{bmatrix}
\tag{A19}
$$

$$[C3020] = \frac{1}{216}\begin{bmatrix}
\begin{pmatrix}-18\\-6\\-3\\-9\\-6\\-2\\-1\\-3\end{pmatrix} & \begin{pmatrix}-6\\-6\\-3\\-3\\-2\\-2\\-1\\-1\end{pmatrix} & \begin{pmatrix}-3\\-3\\-6\\-6\\-1\\-1\\-2\\-2\end{pmatrix} & \begin{pmatrix}-9\\-3\\-6\\-18\\-3\\-1\\-2\\-6\end{pmatrix} & \begin{pmatrix}-6\\-2\\-1\\-3\\-6\\-2\\-1\\-3\end{pmatrix} & \begin{pmatrix}-2\\-2\\-1\\-1\\-2\\-2\\-1\\-1\end{pmatrix} & \begin{pmatrix}-1\\-1\\-2\\-2\\-1\\-1\\-2\\-2\end{pmatrix} & \begin{pmatrix}-3\\-1\\-2\\-6\\-3\\-1\\-2\\-6\end{pmatrix} \\
\begin{pmatrix}-6\\-6\\-3\\-3\\-2\\-2\\-1\\-1\end{pmatrix} & \begin{pmatrix}-6\\-18\\-9\\-3\\-2\\-6\\-3\\-1\end{pmatrix} & \begin{pmatrix}-3\\-9\\-18\\-6\\-1\\-3\\-6\\-2\end{pmatrix} & \begin{pmatrix}-3\\-3\\-6\\-6\\-1\\-1\\-2\\-2\end{pmatrix} & \begin{pmatrix}-2\\-2\\-1\\-1\\-2\\-2\\-1\\-1\end{pmatrix} & \begin{pmatrix}-2\\-6\\-3\\-1\\-2\\-6\\-3\\-1\end{pmatrix} & \begin{pmatrix}-1\\-3\\-6\\-2\\-1\\-3\\-6\\-2\end{pmatrix} & \begin{pmatrix}-1\\-1\\-2\\-2\\-1\\-1\\-2\\-2\end{pmatrix} \\
\begin{pmatrix}\vdots\end{pmatrix} & \begin{pmatrix}\vdots\end{pmatrix} & \begin{pmatrix}\vdots\end{pmatrix} & \begin{pmatrix}\vdots\end{pmatrix} & \begin{pmatrix}\vdots\end{pmatrix} & \begin{pmatrix}\vdots\end{pmatrix} & \begin{pmatrix}\vdots\end{pmatrix} & \begin{pmatrix}\vdots\end{pmatrix} \\
\begin{pmatrix}\vdots\end{pmatrix} & \begin{pmatrix}\vdots\end{pmatrix} & \begin{pmatrix}\vdots\end{pmatrix} & \begin{pmatrix}\vdots\end{pmatrix} & \begin{pmatrix}\vdots\end{pmatrix} & \begin{pmatrix}\vdots\end{pmatrix} & \begin{pmatrix}\vdots\end{pmatrix} & \begin{pmatrix}\vdots\end{pmatrix} \\
\begin{pmatrix}\vdots\end{pmatrix} & \begin{pmatrix}\vdots\end{pmatrix} & \begin{pmatrix}\vdots\end{pmatrix} & \begin{pmatrix}\vdots\end{pmatrix} & \begin{pmatrix}\vdots\end{pmatrix} & \begin{pmatrix}\vdots\end{pmatrix} & \begin{pmatrix}\vdots\end{pmatrix} & \begin{pmatrix}\vdots\end{pmatrix} \\
\begin{pmatrix}\vdots\end{pmatrix} & \begin{pmatrix}\vdots\end{pmatrix} & \begin{pmatrix}\vdots\end{pmatrix} & \begin{pmatrix}\vdots\end{pmatrix} & \begin{pmatrix}\vdots\end{pmatrix} & \begin{pmatrix}\vdots\end{pmatrix} & \begin{pmatrix}\vdots\end{pmatrix} & \begin{pmatrix}\vdots\end{pmatrix} \\
\begin{pmatrix}6\\2\\1\\3\\6\\2\\1\\3\end{pmatrix} & \begin{pmatrix}2\\2\\1\\1\\2\\2\\1\\1\end{pmatrix} & \begin{pmatrix}1\\1\\2\\2\\1\\1\\2\\2\end{pmatrix} & \begin{pmatrix}3\\1\\2\\6\\3\\1\\2\\6\end{pmatrix} & \begin{pmatrix}6\\2\\1\\3\\18\\6\\3\\9\end{pmatrix} & \begin{pmatrix}2\\2\\1\\1\\6\\6\\3\\3\end{pmatrix} & \begin{pmatrix}1\\1\\2\\2\\3\\3\\6\\6\end{pmatrix} & \begin{pmatrix}3\\1\\2\\6\\9\\3\\6\\18\end{pmatrix}
\end{bmatrix} \quad \textbf{(A20)}$$

$$[C3030] = \frac{1}{216}\begin{bmatrix}
\begin{pmatrix}-18\\-6\\-2\\-6\\-9\\-3\\-1\\-3\end{pmatrix} & \begin{pmatrix}-6\\-6\\-2\\-2\\-3\\-3\\-1\\-1\end{pmatrix} & \begin{pmatrix}-2\\-2\\-2\\-2\\-1\\-1\\-1\\-1\end{pmatrix} & \begin{pmatrix}-6\\-2\\-2\\-6\\-3\\-1\\-1\\-3\end{pmatrix} & \begin{pmatrix}-9\\-3\\-1\\-3\\-18\\-6\\-2\\-6\end{pmatrix} & \begin{pmatrix}-3\\-3\\-1\\-1\\-6\\-6\\-2\\-2\end{pmatrix} & \begin{pmatrix}-1\\-1\\-1\\-1\\-2\\-2\\-2\\-2\end{pmatrix} & \begin{pmatrix}-3\\-1\\-1\\-3\\-6\\-2\\-2\\-6\end{pmatrix} \\
\begin{pmatrix}-6\\-6\\-2\\-2\\-3\\-3\\-1\\-1\end{pmatrix} & \begin{pmatrix}-6\\-18\\-6\\-2\\-3\\-9\\-3\\-1\end{pmatrix} & \begin{pmatrix}-2\\-6\\-6\\-2\\-1\\-3\\-3\\-1\end{pmatrix} & \begin{pmatrix}-2\\-2\\-2\\-2\\-1\\-1\\-1\\-1\end{pmatrix} & \begin{pmatrix}-3\\-3\\-1\\-1\\-6\\-6\\-2\\-2\end{pmatrix} & \begin{pmatrix}-3\\-9\\-3\\-1\\-6\\-18\\-6\\-2\end{pmatrix} & \begin{pmatrix}-1\\-3\\-3\\-1\\-2\\-6\\-6\\-2\end{pmatrix} & \begin{pmatrix}-1\\-1\\-1\\-1\\-2\\-2\\-2\\-2\end{pmatrix} \\
(\vdots) & (\vdots) & (\vdots) & (\vdots) & (\vdots) & (\vdots) & (\vdots) & (\vdots) \\
(\vdots) & (\vdots) & (\vdots) & (\vdots) & (\vdots) & (\vdots) & (\vdots) & (\vdots) \\
(\vdots) & (\vdots) & (\vdots) & (\vdots) & (\vdots) & (\vdots) & (\vdots) & (\vdots) \\
(\vdots) & (\vdots) & (\vdots) & (\vdots) & (\vdots) & (\vdots) & (\vdots) & (\vdots) \\
(\vdots) & (\vdots) & (\vdots) & (\vdots) & (\vdots) & (\vdots) & (\vdots) & (\vdots) \\
\begin{pmatrix}6\\2\\2\\6\\3\\1\\1\\3\end{pmatrix} & \begin{pmatrix}2\\2\\2\\2\\1\\1\\1\\1\end{pmatrix} & \begin{pmatrix}2\\2\\6\\6\\1\\1\\3\\3\end{pmatrix} & \begin{pmatrix}6\\2\\6\\18\\3\\1\\3\\9\end{pmatrix} & \begin{pmatrix}3\\1\\1\\3\\6\\2\\2\\6\end{pmatrix} & \begin{pmatrix}1\\1\\1\\1\\2\\2\\2\\2\end{pmatrix} & \begin{pmatrix}1\\1\\3\\3\\2\\2\\6\\6\end{pmatrix} & \begin{pmatrix}3\\1\\3\\9\\6\\2\\6\\18\end{pmatrix}
\end{bmatrix} \quad \textbf{(A21)}$$

The premultiplication of [C30K0] is executed by forming the inner products of $\{UJ\}^T$ with each of the column-vector elements in the hypermatrix, resulting in a 8×8 scalar matrix.

A.3 SUMMARY

The following is a summary of the compact notation used in this dissertation.

Metric Data

$DET_e \equiv$ the determinant of the transformation Jacobian evaluated at the centroid of the element

$EIJ_e \equiv$ the (i,j) element of the inverse of the transformation Jacobian $\left[\frac{\partial \eta_j}{\partial x_i}\right]$ evaluated at the centroid of the element

Mass Matrix

$$[C200] \equiv \int_{-1}^{+1}\int_{-1}^{+1}\int_{-1}^{+1} \{N\}\{N\}^T d\eta_1 d\eta_2 d\eta_3$$

Gradient Matrices

$$[C201] = [C210]^T \equiv \int_{-1}^{+1}\int_{-1}^{+1}\int_{-1}^{+1} \{N\}\frac{\partial \{N\}^T}{\partial \eta_1} d\eta_1 d\eta_2 d\eta_3$$

$$[C202] = [C220]^T \equiv \int_{-1}^{+1}\int_{-1}^{+1}\int_{-1}^{+1} \{N\}\frac{\partial \{N\}^T}{\partial \eta_2} d\eta_1 d\eta_2 d\eta_3$$

$$[C203] = [C230]^T \equiv \int_{-1}^{+1}\int_{-1}^{+1}\int_{-1}^{+1} \{N\}\frac{\partial \{N\}^T}{\partial \eta_3} d\eta_1 d\eta_2 d\eta_3$$

Diffusion Matrices

$$[C211] \equiv \int_{-1}^{+1}\int_{-1}^{+1}\int_{-1}^{+1} \frac{\partial\{N\}}{\partial\eta_1}\,\frac{\partial\{N\}^T}{\partial\eta_1}\,d\eta_1 d\eta_2 d\eta_3$$

$$[C222] \equiv \int_{-1}^{+1}\int_{-1}^{+1}\int_{-1}^{+1} \frac{\partial\{N\}}{\partial\eta_2}\,\frac{\partial\{N\}^T}{\partial\eta_2}\,d\eta_1 d\eta_2 d\eta_3$$

$$[C233] \equiv \int_{-1}^{+1}\int_{-1}^{+1}\int_{-1}^{+1} \frac{\partial\{N\}}{\partial\eta_3}\,\frac{\partial\{N\}^T}{\partial\eta_3}\,d\eta_1 d\eta_2 d\eta_3$$

$$[C212] = [C221]^T \equiv \int_{-1}^{+1}\int_{-1}^{+1}\int_{-1}^{+1} \frac{\partial\{N\}}{\partial\eta_1}\,\frac{\partial\{N\}^T}{\partial\eta_2}\,d\eta_1 d\eta_2 d\eta_3$$

$$[C213] = [C231]^T \equiv \int_{-1}^{+1}\int_{-1}^{+1}\int_{-1}^{+1} \frac{\partial\{N\}}{\partial\eta_1}\,\frac{\partial\{N\}^T}{\partial\eta_3}\,d\eta_1 d\eta_2 d\eta_3$$

$$[C223] = [C232]^T \equiv \int_{-1}^{+1}\int_{-1}^{+1}\int_{-1}^{+1} \frac{\partial\{N\}}{\partial\eta_2}\,\frac{\partial\{N\}^T}{\partial\eta_3}\,d\eta_1 d\eta_2 d\eta_3$$

Convection Matrices

$$[C3010] \equiv \int_{-1}^{+1}\int_{-1}^{+1}\int_{-1}^{+1} \{N\}\frac{\partial\{N\}}{\partial\eta_1}\,\{N\}^T\,d\eta_1 d\eta_2 d\eta_3$$

$$[C3020] \equiv \int_{-1}^{+1}\int_{-1}^{+1}\int_{-1}^{+1} \{N\}\frac{\partial\{N\}}{\partial\eta_2}\,\{N\}^T\,d\eta_1 d\eta_2 d\eta_3$$

$$[C3030] \equiv \int_{-1}^{+1}\int_{-1}^{+1}\int_{-1}^{+1} \{N\}\frac{\partial\{N\}}{\partial\eta_3}\,\{N\}^T\,d\eta_1 d\eta_2 d\eta_3$$

INTERNAL DISTRIBUTION

1. S. T. Baker
2. J. P. Brady
3. K. W. Childs
4. J. H. Clinton
5. J. S. Crowell
6. R. D. Dabbs
7. J. B. Drake
8. J. D. Freels
9. G. E. Giles
10. D. M. Hetrick
11. J. T. Holdeman
12. J. A. Holmes
13. J. R. Kirkpatrick
14. B. L. Lepard, Jr.
15. A. T. Lucas
16. G. S. McNeilly
17. J. E. Park
18. S. H. Park

19-21. C. H. Shappert

22. M. Siman-Tov
23. T. K. Stovall
24. M. J. Taylor
25. R. C. Ward
26. M. W. Wendel
27. R. M. Widgeon
28. K. E. Wilkes

29-38. P. T. Williams

39. G. L. Yoder, Jr.
40. Central Research Library
41. ORNL Y-12 Research Library Document Reference Section
42. Laboratory Records Department
43. Laboratory Records, ORNL (RC)
44. ORNL Patent Office

EXTERNAL DISTRIBUTION

45. Office of the Deputy Assistant Manager for Energy, Research and Development, Department of Energy, Oak Ridge Operations (DOE-ORO), P.O. Box 2008, Oak Ridge, TN 37831-6269.

46-47. Office of Scientific and Technical Information, P.O. Box 62, Oak Ridge, TN 37831.

DATE
FILMED
1/4/94
END